Lead Halide Perovskite Nanocrystals: Enhancing Commercial Viability for Light-Emitting Applications

Alasdair Angus Macintyre Brown

PhD Thesis, November 2020

UNIVERSITY OF Southampton

University of Southampton

Faculty of Engineering and Physical Sciences

School of Engineering

Lead Halide Perovskite Nanocrystals: Enhancing Commercial Viability for Light-Emitting Applications

by

Alasdair Angus Macintyre Brown

ORCID ID: 0000-0002-0714-3851

Thesis for the degree of Doctor of Philosophy

Supervisors: Dr Suan Hui Pu and Prof Liudi Jiang

November 2020

University of Southampton

Abstract

Faculty of Engineering and Physical Sciences

School of Engineering

Doctor of Philosophy

Lead Halide Perovskite Nanocrystals: Enhancing Commercial Viability for Light-Emitting Applications

by

Alasdair Angus Macintyre Brown

Lead halide perovskite nanocrystals (NCs) have exhibited exceptional optoelectronic properties, which are extremely attractive for light-emitting applications. However, inadequate surface passivation and elaborate high-temperature preparation hinder their commercial viability. This project sought to address these problems by investigating and exploiting a promising alternative ligand, octylphosphonic acid (OPA).

Through an initial ligand exchange approach, the mechanism of OPA binding to the surface of $CsPbBr_3$ nanocrystals was revealed. Deprotonation of OPA resulted in an anionic phosphonate moiety, which bound to under-coordinated Pb^{2+} sites. The remaining two free functional groups on the bound ligand promoted the assembly an inter-ligand hydrogen-bonded network. These extensive ligand connections provided a novel mechanism for the passivation of perovskite nanocrystals. This OPA passivation significantly enhanced the photoluminescence quantum yield (PLQY), and the retention of PLQY through antisolvent purification.

An antisolvent purification protocol was devised to enable the fabrication of high-efficiency light-emitting diodes (LEDs) from OPA-passivated $CsPbBr_3$ nanocrystals. A second purification cycle with acetonitrile was crucial, improving the external quantum efficiency (EQE) of OPA-modified NCs from 2.0 % to 7.7 %. Without OPA, the EQE of twice-purified NCs was only 3.6 %; the efficiency enhancement provided by OPA was attributed to a combination of more robust surface passivation and the replacement of long oleyl ligands for less-resistive octyls.

Following these promising results, a new protocol was devised which could prepare OPA-capped $CsPbBr_3$ nanocrystals directly at room temperature for the first time. An understanding of the influence of OPA on the thermodynamics of nucleation and the kinetics of growth facilitated precise control over the nanocrystal diameter. The photoluminescence emission wavelength was tuned from 501 and 517 nm by adjusting the nanocrystal diameter between 6.6 and 13 nm. Vitally, PLQY was maintained above 80 % for all sizes, and the bandwidth remained very narrow (16 to 19 nm). Judicious size tuneability had not previously been achieved for perovskite nanocrystals without using a high temperature synthesis. The developed method attained excellent optoelectronic properties in a more efficient, less complicated, and less costly manner than the common high-temperature, hot-injection approaches. Furthermore, the versatility of the synthetic framework designed offers an excellent foundation to tailor the nanocrystal properties for specific technologies.

Ultimately, this work presented a clear enhancement of the commercial prospects of perovskite nanocrystals for both optically and electrically-driven applications. Currently, the stability of perovskite nanocrystals under electric field remains far below the necessary standards for commercial electrically-driven applications. In contrast, the flexible, cost-effective production of highly emissive nanocrystals exhibited herein could contribute towards their imminent inclusion in consumer electronics, as down-converters or colour filters for wide colour gamut displays.

Table of Contents

List of Tables

List of Figures

List of Figures

Research Thesis: Declaration of Authorship

Print name: Alasdair Angus Macintyre Brown

Title of thesis: Lead Halide Perovskite Nanocrystals: Enhancing Commercial Viability for Light-Emitting Applications

I declare that this thesis and the work presented in it are my own and has been generated by me as the result of my own original research.

I confirm that:

1. This work was done wholly or mainly while in candidature for a research degree at this University;
2. Where any part of this thesis has previously been submitted for a degree or any other qualification at this University or any other institution, this has been clearly stated;
3. Where I have consulted the published work of others, this is always clearly attributed;
4. Where I have quoted from the work of others, the source is always given. With the exception of such quotations, this thesis is entirely my own work;
5. I have acknowledged all main sources of help;
6. Where the thesis is based on work done by myself jointly with others, I have made clear exactly what was done by others and what I have contributed myself;
7. Parts of this work have been published as:-

Brown, A. A. M., Hooper, T. J. N., Veldhuis, S. A., Chin, X. Y., Bruno, A., Vashishtha, P., Tey, J. N., Jiang, L., Damodaran, B., Pu, S. H., Mhaisalkar, S. G., Mathews, N.; Self-assembly of a robust hydrogen-bonded octylphosphonate network on cesium lead bromide perovskite nanocrystals for light-emitting diodes; ***Nanoscale***, 2019, **11**, 12370-12380

Brown, A. A. M., Damodaran, B., Jiang, L., Tey, J. N., Pu, S. H., Mathews, N., Mhaisalkar, S. G.; Lead Halide Perovskite Nanocrystals: Room Temperature Syntheses toward Commercial Viability; ***Advanced Energy Materials***, 2020, 10(34), 2001349

Signature: ..... Date: .....

Acknowledgements

The author would like to take this opportunity to briefly abandon the passive voice.

I was fortunate to have had something of a supervisory cohort throughout my PhD, each of whom kindly shared their expertise and guidance at various points over the course of 38 months.

Firstly, I would like to thank my primary supervisor, Dr Suan Hui Pu. I am grateful for the opportunities you have given me, and for your valuable advice and insights. I greatly appreciate the independence and freedom I was granted to steer the project and pursue my research interests. To my secondary supervisor, Prof Liudi Jiang, I am thankful for your guidance in the first few months in Southampton, which helped me find my feet. I would also like to thank my supervisor at A*STAR, Dr Ju Nie Tey, for your advice and assistance during my 2 years attached to SIMTech.

Next, I address my supervisors, mentors, and colleagues at Nanyang Technological University. To Profs. Nripan Mathews and Subodh Mhaisalkar, I am very thankful that you welcomed me into your group. Most of the work in this thesis would have been impossible without the facilities at NTU, while your generous support over the last year was much appreciated. Dr Sjoerd Veldhuis, my supervisor for the first 6 months, you were the first to point me in the direction of $CsPbBr_3$ nanocrystals and the ideas you shared with me before you left inspired a lot of my work. Dr Xin Yu Chin, the device guru, thank you for all of the insights you shared with me; you helped my chemistry brain adapt to device physics and were always willing to answer my many inquiries. Dr Bahulayan Damodaran, I greatly appreciate your support and guidance. You were always willing to discuss my ideas or concerns, and your chemistry knowledge was invaluable. Dr Parth Vashishtha, thank you for our many discussions, the many many TEM images you helped take, and the fruitful collaboration.

To all of the members of the LED group, Drs Yan Fong, Fadilah, Anil and Natalia, I am grateful to have been part of team where everyone was always helpful, friendly and open to discussion. As the most junior member of the group, I know I benefited enormously from your shared experience, and I thank you all. And to Dr Tom Hooper, I enjoyed our many conversations, especially those where we puzzled over the NMR spectra. NMR became a key part of this work, and your expertise was undoubtedly essential.

To Deb, thank you for all your support throughout my time in Singapore. Your friendship invariably eased the pressures and stresses of PhD life, and your encouragement helped keep me motivated. I know I will look back fondly on my time here.

Lastly, to my friends and family, I am grateful that so many of you came all the way to Singapore just to visit me. Your video calls helped me retain my sanity, especially during this challenging pandemic. I am happy that I will soon be back home, and I am hopeful that I will see a lot more of all of you in person over the coming years.

Abbreviations

3D.....Three Dimensional

ACN .....Acetonitrile

AO .....Atomic Orbital

ATR.....Attenuated Total Reflection

BBO .....β-barium borate

BuOAc .....Butyl acetate

CBM .....Conduction Band Minimum

CNT .....Classical Nucleation Theory

CP.....Cross Polarisation

DDAB.....Didodecyldimethylammonium Bromide

DFT.....Density Functional Theory

DMF .....Dimethylformamide

DMSO.....Dimethylsulfoxide

EtOAc .....Ethyl Acetate

EXE .....External Quantum Efficiency

FA.....Formamidinium

FTIR .....Fourier Transform Infrared Spectroscopy

HETCOR .....Heteronuclear Correlation

HOMO .....Highest Occupied Molecular Orbital

IQE .....Internal Quantum Efficiency

ITO.....Indium Tin Oxide

LARP.....Ligand-Assisted Reprecipitation

LED .....Light-Emitting Diode

LUMO.....Lowest Unoccupied Molecular Orbital

MA .....Methylammonium

MAS.....Magic Angle Spinning

Abbreviations

MeOAc ..... Methyl Acetate

MO ..... Molecular Orbital

NC..... Nanocrystal

NMR ..... Nuclear Magnetic Resonance

OA ..... Oleic Acid

OAm ..... Oleylamine

OAmHBr ..... Oleylammonium Bromide

OctAc..... Octanoic Acid

OctAm ..... Octylamine

ODE ..... Octadecene

OPA ..... Octylphosphonic Acid

PL..... Photoluminescence

PLQY ..... Photoluminescence Quantum Yield

QLED..... Quantum Dot Light-Emitting Diode Display

SAXS ..... Small-Angle X-ray Scattering

TA ..... Transient Absorption

TEM ..... Transmission Electron Microscopy

TGA..... Thermogravimetric Analysis

TOAB ..... Tetraoctylammonium Bromide

TOPO ..... Trioctylphosphine Oxide

TRPL..... Time-Resolved Photoluminescence

UV..... Ultraviolet

VBM..... Valence Band Maximum

XRD..... X-ray Diffraction

XPS ..... X-ray Photoelectron Spectroscopy

Chapter 1 Introduction

1.1 Motivations and Aims

Lead halide perovskite nanocrystals have recently emerged as excellent light-emitting materials.[1–6] They have exhibited extremely narrow emission bandwidths, narrower than currently achievable with state-of-the-art chalcogenide quantum dots, while also obtaining photoluminescence quantum yields (PLQYs) close to 100 %. These two properties highlight their enormous potential to facilitate next-generation wide colour gamut display technologies.[7–10] However, perovskite nanocrystals also offer economically attractive features; they can be prepared from relatively low-cost precursor salts, and their defect tolerant nature provides inherent compatibility with solution-processing techniques. Overall, perovskite nanocrystals have presented exciting potential for future commercial light-emitting applications.

There are some key concerns still holding perovskite nanocrystals back from realising their potential and demonstrating their commercial viability. It has been established that the typical ligands used to passivate the surface of perovskite nanocrystals are prone to facile desorption due to weak, dynamic binding. This fatally compromises their long-term stability and makes it impossible to purify the nanocrystal solutions fully. It is crucial that an understanding of surface-ligand interactions is developed, such that criteria for strong ligand binding to the ionic perovskite surface can be established. Robust ligand attachment is vital for commercially viable nanocrystals.

For electrically-driven light-emitting applications, the conductivity of nanocrystal thin films is an additional essential property. Often the weak binding ligands typically employed have long oily organic components, which are highly resistive and can disrupt the formation of dry, uniform nanocrystal thin-films. It is essential to identify and successfully employ less resistive ligands so that higher efficiency light-emitting diodes can be achieved. The removal of excess unbound ligand material during purification is also vital for device applications. This is closely linked to the binding strength, as bound ligands must remain on the nanocrystal surface while polar solvents remove unbound ligands. Therefore, ultimately, shorter, strong-binding ligands must be discovered to advance the realistic commercial prospects of perovskite nanocrystal materials.

Lastly, it is also important to consider the synthesis conditions of the nanocrystals. All-inorganic cesium-based perovskite nanocrystals ($CsPbX_3$ NCs, X = Cl, Br, I) are undoubtedly the most stable composition and are therefore widely considered the most realistic option for commercial applications.[11–13] Yet, most reported $CsPbX_3$ NCs are synthesised at high temperature (> 140 °C) under inert gas according to the "hot-injection" method.[14,15] Although this method has

demonstrated reliable control over nanocrystal size and achieves high-quality optoelectronic properties, it inherently hinders commercial viability. To fully exploit the potential of perovskite nanocrystals for ambient solution-processing, a room temperature synthesis method should be developed, which can obtain the same exceptional properties and judicious size control offered by high-temperature protocols. One of the critical challenges is to manipulate nucleation and growth processes, such that the nanocrystal diameter can be modulated without temperature variation. This size tuneability must be attained without compromising PLQY, colloidal stability, or reaction yield. Moreover, this should ideally be achieved with short, strong-binding ligands.

In summary, there are two central aims of this work:

1. To replace long, resistive, weak binding ligands with shorter, more conductive, strong binding ligands, develop an understanding of the more robust binding mechanism, and demonstrate enhanced light-emitting diode efficiency.
2. To employ these strong-binding ligands in an open-air, room temperature nanocrystal synthesis, achieving comparable optoelectronic properties and tuneability to the high temperature, hot-injection protocol.

1.2 Thesis Structure

This thesis begins with an overview of the key theoretical basis for the topics discussed in later chapters. The intention is for this to support the reader's understanding of the experimental results and proposed hypotheses. This section will briefly explain the electronic structure of semiconductors and how this relates to their optoelectronic properties, first generally, and then specifically for nanocrystals. The theory underpinning colloidal syntheses and thin-film light-emitting diodes will be discussed, followed by a description of the key properties of lead halide perovskites, and their nanocrystals.

Chapter 2 is a literature review focused on the synthesis of lead halide perovskite nanocrystals, particularly those conducted under ambient conditions, and the development of ligand engineering approaches.

The first research chapter (Chapter 3) discusses the development of a ligand exchange protocol to substitute native weak binding ligands from the $CsPbBr_3$ nanocrystal surface, replacing them with strong-binding octylphosphonic acid (OPA) ligands, and subsequently studying their binding mechanism. Chapter 4 devises and optimises a purification protocol for the OPA-capped $CsPbBr_3$ NCs, assessing the efficacy of purification by analysing the characteristics of light-emitting diodes. Chapter 5 builds upon the previous two chapters, designing a room temperature synthesis to obtain high-quality $CsPbBr_3$ nanocrystals passivated by OPA ligands. The extent of size tuneability, and the influence of OPA on the nucleation and growth of the nanocrystals, were investigated.

The penultimate chapter (Chapter 6) presented a critical analysis of some promising future research directions to enhance the commercial viability of perovskite nanocrystals further. The final chapter (Chapter 7) examined the limitations of this thesis, how it could be improved and expanded upon in future, and ends with the key conclusions drawn from the work as a whole.

1.3 Light-Emitting Semiconductor Nanocrystals: Theoretical Foundations

What is a perovskite? If you were to ask a geologist, they might explain that "perovskite" describes a class of mineral. This mineral was first discovered in the Ural mountains in 1839 and is abundant in the Earth's mantle, hundreds of kilometres below us.[16] But here on the surface, and in the modern-day, perovskites are abundant at the forefront of scientific research. From a chemist's perspective, a perovskite is any material which adheres to the same crystal structure as calcium titanate ($CaTiO_3$).[17] Therefore, there is a wide range of different perovskites with a plethora of interesting and useful properties. For example, barium titanate ($BaTiO_3$) has a high dielectric constant and is ferroelectric,[18] some cuprate perovskites are high-temperature superconductors (e.g. $YBa_2Cu_3O_{(7-x)}$),[19] and some manganese oxide perovskites exhibit colossal magnetoresistance.[20] However, over the last decade, for many *perovskite* has become increasingly synonymous with specifically the metal halide variety.

Metal halide perovskites are semiconductors, whose emergence in 2009 sparked a race within academia to exploit their outstanding properties for numerous applications.[21] This thesis will discuss the study of lead halide perovskite nanocrystals, exploring various means to enhance their commercial viability towards light-emitting applications. This chapter will concisely overview semiconductor theory and semiconductor nanocrystals, explaining their relevance for light emission. This will be followed by an introduction to lead halide perovskites, reviewing recent progress on the synthesis, surface chemistry and light-emitting diode performance of perovskite nanocrystals. The introduction will conclude with a brief explanation of the fundamental spectroscopic tools that have been utilised in this research, to provide a foundation from which the results of this work can be most easily understood.

1.3.1 Semiconductors

Semiconductors are conveniently well-named; they are materials whose conductivity lies between that of good conductors (i.e. metals) and poor conductors (i.e. insulators: glass). The physics behind this medium conductivity bestows exceptional versatility, which has led to semiconductors becoming the backbone of the electronics industry, spanning a broad range of applications.

1.3.1.1 Electronic Structure

To understand why semiconductivity is such a useful property, it is crucial to look at their electronic structure.[22] Starting from the basic building block of any material, an atom, quantum mechanics predicts defined volumes of space around the nucleus where electrons of specific quantised energies and momenta have a high probability (> 90 %) of being found. These defined volumes are named orbitals. An isolated atom would have a set of atomic orbitals (AOs), each of which can contain a maximum of 2 electrons. But atoms are rarely found isolated, and it is the interaction of atomic orbitals that is the fundamental basis of chemistry.

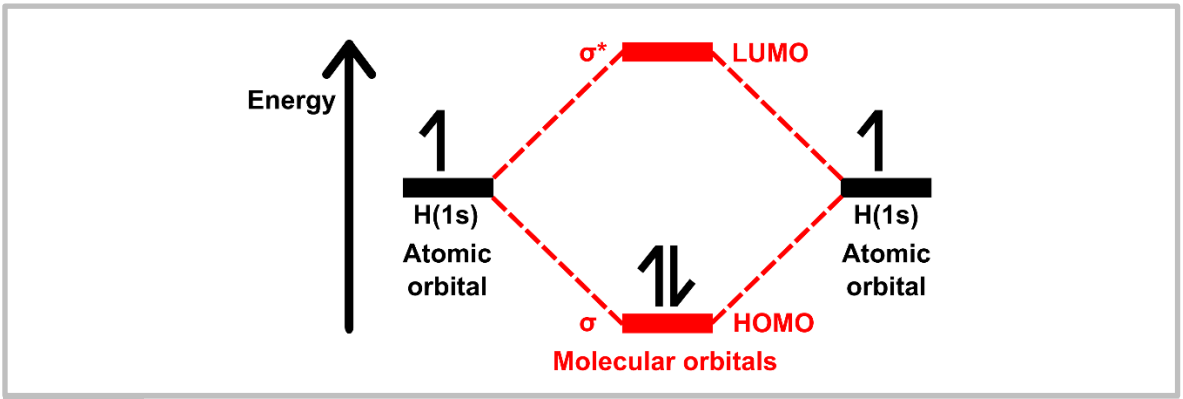

Figure 1.1 **Molecular orbital diagram for dihydrogen**

The highest energy electrons have atomic orbitals with the highest average distance from the nucleus. When atoms interact, it is these highest-energy *frontier* orbitals that participate. When multiple atoms combine to form a molecule, their respective frontier atomic orbitals combine to form a new set of orbitals. The formation of these molecular orbitals (MOs) can be understood by invoking the nomenclature of waves, as validated by the wave-particle duality of electrons. The atomic orbital wavefunctions interfere constructively to form *bonding* orbitals, while destructive interference leads to *antibonding* orbitals. A bonding orbital has lower energy than the atomic orbitals it was formed from, while the antibonding orbitals are higher energy states. The simplest example of this is the homonuclear bonding in a dihydrogen molecule (H_2), illustrated in Figure 1.1. The singly occupied, degenerate hydrogen atomic orbitals combine to form a fully occupied bonding orbital, and an empty antibonding orbital. In molecular systems, the highest energy molecular orbital that contains an electron is known as the highest occupied molecular orbital (HOMO). The

lowest energy molecular orbital that does not contain any electrons is known as the lowest unoccupied molecular orbital (LUMO).

Figure 1.1 only considers a molecule comprised of two atoms. For large extended structures where there are millions of atoms bonded to one another within one crystal, the picture changes somewhat. For every two atomic orbitals that interact, two more molecular orbitals are formed. These MOs are split in energy by each AO interaction, spanning a broader energy range. Thus, for extended networks of interconnected AOs, there are so many discrete MOs with such minute differences in energy between them, that the whole set of MOs can be considered a quasi-continuous *band*.[23] Electrons can hop from one MO to the next within the same band using just thermal energy; thus, the electronic structure of the band is essentially delocalised across the entire material. The progression from a localised molecular electronic structure to a delocalised band structure is illustrated in Figure 1.2.

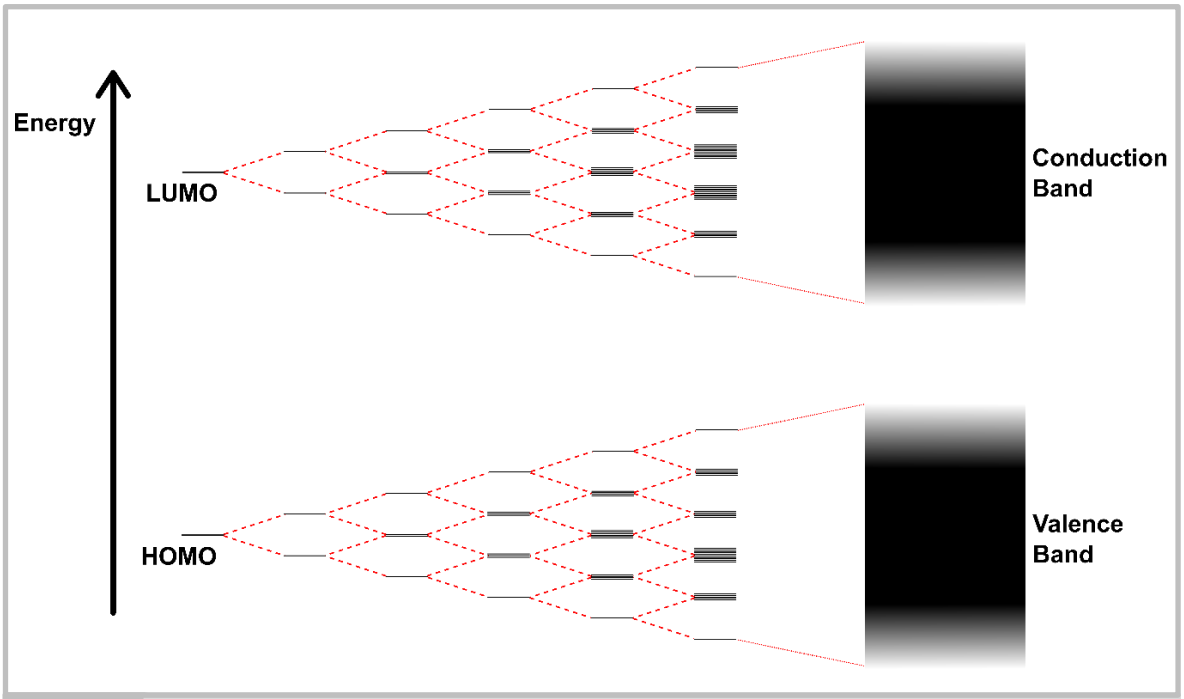

Figure 1.2 **The progression of electronic structure from discrete molecules to extended molecular networks**

The shading on the bands represents the density of states.

The electrical behaviour of a material with a band structure depends on the relative energies of the valence and conduction band edges. Figure 1.3 depicts the position of these bands in different classes of material.[24,25] It is important to note that the shading here represents the probability of states at specific energies being occupied by an electron, not the density of states as in Figure 1.2. In metals, the valence and conduction bands overlap, such that there are many states accessible to

electrons with thermal activation. Therefore, metals display high electrical conductivity. Semiconductors and insulators both have an energy gap between their valence and conduction bands; this energy difference is known as a *bandgap*. Insulators have large band gaps, with energy greater than around 3 eV; thus there is a very low probability that an electron will possess sufficient energy to access the conduction band to carry current, in the absence of an external bias. The same is true for semiconductors. However, semiconductors have smaller band gaps between 25 meV (i.e. thermal energy at room temperature) and 3 eV. As a result, semiconductors can absorb photons of visible light, which have energies between approximately 1.7 and 3 eV.

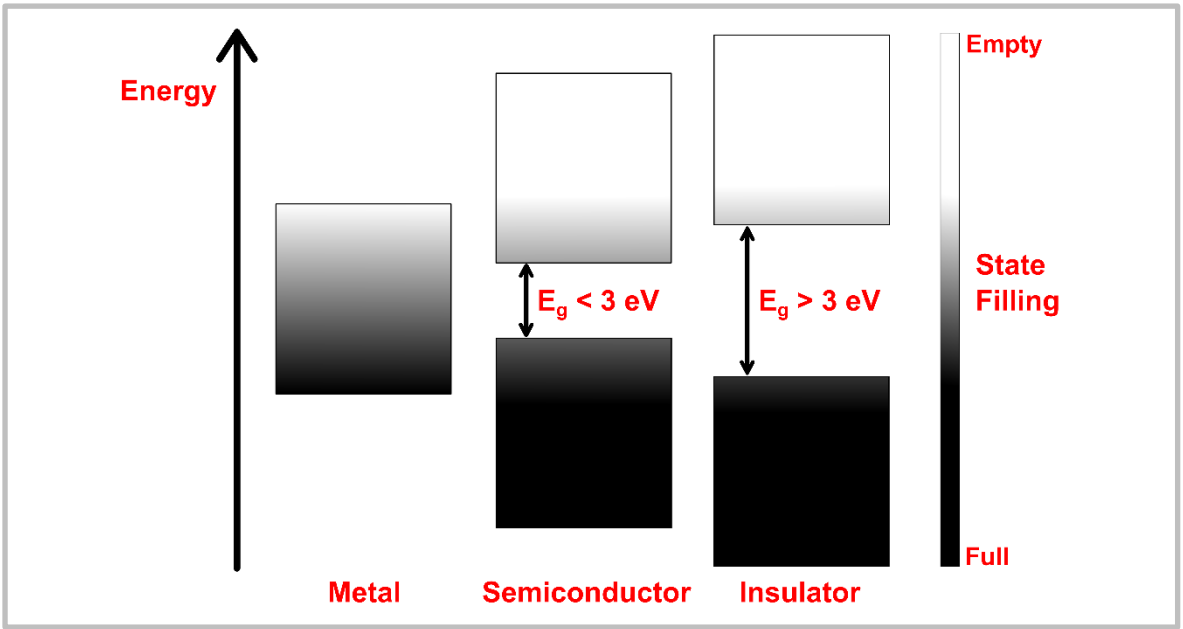

Figure 1.3 **The filling of the electronic structure of different materials at equilibrium**

Shading represents the probability of states at specific energies being occupied by an electron.

1.3.2 Light Absorption and Emission

When a semiconductor absorbs a photon with energy greater than its bandgap, an electron can be excited from its fully occupied valence band to its empty conduction band. This creates a corresponding *hole* in the valence band, which can be considered positively charged, essentially the empty MO where the excited electron previously resided. Together, these charge carriers form as an electron-hole pair, known as an *exciton*. The electron can move through the conduction band of the material due to the abundance of free, accessible states, and the hole can move similarly through the valence band.

Appropriate bandgap energy is not the only criterion for photoexcitation of an electron, however. A photon can only directly excite an electron from the valence band to the conduction band if the transition does not involve a change in crystal momentum, or *k-vector*, such that momentum is conserved. Semiconductors which have a valence band maximum (VBM) and a conduction band minimum (CBM) with the same momentum are known as *direct* bandgap materials. When the VBM and CBM have different momentum, it is known as an *indirect* bandgap. Excitation of electrons across an indirect bandgap requires the simultaneous absorption of a phonon. Phonons are lattice vibrations; they carry momentum, enabling the excitation process to conserve momentum. However, the occurrence of this three-body process has a far lower probability than the two-body excitation in a direct bandgap material. Therefore, direct bandgap materials are much better absorbers of light than indirect bandgap materials. A practical implication of this is that solar cells made from direct bandgap semiconductors, such as gallium arsenide or lead halide perovskites, can operate with much thinner absorber layers than those of indirect bandgap semiconductors, such as silicon.

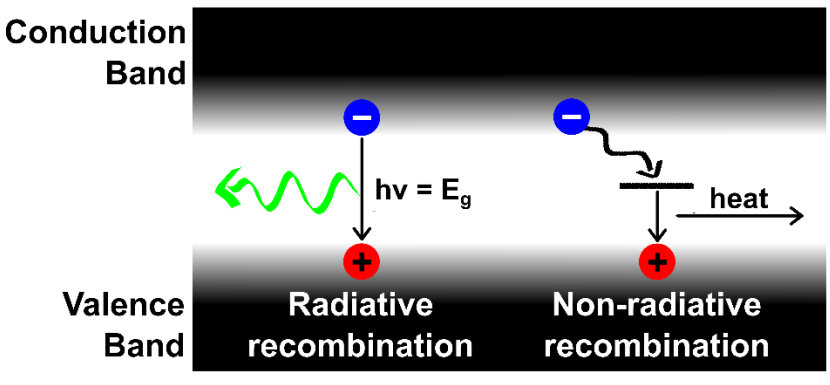

Figure 1.4 **Recombination pathways in semiconductors**

A direct bandgap is even more advantageous for light emission. The emission of a photon from a semiconductor typically occurs through the annihilation of a hole at the VBM by an electron from

the CBM. This process is referred to as *radiative recombination,* and it is the exact reverse process of light absorption. Accordingly, light emission in indirect bandgap materials requires the simultaneous emission of phonon, and is therefore far less probable, and far slower. Crucially, there are competing non-radiative pathways through which the electron can return to the valence band. Such processes typically occur through crystal defects or boundaries and generally occur much more frequently than radiative processes in indirect bandgap semiconductors. In contrast to indirect bandgap absorbers, this problem cannot be circumvented by increasing the layer thickness.

Although direct bandgap semiconductors exhibit faster radiative recombination than indirect bandgap materials, it remains crucial to suppress defect-induced non-radiative recombination. Figure 1.4 illustrates how defects often manifest as *trap* states in the bandgap. These states represent energy levels which spatially localise the charge carriers. Electrons can move into these intermediate states, where they can recombine with a hole in the valence band through the release of thermal energy. The competition between radiative and non-radiative recombination is reflected by the expression for the photoluminescence quantum yield (PLQY, Φ_{PL}) of a semiconductor:[26]

Equation 1.1

$$\Phi_{PL} = \frac{k_r}{k_r + k_{nr}}$$

Where k_r and k_{nr} are simply the rate constants for radiative and non-radiative recombination, respectively. This demonstrates why the suppression of non-radiative recombination is crucial for efficient light emission. In practice, this relates to the preparation and processing of the semiconductor. For applications, the integration of a light-emitting material into a device structure requires careful control of the defect density.

1.3.3 Nanocrystals

Semiconductor nanocrystals (NCs) are crystals of a semiconductor material which are smaller than 100 nm in at least one dimension. They have also become more commonly known as quantum dots, owing to the incorporation of chalcogenide quantum dots in commercial light-emitting diode displays (QLED). As nanocrystals are the focus of this work, it is important to explain both the physics underpinning their luminescence and the chemistry that governs their synthesis. These concepts provide context for the later discussion of the specific properties of lead halide perovskite nanocrystals.

1.3.3.1 Charge Confinement

Nanocrystals are especially well-suited for light-emitting applications because the manipulation of the crystal size provides a further mechanism to boost radiative recombination.[25,27] On the simplest level, an electron and hole which are confined within a smaller volume will have a greater probability of encountering one another. Therefore, radiative recombination events will occur more frequently in smaller crystals. This is known as *spatial confinement*; its effects apply to any crystal sizes. Nanocrystals exploit other effects that occur exclusively for very small crystals, where the electronic structure deviates significantly from that of the bulk. As the number of MOs within a crystal decreases, the electronic structure shifts from a delocalised quasi-continuous band towards a set of discrete, separate states. This is known as *quantum confinement*. As illustrated by Figure 1.5, the most apparent effects of quantum confinement are an increased bandgap, and increased energy separation of states, particularly at the band edges.

To further explain quantum confinement, it is necessary to expand on the physical description of the exciton formed when an electron is excited from the valence band to the conduction band. The exciton is held together by Coulomb interactions, quantified as the *exciton binding energy*. It has an associated radius within the crystal, which quantifies the space it occupies.[28] This known as the *exciton Bohr radius* (a_0). When the radius of a nanocrystal is smaller than a_0, the NC is in the *strong* quantum confinement regime. In this regime, the properties of the NC are particularly sensitive to the NC size, and the NC properties deviate most severely from those of the bulk.

Importantly, the exciton binding energy increases significantly, providing an additional mechanism for the enhancement of radiative recombination. When the NC radius is larger than the exciton Bohr radius - in the *weak* quantum confinement regime - enhanced radiative recombination relative to the bulk is mostly attributable to spatial rather than quantum confinement.[29] Therefore, nanocrystals which exhibit stronger quantum confinement will typically exhibit higher PLQY. It is

important to note that the exciton Bohr radius can vary significantly from one semiconductor to another. For example, the inorganic metal halide perovskite $CsPbBr_3$ has $a_0 \approx 3.5$ nm, while PbTe has $a_0 = 104$ nm.[28] Thus, identically sized nanocrystals of these two materials would exhibit drastically different degrees of quantum confinement.

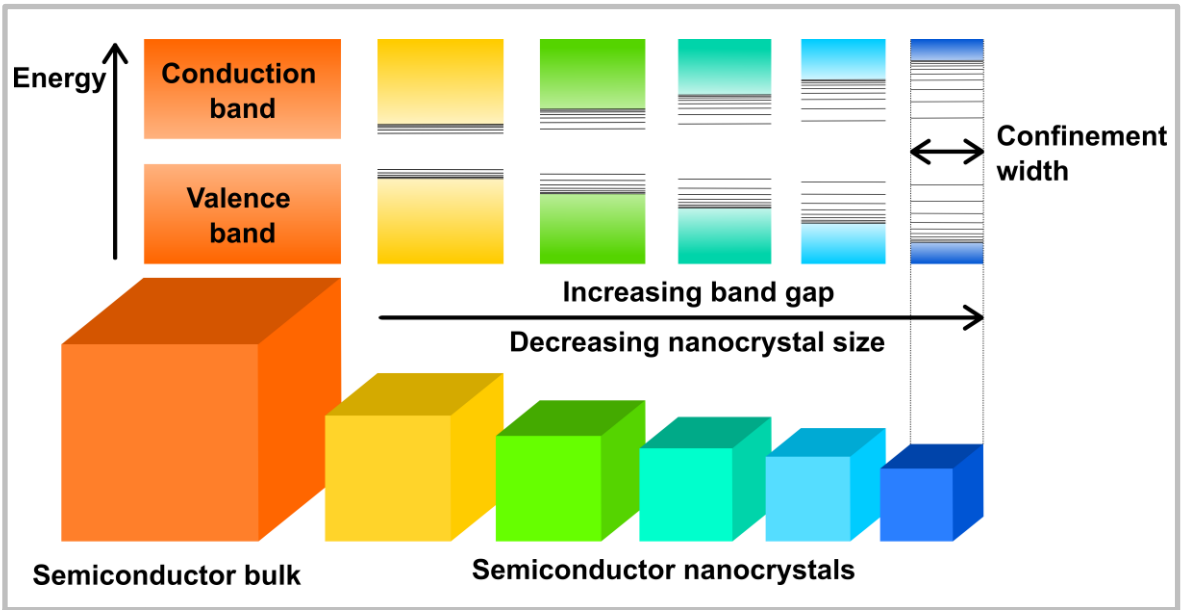

Figure 1.5 **The effects of quantum confinement on the electronic structure of a semiconductor**

As the crystal radius decreases, the confinement width decreases, states near the band edge become more localised and the bandgap increases, causing a change in the emission wavelength.

1.3.3.2 Nanocrystal Synthesis

The enhanced luminescence provided by confinement makes semiconductor nanocrystals exceptionally appealing for light-emitting applications. But how can the crystal size be restricted in practice? Bare nanocrystals are thermodynamically unstable due to their large surface area. Therefore, surfactants must be deployed on the nanocrystal surface to reduce their surface energy and inhibit the agglomeration of adjacent nanocrystals into one larger crystal. A surfactant is an amphiphilic molecule, which contains a small polar "head" group and a long non-polar alkyl "tail". Surfactants that bind to nanocrystals are commonly referred to as *ligands*, which is the nomenclature that will be adhered to in this work.

Ligated nanocrystals are commonly prepared by solution-phase colloidal syntheses. The thermodynamics of these syntheses can be well-explained by classical nucleation theory (CNT).[30,31] Nucleation is the process of crystal growth from crystal seeds, known as *nuclei*. Nucleation can be homogeneous, where nuclei form evenly across the solution phase, or heterogeneous, where nuclei mostly form on nucleating surfaces, such as container walls or impurities. Semiconductor

nanocrystal syntheses are considered homogeneous systems. High purity reagents are sought due to the detrimental effects of defects on the optoelectronic properties.

The thermodynamics of homogeneous nuclei formation are assessed by quantifying the Gibbs free energy (ΔG) of a particle with radius, r. There are two significant contributory terms: the bulk free energy, ΔG_{bulk}, and the surface free energy, ΔG_{surf}.[32] For perfectly spherical particles, these terms are simply summed to give the following definition of the total free energy:

Equation 1.2

$$\Delta G = \Delta G_{bulk} + \Delta G_{surf} = \frac{4}{3}\pi r^3 \Delta G_v + 4\pi r^2 \gamma$$

Here, ΔG_v is the crystal free energy and γ is the surface tension. ΔG (magenta), ΔG_{bulk} (red) and ΔG_{surf} (blue) are plotted as a function of radius in Figure 1.6. For small r, ΔG is positive, indicating that particle growth is unfavourable due to the high surface energy. At larger r, the surface energy cost is outweighed by the energy gained from crystal formation. The maximum in the ΔG curve is important as it represents the free energy required to stabilise particles in solution, the critical free energy (ΔG_c). It can be considered the activation energy for nanocrystal growth and is given by:

Equation 1.3

$$\Delta G_c = \frac{4}{3}\pi \gamma r_c^2$$

Where r_c is the critical radius. This value marks the boundary between the nucleation and growth phases. Below r_c, thermodynamics drive particle redissolution, while above r_c crystal growth is favoured. Thus, the critical radius defines the minimum nanocrystal size required for further growth. It can be described by the following relation:

Equation 1.4

$$r_c = \frac{2\gamma V_m}{N_A k_B T \ln S}$$

Here, V_m is the molar volume, N_A is Avogadro's number, k_B is the Boltzmann constant, T is temperature and S is the supersaturation of the solution. Lowering r_c or ΔG_c can be expected to increase the nucleation rate as a greater proportion of nuclei will grow rather than redissolve. To quantify the effect of experimental parameters on the rate of nucleation of N particles over time, t, an Arrhenius-type exponential equation can be constructed:

Equation 1.5

$$\frac{dN}{dt} = Aexp\left(\frac{16\pi\gamma^3 V_m^2}{3k_B^3 T^3 N_A^2 (\ln S)^2}\right)$$

Where *A* is a pre-exponential factor. Thus, three experimental parameters control the nucleation rate for a particular nanocrystal composition: surface tension, temperature and supersaturation.[33] Surface tension depends on the density of ligands on the nanocrystal surface and the strength of their interaction. The saturation can be controlled through both the concentration of the precursor solution and the solubility of the precursor species. This knowledge is vital because the nucleation rate affects the monodispersity of the nanocrystal size distribution obtained. Ideally, nucleation should be instantaneous, such that the nucleation is complete before any growth.

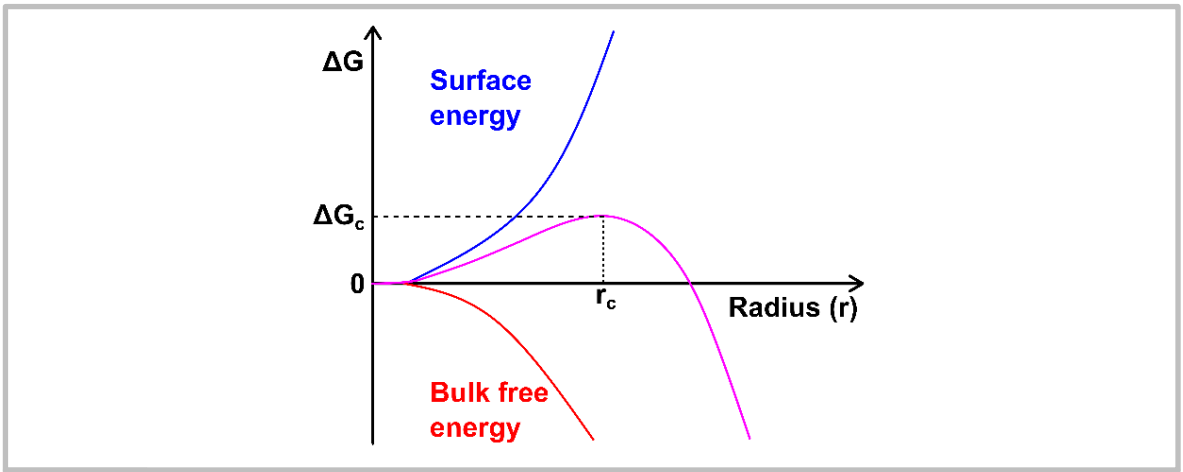

Figure 1.6 **The Gibbs free energy for the nucleation and growth of colloidal nanocrystals**

The Gibbs free energy of a solid particle in solution is plotted as a function of the particle radius (magenta line), alongside the individual contributions of surface energy (blue) and bulk free energy (red). ΔG_c and r_c indicate the activation energy and critical radius, respectively.

In practice, fast nucleation is achieved through exploitation of the LaMer mechanism.[34,35] Figure 1.7 illustrates the growth of nanocrystals over time as a function of the saturation of precursor species in solution. Precursor materials are stably dissolved with selected ligands, which facilitates dissolution through the formation of coordination complexes, known as *monomers*. In the precursor solution, the concentration is kept below the critical saturation point (S_{crit}), where the formation of nuclei is thermodynamically unfavourable. This can be considered the saturation at which $\Delta G < \Delta G_c$, given a fixed temperature and ligand concentration. To initiate any nucleation, the monomer concentration must be raised above S_{crit}. However, to ensure nucleation is rapid, the concentration must be increased to supersaturation (S_{sup}), where the monomers become thermodynamically unstable. Supersaturation can be induced simply by increasing the

concentration of the solution or by reducing S_{crit} through solubility manipulation. Solubility can be reduced by changing the temperature of the solution, or adding a solvent that the monomers are much less soluble in.

New nuclei will continue to form while the concentration remains above S_{crit}. Therefore, the goal of this method is to induce a "burst nucleation" event, which quickly brings the concentration of monomers below S_{crit}, where no new nuclei will form. Existing nuclei will continue to grow while the monomer concentration is greater than the minimum saturation point (S_{min}). The different experimental methods for applying the LaMer mechanism will be discussed later in Section 2.2, in the context of perovskite nanocrystal formation.

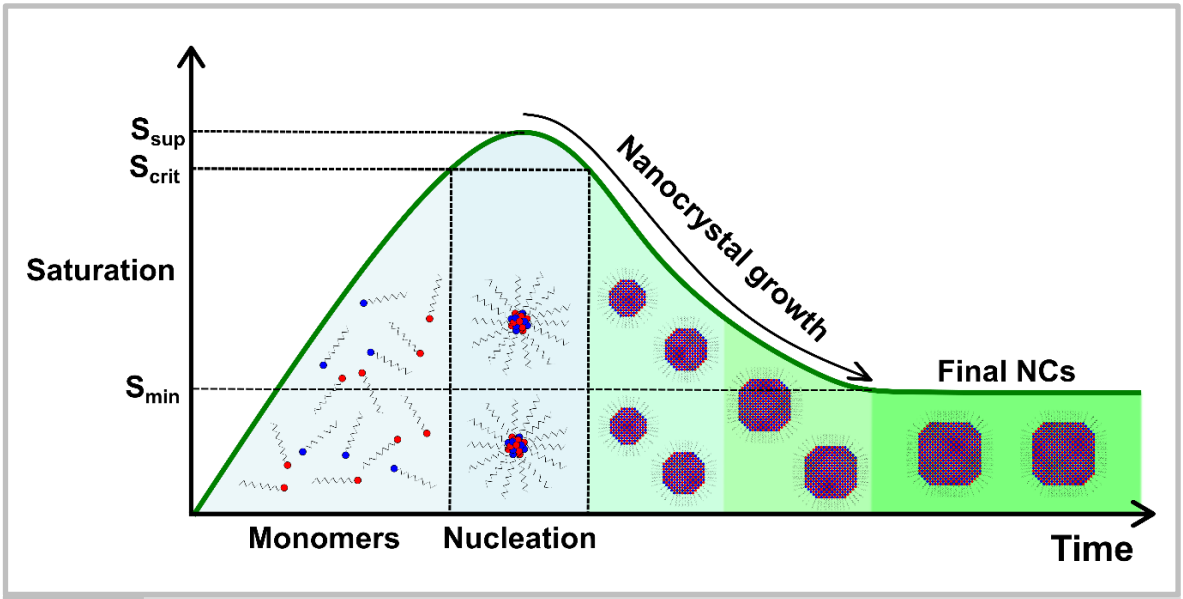

Figure 1.7 **The nucleation and growth of semiconductor nanocrystals**

This scheme shows the change in saturation over time during colloidal synthesis, with the key saturation points and synthesis phases labelled.

The LaMer mechanism implies that nanocrystal growth will cease once the saturation drops below S_{min}. However, this is not necessarily the case. When the monomer concentration becomes very low, the corresponding increase in r_c can result in the redissolution of the smallest fraction of nanocrystals. This facilitates the growth of the largest fraction of nanocrystals. As a result, a broadening of the nanocrystal size distribution is often observed over time. This phenomenon is known as Ostwald Ripening. To avoid significant ripening, nanocrystals are quickly removed from their growth solution, typically by centrifugation, and redispersed in fresh solvent.

It is important to end this section by highlighting the influence of chemistry on all the factors discussed. The polarity of the solvents and the reactivity of the precursor strongly affect the

nucleation rates which can be achieved. Furthermore, the surface chemistry of ligand interactions with the nanocrystal, such as their binding strength, lability, packing density and impact on solubility, are all crucial. These intricacies of ligand binding will be explored in detail in this work.

1.3.4 Light Emitting Diodes

The scope of this thesis spans from the synthesis of semiconductor nanocrystals to their application in light-emitting diodes. It is important to set the foundation for the discussion of device characteristics and performance in later sections and chapters. This section will provide a background of the operating principles and key parameters of light-emitting diodes (LEDs). These principles will be discussed in the context of a thin-film LED, where photons are generated by the radiative recombination of electrons and holes within a layer of emissive semiconducting material less than 1 μm in thickness.

1.3.4.1 Principle of Operation

For electrons and holes to recombine in the emissive layer, charges must first be injected. In an LED, this charge injection is provided by an electric current. The conversion efficiency from electrical power to optical power for a light-emitting diode is known as the wall-plug efficiency (η_{WP}) and is given by:

Equation 1.6

$$\eta_{WP} = EQE\frac{L}{IV}$$

Where *EQE* is the external quantum efficiency, the proportion of electrons injected into the LED that is emitted as photons; *L* is the luminous flux, the power of light emitted, weighted according to the sensitivity of the human eye; and *IV* (the product of current and voltage) is the electrical power applied to the device. Radiant efficiency is an important value for quantifying the overall performance of an LED. However, there are other parameters which give a more informative characterisation of LED operation, these parameters are examined more closely at this stage of research.

There are 3 central figures-of-merit for perovskite light-emitting diodes: EQE, luminous efficacy and luminance.[36] EQE can be expressed as:

Equation 1.7

$$EQE = \eta_{inj} \times IQE \times \eta_{ext} \times \gamma_{CB}$$

where η_{inj} is the efficiency of charge injection into the emitter layer, *IQE* is the internal quantum efficiency of electroluminescence, η_{ext} is the proportion of generated photons that exit the device, and γ_{CB} is the charge balance in the emitter layer. This relation explains that EQE is a device property

which accounts for charge injection into the material, extraction of light from the device and the relative concentrations of holes and electrons. Typically, interfaces with low defect density and good energetic alignment are important for efficient charge injection, while light out-coupling can enhance photon extraction.[37] IQE is a material property, indicating simply the charge carrier conversion capability. IQE can be considered theoretically analogous to the photoluminescence quantum yield (PLQY) of a material, with the only distinction being that carriers are induced by electrical injection rather than photoexcitation. However, it is important to highlight that both IQE and PLQY are strongly dependant on the charge carrier density (n).[38] This dependence can be described by:

Equation 1.8

$$\eta_{rad}(n) = \frac{nk_2}{k_1 + nk_2 + n^2k_3}$$

Where η_{rad} here is the quantum yield of radiative emission (equivalent to either IQE or PLQY), and k_1, k_2, and k_3 are the rate constants corresponding non-radiative, radiative, and Auger (three-body) recombination, respectively. Thus, at lower charge density, η_{rad} will be reduced due to non-radiative losses, while at high n it will be limited by higher Auger recombination rates. As a result, for all realistic material systems where k_1, k_2 and k_3 are not negligible, IQE and PLQY are only practically equivalent for similar charge carrier densities. Another consequence of this is that often the experimental measurement of LEDs produces plots of EQE against current density which are not constant. Typically, EQE will increase gradually to a peak and then reduce drastically, or "roll-off", at high current density. This gradual increase can be described as the "filling" of trap states. Charge balance will also affect the gradient of this plot as the injection rate of holes and electrons is unlikely to be exactly equal; thus there will be an excess portion of one type of charge carrier, which can only recombine non-radiatively.

The luminous efficacy is the luminous intensity of light emitted (in lumens) from the LED per watt of power supplied. The luminous intensity differs from the absolute, or radiant, intensity in that it is weighted according to the luminosity function of the human eye. The luminous intensity is generally more useful when discussing visible light applications as humans are almost always the targeted consumer. In perovskite literature, current efficiency is more regularly reported than luminous efficiency. However, current efficiency arguably does not provide any insight beyond that provided by EQE. As luminous efficacy accounts for the power required to generate light, not just the current, it makes it much simpler to calculate the power consumption of the LED when used for real-life applications. Consequently, it is often referred to more colloquially as the wall-plug efficacy.

The luminance of an LED (also commonly referred to as the brightness), is simply a measure of the intensity of light emitted per unit area. Like the luminous efficacy, it is weighted according to the human eye. The luminance is important for analysing the suitability of an LED for a particular application. For example, LED displays typically operate at a luminance around 100 candela per square metre (cd m^{-2}). In addition to simply ensuring the LED can reach the required luminance, it is essential to determine the EQE at this luminance. EQE can diminish rapidly towards the extremes of its luminance range, due to its dependence on current density as discussed above.

The characterisation of perovskite light-emitting diodes is generally conducted using a system containing a semiconductor parameter analyser and a spectrophotometer. The analyser applies a bias to the LED and measures the current in the device, while the spectrophotometer (equipped with an integrating sphere) records the spectral flux. By integrating the spectral flux, then accounting for the active area of the device and converting according to the luminous efficiency function of the human eye, the luminance can be calculated. Current density-voltage-luminance plots can then be generated to assess diode performance.

EQE is probably the most critical figure-of-merit for an LED, certainly in research. Therefore, it is crucial to outline how it is calculated experimentally. It is calculated as the ratio between the number of charge carriers injected into the device (N_{car}) and the number of photons emitted (N_{ph}).[39] The number of charge carriers injected is calculated simply by:

Equation 1.9

$$N_{car} = I \times q_e$$

Where I is the current measured in the device and q_e is the charge on an electron. N_{ph} is calculated from the following sum:

$$N_{ph} = \sum_{\lambda} \frac{\Phi}{E_{ph}}$$

Where Φ and E_{ph} are the spectral flux and the energy of a photon at a particular wavelength, respectively.

Plotting the electroluminescence intensity against wavelength determines the precise emission wavelength and the width of the emission band (typically quantified by the full width of the peak at half maximum height, FWHM). This indicates the colour of the light emitted by the LED, and the colour purity achieved.

The principle parameters discussed in this section provide useful background and context for the discussion of LED results in later chapters. The origins of more specific features, the intricacies of data collected, and plots generated from LED measurements will be addressed when they arise.

1.3.5 Lead Halide Perovskites

Over the last decade, lead halide perovskites have emerged as an exciting new semiconductor material. Their oft-cited potential for achieving comparable performance to high-cost high-performance optoelectronic materials, such as silicon or gallium arsenide, using low-cost high-throughput solution processing has driven an intensive research focus. Combined with the relatively low cost of perovskite precursor salts, perovskite-based optoelectronics possess substantial commercial appeal. This section will begin by describing the perovskite structure, examining the key structure-property relationships. The focus will then turn to perovskite nanocrystals; the synthesis of these nanocrystals, their surface chemistry, and their application in light-emitting diodes will be reviewed, highlighting significant, relevant developments reported in recent literature.

1.3.5.1 Perovskite Structure

Perovskites are so-called because they adhere to a particular crystal structure. The name originates from a mineral, calcium titanium oxide (a.k.a. calcium titanate), which was named after the mineralogist Lev Perovski upon its discovery in 1839. Calcium titanate was the first example of this structure; therefore, naturally-occurring and synthetic materials which exhibit the same structure were also classified as perovskites. Perovskites have a cuboctahedral crystal structure, with the general formula ABX_3. As depicted in Figure 1.8, this describes a cuboidal unit cell, with an A cation at its centre, surrounded by 8 corner-sharing BX_6^{4-} octahedra. For lead halide perovskites, the B cation is lead (Pb^{2+}), while the X anions are halides - exclusively chloride, bromide, or iodide (Cl^-, Br^- or I^-). Although other B cations can be employed, it has been well established that lead affords vastly superior optoelectronic properties than any other.[40,41]

Usually, perovskites can be described as having three-dimensional structures. In this context, this means that the extended crystal is comprised of interconnected perovskite unit cells extending along three axes. However, there exist many lower-dimensional perovskites where the unit cells are only connected by corner-sharing PbX_6^{4-} octahedra in one or two directions (1D or 2D), or are electronically isolated from one another (0D).[42] This clarification is important as similar terminology can be employed to describe the dimensional confinement of perovskite nanostructures; e.g. nanocubes are confined equally in all dimensions so can be considered zero-dimensional (0D). Similarly, nanowires retain one less confined dimension, so are defined as 1D, while nanoplates are considered 2D.[43]

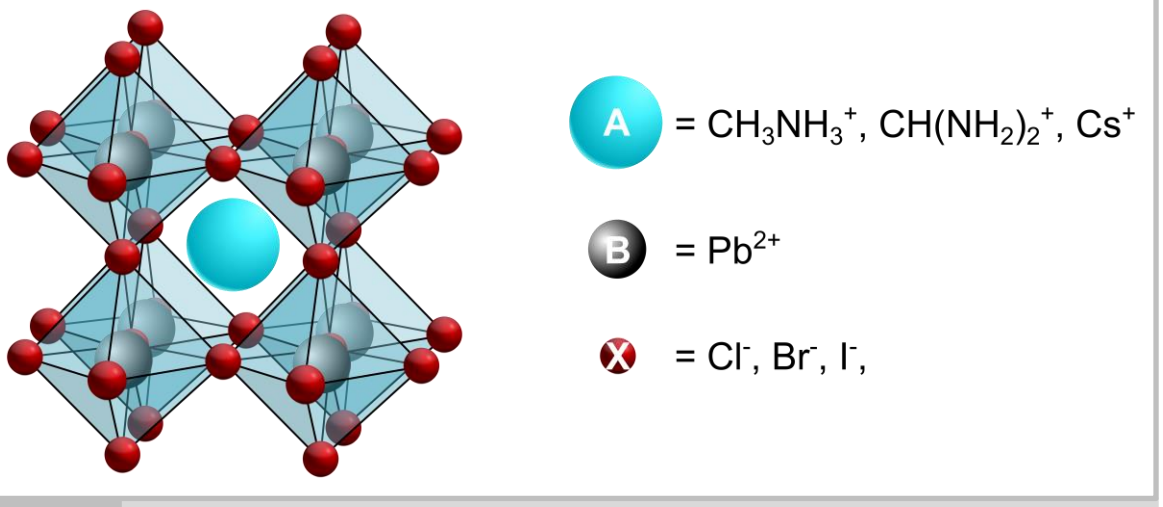

Figure 1.8 **The unit cell of the ideal crystal structure of a lead halide perovskite ($APbX_3$)**

The Pb^{2+} cations (grey) lie at the centre of corner-sharing PbX_6^{4-} octahedra, forming a cube around the larger A cation (cyan).

The viability of an A cation for a 3D lead halide perovskite is governed by the geometry imposed by the lead halide octahedra. The A cation must be small enough to fit into the octahedral holes, but also large enough such that the packing density of the resulting lattice is sufficiently high. Based on the assumption that the ionic bonding of rigid spheres can well represent the structure, the Goldschmidt Tolerance Factor (t) determines whether the radii of the constituent ions allow a suitable packing density.[44] It is calculated as follows:

Equation 1.10

$$t = \frac{(r_a + r_x)}{\sqrt{r_b + r_x}}$$

Where r_a, r_b, and r_x are the radii of the ions at each lattice site. For an A cation which fits perfectly into the lattice, $t = 1$. It has been found that generally, for the successful formation of lead halide perovskites with corner-sharing PbX_6^{4-} octahedra, $0.8 \leq t \leq 1$.[45] Towards the lower bound of this range, lower-symmetry tetragonal, orthorhombic or monoclinic structures are often observed.[46,47] If $t > 1$, the A cation is too large, and if $t < 0.8$, the A cation is too small. Based on these restrictions, single A cation 3D lead halide perovskites have been reported with methylammonium (CH_3NH_3, MA), formamidinium ($CH(NH_2)_2$, FA) or cesium (Cs) cations. It is important to note, however, that one type of ionic site within a perovskite structure need not contain the same ion throughout the structure. Thus, A cations which are too small to form the 3D perovskite alone can be doped in minor concentration into the stable compositions. The most common example of this is rubidium (Rb), whose incorporation in the perovskite structure has been correlated to enhanced performance of solar cells and light-emitting diodes.[48–50]

The freedom to choose between at least 3 different cations and 3 different anions, and to mix them in the desired proportions, represents substantial compositional lability. This is a particularly useful feature because the optoelectronic properties of perovskites are strongly dependent on the composition. To understand this dependence, we must consider the band structure of an $APbX_3$ perovskite. As shown in Figure 1.9, both the valence and conduction bands are formed by the interaction of the lead and halide atomic orbitals - i.e. the chemical bonding in the PbX_6 octahedra.[51] This essentially indicates that charge carriers will diffuse from one unit cell to another along the three axes formed by the corner-sharing PbX_6^{4-} octahedra. Thus, the energy of the valence band maximum and, to a lesser extent, the conduction band minimum, varies significantly for different halides. This directly alters the bandgap of the perovskite, which is a crucial optoelectronic parameter, as it defines both the light absorption and emission profile of the material. As a result, the colour of the light emitted can be precisely controlled by the halide composition. The least electronegative halide, iodide, forms the lowest bandgap perovskite, followed by bromide and chloride, while mixed halide compositions can access any band gap values in between.

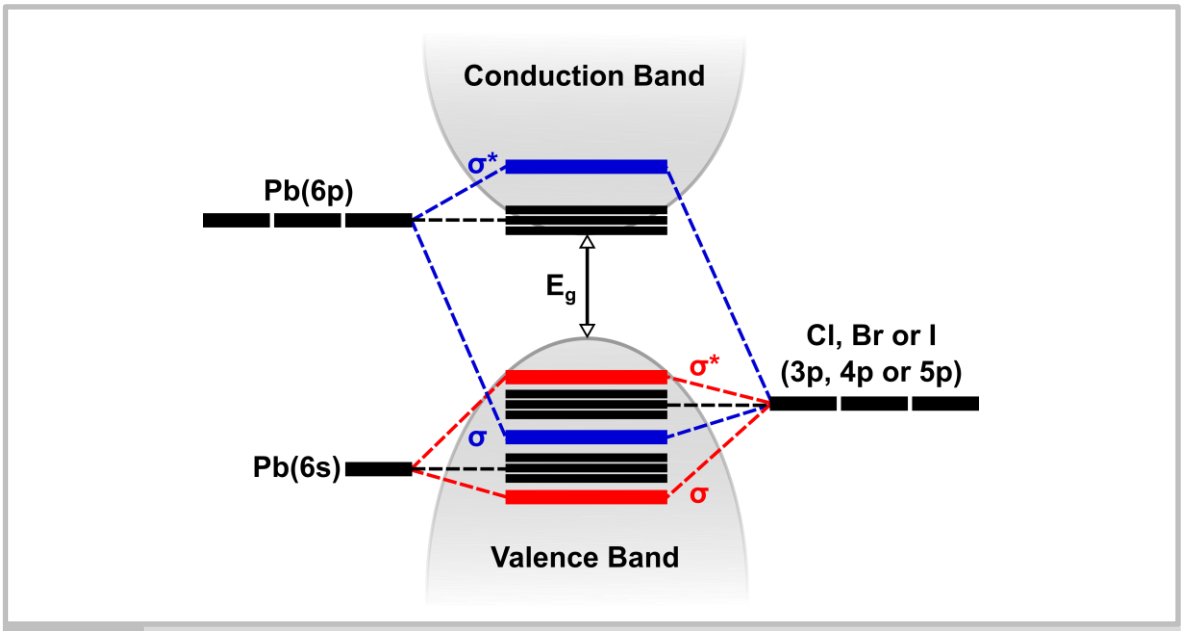

Figure 1.9 **General band diagram for $APbX_3$ perovskite**

The red and blue levels represent molecular orbitals formed by the interaction of frontier lead and halide atomic orbitals. The black levels represent defects, which only produce benign intra-band or shallow states. This figure was adapted from [4,51].

The A cation has a lesser impact on the frontier electronic structure because its interaction with PbX_6 octahedra is largely electrostatic.[52,53] Rather than directly altering the energy of the frontier atomic orbitals, the A cation influences the bandgap by inducing relative contraction or expansion of the lattice, depending on its ionic radius.[54] The effect on the bandgap is minor relative to the

halides, but the trend is the same: the largest cation forms the perovskite with the smallest bandgap. Bulk $FAPbI_3$ has the smallest bandgap of 1.47 eV (843 nm),[55] while nanostructures of $CsPbCl_3$ can exhibit bandgaps as high as 3.10 eV (400 nm).[56] Conveniently, the bandgap range accessible for lead halide perovskites essentially covers the whole spectrum of visible light ($\lambda \approx 400$ to 800 nm) and even into the near-infrared, making lead halide perovskites viable candidates for countless potential optoelectronic applications.

1.3.5.2 Defect Tolerance

Any real crystalline material will possess point defects. These structural imperfections can occur in three common forms: there are vacancies, which are simply sites with missing atoms; antisites, where an atom occupies a different site than that it is expected to; and interstitials, where atoms occupy sites in the lattice that should be vacant. The relative formation energies of each type of defect will vary based on the material and the structure. For example, antisite defects will be far more likely in materials where two sites accommodate ions of similar radii. The defect tolerance of a material describes the degree to which the formation of energetically viable defects affects its electronic properties. Lead halide perovskites are generally considered highly tolerant of defects.

This high tolerance originates from the benign nature of thermodynamically viable trap states.[1,57] Interstitial, antisite defects, and Pb^{2+} vacancies are highly unlikely to form; in reality, only a significant number of X site vacancies are observed. These halide vacancies only manifest as in-band or shallow trap states, allowing ideal optoelectronic properties to be maintained with defect densities that would render other materials useless.[51] This is illustrated in Figure 1.9, where the black levels represent defect states. The in-band defect states can be attributed to the antibonding character of the valence band maximum, while the states close the edge of the conduction band are shallow due to spin-orbit effects.[1]

The defect tolerant nature of lead halide perovskites underpins some of its most attractive properties. Perovskite materials can be processed in ambient conditions with laboratory-grade solvents, as the defects introduced do not have a substantial effect on their properties. This means that they are especially well-suited to solution-processing, which in turn opens the realistic possibility that large-scale high throughput industrial methods will be viable and cost-effective. The printing of electronics, using continuous roll-to-roll deposition, is tremendously appealing for commercial applications.

The first reported application for lead halide perovskite materials was the incorporation of $MAPbI_3$ as a sensitiser in a dye-sensitised solar cell.[21] It was soon realised that a liquid electrolyte was unnecessary and solid-state perovskite solar cells were demonstrated in 2012.[58,59] Since then,

perovskite solar cells have emerged as one of the most efficient, recently recording power conversion efficiency of 25.5 %.[60] Furthermore, perovskite-silicon tandem solar cells have hit 29.1 %, matching the record efficiency for GaAs, a far more costly technology which represents the state-of-the-art for single-junction cells.

Unsurprisingly, given the looming spectre of climate change,[61] solar cells have remained the central focus for perovskite researchers. However, over the last 5 years, there has also been intense interest in other optoelectronic applications;[62] these include photodetectors,[63–65] lasers,[2,66] gas sensors,[67,68] X-ray scintillators,[69] transistors,[70] and light-emitting diodes.[2,3,8,71]

1.3.5.3 Instability

So far, the narrative has concentrated on the many exciting properties of perovskite materials. It is pertinent also to address the most prominent concern: instability. This encompasses thermal, phase, environmental and device instability, all of which will be briefly discussed.

Instability is undoubtedly the biggest challenge facing lead halide perovskite optoelectronics. Like many of the advantages of perovskites, instability is closely linked to the highly ionic nature of the material. Ionic bonding facilitates crystallisation under ambient conditions but also leads to decomposition at lower temperatures than most other semiconductors. This thermal instability is most significant for the organic-inorganic hybrid compositions, $MAPbX_3$ and $FAPbX_3$, due to the volatility of the organic species.[72] Thermal degradation of CH 3 NH 3 PbI 3 perovskite into NH 3 and CH 3 I gases observed by coupled thermogravimetry–mass spectrometry analysis Taking $MAPbX_3$ ($MA = CH_3NH_3$) as an example, the thermal degradation pathways are described by:

Pathway 1

$$\boldsymbol{CH_3NH_3PbX_3\ (s) \longrightarrow PbX_2(s) + CH_3NH_2(g) + HX(g)}$$

Pathway 2

$$\boldsymbol{CH_3NH_3PbX_3\ (s) \longrightarrow PbX_2(s) + CH_3X(l/g) + NH_3(g)}$$

It should be noted that while CH_3Cl and CH_3Br are gases at room temperature, CH_3I is a volatile liquid.

It has been reported that Pathway 1 is thermodynamically favoured, while Pathway 2 is kinetically favoured.[73] Therefore, as the temperature increases, Pathway 2 becomes more favourable. Regardless, both pathways are driven by the formation of gaseous decomposition products. It has been found that this results in the decomposition of $MAPbI_3$ at temperatures as low as 85 °C. Thus,

under the conditions of electronic device operation, $MAPbI_3$ is susceptible to degradation. $FAPbI_3$ exhibits higher stability due to the larger FA cation ($CH(NH_2)_2$), above 100 °C,[74,75] however, the all-inorganic composition of $CsPbI_3$ provides the highest thermal stability.[76] Despite this fact, pure cesium lead iodide is rarely used for solar cells because its bandgap is larger and provides less ideal coverage of the solar spectrum than MA or FA-based perovskites. The thermal stability trend is consistent across different halide contents, as it is mostly dependant on the cation.

Phase instability is also an important consideration. For some of the lead halide perovskite compositions, the photoactive phases are not thermodynamically stable at room temperature. The thermodynamically stable phase for both FA and Cs-based iodide compositions is photo inactive because the extended network of corner-sharing PbI_6^{4-} is disrupted. The photoactive cubic, orthorhombic or tetragonal phases are usually formed with annealing or solvent engineering,[13,77], but they remain susceptible to conversion back the more stable, inactive phase. Other halide compositions also exhibit phase transitions, but the stable phases at room temperature remain photoactive. Figure 1.10 illustrates the phase transitions from orthorhombic to tetragonal to cubic, which occur in $CsPbBr_3$ as the temperature increases from room temperature to above 130 °C. Interestingly, the transition temperatures are lower for nanocrystals (QD) than for the bulk perovskite, emphasising that many properties are altered when the crystal size becomes very small.

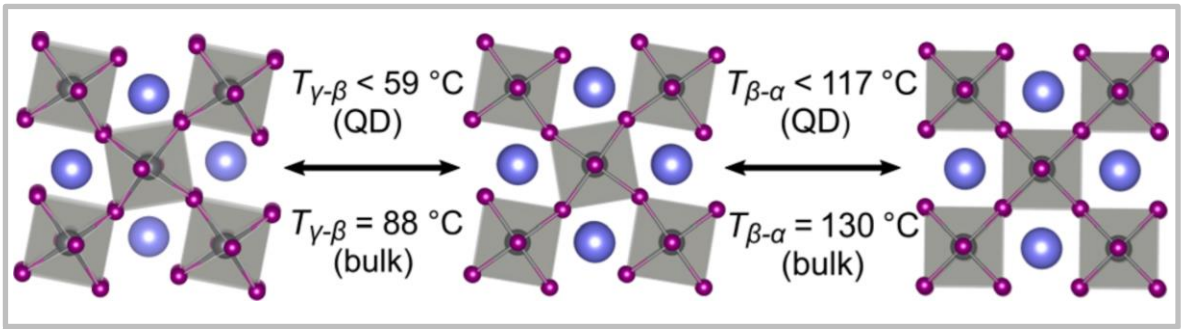

Figure 1.10 **An illustration of the phase transitions that occur in $CsPbBr_3$**

From an orthorhombic structure at room temperature (left), $CsPbBr_3$ adopts a tetragonal (middle) then cubic (right) phase as the temperature increases. This figure was reprinted with permission.[78] © 2018 American Chemical Society.

Both thermal and phase instability are strongly related to environmental instability. Atmospheric gases, particularly water and oxygen, have been shown to accelerate the degradation of lead halide perovskites.[79–81] Water can permeate into the perovskite lattice, reacting to form hydrated species. MA reacts most readily with water due to its more acidic proton, followed by FA, while the inorganic Cs again provides better stability.[82] Water also expedites phase conversion as it destabilises meta-stable perovskite phases.[11] It has been suggested that, in contrast, oxygen does not degrade the perovskite in its ground state. Under illumination, however, photo-oxidation drives decomposition. This has been attributed to the formation of superoxide (O_2^-) when photo-excited electrons are

injected from the perovskite conduction band.[83] Thus, independently, oxygen and light illumination are relatively harmless, but together they cause significant degradation.[59] As photo-oxidation follows a similar mechanism to thermal decomposition, the same stability trend applies, where FA and Cs-based perovskites are most resistant to oxidation.

The above discussion of instability leaves a pessimistic impression of the realistic commercial prospects of lead halide perovskites. However, in a short period, there have been many developments that have greatly enhanced stability. The intense research on bulk perovskites for solar cells has led to device stability approaching commercial viability.[84] This has involved extensive optimisation of film crystallisation and processing conditions, fine-tuning of the perovskite composition and the exploration of a vast array of surface passivation and interface modification strategies. The stability of perovskite light-emitting diodes currently lags behind that of solar cells, but it is a newer field, whose focus to date has mostly been on improving device efficiency.

Perovskite nanocrystals offer a promising route to higher stability light-emitting diodes. Their crystallisation occurs in the liquid phase, where exposure to oxygen and moisture can be limited, and the resulting ligand shell provides environmental protection. The primary concern for perovskite nanocrystals is their operational stability in LEDs. The operating conditions of an LED are significantly more strenuous than that of a solar cell, such that significant luminance decay tends to occur within minutes.[85,86] The dominant mechanisms for degradation under electric field are not clear. The diffusion of mobile A cations and halide ions within the device, known as *ion migration,* are believed to play a prominent role.[87] Joule heating due to the high current density of operation has also been shown to lead to luminance decay.[88] As with bulk perovskites, thermal degradation mechanisms can be suppressed with the adoption of all-inorganic perovskites,[89] most commonly green-emitting $CsPbBr_3$. The ligands employed, specifically the nature and strength of their interaction with the perovskite structure, also appear to have a substantial influence on stability. This will be discussed in detail in the following literature review section.

Ultimately, electroluminescent perovskite nanocrystals are still a very new technology. There is great hope that perovskite LEDs can follow the ascent of perovskite solar cells, whose stability was enhanced much more rapidly than many had anticipated. Regardless, even if sufficiently stable electroluminescence proves unobtainable, the impressive stability of ligand-capped perovskite nanocrystals means that they retain great promise for optically-driven light-emitting applications, such as downconversion or optically pumped lasing. The commercial viability of perovskite nanocrystals is far from dependant on their electroluminescence stability.

1.3.6 Perovskite Nanocrystals

The extension of lead halide perovskite research from solar cell applications to light-emitting devices was intuitive. Many of the properties which make perovskites promising photovoltaic absorbers are also desirable for an electroluminescent material. A low charge trap density, and the high tolerance of the electronic structure for these traps, keep non-radiative recombination relatively low, such that a significant proportion of carriers can be extracted to the electrodes (as in a solar cell) or recombine radiatively (as in an LED). High charge carrier mobility,[90] long and balanced charge carrier diffusion lengths,[91,92] and a large photon absorption coefficient,[21] all aid efficient photon collection and emission. However, for 3D perovskites, a low exciton binding energy inhibits radiative recombination.[53] Furthermore, the rate of radiative recombination in 3D perovskites is slow.[93] This is ideal for solar cells, as it allows a large fraction of photoexcited charges to be extracted before any recombination occurs. But it also leads to very low PLQY due to the large crystallites that comprise bulk 3D perovskite films. To design lead halide perovskite materials with high PLQYs suitable for light emission, the exciton binding energy must be increased to promote faster radiative recombination.[38] As explained earlier in this chapter, the key to this is charge confinement.[71]

The properties of nanocrystals usually deviate from those of the bulk material. For perovskite nanocrystals, the reduced dimensions confine excitons, driving up the rate of radiative recombination, dramatically enhancing PLQY. Nanocrystals are sometimes referred to as "quantum dots" (QDs), which is a common term for other emissive nanomaterials. These quantum dots lie in their strong quantum confinement regime as their crystal size is smaller than its Bohr exciton diameter.[94] However, for perovskites, often the sizes of the nanocrystals synthesised are larger than their Bohr exciton diameter, such that quantum confinement is weak. The bandgaps of perovskite nanocrystals are typically only slightly larger than those of the bulk, and their spectral dynamics are similar.[14,29] Regardless, perovskite nanocrystals can still achieve much faster radiative recombination, leading to high PLQY. This is mostly attributed instead to spatial confinement - the increased probability of bimolecular recombination processes because charges are confined to small volumes.[95]

Although confinement increases the rate of radiative recombination, the enormous increase of surface area can bring a dramatic increase in charge trap density. It is impossible to fully passivate the surface of a nanocrystal with ligands due to steric hindrance, therefore defect intolerant materials such as chalcogenides (e.g. CdSe) require core-shell structures to obtain sufficiently high PLQY.[96] This involves the epitaxial growth of a different inorganic semiconductor on the surface of

the nanocrystal. It is a more complicated process, which inevitably restricts scalability and drives up the energetic and financial expenditure.

Perovskite nanocrystals do not require core-shell structures. As surface defects can be considered vacancies, their effect on the electronic structure of the perovskite is benign in comparison with chalcogenides. This has been highlighted by density functional theory (DFT) calculations, which predicted that up to 75 % of the CsBr surface termination layer of a $CsPbBr_3$ nanocrystal could be removed without inducing significant localisation of electronic states at the band edges. These states would be expected to act as deep charge-trapping sites.[97] Although shallow traps still diminish the PLQY somewhat, the critical implication here is that these are tolerable, such that the inevitable but minor fraction of defects left unpassivated by ligands does not prevent perovskite nanocrystals from obtaining near-unity PLQY.

The above assertions do not diminish the importance of ligands. Far from it, without core-shell structures, ligands take on multiple responsibilities. In addition to passivating surface defects, they must enable dispersion in organic solvents, protect the surface from environmental degradation, and they have a pivotal impact on the conductivity of nanocrystal thin-films.[98,99] Moreover, stepping back to consider the synthesis of the nanocrystals, the ligands have an enormous influence over the nanocrystal formation. The precursor formulation (e.g. solubility),[100] and the thermodynamics and kinetics of nanocrystal nucleation and growth are highly contingent on the ligand composition and concentration.[33,101,102] The following literature review section will explore the various ligands employed in recent works, examining their relevance to the commercial viability of perovskite nanocrystal syntheses and the resulting properties.

1.3.6.1 Suitability for Light-Emitting Applications

There are a wide range of materials currently competing for prominence in various light-emitting applications. These include mature, ubiquitous inorganic III-V semiconductors such as indium gallium nitride ($In_xGa_{1-x}N$), and more recently emerged emissive organic materials and inorganic quantum dots, which have enabled OLED and QLED technologies, respectively. It is therefore vital to discuss how perovskite nanocrystals compare to their would-be competitors.

As alluded to earlier in this section, perovskite nanocrystals exhibit several exceptional optoelectronic characteristics. Particularly, the narrow linewidths attainable from perovskite nanocrystal emission (FWHM < 20 nm) indicate that they could facilitate wider colour gamut displays than any competitor. Despite this, their biggest selling point is the potential for extremely low-cost manufacture. While state-of-the-art emissive organic materials require complex multi-

step synthesis, and core-shell quantum dot syntheses are lengthy and elaborate, perovskite nanocrystals can be prepared with near-unity PLQY at room temperature in open air. The perovskite precursors are relatively inexpensive, and need only be standard laboratory-grade purity, owing to perovskites' unique defect tolerant nature. Combined with their compatibility with scalable, high throughput solution-processing techniques, which quantum dots and some organic emitters also possess, large-area perovskite films could be manufactured very cheaply.

Perovskite LEDs were only first reported within the last decade, yet they have already achieved EQEs comparable to OLEDs and QLEDs (> 20 %) for red[103] and green[104] emission. Blue perovskite NC LEDs have substantially lower EQE than their OLED counterparts,[105] but they have been improving rapidly, recently reaching 12.3 %.[98]

There are significant disadvantages of perovskite nanocrystals too. Stability is undoubtedly the primary concern. The lifetimes (time required for the initial brightness to decay by 50 %) of perovskite nanocrystal LEDs are typically less than 10 hours.[98,104] This is in sharp contrast to OLEDs and QLEDs, which have demonstrated lifetimes exceeding 10^5 and 10^6 hours,[106,107] respectively, for red and green emission. The stability of emerging blue LEDs remains a challenge for OLEDs and QLEDs, as lifetimes still lag far behind $In_xGa_{1-x}N$.[108] Currently, it appears unlikely that perovskite nanocrystals will ever be able to sufficiently withstand the stress of electroluminescent operation. Photoluminescent applications of perovskite nanocrystals, such as colour conversion or filtering on blue $In_xGa_{1-x}N$ LEDs, offer a less strenuous application, for which their excellent colour purity is a major advantage. With no charge injection necessary, encapsulation of perovskite nanocrystals in a highly stable polymer or inorganic matrix can greatly improve environmental stability.[9]

Another prominent issue is the toxicity of lead-based perovskites. While the European Union's Restriction of Hazardous Substances (RoHS) directives allow 10 times as much Pb^{2+} in electronics as the Cd^{2+} in leading CdS(e) quantum dots,[3] Core-shell InP/ZnSe/ZnS quantum dots have emerged as a promising non-toxic, environmentally-friendly competitor.[109–111] Thus, the future viability of perovskite nanocrystals for a particular application will depend on the relative expectations and priorities of cost, stability and toxicity. Ultimately, it seems that perovskite nanocrystals would have a distinct advantage for applications where cost and scalability are closely linked to the commercial viability of the product.

Chapter 2 Literature Review

The previous chapter provided a general overview of the theoretical foundations most relevant to this work. This facilitated a narrower, more focused, literature discussion in this chapter. The recent key developments of perovskite nanocrystal syntheses will be evaluated, focusing particularly on the methodology and the efficacy of the ligand chemistry reported. A significant portion of this literature review was recently published as a Progress Report in Advanced Energy Materials.[112]

2.1 Lead Halide Perovskite Nanocrystals

The properties of the organic ligands used have an enormous influence on many properties of perovskite nanocrystal inks and resulting electroluminescent devices. The nature of the interaction between the ligand binding group and the nanocrystal surface is crucial to the efficacy and stability of surface defect passivation.[113,114] The length, bulk and branching of the ligand tail strongly affect the colloidal stability of the nanocrystals and their conductivity when deposited as thin-films for electronic devices.[99,100,115] Furthermore, the one-pot nature of the colloidal synthesis means that the impact of purification processes, which are necessary to remove reaction by-products and excesses, must also be considered.[116–118]

Beyond the properties of specific ligands, the synthetic methodology employed also influences the commercial attraction of perovskite nanocrystals. Most commonly, high-temperature, air-free "hot-injection" syntheses are employed, which are challenging to scale up.[14] Room temperature processes, especially those conducted without environmental controls, present a far more economically attractive proposition.[100,119] Other relevant factors include synthetic reproducibility and the suitability of the deposition methods for large-scale processing.

This review will begin with a discussion of perovskite nanocrystal syntheses. The achievements of high-temperature syntheses will be outlined, as will their inherent limitations. This will be followed by an analysis of efforts to design room temperature alternatives, identifying critical successes and aspects which still require significant improvement. Important ligand engineering approaches of both the *in-situ* and post-synthetic variety will then be detailed. The review will end with a look into the most promising future routes to enhanced commercial viability.

2.2 Perovskite Nanocrystal Syntheses

In 2014, Schmidt et al. reported the first synthesis of colloidal perovskite nanocrystals.[120] They described a protocol for the preparation of $MAPbBr_3$ nanocrystals, whereby solutions of MABr and $PbBr_2$ in dimethylformamide (DMF) were consecutively added to a hot (80 °C) solution of oleic acid (OA) and octadecylammonium bromide in octadecene (ODE). The resulting 6 nm particles achieved PLQY of around 20 %. One year later, an improved method was outlined by Zhang et al.[121] They dissolved both MABr and $PbBr_2$ together in DMF with the OA and *n*-octylamine (OctAm) ligands, injecting this solution into toluene to obtain 3.3 nm sized $MAPbBr_3$ nanocrystals with PLQY up to 70 %. They suggested that OctAm was responsible for the reaction kinetics (i.e. size control), while the longer OA ligand afforded colloidal stability. The same method was extended to chloride, iodide, and mixed halide compositions, obtaining emission wavelengths ranging from 407 nm to 734 nm.

In the years following these seminal works, there were several more syntheses reported for $MAPbX_3$ nanocrystals.[122–124] However, concerns over the stability of the MA-containing perovskites turned the focus towards more stable formamidinium and cesium-based perovskite nanocrystals. The rest of this review will address these two compositions, as the higher stability offers a far more realistic option for future commercial applications. Given the immense quantity of recent literature regarding perovskite nanocrystals, this review will also narrow its focus to mostly assess the pure bromide compositions. Further reasoning for this was that the work contained in this thesis will be similarly focused on these green-emitting materials and that the near-UV and near-infrared emission of the chloride and iodide compositions, respectively, have less broad commercial appeal for light-emitting devices.

2.2.1 High-Temperature Syntheses

Elevated temperatures are often utilised to manipulate the nucleation thermodynamics of colloidal syntheses. Generally, an increased nucleation temperature enhances the critical radius, ensuring that small nanocrystals are stabilised with respect to redissolution. Temperature also represents an easily modulated parameter for the tuning of nanocrystal size, according to the same mechanism. Furthermore, higher temperatures are sometimes necessary to solubilise desired precursor salts or ligands in the reaction medium. The most common high-temperature synthesis method for perovskite nanocrystals is *hot-injection*.

2.2.1.1 Hot-Injection

The hot-injection method is very commonly utilised for the synthesis of a range of semiconducting nanocrystals. It involves the injection of one precursor solution into the other at elevated

temperature and under inert gas. The resulting supersaturation of monomers initiates rapid nucleation of nanocrystals, which are stabilised at the nanoscale by long-chain ligands also dissolved in the reaction mixture. The reaction vessel is typically quickly cooled by ice water to arrest further nucleation and limit growth.

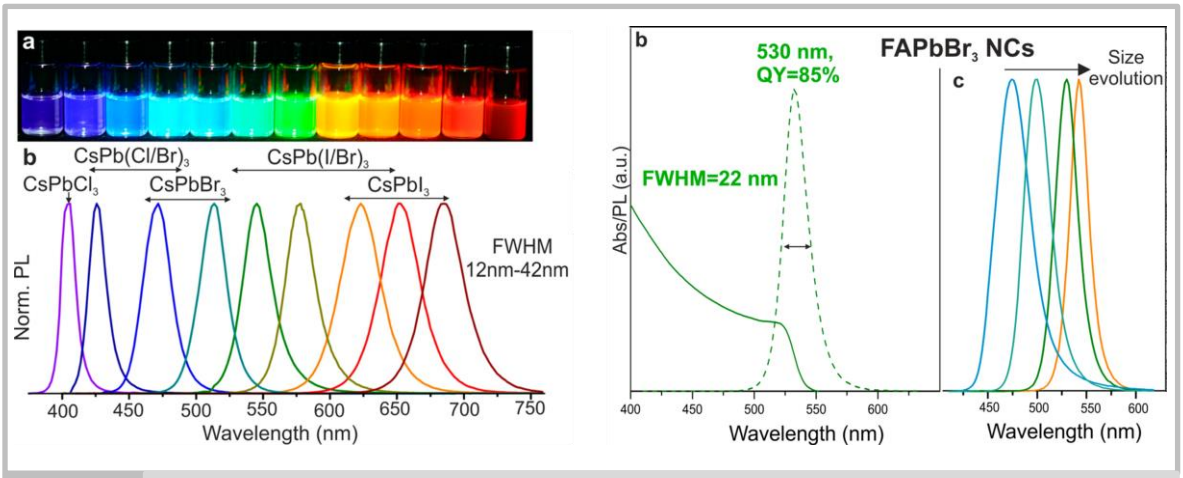

Figure 2.1 **Halide composition tuneability of $CsPbX_3$ nanocrystals (X = Cl, Br, I) (left) and the size tuneability of $FAPbBr_3$ nanocrystals (right), all prepared by hot-injection syntheses**

These figures were reprinted with permission.[78,125] © 2015 and 2016 American Chemical Society.

For perovskites, which are notoriously more sensitive to environmental degradation and decomposition than other semiconductor materials, the hot-injection method was very appealing. The Schlenk line setup necessary for hot-injection offers the capability to thoroughly dry solvents and ligands, such that moisture can be almost eliminated, and thus prevented from interfering with the reaction. This method was first exploited for perovskite nanocrystals in 2015, by the Kovalenko group.[14] They demonstrated the synthesis of monodisperse cubic $CsPbBr_3$ nanocrystals by injecting a cesium oleate solution into a heated mixture of $PbBr_2$, OA and oleylamine (OAm) in the non-polar ODE solvent. The reaction was quenched within 3 s, resulting in nanocrystals with sizes ranging from 4 nm to 15 nm, adjusted by varying the reaction temperature between 140 – 200 °C. They recorded excellent PLQYs of up to 90 %. Moreover, manipulation of the halide composition enabled them to tune the emission wavelength from 410 nm to 700 nm, as illustrated in Figure 2.1.

The same group later adapted their method to synthesise $FAPbBr_3$ nanocrystals, dissolving FA(acetate) and $Pb(acetate)_2$ together with OA in ODE then injecting oleylammonium bromide (OAmHBr) to induce nucleation. [125] This decoupling of the Pb:Br ratio enabled simultaneously FA-rich and halide-rich conditions, which were necessary for colloidal stability and high PLQY,

respectively. As shown in Figure 2.1, they exhibited similar size tuneability to the Cs-based system, modifying the nanocrystal edge length from 5 nm to 12 nm to obtain PL emission between 470 nm and 540 nm. Accessing higher wavelengths with a pure bromide composition was significant because emission above 530 nm is desirable for wide colour gamut display applications.[10]

Imran et al. exploited a similar approach for their $APbX_3$ nanocrystal synthesis (A = MA, FA, Cs; X = Cl, Br, I).[15] They dissolved Cs(oleate) and $Pb(acetate)_2$ with OA and OAm in ODE, injecting benzoyl halides to nucleate the nanocrystals under halide-rich conditions. PLQYs of up to 92 % were achieved, and improved stability was observed. This was attributed to the substitution of surface Cs^+ for alkylammonium.

All methods mentioned so far immediately quenched the reaction in an ice bath after inducing nucleation, with the size primarily governed by the injection temperature. This is extremely challenging to scale up reproducibly, becoming impractical beyond a certain point. It is a crucial disadvantage of hot-injection syntheses from a commercial perspective. However, Dutta et al. demonstrated that it was possible to tune the nanocrystal size at a constant temperature. They modulated the concentration of OAmHBr included in the precursor solution alongside $PbBr_2$, OA and OAm, thereby controlling the size of the $CsPbBr_3$ nanocrystals grown when Cs(oleate) was injected. $CsPbBr_3$ nanocrystals were obtained with sizes between 3.5 and 17 nm, all from reactions at 160 °C. Furthermore, maintaining the nanocrystal solution at the injection temperature for 30 mins caused only a slight red-shift in the photoluminescence. Thus, the problematic temperature quenching step was not required to obtain narrow size dispersions. This approach was more realistically scalable, and presumably more reproducible.

It was clear that hot-injection has been an extremely successful method for perovskite nanocrystal synthesis. It provides full size and compositional flexibility and has consequently proven a reliable approach for various endeavours from fundamental studies,[29,87,126] ligand engineering[114,127,128] and highly efficient optoelectronic devices, such as light-emitting diodes (LEDs)[98,129] and solar cells.[130] Despite its success, there remains some inherent drawbacks. The Schlenk line setup and elevated temperatures required are costly, while the preparation and drying of the precursors make it a very time-consuming process.

2.2.2 Open Air Syntheses

There have been some perovskite nanocrystal syntheses developed that exploit temperature control but without the environmental control imposed by a Schlenk line. These will be referred to here as “open-air syntheses”.

One of the most interesting and distinct open-air syntheses was the so-called phosphine oxide route, pioneered by Almeida et al.[131] They discovered that coordination by Lewis basic trioctylphosphine oxide (TOPO) ligands promoted the dissolution of $PbBr_2$ in a non-polar solvent. Thus, when a solution of Cs(oleate) and OA was injected at elevated temperature (25 to 140 °C), OA competed for coordination with TOPO, releasing $PbBr_2$ to react and form $CsPbBr_3$ nanocrystals. The lack of amines in the precursors and the corresponding highly acidic reaction conditions suppressed Ostwald ripening, such that there was minimal change in the photoluminescence of the nanocrystals after 10 mins. Accordingly, they reported impressive reaction yields of up to 62.5 %. The maximum PLQY achieved was a modest 61 %. However, the method is very promising from a commercial perspective.

The same group recently extended their method to $FAPbBr_3$ nanocrystals. They reported PLQY of up to 70 % at room temperature, with higher temperatures causing the PLQY to drop. Unfortunately, without heating, smaller nanocrystals were obtained, which were blue-shifted from the desirable pure green emission usually offered by $FAPbBr_3$ NCs. Also, they could not reproduce the high yields achieved for the $CsPbBr_3$ synthesis, and the nanocrystals shapes were somewhat irregular. They attributed these problems to the disruptive influence of the interaction between the acidic FA cation and TOPO. Despite the issues, useful insights were gained, and this work highlighted the attractive capability to prepare high-quality perovskite nanocrystals at room temperature.

2.3 Room Temperature Syntheses

Room temperature processes, especially those conducted without environmental controls, present a more economically attractive proposition than high-temperature methods. In this section, the recent progression of room temperature perovskite nanocrystal syntheses was outlined. Consideration was also given to other factors relevant to commercial viability, such as reproducibility, scalability, and the impact of antisolvent purification protocols.

2.3.1 Ligand-Assisted Reprecipitation

The most common room temperature synthesis method is ligand-assisted reprecipitation (LARP). It is straightforward, requiring only basic wet chemistry apparatus: a beaker and a syringe. It is therefore inherently scalable, and more appealing to industry from financial, energy and complexity perspectives.

In the first LARP approaches, the precursor halide salts (i.e. AX and PbX_2) were dissolved stoichiometrically in a polar solvent, normally dimethylformamide (DMF) or dimethyl sulfoxide (DMSO). This solution was injected into a solvent that it is miscible with, but in which the constituent perovskite ions are much less soluble (usually toluene), creating a supersaturated state. Consequently, the perovskite structure immediately nucleated. To limit crystal growth to the nanoscale, organic ligands are added to either solvent before nucleation. The long organic chains of the ligands attached to adjacent crystals repel one another, deterring crystal aggregation, while also enabling the stable colloidal dispersion of the nanocrystals in non-polar organic solvents.

The first use of LARP for $CsPbX_3$ NC synthesis was reported by Li et al. in 2016.[7] They added OA and OAm, the same ligands typically used for early hot-injection approaches, to the halide salt precursor in DMF. They obtained NCs with PLQY > 70 % for various emission wavelengths between 478 and 640 nm ($CsPbClBr_2$ to $CsPbBrI_2$), with a maximum PLQY of 95 % for the pure bromide composition. This demonstrated that elevated temperature and an inert atmosphere were not prerequisites for high-quality $CsPbX_3$ nanocrystals. However, these NCs were not coated as thin-films, presumably because the low reaction yield resulted in a low NC concentration which was not viable for thin-film deposition and subsequent electronic device fabrication.

Veldhuis et al. pinpointed the low solubility of CsBr in DMF as a factor limiting the reaction yield of LARP.[86] To address this, they employed a crown ether to bind to Cs^+, facilitating better solubility. The cavity size of the crown ether determines the size of ion that it will selectively bind to,[132] thus dibenzo-21-crown-[7] (cavity size from 3.4 to 4.3 Å) was chosen to match Cs^+ (ionic radius = 3.3 Å). Using OA and OctAm ligands, a $CsPbBr_3$ NC solution was obtained, from which the NCs could be

precipitated by centrifugation. The mechanism proposed for NC formation is shown in Figure 2.2. Redispersion of this precipitate in fresh toluene provided a $CsPbBr_3$ NC ink from which continuous NC thin-films could be deposited. This enabled the fabrication of NC-based LEDs, leading to a modest external quantum efficiency (EQE) of 2.64 %. It is important to note that this efficiency was achieved by coating two NC films successively, with the LED fabricated from a single coating giving a lower EQE of 1.27 %. This implied that the NC ink concentration remained below the ideal concentration. However, as the volume of toluene in which the NC precipitate was redispersed was controlled, the solubility limitation here must lie with the ligands, and their ability to stabilize the dispersed phase at higher concentration.

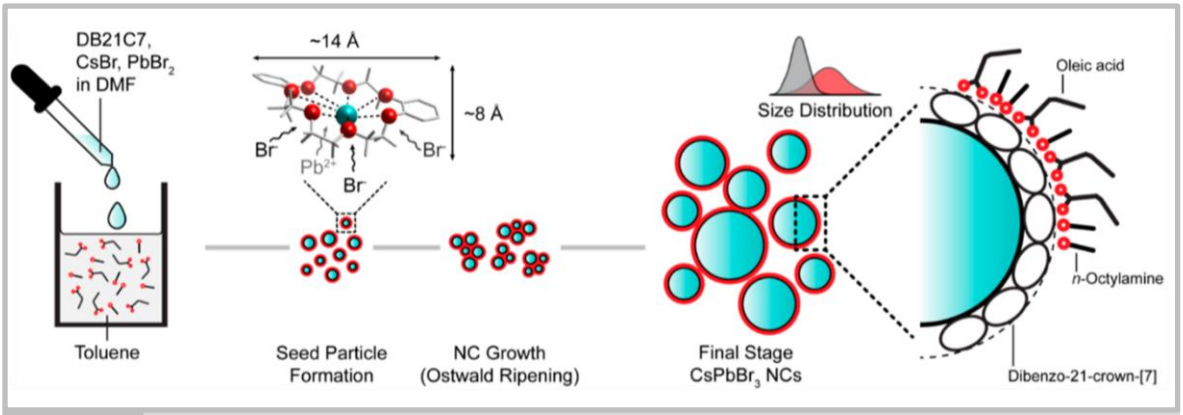

Figure 2.2 **The proposed formation mechanism of the crown ether-enabled ligand assisted reprecipitation synthesis of $CsPbBr_3$ nanocrystals**

This figure was reprinted with permission.[86] © 2018 American Chemical Society.

Moyen et al. took a different approach to improve the yield of $CsPbBr_3$ NC syntheses.[133] They separated the ligands into different precursor solutions (oleylamine in DMF and oleic acid in toluene) to obtain greater control over the ratio between the two ligands on the NC surface. As a result, the reaction yield was increased by around 300 %. In addition to this synthetic modification, they developed a ligand removal protocol. They first expelled large particles by centrifugation, before adding methyl acetate as an antisolvent to precipitate the NCs, removing by-products and presumably some proportion of surface ligand. After redispersing the NCs and depositing a thin-film, they reduced the surface ligand density further, and concurrently increased the NC size, by annealing at 120 °C. The removal of excess insulating ligand material is considered key to improving charge transport in a NC film. The increase of NC size is also likely to be helpful, as it would increase the proportion of intracrystal charge diffusion through the film, relative to much slower intercrystal diffusion. Accordingly, a 13-fold EQE enhancement was observed for LEDs fabricated from annealed films. Furthermore, exposing the annealed films to UV light increased the EQE a further 2.8 times.

This was attributed to surface passivation by either light-assisted water adsorption or photo-oxidation.

Annealing and UV exposure are certainly industrially applicable processes. In general, post-deposition ligand removal is a useful feature as the NC ink could conceivably be distributed containing high concentrations of ligand to ensure stability, without the need for any further wet chemistry to purify before deposition. However, this approach may not be the most conducive to thin-film stability, as there is a thin line between passivation and degradation by oxidative species, particularly as the perovskite lattice is highly ionic.

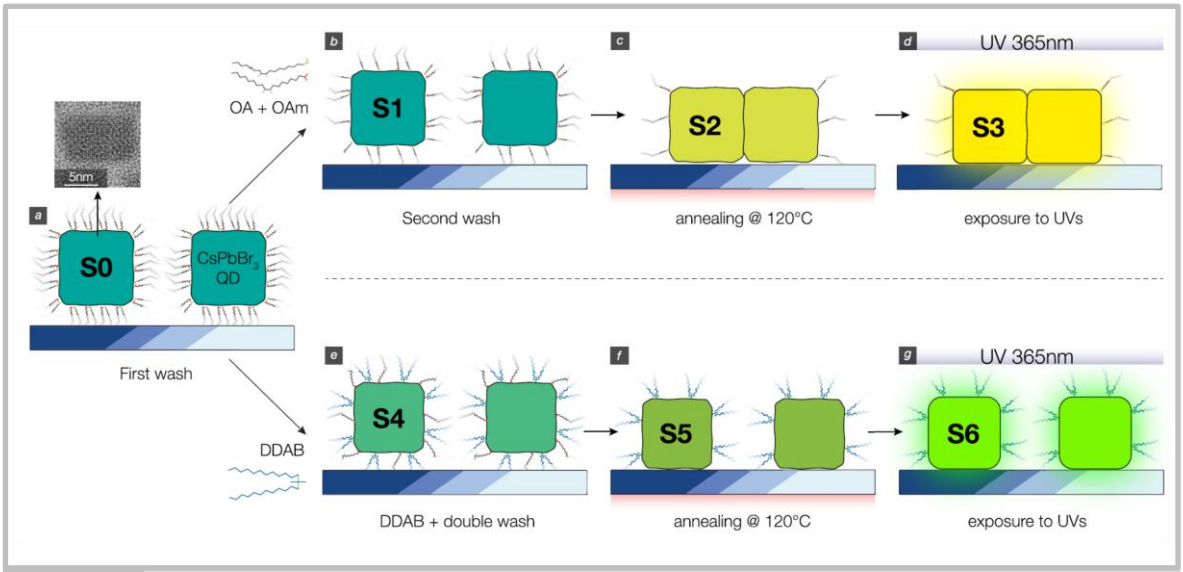

Figure 2.3 **A schematic of the post-treatment of $CsPbBr_3$ NCs synthesised at room temperature**

Reproduced with permission.[134] © 2018 American Chemical Society.

The same group expanded their approach soon after, introducing a ligand exchange protocol with didodecyldimethylammonium bromide (DDAB).[134] They demonstrated that DDAB ligands were more resistant to antisolvent washing and annealing, such that oleic acid and oleylamine are mostly removed, while DDAB mostly remained. This hypothesis is illustrated in Figure 2.3. The effective replacement of the long oleyl ligands with DDAB led to a 10 times improvement in LED efficiency. Interestingly, the efficiency increased by a further 25 % when a higher concentration NC ink was spin-coated at a higher speed. This was attributed to a more uniform film of similar thickness. It has previously been observed for chalcogenide quantum dots that are smoother and more compact films have higher LED efficiency as current leakage is minimized.[135]

To circumvent the issues related to long ligands entirely, Akkerman and co-workers utilized very short ligands, propionic acid and butylamine, to synthesize $CsPbBr_3$ NCs (Figure 2.4).[69] These NCs formed large, aggregated clusters but maintained confined domains of 15 to 20 nm. Consequently,

PLQY of 58 % was obtained, similar to that achieved with longer ligands. A turbid suspension of these NCs could be spin-coated or drop-cast, with only 10 mins of drying at ambient conditions required due to the low boiling point ligands and solvents used. The lack of potentially lengthy purification or treatment steps is very appealing and would significantly reduce solvent wastage. However, it is important to note that although conducted at room temperature, this synthesis was performed inside a nitrogen-filled glovebox. Solar cells were fabricated from these NCs, by depositing multiple layers of NCs to obtain a film of a suitable thickness (around 1 µm) and optical density. No LEDs were reported; it is likely that depositing a uniform film of <50 nm from the turbid ink of NC clusters would have been very challenging.

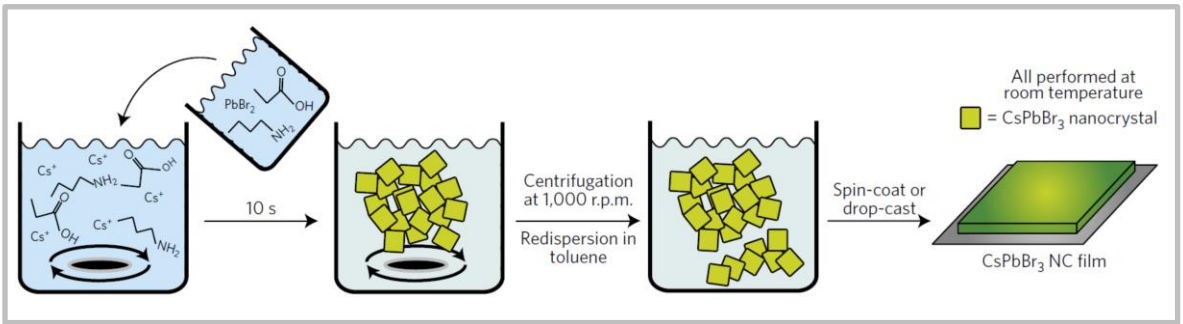

Figure 2.4 **Schematic of a room temperature $CsPbBr_3$ synthesis employing short ligands and low boiling point solvents**

Reproduced with permission.[136]

Ye et al. adapted Akkerman's approach for LED applications.[137] They added carefully optimized amounts of oleic acid and oleylamine to as-synthesised $CsPbBr_3$ NCs, followed by ethyl acetate to precipitate the NCs. By redispersing the nanocrystals and repeating the cycle 4 times, they achieved complete ligand exchange while minimizing excess oleyl ligand in the final NC ink. Ligand exchange significantly improved colloidal stability, leading to LEDs with a reasonable EQE of 5.4 %. This improved efficiency highlighted the benefits of adding the longer ligands post-synthetically, as they do not need to be added in excess.

2.3.2 Polar Solvent-Free Syntheses

More recently, room temperature syntheses of $CsPbX_3$ have avoided the use of DMF or DMSO entirely, through the design of polar solvent-free injection methods. A key motivation for this is the extreme susceptibility of perovskite NCs to degradation by polar solvents. When DMF is used in the reaction mixture, there will likely be some degradation or aggregation before DMF is removed by centrifugation. Polar solvent-free syntheses tend to employ chemistry very close to that of hot-injection syntheses, where only non-polar, non-coordinating solvents are used.

The first polar solvent-free synthesis of $CsPbBr_3$ NCs was reported by Wei et al. in 2017.[119] Analogous to the hot-injection synthesis, they separated the cesium salt, and lead bromide into different precursors. Cesium oleate was dissolved in toluene with oleic acid at room temperature, while $PbBr_2$ was dissolved in toluene with the aid of tetraoctylammonium bromide (TOAB). TOAB can solvate $PbBr_2$ through the formation of the complex $[(C_8H_{17})_4N]^+[PbBr_3]^-$. Injection of the cesium precursor into the lead bromide precursor immediately nucleated $CsPbBr_3$ NCs. It was explained that an advantage of using toluene instead of DMF was the lack of aggregated or very large NCs. Excessively large NCs cannot be colloidally stabilized, so they are expelled by centrifugation, often severely reducing reaction yields. With toluene as the only solvent, they obtained $CsPbBr_3$ NCs with PLQY > 80 %. Furthermore, they demonstrated the scalability of their approach by conducting a 1 L scale synthesis (4000 % scale-up), achieving comparable PLQY. Despite this, the EQE obtained from LEDs using these NCs was very low (0.015 %).

Song et al. sought to improve the suitability of this polar solvent-free synthesis for LED applications by utilizing shorter ligands.[41] Firstly, the oily oleic acid ligand was replaced by octanoic acid, in which Cs_2CO_3 can be dissolved directly at room temperature. Secondly, in addition to TOAB, DDAB was added to the crude solution 5 minutes after nucleation. The nitrogen content before and after DDAB treatment was studied by XPS, proving that only DDAB and octanoic acid act as ligands on the NC surface. TOAB acts only as a solvation agent, as the large steric hindrance of its 4 octyl groups prevents binding to the surface.

2.4 Antisolvent Purification

Effective antisolvent purification is essential to ensure that NC inks are free from reaction by-products and excesses. A commercial NC ink must be highly reproducible with minimal impurities. For electronic device applications, removal of excess ligand material is crucial. This is because these ligands are usually organic and very poor conductors. Therefore, the excess ligand will impede current flow and reduce device performance, and not necessarily in a consistent manner. Furthermore, often the ligands employed are viscous and oily, such that the physical properties of the solution and thin-film may be altered if they are present in excess.

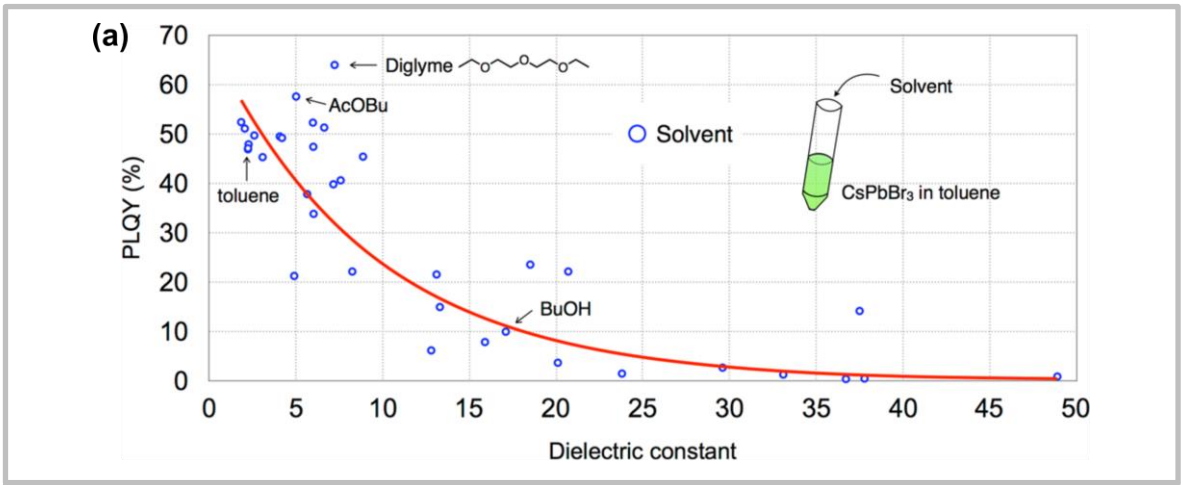

Figure 2.5 **The influence of different purification antisolvents on the PLQY of $CsPbBr_3$ nanocrystals**

Reproduced with permission.[118] © 2018 American Chemical Society.

There have been a few reports focused on identifying suitable antisolvents. A consensus is that the solvent must be aprotic, as protic solvents can promote the extraction of lead ions from the nanocrystal.[116–118] The solvent must also be of medium polarity; that is, polar enough to precipitate the NCs easily, but not so polar as to remove bound ligands or degrade the perovskite crystal during short- term exposure. Typically, short esters have been most successful. Depending on the ligand system employed, butyl acetate,[117] ethyl acetate,[15,100,103,116,138–143] mixtures of ethyl and methyl acetate,[122,144] and methyl acetate alone,[134,145–148] have been employed. Figure 2.5 shows a screening study of 36 potential antisolvents; it concurred on the efficacy of short esters but indicated that diethylene glycol dimethyl ether (diglyme) was the most effective.[118] They subsequently demonstrated that purifying $CsPbBr_3$ NCs with diglyme instead of methyl acetate yielded higher LED efficiency.

Strongly bound ligands are highly desirable for complete purification, as they allow the NCs to be fully precipitated, thus minimizing mass loss, without the risk of minor degradation or ligand removal, which would limit the reproducibility of purification. Furthermore, it is reasonable to assume that an antisolvent with higher polarity (or higher dielectric constant) will remove impurities more effectively; thus NCs which can withstand more polar solvents should be more thoroughly purified. This point is well [145]illustrated by the octylphosphonic acid ligands utilized by Tan et al. They demonstrated that with these strongly bound ligands, the NCs could withstand 8 purification cycles with methyl acetate without significant loss of PLQY, as shown in Figure 2.6.

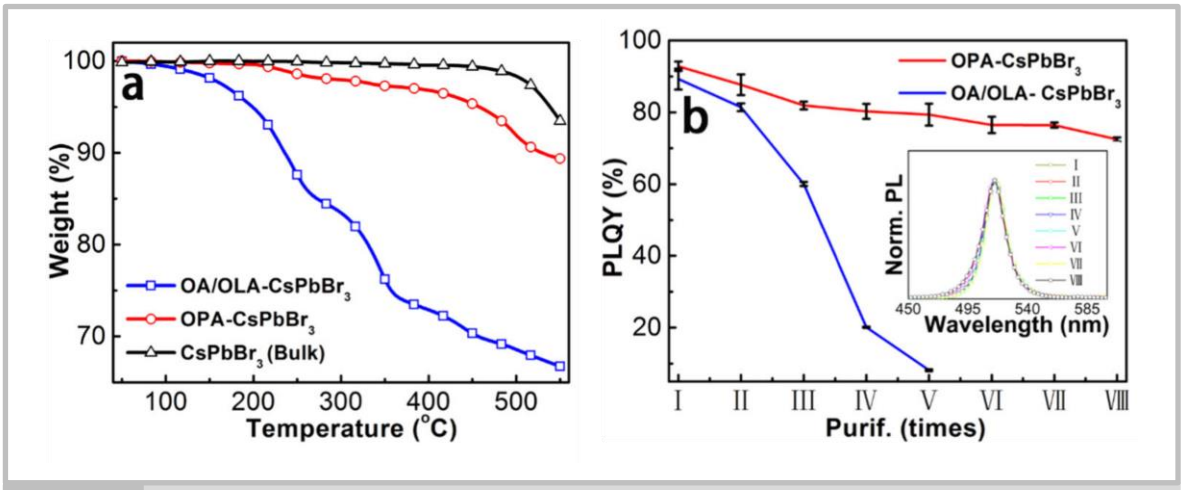

Figure 2.6 **A comparison of $CsPbBr_3$ nanocrystals with octylphosphonic acid (OPA) or oleic acid/oleylamine (OA/OLA) ligands**

(a) thermogravimetric analysis, (b) the change in PLQY over multiple methyl acetate purification cycles (inset shows PL curves for all OPA samples). Adapted with permission.[145] © 2018 American Chemical Society.

2.5 Ligand Engineering

2.5.1 Beyond Dynamic Ligand Binding

Since the first hot-injection syntheses using the acid/base OA/OAm ligand pair, many reports have sought to avoid amine ligands. The drive to replace amine ligands was primarily based on stability concerns, as amine-capped nanocrystals would readily precipitate from solution. This was attributed to the highly dynamic binding of the acid/base pair, such that rapid proton transfer between the amine/ammonium and carboxylic acid/carboxylate occurs readily.[149] As a result, the ligands are prone to desorption from the NC surface. New ligands have been sought that bind more strongly and, crucially, irreversibly to perovskite NC surfaces. A wide range of alternative ligands has been explored, most often using high-temperature syntheses. However, probably, most, if not all, of these ligands could also be applied in room temperature syntheses, utilizing solubilizing agents if necessary.

2.5.2 Quaternary Ammonium Halides

Quaternary ammonium halides have become ubiquitous ligands for $CsPbBr_3$ NCs,[100,117,126,128,134,139,150,151] representing a logical upgrade on the initial amine ligands. Quaternary ammonium halides contain the same binding functionality that a primary amine provides, but are unable to participate in proton exchange. DDAB is particularly appealing as it provides better colloidal stability from shorter alkyl chains. It contains two C_{12} alkyl chains, affording greater steric bulk. Recently, a study by Park et al. compared $CsPbBr_3$ NCs capped with quaternary ammonium bromide ligands with 1, 2, 3 or 4 long-chain groups attached to the N^+ centre.[99] They confirmed that 2 long chains (with the other 2 being methyls) provided the highest EQE in LEDs, but also that using the slightly shorter decyl groups enhanced EQE relative to the dodecyl groups on DDAB.

It is likely that the ability of DDAB to interrupt interparticle ligand-ligand interdigitation was also critical to the colloidal stability it afforded. The interdigitation of straight-chain ligands on adjacent particles has been correlated to lower solubility, due to the high enthalpic cost of untangling the chains.[152] The "triple ligand" approach mentioned earlier, where TOAB solubilized $PbBr_2$, Cs_2CO_3 was dissolved in octanoic acid (OctAc), and DDAB passivated the NC surface, enabled $CsPbBr_3$ NC LEDs with up to 6 % EQE.[100] This efficiency was partly attributable to the substitution of oleic acid for octanoic acid; NCs synthesised with octanoic acid showed higher electron and hole currents in single carrier devices, indicating improved electron injection and conductivity in the film. Generally, higher currents can also be attributed to a lower quantity of excess unbound ligand or other

insulating synthetic by-products in the film. The greater colloidal stability provided by DDAB allowed high-quality, highly concentrated NC inks to maintain their properties through two antisolvent washing cycles with ethyl acetate.

To push the EQE of their NC LEDs higher, Song et al. employed a simple FA doping strategy. By dissolving formamidine acetate in OctAc alongside Cs_2CO_3, $Cs_{1-x}FA_xPbBr_3$ NCs were obtained. This resulted in a dramatic improvement from around 6 % to 11.6 % EQE with an optimum value of x = 0.15, which was supported by time-resolved photoluminescence (TRPL) showing a doubling of the radiative recombination lifetime (τ_2). They also demonstrated impressive scalability; Figure 2.7 demonstrates that high EQE was maintained when the reaction scale was increased 100 times. The decoupling of passivation from the nucleation and growth processes may provide a useful mechanism to circumvent PLQY loss with upscaling.

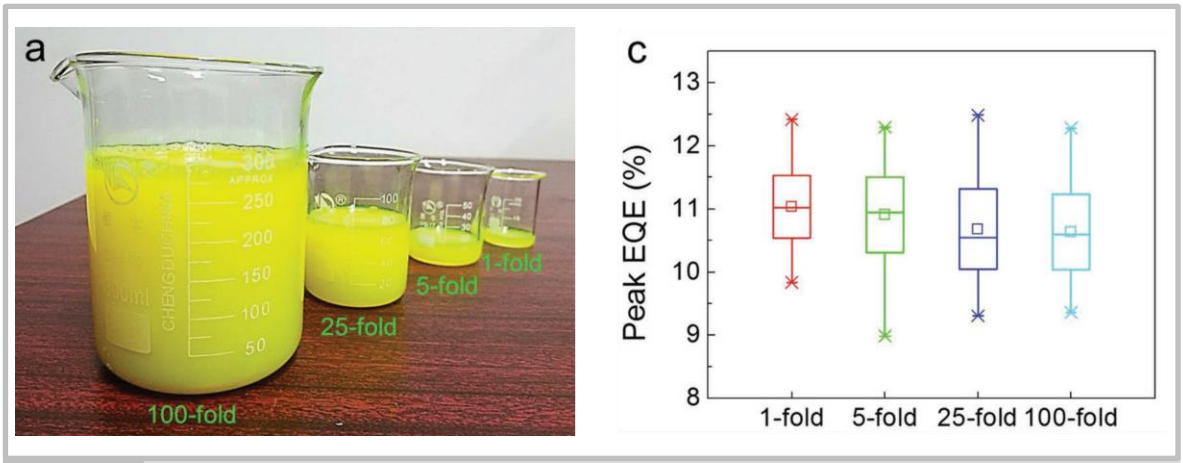

Figure 2.7 **Scaled up $Cs_xFA_{1-x}PbBr_3$ nanocrystal syntheses using OctAc and DDAB ligands**

(a) Images of reaction scale, and (b) the change of peak EQE with increasing reaction scale. Adapted with permission.[100] © 2018 American Chemical Society.

2.5.3 Metal Halides

Song et al. developed their triple ligand $Cs_{1-x}FA_xPbBr_3$ NC synthesis further by including a second post-nucleation treatment after DDAB.[150] They introduced a metal bromide solution (MBr_x, M = Zn^{2+}, Mn^{2+}, Ga^{3+} or In^{3+}), dissolved in toluene with TOAB, after a further 3 minutes.[150] The metal bromides acted only as passivating agents; X-ray photoelectron spectroscopy (XPS) showed a 3 times reduction in octanoic acid content, alongside an increase in the Br:Pb ratio, suggesting the metal bromides substituted for octanoic acid on the NC surface. This further reduction in surface ligand density on the NCs was correlated to the resulting exceptional EQE of 16.48 % from LEDs. This was accompanied by an increase in operational stability from 37 mins to 136 mins. Despite NC solutions with and without MBr_x passivation showing solution PLQYs > 90 %, it was found that after MBr_x passivation, the retention of PLQY from solution to thin-film was much better. This highlighted

the importance of reporting thin-film PLQY, not only solution PLQY when correlating NC properties to LED performance.

It is not clear strictly which factors govern the degree of PLQY drop from solution to film. Although managing the morphology of perovskite NC films is much less complicated than controlling the crystal growth of quasi-2D or 3D perovskite during coating, the uniformity of films remains important. A study on CdSe/ZnS quantum dots has shown that spin-coating nanoparticle films from a highly volatile solvent (hexane) yields rougher films than a less volatile solvent (octane) as strong capillary forces from rapid evaporation induce film thickness fluctuations.[135] This resulted in poorer charge injection efficiency in LEDs and approximately 40 % lower EQE.

2.5.4 Anionic Ligands

In contrast to quaternary ammonium halides, where the ammonium binds strongly to anionic sites while the halide binds to under-coordinated lead sites (i.e. halide vacancies), there have been several recent reports where anionic surface ligands are used to passivate these positively charged sites. While these ligands have so far mostly been utilized for hot-injection syntheses, their solubility in non-polar solvents, alone or with assistance from co-ligands such as TOAB or trioctylphosphine oxide (TOPO), implies that they should be compatible with established room temperature syntheses.

2.5.4.1 Softer Carboxylic Acids

At the start of this chapter, the common use of simple carboxylic acids, such as oleic and octanoic acid was discussed, and their generally weak binding to perovskite nanocrystals was highlighted. Nenon et al. correlated this to a hard-soft mismatch between the ligand binding group and the lead ions;[113] that is, the electron density on the carboxylic acid group was too high to interact sufficiently strongly with the large, diffuse charge on Pb^{2+}. Consequently, they showed that ligand substituents which withdraw electron density from the carboxylic acid group, such as aromatic or fluorinated aliphatic groups, facilitated stronger ligand binding. This theory was summarized by the depiction of a $CsPbX_3$ NC surface in Figure 2.8. Softer acid groups, such as phosphonic and sulfonic acids, were found to bind similarly strongly.

Pan et al. utilized a softer, bidentate carboxylic acid, 2,2-iminodibenzoic acid (IDA), as a post-synthetic ligand treatment for $CsPbI_3$ NCs.[138] They noted that their attempt to incorporate IDA in the synthesis led to NC agglomeration, presumably because it is too short to provide sufficient colloidal stability. Instead, they simply added IDA powder to the $CsPbI_3$ NC solution after a standard

hot-injection synthesis. IDA stabilized the NCs effectively, enabling retention of PLQY for over 15 days, in stark contrast to the untreated NCs whose PLQY was completely quenched after 7 days. In the case of $CsPbI_3$, this was presumably due to conversion to the thermodynamically favoured, non-emissive phase upon aggregation. It is conceivable that short bidentate ligands such as IDA could be incorporated into room temperature syntheses with appropriate solubilizing agents; however, a longer chain co-ligand would be required to ensure colloidal stability.

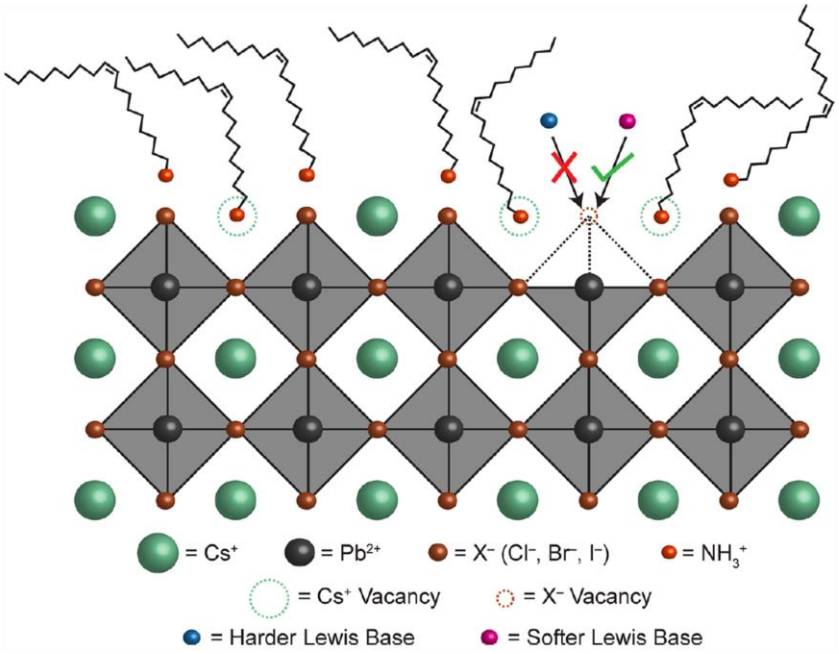

Figure 2.8 **Depiction of the relative capabilities of hard and soft Lewis base ligands to bind to the surface of $CsPbX_3$ nanocrystals**

Reproduced with permission.[113] © 2018 American Chemical Society.

2.5.4.2 Phosphonic Acids

As well as softer carboxylic acids, there have been a few reports of $CsPbBr_3$ NCs synthesised using phosphonic acid ligands. As mentioned earlier, the replacement of oleic acid and oleylamine with octylphosphonic acid (OPA) improved antisolvent tolerance remarkably.[145] To solubilize OPA in the reaction mixture, TOPO was added, helping to solubilize phosphonic acids through hydrogen bonding interactions. This approach should also be useful for solubilizing other acids in non-polar solvents.

Interesting binding chemistry between phosphonic acids and the $CsPbBr_3$ surface was reported by Zhang et al.[142] They discovered that the conditions of their hot-injection synthesis (Figure 2.9) drove a condensation reaction, forming phosphonic acid anhydrides from phosphonic acids. These phosphonic acid anhydride species could then form bidentate bonds to the $CsPbBr_3$ NC surface, presumably because the distance between adjacent hydroxyl groups on the anhydride was similar

to the spacing between lead sites of the NC. The phosphonic acid ligands promoted the formation of nanocrystals with a truncated octahedron shape. As illustrated in Figure 2.9, this unusual shape presented some more complex faceting than the typical cubic $CsPbBr_3$ NCs. The introduction of phosphonic acid anhydrides to room temperature syntheses could provide an alternative passivation strategy to explore, where the bidentate anchoring may improve NC stability. However, Zhang and co-workers pointed out that while the colloidal stability with these phosphonic acid ligands was high, they were prone to desorption when the dispersion was heated to 50 °C. Further investigation is required into whether this thermal instability is also observed for thin films of NCs. It would represent a serious problem for utilizing phosphonic acid capped perovskite NCs in electronic devices, where Joule heating can be expected to raise the local operating temperature.[88]

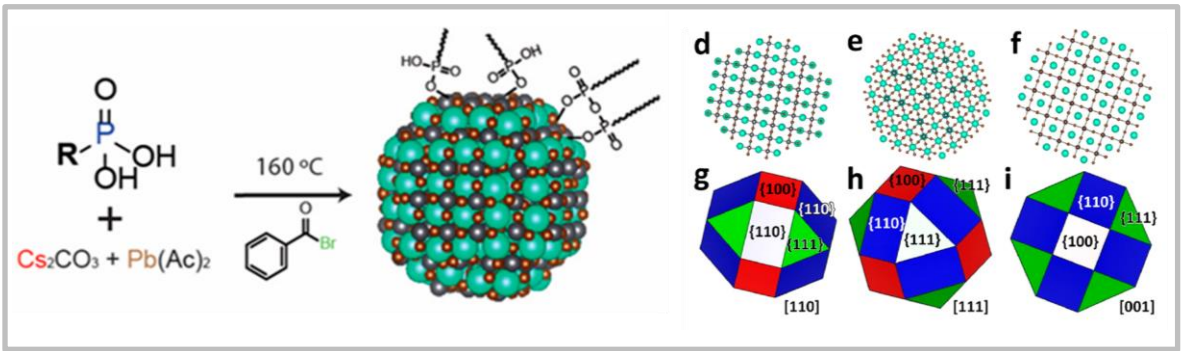

Figure 2.9 **Scheme representing the synthesis of $CsPbBr_3$ with phosphonic acid ligands and the different growth facets of the resulting truncated octahedron shaped particles**

Adapted with permission.[142] © 2019 American Chemical Society.

2.5.5 Zwitterionic Ligands

A distinctly different ligand engineering approach was taken by Krieg et al. Rather than combining anionic or cationic species as co-ligands, they exploited zwitterionic ligands, which are dipolar molecules with two oppositely charged functional groups.[153] These bind in a bidentate manner, coordinating to cationic and anionic surface sites simultaneously, thus affording additional stability according to the chelate effect.[154] Hot-injection $CsPbBr_3$ NC syntheses were tested with three different types of zwitterion, all of which had quaternary ammonium groups but different anionic groups. These included a sulfobetaine (3-(N,N-dimethyloctadecylammonio)-propanesulfonate), which contains a sulfonate group, a phosphocholine (N-hexadecylphosphocholine), which contains a phosphate group, and a *γ*-amino acid (N,N-dimethyldodecylammoniumbutyrate), which contains a carboxylate group. Figure 2.10 shows the structures of each of these ligands, alongside schematics illustrating their tight binding nanocrystal surface. The sulfobetaine was studied in more detail; they found that by adjusting the length of the alkyl spacer, thus changing the gap between the functional

groups, the ligand could be tailored for chloride, bromide and iodide NCs, which have different lattice parameters. The sulfobetaine exhibited is particularly attractive commercially as it is a ubiquitous low-cost detergent. Later, Ochsenbein et al. demonstrated that this long-chain sulfobetaine does not severely inhibit inter-nanocrystal conductivity, by fabricating blue and green-emitting LEDs from $CsPbBr_xCl_{3-x}$ NCs, yielding reasonable EQEs of 1.4 % and > 6 %, respectively.[155]

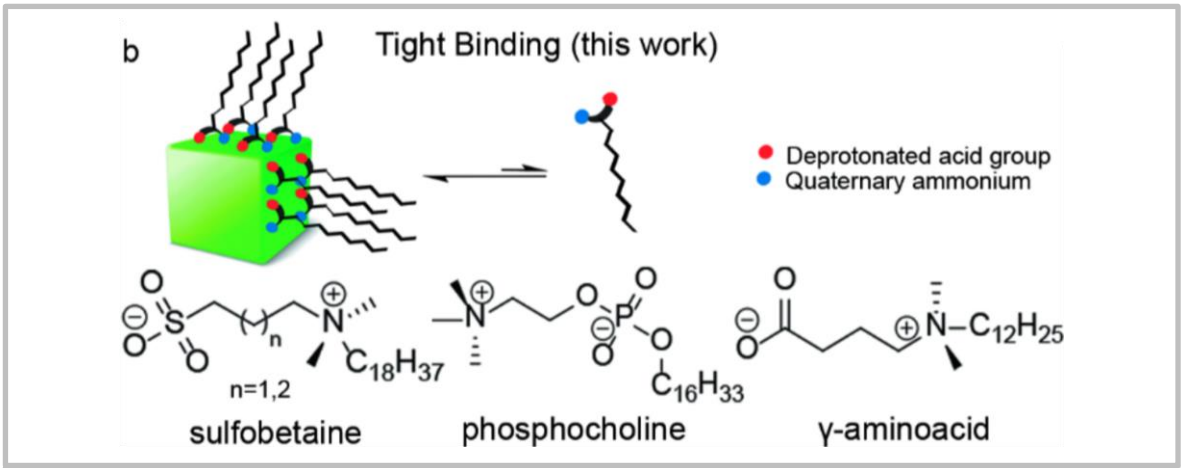

Figure 2.10 **Illustration of the binding mechanism of zwitterionic ligands to $CsPbBr_3$ nanocrystals and their chemical structures**

Adapted with permission.[153] © 2018 American Chemical Society.

Zu et al. recently adopted the same sulfobetaine zwitterionic ligand for a pseudo-room temperature $FAPbBr_3$ nanocrystal synthesis.[156] They dissolved the ligand with $PbBr_2$ and FABr in DMF at 90 °C, injecting the hot solution into a room temperature solution of dichloromethane. The resulting $FAPbBr_3$ nanocubes exhibited an appealing emission wavelength of 534 nm, with FWHM of 20.5 nm and exceptional PLQY of 90.6 %. This served as a good example that ligand improvements first developed for hot-injection syntheses can translate well to room temperature syntheses, with some careful adjustments.

2.6 Summary

There has been vast progress on perovskite nanocrystal syntheses over the brief six-year period since the first report. There have been many modifications made to the high-temperature hot-injection method. The initial weakly binding carboxylic acid/amine ligands have been replaced by a library of strongly binding ligands including quaternary ammonium halides, anionic ligands such as softer and multidentate carboxylic acids, phosphonic acids and sulfonic acids, and zwitterionic ligands, such as a long chain sulfobetaine and soy lecithin. Although most of these novel ligands have not yet been utilized for room temperature syntheses, the methodology framework outlined here, particularly the use of bulky solubilizing agents such as tetraoctylammonium halides and trioctylphosphine oxide, should soon facilitate this.

The capability to prepare state-of-the-art semiconducting nanomaterials from low-cost precursors in open air at room temperature is undoubtedly appealing to industry. Thus, transferring and optimising the promising passivation improvements mentioned here for room temperature syntheses would represent an important step towards realizing the commercial potential of perovskite nanocrystals.

Chapter 3 The Study of Phosphonic Acid Ligand Binding to $CsPbBr_3$ Nanocrystals

3.1 Introduction

The weak, dynamic binding of standard carboxylic acid and alkylamine ligands compromises the colloidal stability of $CsPbBr_3$ nanocrystals and prevents complete purification without degradation of their optoelectronic properties. Without long-term stability and robust ligand passivation, the commercial viability of $CsPbBr_3$ nanocrystal is severely limited.

Octylphosphonic acid was identified as a highly promising replacement ligand due to its apparent robust, solvent-resistant binding to the $CsPbBr_3$ surface. However, the mechanism for this stronger binding remained unexplained. Understanding the mechanism responsible was vital to the rational design of ligand systems which can raise the passivation of $CsPbBr_3$ nanocrystals towards a commercially viable level.

In this chapter, the interaction between octylphosphonic acid (OPA) ligands and the surface of $CsPbBr_3$ nanocrystals was studied. A ligand exchange protocol was developed to obtain nanocrystals with OPA bound to their surface. The effect of OPA on the photoluminescence properties was first quantified, then the ligand exchange and binding mechanisms were elucidated through various materials characterisation techniques.

3.2 Materials and Methods

This section describes the experimental methodology adhered to in this chapter.

3.2.1 Chemicals

Lead bromide ($PbBr_2$, ≥ 99.999 % trace metals basis), cesium carbonate (Cs_2CO_3, 99.9 % trace metals basis), 1-octadecene (ODE, 90%), oleic acid (OA, 90%), oleylamine (OAm, 70%), octylphosphonic acid (OPA, 98%), trioctylphosphine oxide (TOPO, 99%), toluene (anhydrous, 99.8%), ethyl acetate (anhydrous, 99.8%), and acetonitrile (anhydrous, 99.8%) were purchased from Sigma- Aldrich. All chemicals were used without further purification. OA and OAm were dried separately under vacuum at 120 °C for a minimum of 2 hours before use.

3.2.2 Cesium Lead Bromide Nanocrystal Synthesis

3.2.2.1 Cesium Oleate Preparation

Cs_2CO_3 (0.41 mmol, 0.268 g) and ODE (10 mL) were dried under vacuum at 120 °C for 30 min. Dried OA (3.16 mmol, 1 mL) was added to this under nitrogen, and the solution was dried under vacuum at 120 °C for 90 min. The solution was then heated at 140 °C under nitrogen for 30 min to ensure complete formation of Cs(oleate). The Cs(oleate) solution was kept at 120 °C under vacuum until required.

3.2.2.2 Standard Synthesis Method

$CsPbBr_3$ nanocrystals were synthesised according to a published hot-injection method.[14] $PbBr_2$ (0.38 mmol, 0.138 g) and ODE (10 mL) were dried under vacuum at 120 °C for 15 min. Dried OA (3.16 mmol, 1 mL) and dried OAm (3.02 mmol, 1 mL) were added under nitrogen, and the solution was dried under vacuum at 120 °C for 60 min. The $PbBr_2$ solution was heated to 170 °C under nitrogen. 0.8 mL Cs(oleate) was swiftly injected into the $PbBr_2$ solution with vigorous stirring, and the reaction was quenched after 5 s in an ice water bath, with vigorous swirling to promote homogenous cooling.

3.2.2.3 OPA/TOPO Synthesis Method

$CsPbBr_3$ nanocrystals were also synthesised according to the method of Tan et al.[145] This was identical to the above standard method, except that OPA (1.03 mmol, 0.2 g) and TOPO (5.17 mmol, 2 g) replaced OA and OAm as the ligands.

3.2.2.4 Nanocrystal Purification

3.2.2.4.1 Nanocrystal Isolation

For nanocrystals synthesised by the standard method, 12.5 mL crude NC dispersion was centrifuged for 10 min at 8000 rpm. The precipitate was redispersed in 2.5 mL toluene and centrifuged for 10 min at 3000 rpm. The precipitate was discarded, and the supernatant was retained for antisolvent washing.

3.2.2.4.2 OPA Ligand Exchange

For OPA-treated samples, a solution of OPA in toluene (0 to 50 mM) was added at 1:1 v/v to the NC dispersion. For untreated reference samples, toluene was added instead of the OPA solution at the same ratio to maintain the same dilution.

3.2.2.4.3 Antisolvent Purification

An optimised purification protocol was developed in Section 4.3. Ethyl acetate was added to the $CsPbBr_3$ dispersion at a 3:1 v/v ratio, and the mixture was centrifuged for 10 min at 8000 rpm. The precipitate was redispersed in 50 % the initial volume of toluene and centrifuged for 10 min at 3000 rpm. The precipitate was discarded, and the supernatant was retained. Acetonitrile was added to the toluene dispersion at a 1:1 v/v ratio, and the mixture was centrifuged for 10 min at 8000 rpm. For solid-state characterisation, the precipitate was dried under vacuum then collected as a powder. For solution state characterisation, the precipitate was redispersed in 50 % the initial volume of toluene and centrifuged for 10 min at 3000 rpm. The resulting supernatant was considered the fully purified nanocrystal ink.

3.2.3 Characterisation Methodology

3.2.3.1 Optical Absorption Spectroscopy

Absorbance spectra were obtained using a Shimadzu UV-3600 spectrophotometer. The samples were prepared in Quartz cuvettes and diluted by a factor of between 60 and 600 (5 – 50 µL NC ink in 3 mL solvent). Typically, the spectra were recorded over a wavelength range of 600 – 350 nm. The measurement settings were as follows: interval = 0.5 nm, integration time = 0.1 s.

3.2.3.2 Photoluminescence Spectroscopy

Photoluminescence spectra were collected using a Horiba Fluoromax-4 spectrophotometer. The samples were prepared in Quartz cuvettes and diluted by a factor of between 60 and 600 (5 – 50 µL NC ink in 3 mL solvent). A laser excitation wavelength of 365 nm was used. The other measurement settings were as follows: interval = 0.5 nm, integration time = 0.1 s, excitation slit width = 1 nm, emission slit width = 0.5 nm.

Where appropriate, the measured PL intensity was corrected for the absorbance intensity at the excitation wavelength according to:

Equation 3.1

$$I_{corr} = \frac{I_{meas}}{(1 - 10^{-A})}$$

Where A was the absorbance at the excitation wavelength (i.e. at 365 nm).

3.2.3.3 Photoluminescence Quantum Yield Measurement

Photoluminescence quantum yield was measured using a 445 nm diode laser (Cobolt) to excite the sample. The samples were prepared in Quartz cuvettes and diluted such that absorption was approximately 20 %. The emission was collected by a Labsphere integrating sphere coupled to an Andor Kymera monochromator in which the emission intensity was registered by a photomultiplier tube. The laser intensity used was 5 mW/cm^2.

3.2.3.4 Transmission Electron Microscopy

Electron micrographs were obtained using a Tecnai G2 F20 with a Schottky field emitter operated at 200 kV. Selected samples were diluted by a factor of 100 and drop-cast on a carbon-copper grid. For examination, the grids were mounted on an FEI Double Tilt Analytical Holder. The instrument operated at a beam current of > 100 nA, providing high probe current (> 0.5 nA in 1 nm probe).

3.2.3.5 Small-Angle X-ray Scattering

Small-angle X-ray scattering (SAXS) measurements were conducted using a Xenocs Nano-inXider, equipped with a Dectris Pilatus3 hybrid pixel detector. This allowed measurement of the effective scattering vector magnitude in the range of $0.0821 < q < 4.47$ nm^{-1}. The samples were measured in sealed glass capillaries under vacuum at room temperature. Particle size distributions were obtained (form-free) from scattering curves using the Monte Carlo-based software package McSAS, using a convergence criterion of 5, with 20 calculating repetitions, and 500 contributions.[157]

3.2.3.6 Solution Nuclear Magnetic Resonance Spectroscopy

Solution nuclear magnetic resonance experiments were completed on a Bruker Avance I 9.40 T (υ_0 (^{1}H) = 400.13 MHz) spectrometer with a Bruker 5 mm BBO probe. A ^{1}H one-pulse sequence, with a $\pi/2$ pulse length of 10 µs and a recycle delay of 1 s, was employed. Samples were prepared with toluene-d8 solvent and were referenced internally.

3.2.3.7 Solid-State Nuclear Magnetic Resonance Spectroscopy

All solid-state nuclear magnetic resonance experiments were completed on a Bruker Avance III HD 600 MHz spectrometer with a Bruker 1.9 mm HXY MAS probe. The ^{13}C NMR experiments were completed at 14.1 T (υ_0 (^{13}C) = 150.92 MHz) with a magic angle spinning (MAS) frequency of 12 kHz. A ^{13}C cross-polarisation (CP) MAS pulse sequence, with a contact pulse length of 5000 µs and high power proton decoupling, was employed and resulting data was referenced with respect to adamantane ($C_{10}H_{16(s)}$; δ_{iso} = 38.48, 40.49 ppm). The 2D ^{31}P–^{1}H heteronuclear correlation (HETCOR) NMR experiments were completed at 14.1 T (υ_0 (^{31}P) = 242.97 MHz and υ_0 (^{1}H) = 600.19 MHz) with a MAS frequency of 15 kHz. A ^{31}P–^{1}H CP HETCOR sequence, with a contact pulse length of 5000 µs and high power proton decoupling, was employed and resulting data was referenced with respect to ammonium dihydrogen phosphate ($(NH_4)_2HPO_{4(s)}$; δ_{iso} = 0.99 ppm). A ^{1}H $\pi/2$ pulse length of 2.5 µs, determined on adamantane, and a recycle delay of 2 s, were used in all CP experiments.

3.2.3.8 Fourier Transform Infrared Spectroscopy

Attenuated total reflectance Fourier transform infrared (ATR-FTIR) measurements were performed using a Perkin Elmer Frontier, equipped with a Diamond ZnSe ATR crystal. Spectra were collected from 4000 to 500 cm^{-1} (100 scans; 1 cm^{-1} per step).

3.2.3.9 Thermogravimetric Analysis

Thermogravimetric analysis was conducted using a TA Q500 instrument. Purified $CsPbBr_3$ NCs were dried under vacuum to obtain a dry powder. In each measurement, 5 to 10 mg of $CsPbBr_3$ NC powder was placed in an alumina crucible on a platinum pan. The sample was measured under a nitrogen atmosphere with temperature ranging from room temperature to 600 °C at a ramp rate of 10 °C min^{-1}.

3.3 Results and Discussion

3.3.1 The Development of a Ligand Exchange Strategy

Cesium lead bromide nanocrystals are most often synthesised by the hot-injection method.[14] According to this method, a cesium oleate precursor is injected into a heated solution of lead bromide in a non-coordinating solvent (octadecene, ODE) containing oleic acid (OA) and oleylamine (OAm) ligands. The reaction mechanism can be described by:

Equation 3.2

$$\mathbf{2Cs(RCOO) + 3PbBr_2 \longrightarrow 2CsPbBr_3 + Pb(RCOO)_2}$$

Meanwhile, it is well-established that the ligands enter into the following dynamic equilibria between unbound (left) and bound (right) states:

Equation 3.3

$$\mathbf{RCOOH + RNH_2 \rightleftharpoons RCOO^- + RNH_3^+}$$

Equation 3.4

$$\mathbf{HBr + RNH_2 \rightleftharpoons Br^- + RNH_3^+}$$

Where *R* designates alkyl groups, typically oleyl ($CH_3(CH_2)_7CH{=}CH(CH_2)_8$).

Equation 3.2 shows that this synthesis produces a by-product, $Pb(RCOO)_2$. It is desirable to remove this impurity, in addition to the oily ODE solvent, unbound ligand species, and any leftover reactants. To expel these species from the nanocrystal solution, the nanocrystals must be precipitated by centrifugation and redispersed in fresh solvent. However, redispersion disrupts the binding equilibria shown in Equation 3.3 and Equation 3.4. As most of the unbound species are withdrawn from the system by centrifugation, upon redispersion a proportion of bound species desorb from the NC surface to re-establish the equilibria. This results in a reduction of PLQY and colloidal stability. Essentially, the weak binding of OA and OAm prevents effective purification.

Phosphonic acids have been suggested as better alternative ligands to OA and OAm. Before the commencement of this work, Tan et al. reported $CsPbBr_3$ NCs synthesised using octylphosphonic acid (OPA) and trioctylphosphine oxide (TOPO) in place of OA and OAm.[145] They found that the OPA/TOPO-capped NCs could maintain high PLQY (> 75 %) after 8 purification cycles with methyl acetate, while the PLQY of identically purified OA/OAm NCs dropped below 10 % after only 5 cycles. Such a contrast in antisolvent resistance indicated that the OPA/TOPO ligand system followed a different, more effective ligand binding mechanism. No characterisation was provided to support a new mechanism, but the authors speculated that the phosphonic acid might bind in a bidentate

mode, which was presumed to be a stronger interaction. They also stated that high-quality NCs could not be obtained using only TOPO, suggesting that OPA was the active binding ligand.

To uncover the origin of the observed strong binding of octylphosphonic acid ligands to $CsPbBr_3$, the ligand binding must be analysed and compared with that of the standard OA/OAm ligand system. There were two different routes identified to compare the ligand binding of OA/OAm and OPA. Nanocrystals could be synthesised with each ligand system, where OPA and TOPO influence the nucleation and growth processes, as well as binding to the surface of the final NCs. Alternatively, nanocrystals could be synthesised according to the well-studied OA/OAm method, with a post-synthesis ligand exchange developed to introduce OPA ligands to the NC surface. The latter was the selected approach. The primary reason was that it decoupled the ligand-surface interaction from the size, shape, and faceting of the NCs. The size distribution, shape and surface termination can all vary when the ligand system or synthetic method are altered. For example, in the paper mentioned above,[145] the OPA/TOPO NCs appeared pseudo-spherical under an electron microscope, whereas OA/OAm are widely reported to adopt cubic, or at least cuboidal, shapes. Notably, a paper published after the completion of this work reported the high-temperature synthesis of $CsPbBr_3$ NCs with solely phosphonic acid ligands, elucidating a truncated octahedron NC shape with different faceting.[142] Thus, analysing ligand binding to NCs synthesised identically in the same batch, according to a well-studied procedure, was a fairer, more accurate and more reproducible approach.

Cesium lead bromide nanocrystals were synthesised according to the hot-injection method outlined by Protesescu et al.[14] This method has been frequently employed in literature, with generally only minor alterations. However, various post-synthetic processes to isolate and purify the nanocrystals have been reported. Thus, it was essential to identify an effective protocol to follow here.

3.3.1.1 Nanocrystal Isolation

At elevated temperatures, perovskite nanocrystal growth occurs almost immediately after nucleation. Therefore, even the fraction of a second that it takes to inject the precursor will introduce some overlap between nucleation and growth phases. This results in some broadening of the size distribution. The simplest way to analyse the NC size distribution is photoluminescence spectroscopy. The emission wavelength of a NC is dependent on its size; therefore, the full-width half maximum (FWHM) of the photoluminescence peak provides a qualitative assessment of the size distribution. Accordingly, the isolation stage was guided by the narrowing of the PL peak.

To isolate the majority size fraction of the NCs, a two-step centrifugation protocol was employed. The crude solution was centrifuged at high speed to precipitate a significant proportion of the NCs, leaving the fraction containing the smallest NCs in the supernatant. The precipitate was then redispersed in a smaller volume of fresh toluene, a far less viscous non-polar solvent which is a more appropriate solvent than the reaction medium, octadecene. The second step was slower speed centrifugation, intended to precipitate out only the largest and most colloidally unstable NCs. Figure 3.1 shows the photoluminescence spectra before and after the low-speed centrifugation step. The emission band narrowed substantially, indicating a narrowing of the NC size distribution. The shift of the PL peak wavelength from 512 to 506 nm confirmed the preferential removal of larger NCs. This was determined an effective isolation protocol, so it was used throughout this chapter.

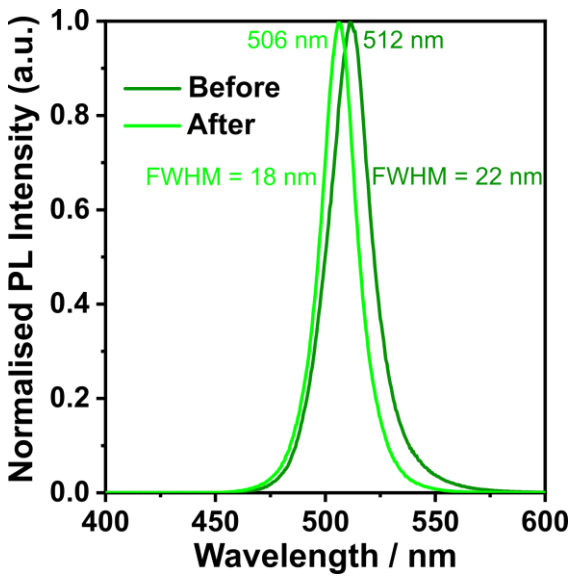

Figure 3.1 **Photoluminescence spectra before and after the final isolation step**

3.3.1.2 Ligand Exchange Optimisation

The isolated $CsPbBr_3$ nanocrystal dispersion served as a starting point to develop the ligand exchange protocol. To begin with, a small quantity of octylphosphonic acid was weighed and added to the NC dispersion. There was an immediate and noticeable change from a transparent yellow-green to an opaque orange solution. This was indicative of NC agglomeration, forming larger NCs with a smaller bandgap and therefore red-shifted absorption. Instead, OPA was first dissolved in toluene. OPA was found to fully dissolve in toluene at concentrations ≤ 16 mM (≈ 10 mg mL^{-1}). OPA solutions were added to the NC dispersion at a 1:1 v/v ratio.

Photoluminescence spectroscopy was used to quantify the change in photoluminescence intensity when OPA solutions of different concentrations were added to $CsPbBr_3$ NC dispersion aliquots. After correcting for small differences in absorption, photoluminescence allows for comparison of

the relative PLQY of NC dispersions, which is correlated to the degree of defect passivation on the surface of the NCs. Figure 3.2a plots the PL intensity as a function of the OPA solution concentration added. There is a significant enhancement with OPA addition; the maximum PL intensity is almost 2 times higher than the original NC dispersion. This was a clear indication that OPA had strongly passivated the surface of the $CsPbBr_3$ nanocrystals.

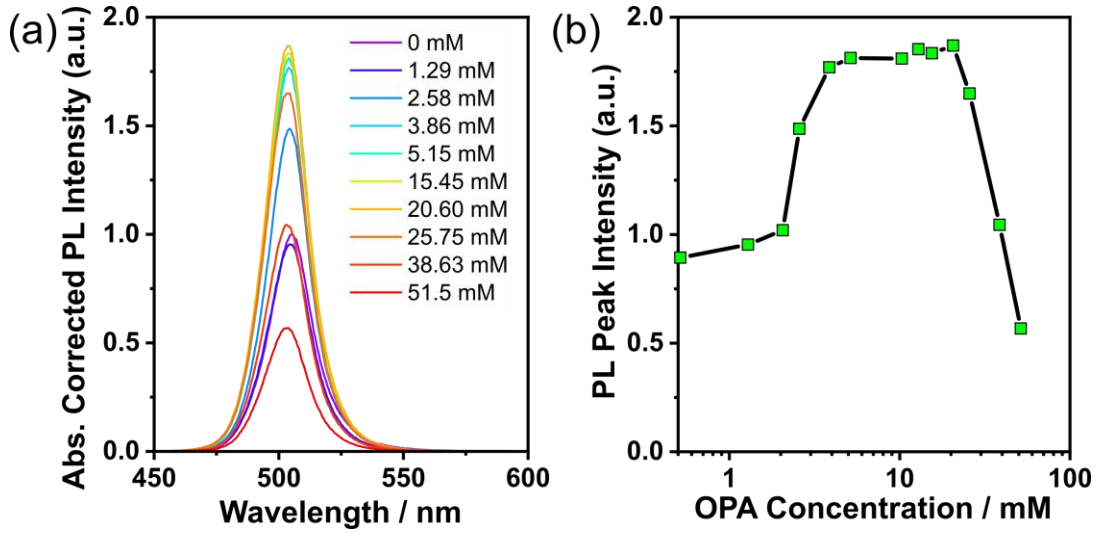

Figure 3.2 **Photoluminescence intensity with different OPA concentrations**

(a) the photoluminescence spectra, and (b) the photoluminescence peak intensity, of $CsPbBr_3$ nanocrystals after the addition of different concentrations of OPA solution.

There were four distinct passivation regimes observed in Figure 3.2b. There was a relatively flat regime at low OPA concentration, up to a threshold concentration, after which there was a steep increase of PL intensity with OPA concentrations up to approximately 4 mM. This was followed by a much more gradual increase up to around 20 mM, then a sharp decrease at higher concentrations. At low OPA concentration, the PL intensity was less than the original dispersion. This may indicate that there was only enough OPA to induce the desorption of the native ligands, not to bind to the vacated sites. The change between the second and third regimes suggested there may have been two different binding mechanisms, modes, or sites, such that the passivation in the third regime was weaker. The degradation of PL intensity above 20 mM could be attributed to a few different factors. It could be that at high concentrations the strength of the lead-phosphonate bond overcomes the crystal cohesive energy, extracting lead from the NC, inducing deep trap states.[113] Alternatively, the replacement of too many long oleyl (C_{18}) ligand chains with octyls (C_8) may destabilise the colloidal dispersion, leading to NC agglomeration; or the presence of excess acid could promote phase transformation to less emissive zero-dimensional Cs_4PbBr_6 nanocrystals.[158]

The ligand binding study discussed in this chapter was conducted concurrently with the light-emitting diode optimisation discussed in the next chapter. An antisolvent purification regime was developed by analysing the effect of different purification processes on LED performance, which will, therefore, be explained thoroughly in the next chapter. Here, the optimised purification process will only be briefly outlined. It was determined that a two-step purification protocol was most effective. The first step used ethyl acetate (EtOAc) as the antisolvent, added at 3:1 v/v ratio with the original toluene dispersion (1w). The second step used acetonitrile (ACN) at 1:1 v/v (2w).

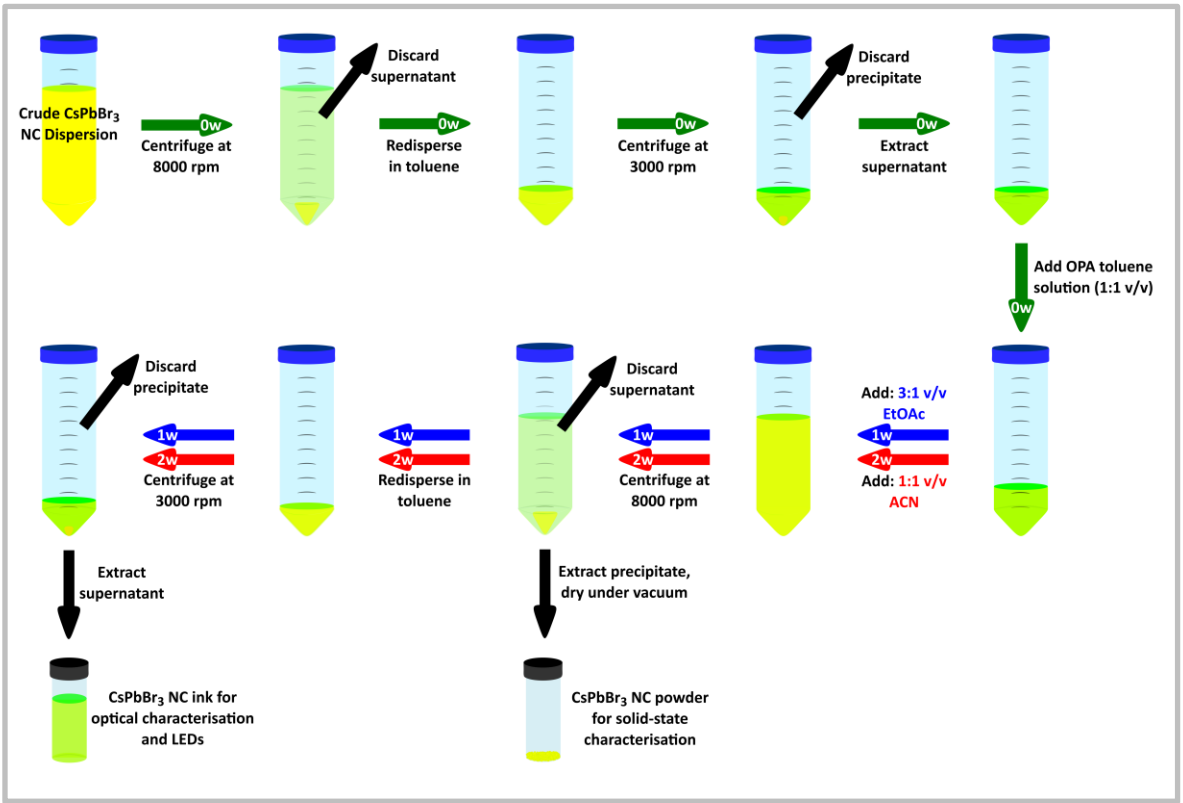

Figure 3.3 **Optimised isolation and purification protocol for $CsPbBr_3$ nanocrystals**

The labels 0w, 1w, and 2w, designate the isolation, first purification, and second purification cycles, respectively.

Figure 3.3 illustrates the isolation, ligand exchange and purification protocol. After addition of the antisolvent, the NC solution underwent the same centrifugation processes as in the isolation phase (0w). The faster centrifugation step precipitated the vast majority of the NCs, with only the smallest fraction remaining in the supernatant. The slow centrifugation step ejected NCs which have aggregated or NCs which have been colloidally destabilised by the antisolvent. The resulting NC solution was therefore stable and had retained a narrow size distribution. It was also determined that a higher OPA concentration was conducive to better retention of photoluminescence through the purification process. Therefore, the ligand exchange procedure employed for the subsequent ligand exchange and binding study utilised an OPA concentration of 15.45 mM. The photoluminescence quantum yield (PLQY) of the final purified $CsPbBr_3$ NC ink was 62 %,

substantially higher than the untreated NCs (43 %). All further characterisation of OPA-treated NCs was conducted on samples purified according to this protocol.

3.3.1.3 Assessing Colloidal Stability

The strong passivation implied by enhanced photoluminescence intensity should theoretically also improve stability. Colloidal stability is crucial for the commercial viability of perovskite nanocrystal ink. To assess the stability of untreated and OPA-treated $CsPbBr_3$ NCs, the photoluminescence spectra of dilute fully-purified NC dispersions were measured periodically over 8 days. The superimposition of the PL spectra obtained for untreated (REF-2w) and OPA-treated (OPA-2w) solutions are shown in Figure 3.4a and b, respectively.

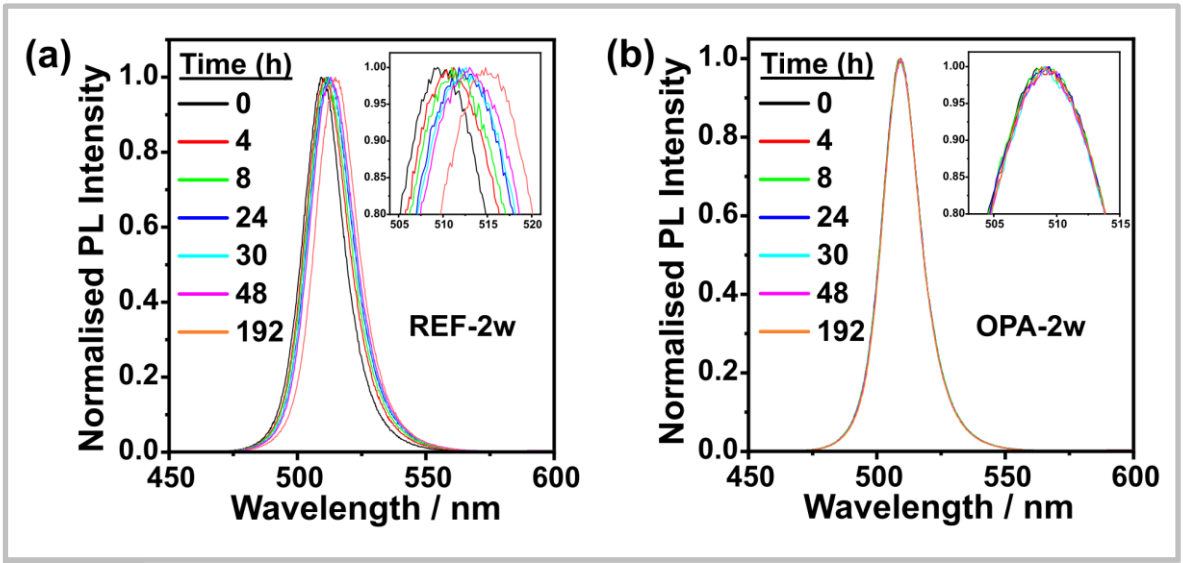

Figure 3.4 **Photoluminescence spectra of untreated (REF-2w) and OPA-treated (OPA-2w) $CsPbBr_3$ nanocrystal solutions measured periodically over 8 days**

The photoluminescence spectrum of the untreated $CsPbBr_3$ NC solution exhibited a redshift of 6 nm after 8 days (192 h), from a peak wavelength of 509 to 515 nm. There was also a slight broadening, which increased the FWHM from 18 nm to 19 nm. The red-shifting of the emission demonstrated that the average NC size was increasing over time. This was attributed to the desorption of weakly-bound OA/OAm ligands, which would destabilise the colloidally dispersed NCs. NC growth would reduce surface energy, thus restabilising the NCs. In contrast, the PL spectra of the OPA-treated NC solution did not change at all over 8 days; the PL peak position and FWHM remained at 509 nm and 17 nm, respectively. This provided strong evidence that OPA was bound robustly to $CsPbBr_3$ NCs, dramatically increasing the colloidal stability. It is worth noting that dilution, as required for solution PL measurement, has been reported to induce desorption of OA and OAm ligands.[113] A recent report by Zhang et al., demonstrated that NCs capped by tetradecyl-

and octadecyl-phosphonic acid ligands fully retained their PL intensity at very low concentration.[142] Thus, the improved PL stability with OPA observed here may be attributable to a lack of dilution-induced ligand desorption.

The optimised ligand exchange and purification protocols produced a $CsPbBr_3$ nanocrystal ink suitable for detailed characterisation of OPA ligand binding.

3.3.2 Nanocrystal Characterisation

3.3.2.1 Size Determination

The fully purified OPA-treated $CsPbBr_3$ nanocrystals were studied with high-resolution transmission electron microscopy (HR-TEM). This technique revealed the shape, size, and dispersity of the NCs. Figure 3.5a demonstrates that the NC were cubic, with a narrow size distribution around an edge length of 10.1 nm. The black spots have been regularly observed in literature; a recent study attributed them to $PbBr_2$, formed by defect-induced decomposition at the NC surface under electron beam irradiation.[159] Given the aforementioned defect tolerance of the perovskite structure, NCs moderate PLQY can still be expected to have a relatively large number of surface defects (i.e. halide vacancies), so the appearance of some black spots on the TEM images was anticipated. Additional TEM images at various magnifications are displayed in Figure A1 (Appendix).

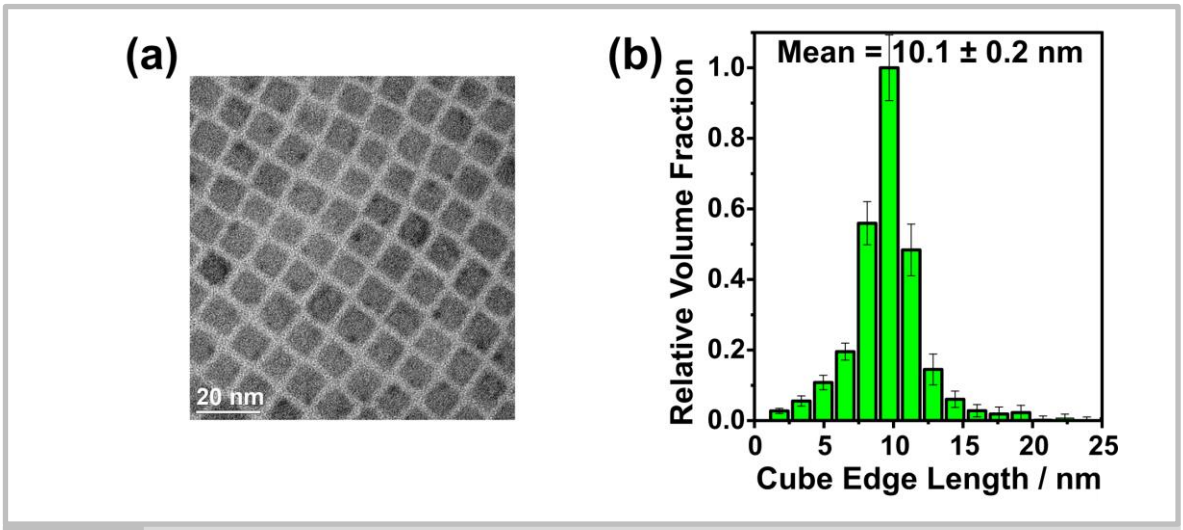

Figure 3.5 **Analysis of the size of OPA-treated $CsPbBr_3$ nanocrystals**

(a) Transmission electron microscope images of $CsPbBr_3$ nanocrystal superlattice, and (b) the nanocrystal edge length distribution extracted from small-angle X-ray scattering data.

The size of the nanocrystals was measured more precisely with small-angle X-ray scattering (SAXS). SAXS analyses a far larger sample size than simply individually measuring NC edge lengths on a TEM image. Using a Monte-Carlo fitting of the SAXS data, an average NC edge length of 10.1 ± 0.2 nm was obtained, which was consistent with the qualitative analysis of the TEM images. The NC size distribution obtained is shown in Figure 3.5b.

3.3.3 Spectroscopic Analysis of Octylphosphonic Acid Binding

The previous sections of this chapter established that an effective OPA ligand exchange strategy had been developed. OPA was found to enhance the photoluminescence intensity and stability, maintaining a narrow size distribution of regularly-shaped cubic nanocrystals. This section will investigate the mechanism of OPA binding to the $CsPbBr_3$ nanocrystal surface, which was responsible for the improvement observed.

The study of ligand binding to the surface of $CsPbBr_3$ NCs was primarily conducted using nuclear magnetic resonance spectroscopy (NMR). NMR is valuable for the study of ligand-surface interactions as it analyses the electronic environments around a specific nucleus. When a ligand interacts with the nanocrystal surface, the electronic environment of its binding group should be altered significantly. Previous work in the literature provided insight around what changes in the electronic environment may indicate for a particular species.

3.3.3.1 Solution Nuclear Magnetic Resonance Spectroscopy

Solution phase NMR has often been employed to study nanocrystal surfaces. However, it can be challenging to identify the resonances corresponding to bound ligand molecules in solution NMR spectra. The chemical shift observed for a molecule depends on its orientation with respect to the direction of the magnetic field, but when the molecules can rotate freely, the variation averages out into a single sharp peak. However, ligand binding to the nanocrystal surface inhibits rotation, so broad peaks with lower intensity are typically observed instead.

The solution ^1H NMR spectra were presented in Figure A2 for untreated reference (REF) and OPA-treated (OPA) $CsPbBr_3$ NC solutions, after the first (1w) and second (2w) antisolvent washing steps. The ligand resonances of interest were of very low intensity compared to the solvent impurity peaks. Nevertheless, tentative assignments of oleyl and octyl proton resonances were made. Oleyl proton resonances were observed in all samples, whereas small octyl proton resonances were only observed in the OPA-treated samples. This unsurprisingly indicated that OPA was present in the OPA-treated samples, but it was not certain from the breadth whether it was bound to the nanocrystal surface or free in solution.

3.3.3.2 Solid-State Magnetic Resonance Spectroscopy

To circumvent the difficulties distinguishing between bound and unbound ligand resonances, and the presence of solvent impurity peaks, solid-state NMR can be performed instead. For the rest of this chapter, solid-state NMR (ssNMR) was preferred because most of the ligand resonances observed should be those bound to the surface. It also provided a more accurate presentation of

ligand binding in the thin-films employed in optoelectronic devices. Thus, findings made could be more reliably correlated to the performance of light-emitting diodes.

Nanocrystal powder samples for ssNMR analysis were collected by drying the NC precipitate, obtained after the first centrifugation step. Figure 3.6 demonstrates that the NC powders remained strongly luminescent, indicating that there was no significant NC aggregation upon drying. Samples were obtained for untreated reference (REF) and OPA-treated (OPA) NCs, after the first (1w) and second (2w) antisolvent washing steps. This provided 4 samples: REF-1w, OPA-1w, REF-2w and OPA-2w. A $CsPbBr_3$ NC powder was also prepared with OPA/TOPO ligands according to the method of Tan et al.,[145] collected without purification (OPA/TOPO). For reference, this was also analysed by ssNMR, as were crystalline OPA and TOPO.

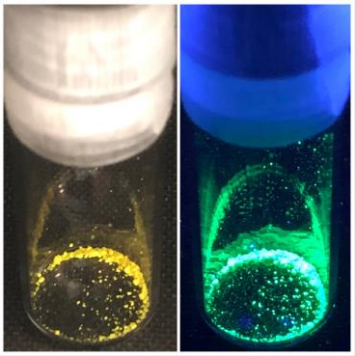

Figure 3.6 **Photographs of $CsPbBr_3$ nanocrystal powder under visible light (left) and ultraviolet light (right)**

The ^{13}C NMR spectra for all samples are displayed in Figure A3. As all the ligands used contain alkyl chains, there are multiple carbon environments, most of which have similar chemical shifts. Therefore, it was unfeasible to assign many of the peaks to a specific carbon environment on a particular ligand. However, there was a difference between the pattern of peaks between 0 and 50 ppm for the untreated and OPA-treated samples. Additional peaks were observed in the OPA samples in the same region as the peaks in the spectrum of crystalline OPA. This indicated that OPA treatment changed the composition of ligands on the NC surface.

Two peaks that could be confidently assigned were the carboxylic acid signal (around 180 ppm) and the carbon adjacent to the amine group of oleylamine (around 40 ppm). As oxygen and nitrogen are more electronegative than carbon, they draw electron density away, thus deshielding the carbon nucleus, causing a downfield shift (i.e. to higher ppm). This effect was more substantial for the carboxylic acid because oxygen is far more electronegative. These peaks had lower intensity because there was only one carbon atom in the same environment per ligand molecule. In the long

alkyl chains, most of the carbon nuclei were in virtually identical electronic environments, which resulted in one higher intensity peak. The peak corresponding to the carboxylic acid was only present in the untreated samples, but the peak indicative of the amine ligand was observed in all samples. This suggested that OPA replaced a substantial quantity of oleic acid, but that oleylamine remained on the NC surface. Bound oleylammonium species have previously been shown to bind more strong to the surface of $CsPbBr_3$ NCs than oleates, due the three hydrogen bonds formed between $–NH_3$ groups and surface bromide sites.[160]

^{31}P was the most useful nucleus for NMR analysis of phosphonic acid binding. The ^{31}P nucleus is highly sensitive, 100 % abundant and its nuclear spin of one-half gives narrow linewidths. Also, there was only one ^{31}P nucleus per molecule so the spectrum should be more easily interpreted. The ^{31}P proton-decoupled NMR spectra for each of the OPA-modified NC powders, and the OPA/TOPO sample, are shown in Figure 3.7.

The ^{31}P spectrum for OPA-1w has 4 resonances paired in 2 distinct environments around 32 and 25 ppm. All 4 resonances were shifted substantially upfield from the crystalline OPA resonance at 37.5 ppm. Previous studies of phosphonic acid ligand binding to metal oxide surfaces have observed similar upfield shifts.[161,162] Typically, neutral phosphonic acid species presented smaller shifts, while deprotonated phosphonates exhibited larger shifts, depending on the degree of deprotonation. Larger shifts upon ligand binding have been considered an indication of stronger ligand-metal interactions.[163] Although other studies analysed various alkylphosphonic acids and many different surfaces, the chemical shifts reported can reliably inform assignments of ^{31}P NMR spectra here. Based on the correlation between ligand deprotonation and shift magnitude, the resonances around 32 ppm were assigned as bound neutral phosphonic acid species (OPA), and the resonances around 25 ppm were attributed to bound monoionic hydrogen phosphonate groups (OPA^-). It has been previously reported that binding to divalent metal sites, such as the Pb^{2+} here, occurs preferentially through the charged hydrogen phosphonate, rather than the Lewis base-type interaction of the neutral acid.[164,165] De Keukeleere et al. suggested that coordinating to Lewis acid metal sites provides greater stabilisation of phosphonate species than protonation.[166]

The small splitting between the two resonances of OPA and OPA^- were attributed to the two different possible binding modes for each group. A neutral phosphonic acid group can be expected to coordinate to the NC surface through either the lone pair on the oxygen of the P=O or the P-O-H moieties. The 5 ppm upfield shift observed is comparable to the shift reported for methylphosphonic acid binding to silica nanoparticles through P=O.[161] The subsequent deprotonation of each neutral bound ligand led to three possible hydrogen phosphonate binding modes, depicted in Figure 3.8. However, the deprotonation of neutral OPA bound through P-O-H

can be expected to occur preferentially at the bound P-O-H over the free P-O-H. This is because the coordination of the lone pair on the oxygen to the NC weakens the O-H bond. This explains why only two, rather than three, different OPA^- modes were observed. All NMR resonance assignments are tabulated in Figure 3.7, and the proposed binding modes are illustrated in Figure 3.8.

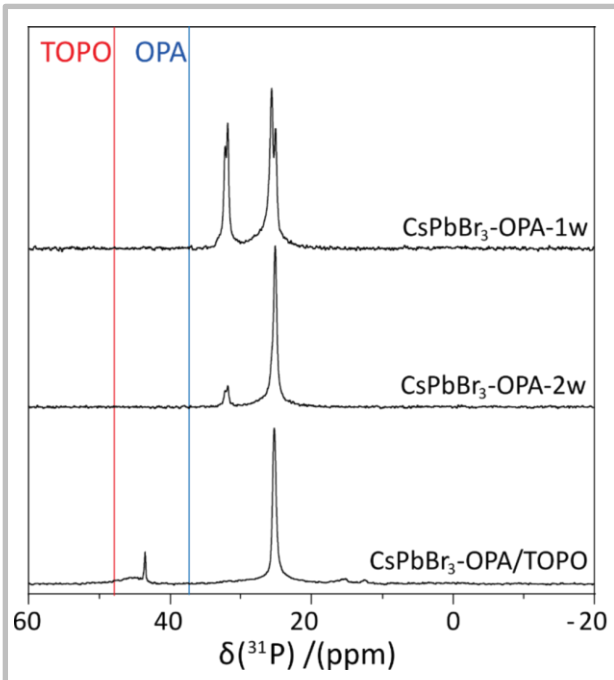

Ligand	$\delta_{iso}(^{31}P)$ (ppm)	Δδ (ppm)
OPA, free	37.5 ± 0.1	0
OPA, bound	32.2 ± 0.1	-5.3
	31.8 ± 0.1	-5.7
OPA^-, bound	25.6 ± 0.1	-11.9
	25.1 ± 0.1	-12.4
OPA^{2-}, bound	15.4 ± 0.3	-22.1
	12.5 ± 0.2	-25.0
TOPO, free	47.9 ± 0.1	0
TOPO, bound	43.5 ± 0.1	-4.4

Figure 3.7 **1D ^{31}P proton-decoupled NMR spectra of OPA-modified $CsPbBr_3$ nanocrystals**

The chemical shifts corresponding to crystalline OPA and TOPO are marked. The chemical shifts and the corresponding assigned ligand binding group are tabulated alongside.

Multiple ^{31}P resonances for a single phosphonic acid ligand have been observed before. Octadecylphosphonic acid was found to exhibit different chemical shifts, dependant on which crystal facets of wurtzite CdSe nanocrystals that it was bound to.[164] However, cubic $CsPbBr_3$ NCs usually present only CsBr-terminated facets, such that complete $PbBr_6^{4-}$ octahedra are maintained, so similar reasoning was unlikely to be valid here.

The ^{31}P spectrum for OPA-2w demonstrated the effect of the second antisolvent purification cycle, using acetonitrile (ACN). Three of the four resonances were diminished almost entirely, leaving a single significant sharp resonance at 25.1 ppm. This indicated that one binding mode was more resistant to the treatment of polar solvent. Although OPA-1w was also subjected to a purification cycle, ethyl acetate is significantly less polar than ACN. Referring again to Figure 3.8, only one of the proposed modes involved binding through a charged site; the other three were Lewis base-type, lone-pair donors. Thus, it was a logical hypothesis that binding through a charged site was more

robust, and consequently more resistant to removal by polar solvents. This was supported by the highly ionic nature of the bonding in perovskite lattice. Furthermore, the slightly larger shift between crystalline OPA and this resonance indicated that there was more electron density around the ^{31}P nucleus in that binding mode. This could be attributed to the more electrostatic nature of binding between charged sites, in contrast to Lewis base-type interactions where the electron pair is donated into an empty Pb^{2+} orbital, drawing electron density further from the ^{31}P nucleus.

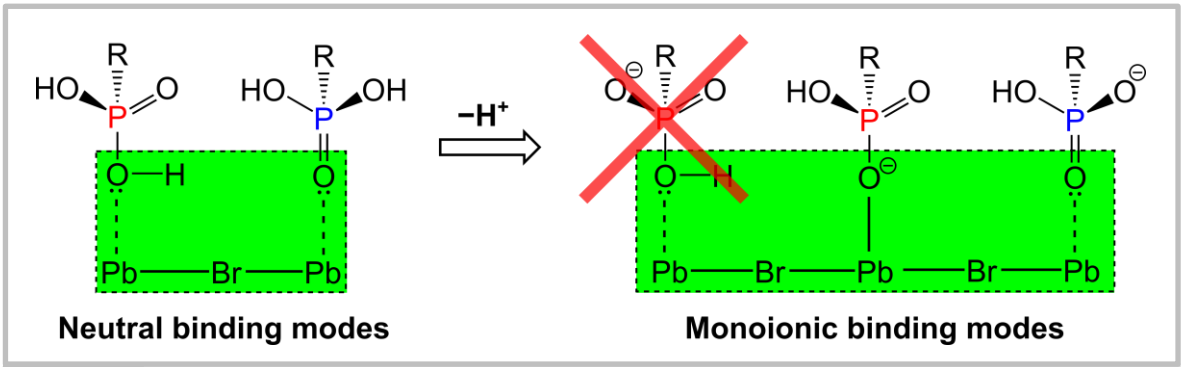

Figure 3.8 **The proposed binding modes of octylphosphonic acid and octylphosphonate to $CsPbBr_3$ nanocrystals**

Interestingly, the ^{31}P spectrum for OPA-TOPO was very similar to OPA-2w, with an intense resonance at 25.0 ppm. This suggested that the ligand exchange and purification protocol obtained comparable ligand binding to the OPA/TOPO synthesis. Ligand exchange can therefore be considered a valid approach to elucidate the ligand binding obtained from hot-injection synthesis. The insight gathered here demonstrated that monitoring ligand attachment at room temperature can unveil binding mechanisms that are concealed by the fast kinetics of high-temperature syntheses. The other minor peaks in the OPA/TOPO spectrum can be attributed to some bound TOPO (43.5 ppm) and small quantities of fully deprotonated phosphonate species (< 20 ppm).

Two-dimensional NMR spectroscopy provides insight into the proximity of different nuclei. In this case, assessing the proximity of ^{31}P and ^{1}H nuclei was useful to confirm the degree of deprotonation. The most suitable 2D NMR technique for this purpose was heteronuclear correlation (HETCOR), which exhibits correlation peaks between nuclei that are within approximately 5 Å of one another.

The ^{31}P–^{1}H HETCOR spectra for crystalline OPA, OPA-1w, OPA-2w and OPA/TOPO-0w samples are shown in Figure 3.9. Starting with the crystalline OPA sample in Figure 3.9a, there are two clear correlation peaks. These were assigned to the CH_2 protons on the carbon adjacent to the P atom (P—CH_2), and the P–OH protons, which are orientated in the crystal structure such that they participate in hydrogen bonding with adjacent OPA molecules (P—OH^h).[167] Both of these correlation peaks were also observed for OPA-1w (Figure 3.9b) and OPA-2w (Figure 3.9c), for all ^{31}P resonances. The ^{1}H chemical shifts of hydrogen-bonded P–OH protons are well known; ^{1}H chemical shifts of 9.9

–16.0 ppm have been observed previously, where the shift magnitude was correlated to the hydrogen bonding distance.[167]

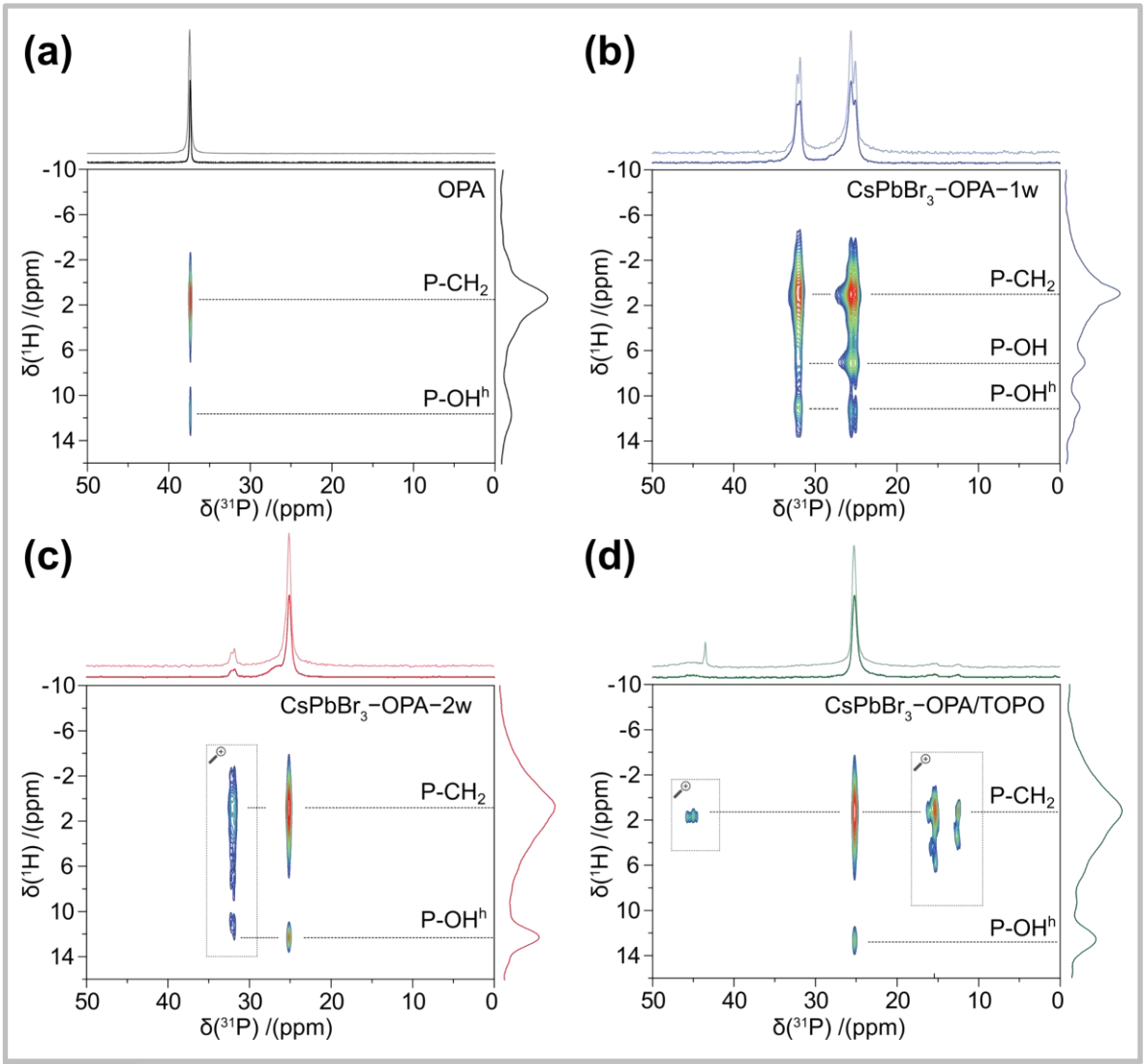

Figure 3.9 **^{31}P–^{1}H heteronuclear correlation NMR spectra for (a) crystalline OPA, (b) OPA-1w, (c) OPA-2w and (d) OPA/TOPO-0w $CsPbBr_3$ nanocrystal samples**

The corresponding 1D ^{31}P spectra are shown above the 1D projection from the HETCOR spectra for comparison. Regions enclosed by dashed boxes have been magnified for clarity.

The presence of P–OH^{h} resonances for all binding modes indicated that bound OPA molecules were hydrogen bonding to other nearby electronegative sites. It was hypothesised that this hydrogen bonding occurred between the P–OH and P=O sites on adjacent bound OPA ligands. This was strongly supported by the narrow resonances obtained, which were indicative of long-range order. ^{31}P resonances in solid-state NMR are typically much broader for bound phosphonic acids due to a wide distribution of distinct binding geometries and orientations. The formation of hydrogen bonds

between adjacent OPA ligands would require alignment into a consistent orientation, with every ligand in a hydrogen-bonded chain exhibiting similar binding geometry, leading to a much narrower distribution of ^{31}P environments. It was important to note that because the perovskite lattice is highly ionic, the binding energy to its surface was unlikely to be strongly dependent on the orbital overlap, and by extension, ligand orientation. Thus, maximisation of ligand-metal orbital overlap was not expected to drive the extensive ligand alignment observed in the HETCOR NMR spectra (Figure 3.9) – particularly when such alignment has not been observed for more covalent nanocrystals. Therefore, there was strong evidence for inter-ligand hydrogen bonding here. Such a phenomenon had not previously been observed on nanocrystal surfaces. This could be attributed to the large distance between binding sites on the $CsPbBr_3$ nanocrystal surface.[168] The binding sites on other nanomaterials, such as metal oxides and chalcogenides, are usually closer together, such that the bridging of multiple sites by one phosphonic acid molecule is more favourable.[169]

The OPA–1w sample displayed an additional ^{1}H resonance at 7 ppm (Figure 3.9b), which showed correlation peaks with all OPA binding modes. This peak was attributed to P–OH protons which were not hydrogen bonding, referred to as free P–OH. Thus, in OPA–1w, hydrogen bonding must only have occurred in pairs or small groups, terminated by free P–OH groups. The restriction of hydrogen bonding can be understood with reference to Figure 3.8; neutral OPA bound by P=O has two free P–OH groups, thus this mode would terminate any hydrogen-bonded chain. In contrast, no significant free P–OH resonance was observed in the HETCOR spectrum for OPA–2w (Figure 3.9c). This indicated that after ACN purification, the hydrogen bonding network between OPA ligands became far more extensive, such that only a small fraction of free P–OH remained. An implication of this was that ligands coordinated to the surface by weaker binding modes were reconfigured rather than removed.

Given the novelty of the hypothesis, it was important to assess alternative potential explanations to hydrogen bonding between OPA ligands. The resonance assigned to free P–OH could instead have been assigned to $–NH_3^+$ protons on adjacent bound oleylammonium ligands. In this scenario, the disappearance of the resonance upon ACN purification could have been attributed to the desorption of oleylammonium. However, the ^{13}C NMR spectrum in Figure A3 ruled out this theory because the resonance corresponding to the carbon adjacent to $–NH_3^+$ was observed in both OPA-1w and OPA-2w. Another theoretically feasible explanation could have been that P–OH groups were hydrogen bonding to adjacent Br^- ions. Firstly, the distance between P–OH and Br^- was probably too large for hydrogen bonding to occur. But more convincingly, the chemical shifts of $P–OH^h$ in OPA-1w and OPA-2w were very similar to that of crystalline OPA. Overall, inter-ligand hydrogen bonding between octylphosphonates was the only hypothesis that was consistent with all the NMR data.

The presence of extensive inter-ligand hydrogen bonding also served to rule out higher denticity binding modes. Any bi- or tridentate-bound OPA species would not have both free P–OH and P=O, therefore it would terminate any hydrogen bonding chain. Thus, given that HETCOR NMR analysis showed the vast majority of P–OH moieties are engaged in hydrogen bonding, there cannot be a significant amount of multidentate binding present.

The OPA/TOPO sample in Figure 3.9d presented a very similar HETCOR spectrum to that of OPA–2w. The P–OH protons observed were predominantly hydrogen bonding, which confirmed the ligand exchange and purification protocol successfully replicated the OPA binding achieved by the hot-injection approach. The similarity also served as further evidence that OPA did not hydrogen bond to oleylammonium on the NC surface. Also, the minor ^{31}P resonances below 20 ppm in Figure 3.9d did not exhibit any correlation peaks with P–OH protons, which provided more evidence that they corresponded to fully deprotonated phosphonate moieties.

3.3.3.3 Fourier Transform Infrared Spectroscopy

To corroborate the hypotheses constructed based on NMR spectroscopy, attenuated total reflection (ATR) Fourier transform infrared (FTIR) spectroscopy was conducted on all four samples (REF-1w, REF-2w, OPA-1w and OPA-2w). FTIR spectra present bands corresponding to internal vibrations of the ligand molecules, such as bond stretching and bending. Two key sections, the C–O stretching (1750 – 1350 cm^{-1}) and P–O stretching (1750 – 1350 cm^{-1}) regions of the FTIR spectra of all samples were shown in Figure 3.10.

The most obvious contrast between the untreated and OPA-treated samples in the C–O stretching region was the disappearance of two bands at 1524 and 1402 cm^{-1}. These bands were both attributed to asymmetric and symmetric lead carboxylate stretches (C–O–Pb), respectively.[170] Thus, their disappearance indicated that oleate ligands were removed from the NC surface by OPA treatment. The diminished C=O stretching peak above 1700 cm^{-1} provided further evidence of this. The bands at 1575 cm^{-1} and 1465 cm^{-1} were attributed to NH_2 bending vibrations. The retention of these bands with OPA treatment confirmed that oleylamine ligands remained on the NC surface, as indicated by NMR.

Analysis of the P–O stretching region was more difficult due to the convolution of bands. In molecules that contain both P–OH and P–O_2^- vibrations, the bands are known to become very complex.[171] Furthermore, in molecules that contain P–OH and P=O groups, the P=O band is typically broadened and weakened by hydrogen bonding. It has been suggested that this broadening can make it impossible to assign.[172] Interactions between the functional groups and the surface of

$CsPbBr_3$ nanocrystals should only complicate matters further. However, it can be stated that there was a clear difference between the pattern of peaks in the P–O stretching regions of OPA–1w and OPA–2w. OPA–1w exhibited a greater distribution of intense peaks in both the typical P–(O–Metal) and P–(O–H) regions at 1080 – 980 cm^{-1} and 950 – 880 cm^{-1}, respectively. This suggested that OPA–1w contained significant proportions of different binding modes. The reduction of most of these peaks in OPA–2w, and the increase of one peak at 1105 cm^{-1}, was consistent with the reconfiguration of bound OPA into a single dominant mode upon ACN purification. It is important to emphasise that any conclusions drawn from the P–O region of the spectra alone were speculative. Nonetheless, it strengthens the binding mechanism hypothesis that no contrary evidence was unearthed by FTIR.

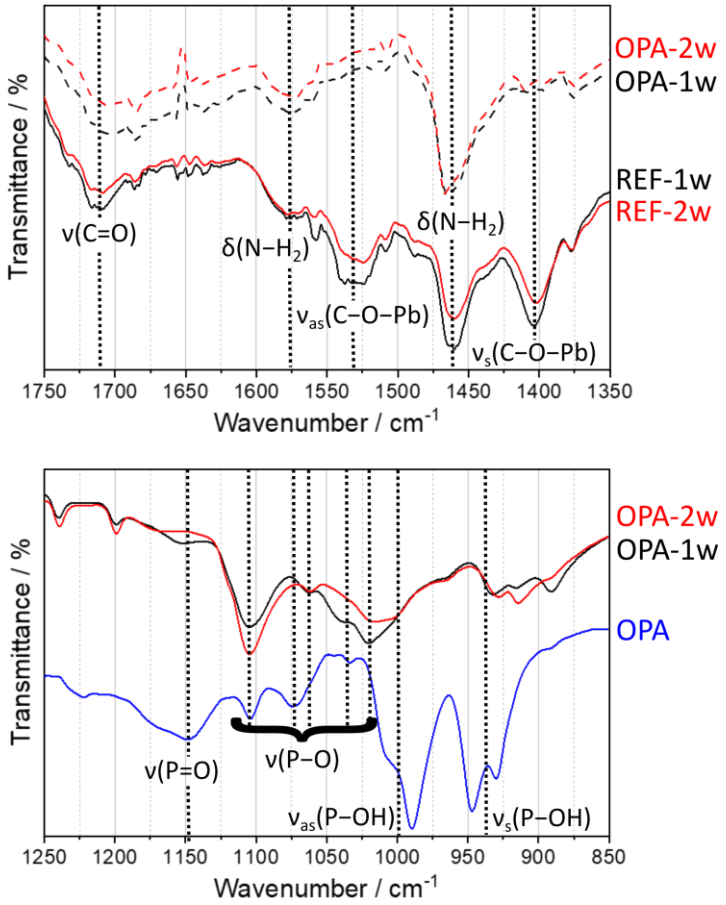

Figure 3.10 **Fourier transform infrared spectra of $CsPbBr_3$ nanocrystals**

The upper spectrum shows the typical C–O stretching regions. The lower spectrum shows the typical P–O stretching region.

3.3.3.4 Thermogravimetric Analysis

The final analytical method employed was thermogravimetric analysis (TGA). It is a very straightforward technique, which measures the mass of a sample with changing temperature. For nanocrystal samples, TGA is typically used to quantify the mass of bound organic ligand. The organic

material will decompose at a lower temperature than the inorganic nanocrystal. TGA was conducted on all 4 samples; the percentage mass loss of the samples between 100 and 550 °C was plotted in Figure 3.11. Coloured shading was added to highlight distinct regions of decomposition for different ligands.

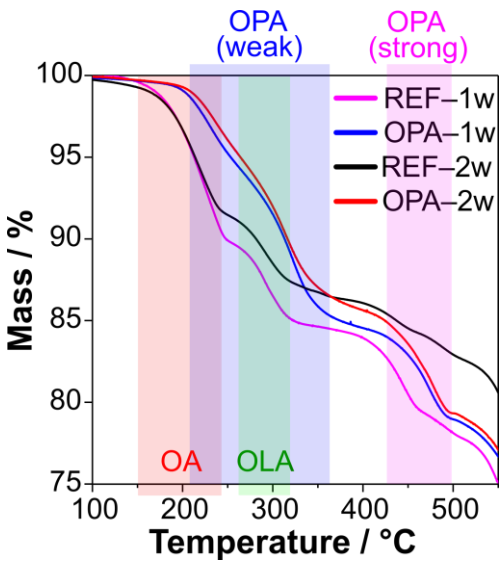

Figure 3.11 **Thermogravimetric analysis of $CsPbBr_3$ nanocrystal samples**

The shaded regions indicate the decomposition of different ligands.

There was a significant mass loss between around 150 and 240 °C for only the untreated samples (red shading). This was attributed to the decomposition of oleate ligands, as NMR indicated that it was the one ligand only present in the untreated samples. REF–2w exhibits notably less mass loss in this region than REF–1w, supporting the hypothesis that ACN purification removes a significant fraction of oleate. There was a second broad mass loss region identified between around 210 and 360 °C (blue shading), which was only substantial for the OPA-treated samples. This could be attributed to the three weaker OPA binding modes. Within this range, there appeared to be a narrower separate mass loss region between around 260 and 310 °C (green shading), where the gradient of mass loss became steeper for all samples. This most likely corresponded to oleylammonium, as earlier analysis suggested it should be present in all samples.

There was no significant mass loss from 310 °C to around 450 °C, above which $CsPbBr_3$ should begin to decompose. Previous work indicates that octylphosphonate ligands also decompose around this temperature.[145] Therefore, the steeper mass loss for the OPA–2w sample between 430 and 500 °C (magenta shading) could be attributed to the decomposition of OPA in the strongest binding mode, which NMR demonstrated was only the dominant mode in OPA–2w. The decomposition of strongly-

bound OPA ligands at higher temperature demonstrates that octylphosphonate ligands improved the thermal stability of $CsPbBr_3$ nanocrystals.

It should be noted that the molar masses of oleic acid, oleylamine and octylphosphonic acid are 282.47, 267.49 and 193.21 g mol^{-1}, respectively. Thus, the decomposition of one oleyl ligand molecule corresponds to a greater mass loss. This fact, alongside the convolution of mass loss troughs for different ligands, and the decomposition of the NC itself above 450 °C, highlight that the TGA results must be considered only qualitatively. Overall, the most reliable conclusion that could be drawn from the TGA was that ACN purification significantly reduced the quantity of ligand in the untreated samples but had a negligible effect on the OPA-modified samples. This was important because it indicated that bound octylphosphonate ligands exhibit greater resistance to polar solvents than oleate ligands.

3.3.4 Finalised Mechanisms

3.3.4.1 Ligand Exchange Mechanism

The spectroscopic analysis provided convincing evidence that octylphosphonic acid bound to the surface of $CsPbBr_3$ nanocrystals. It was also found that a significant fraction of oleate was removed from the surface, but oleylammonium remained. Nenon et al. have shown that oleate does not interact strongly with lead sites on $CsPbBr_3$ because there is a hard-soft mismatch; essentially, the charge density on the oleate group is too high relative to the diffuse charge on Pb^{2+}.[113] In contrast, the softer phosphonate group was found to interact sufficiently with under-coordinated Pb^{2+} sites to fill halide vacancies on the NC surface. These findings are supported by Smock et al. They observed that phosphonic acid ligands bind irreversibly to $CsPbBr_3$ NCs rather than participating in a binding equilibrium.[114]

Based on the above logic, and the evidence outlined in the previous sections, a mechanism was proposed for the ligand exchange. When OPA was introduced to the OA/OAm-$CsPbBr_3$ NC dispersion, it was deprotonated by free oleylamine. As the resulting octylphosphonate species would be effectively removed from the system on account of their irreversible binding to the NC surface, this consumption of oleylamine would shift the established binding equilibria towards the unbound species, according to Le Chatelier's principle. The shift of the equilibria would drive the desorption and deprotonation of oleylammonium, increasing the concentration of free oleylamine. The additional oleylamine could then deprotonate more OPA, thus establishing a synergistic ligand exchange cycle. This mechanism is consistent with the observation that the concentration of oleylammonium on the NC surface was maintained, while the concentration of oleate was reduced. The chemical equations describing the proposed mechanism are as follows:

Equation 3.5

$$\boldsymbol{R'PO(OH)_2 + RNH_2 \longrightarrow R'PO(OH)O^- + RNH_3^+}$$

Equation 3.6

$$\boldsymbol{RCOOH + RNH_2 \rightleftharpoons RCOO^- + RNH_3^+}$$

Equation 3.7

$$\boldsymbol{HBr + RNH_2 \rightleftharpoons Br^- + RNH_3^+}$$

Where R and R’ are oleyl and octyl groups, respectively. Equation 3.7 makes clear that Br^- desorbed from the surface, together with oleate. This was presumably crucial to the extensive hydrogen-

bonded phosphonate network because bromide ions on the nanocrystal surface would interrupt inter-ligand chains.

This ligand exchange mechanism should not be exclusive to phosphonic acids. Any acid that can be deprotonated by oleylamine and is soft enough to bind irreversibly with Pb^{2+} sites should adhere to a similar mechanism. Potential alternatives include sulfonic acids, phosphinic acids, or even carboxylic acids with electron-withdrawing substituents which can reduce the charge density on the acid group.

3.3.4.2 Ligand Binding Mechanism

The binding mechanism was thoroughly explained alongside the NMR data in the previous section. To summarise, initially OPA molecules bound in four different modes, two through a neutral phosphonic acid group, and the other two through a monoionic hydrogen phosphonate group. Upon treatment with the highly polar ACN solvent, ligand rearrangement occurred, such that the majority of remaining OPA molecules were bound through the $P–O^-$ of a hydrogen phosphonate group. The vast majority of these bound phosphonate ligands were engaged in inter-ligand hydrogen bonds, formed between the P=O and P–OH groups of adjacent ligands. The complete mechanism was illustrated in Figure 3.12.

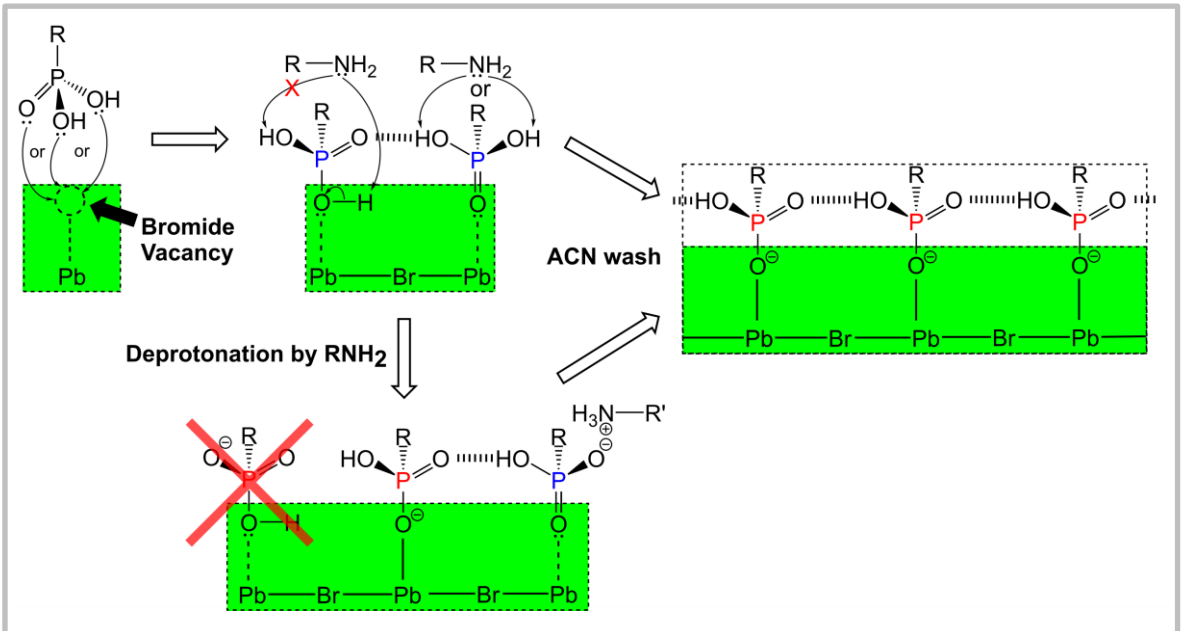

Figure 3.12 **Full proposed binding mechanism of octylphosphonic acid on $CsPbBr_3$ nanocrystals**[140]

The inter-ligand hydrogen bonding unveiled here represented a particularly appealing property of phosphonic acids. It provided an additional stabilisation mechanism, separate from the strength of the interaction between the binding group and the nanocrystal surface. Similar surface chemistry could be envisaged for sulfonic acid groups binding to a surface as a Lewis base through its sulfonyl

group. However, a Lewis Base-type interaction is unlikely to bind as strongly, and sulfonic acids would instead be expected to bind to the ionic perovskite surface through the S–O^- of a sulfonate group. In this configuration, extended inter-ligand hydrogen bonding chains would not be viable.

3.4 Summary

In this chapter, a ligand exchange protocol was developed to deposit octylphosphonic acid ligands on the surface of $CsPbBr_3$ nanocrystals. OPA was found to replace oleate ligands, while oleylammonium ligands remained. With an optimised OPA concentration of around 20 mM, the photoluminescence of the nanocrystals was approximately doubled after ligand exchange, leading to a PLQY of 62 % for the fully purified nanocrystal ink.

Solid-state nuclear magnetic resonance spectroscopy unveiled that OPA initially bound through four different binding modes. After the final purification cycle with acetonitrile, the four binding modes configured into a single dominant binding mode – the monodentate coordination of a singly deprotonate octylphosphonate moiety to under-coordinated Pb^{2+}. Intriguingly, $^{31}P–^{1}H$ heteronuclear correlation NMR indicated that the OPA ligands were arranged in an extensive inter-ligand hydrogen bonding network on the nanocrystal surface. This hydrogen bonding arrangement may explain the enhanced solvent resistance exhibited by OPA-capped $CsPbBr_3$. The detailed understanding of the strong binding mechanism will help guide the future design of more commercially viable nanocrystals.

Overall, the successful ligand exchange of strong binding OPA ligands onto the nanocrystal surface, and the corresponding enhanced PLQY, were promising indicators that more robust passivation was achieved. The replacement of long oleyl ligands for shorter octyl ligands offers potential for more conductive nanocrystal thin films, but this must be investigated further through the fabrication of prototype light-emitting diodes.

Chapter 4 Octylphosphonate-Capped $CsPbBr_3$ Nanocrystals for Light-Emitting Diodes

4.1 Introduction

Chapter 3 outlined a ligand exchange strategy that replaced oleate ligands on the surface of $CsPbBr_3$ nanocrystals with octylphosphonate. The stronger binding of OPA enhanced the photoluminescence intensity almost two-fold. It was hypothesised that the more robust binding would enable complete purification, such that there was less unbound ligand material in thin films deposited from the nanocrystal ink. Both this and the substitution of long oleyl ligands for octyls were expected to improve the conductivity of NC thin films.

In this chapter, a purification protocol was devised for OPA-capped $CsPbBr_3$ NCs prepared by ligand exchange. The efficacy of purification was assessed through the optoelectronic characteristics of prototype light-emitting diodes. The aim was to optimise a purification process to remove as much unbound ligand as possible without substantially degrading PLQY. Comparison of LED characteristics resulting from films of OA/OAm-capped and OPA-treated $CsPbBr_3$ nanocrystals was then used to elucidate the influence of OPA ligands.

4.2 Materials and Methods

In this section, the experimental procedures utilised in this chapter will be outlined.

4.2.1 Chemicals

Lead bromide ($PbBr_2$, ≥ 99.999 % trace metals basis), cesium carbonate (Cs_2CO_3, 99.9 % trace metals basis), 1-octadecene (ODE, 90%), oleic acid (OA, 90%), oleylamine (OAm, 70%), octylphosphonic acid (OPA, 98%), toluene (anhydrous, 99.8%), ethyl acetate (anhydrous, 99.8%), and acetonitrile (anhydrous, 99.8%), methyl acetate (anhydrous, 99.9%), acetone (≥ 99.5 %) and 1-butanol (anhydrous, 99.8%) were purchased from Sigma- Aldrich. All chemicals were used without further purification. OA and OAm were dried separately under vacuum at 120 °C for a minimum of 2 hours before use.

4.2.2 Cesium Lead Bromide Nanocrystal Synthesis

4.2.2.1 Cesium Oleate Preparation

Cs_2CO_3 (0.41 mmol, 0.268 g) and ODE (10 mL) were dried under vacuum at 120 °C for 30 min. Dried OA (3.16 mmol, 1 mL) was added to this under nitrogen, and the solution was dried under vacuum at 120 °C for 90 min. The solution was then heated at 140 °C under nitrogen for 30 min to ensure complete formation of Cs(oleate). The Cs(oleate) solution was kept at 120 °C under vacuum until required.

4.2.2.2 Standard Synthesis Method

$CsPbBr_3$ nanocrystals were synthesised according to a published hot-injection method.[14] $PbBr_2$ (0.38 mmol, 0.138 g) and ODE (10 mL) were dried under vacuum at 120 °C for 15 min. Dried OA (3.16 mmol, 1 mL) and dried OAm (3.02 mmol, 1 mL) were added under nitrogen, and the solution was dried under vacuum at 120 °C for 60 min. The $PbBr_2$ solution was heated to 170 °C under nitrogen. 0.8 mL Cs(oleate) was swiftly injected into the $PbBr_2$ solution with vigorous stirring, and the reaction was quenched after 5 s in an ice water bath, with vigorous swirling to promote homogenous cooling.

4.2.2.3 Nanocrystal Purification

4.2.2.3.1 Nanocrystal Isolation

For nanocrystals synthesised by the standard method, 12.5 mL crude NC dispersion was centrifuged for 10 min at 8000 rpm. The precipitate was redispersed in 2.5 mL toluene and centrifuged for 10 min at 3000 rpm. The precipitate was discarded, and the supernatant was retained for antisolvent washing.

4.2.2.3.2 OPA Ligand Exchange

For OPA-treated samples, a solution of OPA in toluene (0 – 50 mM) was added at 1:1 v/v to the NC dispersion. For untreated reference samples, toluene was added instead of the OPA solution at the same ratio to maintain the same dilution.

4.2.2.3.3 Antisolvent Purification

The optimised purification protocol developed in this chapter was as follows. Ethyl acetate was added to the $CsPbBr_3$ dispersion at a 3:1 v/v ratio, and the mixture was centrifuged for 10 min at 8000 rpm. The precipitate was redispersed in 50 % the initial volume of toluene and centrifuged for 10 min at 3000 rpm. The precipitate was discarded, and the supernatant was retained. Acetonitrile was added to the toluene dispersion at a 1:1 v/v ratio, and the mixture was centrifuged for 10 min at 8000 rpm. For solution state characterisation, the precipitate was redispersed in 50 % the initial volume of toluene and centrifuged for 10 min at 3000 rpm. The resulting supernatant was considered the fully purified nanocrystal ink.

4.2.3 Characterisation Methodology

4.2.3.1 Optical Absorption Spectroscopy

Absorbance spectra were obtained using a Shimadzu UV-3600 spectrophotometer. The samples were prepared in Quartz cuvettes and diluted by a factor of between 60 and 600 (5 to 50 µL NC ink in 3 mL solvent). Typically, the spectra were recorded over a wavelength range of 600 to 350 nm. The measurement settings were as follows: interval = 0.5 nm, integration time = 0.1 s.

4.2.3.2 Photoluminescence Spectroscopy

Photoluminescence spectra were collected using a Horiba Fluoromax-4 spectrophotometer. The samples were prepared in Quartz cuvettes and diluted by a factor of between 60 and 600 (5 – 50 µL NC ink in 3 mL solvent). A laser excitation wavelength of 365 nm was used. The other

measurement settings were as follows: interval = 0.5 nm, integration time = 0.1 s, excitation slit width = 1 nm, emission slit width = 0.5 nm.

4.2.3.3 Photoluminescence Quantum Yield Measurement

Photoluminescence quantum yield was measured using a 445 nm diode laser (Cobolt) to excite the sample. The samples were prepared in Quartz cuvettes and diluted such that absorption was approximately 20 %. The emission was collected by a Labsphere integrating sphere coupled to an Andor Kymera monochromator in which the emission intensity was registered by a photomultiplier tube. The laser intensity used was 5 mW/cm^2.

4.2.3.4 Time-Resolved Photoluminescence Spectroscopy

Time-resolved photoluminescence was measured using a picosecond-pulse light source at 405 nm, with 5-MHz repetition-rate and a beam spot of 10 µm. A Micro Photon Devices single-photon avalanche photodiode (LDHP-670) detector collected the signal, which was filtered by an Acton monochromator (SpectraPro 2300). A time-correlated single-photon counting card (Pico Harp TSCPC module and Picosecond Event Timer 300) was used to acquire the signals. Biexponential functions were fitted to extract charge-carrier lifetimes from the resulting decay curves. The temporal resolution was 50 ps.

4.2.4 Light-Emitting Diodes

4.2.4.1 Fabrication

The device layout utilised for LED fabrication was presented in Figure 4.1a. The device stack composition was shown in Figure 4.1b. Pre-etched indium-tin oxide (ITO) glass substrates (sheet resistance of 8 $\Omega\ cm^{-1}$) were washed consecutively under sonication in a detergent solution (10 % v/v in deionized water), deionized water, acetone, and twice in isopropanol. The substrates were dried and treated for 15 min by UV-ozone. PEDOT:PSS (Clevios Al4083) was filtered with a 0.45 µm PVDF filter, spin-coated for 1 min at 4000 rpm (acceleration = 200 rpm s^{-1}) and thermally annealed for 10 min at 130 °C. The substrates were transferred into an argon-filled glovebox for the remainder of the fabrication processes. Purified $CsPbBr_3$ nanocrystal solutions were drop-cast onto PEDOT:PSS, and after a 3 minute delay to allow any self-assembly to occur, were spin-coated for 1 min at 2000 rpm (acceleration = 250 rpm s^{-1}). 2,4,6-Tris[3-(diphenylphosphinyl)phenyl]-1,3,5-triazine (POT2T) was thermally evaporated under high vacuum (10^{-6} Torr) to achieve a thickness of

45 nm. Ca (7 nm) and Al (100 nm) were sequentially thermally evaporated through a metal shadow mask. The active area of all devices used was 3 mm^2.

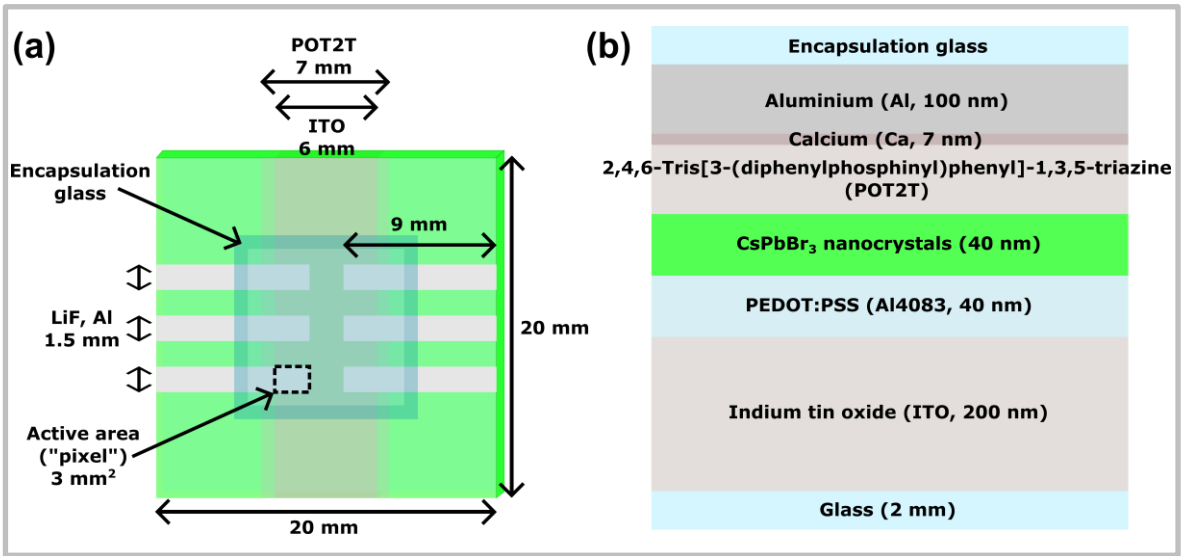

Figure 4.1 **Schematics of the light-emitting diode layout and stack used**

(a) Plan view of electrode pattern and dimensions, and (b) the composition of the device stack.

4.2.4.2 Device Characterisation

LED devices were encapsulated within a glass cavity, sealed with UV-curable epoxy resin, before being withdrawn from the argon-filled glovebox for electroluminescence characterization. A Keithley 2612B was used to obtain the current-voltage characteristics of the LED devices. A scan rate of 1 V s^{-1} (step size 0.1 V, step interval 0.1 s) was used. An integrating sphere (OceanOptics FOIS-1) coupled to a calibrated spectrophotometer (OceanOptics QEPro) was used to capture light emission. An OceanOptics HL-3 Plus vis-NIR light source, was used to calibrate the absolute irradiance measurement of the spectrometer. The edge emission contribution is lost outside the integrating sphere due to the placement of LED devices; therefore, only forward emission is collected. This method was previously used to measure the external quantum efficiency of organic light-emitting diodes.

4.3 Results and Discussion

Two key factors underpinned the hypothesis that OPA ligands would enhance the efficiency of $CsPbBr_3$ NC LEDs. Firstly, a stronger interaction with the NC surface should improve the internal quantum efficiency (IQE) by passivating halide vacancies, which should make the NCs more resistant to the antisolvent purification treatments. The second point was that the replacement of the oily, long-chain oleic acid with octylphosphonic acid, which has a significantly shorter alkyl chain, should improve charge transport through the NC film. In this chapter, these points were demonstrated by comparing the efficiency of LEDs fabricated from standard OA/OAm-capped and OPA-treated $CsPbBr_3$ NCs. Using a ligand exchange approach for this comparison instead of a direct synthesis using OPA provided the same benefits as those outlined in the previous chapter. Using identical nanocrystals, and changing only the ligand system, was undoubtedly the fairest comparison. It allowed the results to be more confidently attributed to the properties of octylphosphonic acid ligands, with fewer other potentially influential variables.

To accurately compare the two ligand systems, it was vital to first develop an antisolvent purification protocol. Purification should remove as many impurities and as much unbound ligands material as possible without substantial degradation of the nanocrystals' optoelectronic properties. Thus, the optimum degree of antisolvent washing must be determined if high-performance light-emitting diodes were to be obtained.

4.3.1 Antisolvent Screening

Antisolvent selection is crucial to effective purification. The role of an antisolvent is to extract impurities and unbound ligand molecules from a nanocrystal solution. This is typically achieved by precipitating the nanocrystals, while the other species remain in solution. The nanocrystal precipitate can then be separated by centrifugation. Ideally, an antisolvent should avoid degrading the nanocrystal surface or removing bound ligands. To screen for potential antisolvents, $CsPbBr_3$ NCs were purified with various antisolvents while qualitatively monitoring these two parameters. This simply involved observing any colour change or turbidity, which would indicate NC agglomeration or a loss of colloidal stability, respectively.

Five different potential antisolvents were selected based on their common use in the literature. The volume ratio at which they were added to the NC dispersion was also informed by literature, but essentially a lower ratio was used for more polar solvents. The tested antisolvents and their volume ratio were as follows: acetonitrile (1:1 v/v), acetone (1:1 v/v), 1-butanol (1:1 v/v), ethyl acetate (3:1

v/v) and methyl acetate (3:1 v/v). Each was added to an aliquot of isolated NC dispersion, followed by centrifugation at 8000 rpm and redispersion in toluene (20 % of the initial dispersion volume). Figure 4.2 shows a photograph of the resulting "purified" NC dispersions side-by-side, with a vial of the unpurified NC dispersion included for reference.

1-butanol caused the most obvious change; the NC dispersion became orange and opaque, indicating drastic NC agglomeration and precipitation. 1-Butanol is a protic solvent, which have been shown to promote the formation of metal ions, decomposing the NCs.[116] Acetone also caused a colour change, although it was less severe and colloidal stability was maintained. The sample purified with methyl acetate retained the original green-yellow colour but became turbid. Ethyl acetate, on the other hand, did not inflict any loss of colloidal stability. Ethyl acetate is less polar than methyl acetate, so presumably, it was less able to compete with ligands for coordination of the ionic perovskite lattice. However, the most polar solvent tested, acetonitrile, also did not visibly degrade the NC dispersion. The explanation for this could be that acetone and methyl acetate are stronger (albeit still weak) Lewis bases, which enhanced their ability to coordinate with Lewis acidic lead sites. It was likely that the capability of an antisolvent to avoid destabilising or degrading $CsPbBr_3$ NCs was dependent on a combination of solvent polarity (or dielectric constant), Lewis basicity, and the volume ratio employed. A detailed study could have been conducted to analyse the influence of each of these factors. But considering the goals of this work, simply identifying solvents which did not degrade the NC solution was sufficient. Therefore, acetonitrile and ethyl acetate were selected for further testing.

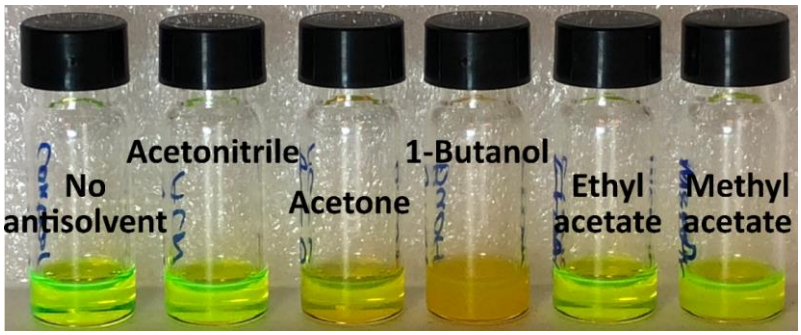

Figure 4.2 **$CsPbBr_3$ nanocrystal aliquots after purification by various antisolvents**

4.3.2 Purification Optimisation

The further testing of ethyl acetate and acetonitrile as antisolvents involved a combination of photoluminescence measurements and LED performance characterisation. This enabled analysis of the internal quantum efficiency (i.e. PLQY), charge injection, and charge extraction. High PLQY values for perovskite nanocrystals are ubiquitous in the literature; the main difficulty tends to be maintaining high PLQY for a nanocrystal ink which contains a sufficiently low quantity of organic

ligand. This is crucial for the deposition of conductive nanocrystal thin-films, which facilitate LEDs with efficient charge injection and, consequently, high external quantum efficiency.

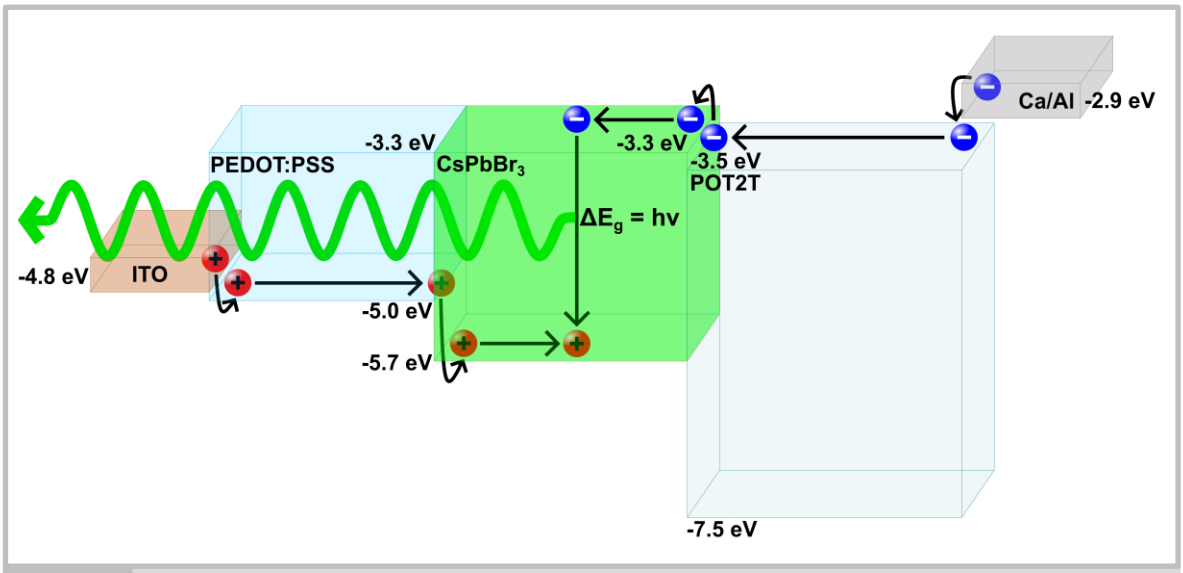

Figure 4.3 **Energy level diagram for the LED structure employed**

The cuboids represent the band gaps of the materials, where the bottom is the valence band maximum, and the top is the conduction band minimum. For the electrodes, ITO and calcium/aluminium, the work functions are shown.

All LEDs fabricated in this section had the following structure: indium tin oxide (ITO, 200 nm) / PEDOT:PSS (40 nm) / $CsPbBr_3$ NCs (40 nm) / POT2T (45 nm) / calcium (Ca, 7 nm) / aluminium (Al, 100 nm). The full details were described in Section 4.2. The energetic alignment of each components' electronic structures is outlined by the band diagram in Figure 4.3.

4.3.2.1 Single Purification

The promising photoluminescence enhancement observed with short OPA ligands suggested that higher LED efficiency should be achievable. Initially, LEDs were fabricated with $CsPbBr_3$ NC inks purified once by either EtOAc or ACN, with and without OPA treatment (15.45 mM). This was to establish a baseline from which the purification protocol could be improved. A photograph of the four LED substrates is shown in Figure 4.4. It was evident that the OPA–ACN film was the most luminescent, followed by OPA–EtOAc, which was brighter than both untreated samples. However, it was noticeable that the LED pixels (identified in Figure 4.1a) were not visible through the ITO side of the substrate, unlike the rest of the substrates. This phenomenon is often observed where NC inks contain an excessive quantity of oily ligand material. While the origin has not been investigated, the luminescence quenching was only on the area where the electron transport material (POT2T) was deposited. Thus, it was likely that the quenching was attributable to some reaction between

the impurities or excess ligands in the NC film with the organic small molecules thermally deposited on top of it.

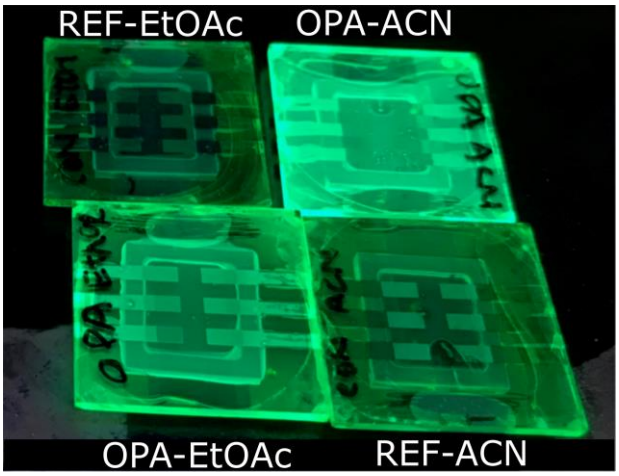

Figure 4.4 **Photograph of LEDs under UV light**

The films were fabricated from $CsPbBr_3$ nanocrystal inks purified with different antisolvents, with (OPA) and without (REF) OPA treatment.

Observation of this luminescence quenching on the active area is typically an indication that the devices will not function. Measurement of the LED confirmed this; the current density-voltage-luminance (J-V-L) plots in Figure 4.5a show that the OPA–ACN device exhibited an Ohmic response to increasing voltage with no detectable electroluminescence. Thus, one purification cycle with ACN was conclusively insufficient. REF–EtOAc was the only sample to yield substantial current density, with a turn-on voltage of around 2.6 V, which was comparable with typical values in the literature. REF–EtOAc also exhibited respectable maximum luminance of almost 1000 cd m^{-2}, but Figure 4.5b demonstrates that the maximum EQE was limited to 0.56 %. This result indicated that purification removed enough impurities and excess ligand materials, but in doing so, surface passivation of the NCs was degraded significantly, restricting the quantum efficiency.

The J-V curve of the OPA–EtOAc device indicated that the film was far more resistive that REF–EtOAc, as the current density was around two orders of magnitude lower. This may be attributed to the addition of ligand material during the ligand exchange process, such that purification must remove a larger quantity of excess ligand to obtain sufficiently conductive films. The increased turn-on voltage supported this, as highly resistive films require a greater voltage to obtain sufficient current density for significant charge recombination. A similar J-V curve was observed for REF–ACN; this suggests that ACN does have some capability to extract native free OA and OAm ligands, but that EtOAc was more effective. The plots of EQE against voltage for both REF–ACN and OPA–EtOAc were very noisy. The noise originates from the high signal-to-noise of the detected electroluminescence spectrum due to the very low luminance of the device. It was nonetheless

clear that the OPA–EtOAc device had a significantly higher maximum EQE than the REF samples. Due to the highly resistive nature of the films, the enhancement could only be attributable to improved passivation rather than improved conductivity.

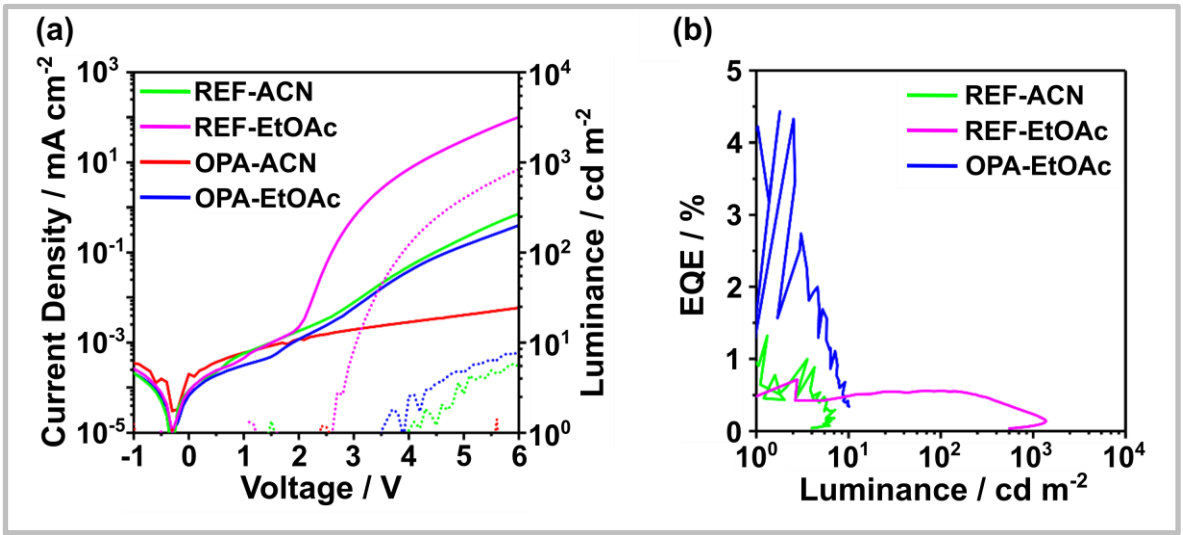

Figure 4.5 **Optoelectronic characterisation of LEDs fabricated from $CsPbBr_3$ nanocrystal inks purified with either ethyl acetate or acetonitrile, with and without OPA treatment**

(a) Current density-voltage (solid lines) and luminance-voltage (dotted lines) plots, and (b) EQE against luminance plots.

4.3.2.2 Triple Purification

To obtain more reliable evidence of the efficiency improvement afforded by OPA, it was necessary to refine the antisolvent purification protocol further. For the next batch of LEDs, three purification cycles were employed for each NC ink instead of one. Although EtOAc appeared to be more effective in the first experiment, different combinations of EtOAc and ACN purification cycles to test whether the two antisolvents could have complementary effects. Three different purification regimes were tested, each including three consecutive purification cycles: EEE, AEE and EEA, where E = 3:1 v/v EtOAc, and A = 1:1 v/v ACN. Each purification regime was tested on untreated (REF) and OPA-treated $CsPbBr_3$ NC inks.

The photoluminescence quantum yield of each of the six NC inks was measured before LED fabrication. Table 4.1 shows the PLQY values, which were all similar. For the REF samples, the highest PLQY came from purely EtOAc purification (EEE). This suggested that without OPA treatment, any ACN purification cycles degrade surface passivation. Surprisingly, OPA–EEE and REF–EEE had the same PLQY, indicating that three EtOAc purification cycles diminished any surface passivation enhancement provided by OPA. It is worth noting that in contrast to the REF samples,

the inclusion of an ACN purification cycle had little effect on the purification. This implied that OPA ligands might be more robust towards ACN purification than the OA/OAm ligand system.

Table 4.1 **Photoluminescence quantum yield of $CsPbBr_3$ nanocrystal inks purified with different antisolvent purification protocols, with and without OPA treatment**

Sample	Photoluminescence Quantum Yield / %
REF–EEE	31
REF–AEE	23
REF–EEA	21
OPA–EEE	31
OPA–AEE	27
OPA–EEA	30

The J-V-L and EQE-luminance plots for all six LEDs were shown in Figure 4.6a and b, respectively. In contrast to the once-purified samples, all thrice-washed samples produced functional LEDs. All LEDs exhibited very similar J-V curves, with clear diode behaviour. However, there was obvious segregation of the V-L plots of REF and OPA samples; the three OPA-treated samples had lower turn-on voltages and higher maximum luminance than the three untreated samples. The lower turn-on voltage was indicative of less resistive NC films, which was attributable to the shorter octyl ligand replacing the long oleyl ligand. Although losing the passivation effect of the OPA ligands was not ideal, it was useful in that the effect on charge injection was highlighted. The reduced injection efficiency had a more pronounced effect on the EQE. The untreated samples, REF–EEE, REF–AEE and REF–EEA provided low maximum EQE of 0.26 %, 0.17 % and 0.42 %, respectively. Meanwhile, OPA–EEE, OPA–AEE and OPA–EEA LEDs had EQE of 1.87 %, 1.01 % and 2.24 %, respectively. Thus, OPA undoubtedly enhanced the EQE despite no significant increase of PLQY. This implied that charge injection efficiency was much improved, as charge balance and outcoupling efficiency should be comparable for the same device structure.

Both the sets of untreated and OPA-treated samples showed the same trend with regards to purification. The AEE purification protocol gave the lowest EQE, followed by EEE, with EEA providing the highest EQE. This suggested that when ACN was used for the first purification cycle rather than EtOAc, less excess ligand was removed. The very poor LED characteristics obtained when the NCs were purified once by ACN corroborate this assertion. In contrast though, when ACN was used for the final purification cycle, EQE was enhanced. This can be rationalised by considering the decreasing concentration of the NC dispersion through the purification cycles. After centrifugation with antisolvent, a minor fraction of smaller NCs remained in the discarded supernatant, as

indicated by a pale green colour. Similarly, a small precipitate containing some agglomerated NCs was discarded after the second, low-speed centrifugation step. Thus, although the volume ratio of ACN used for the first and last purification cycles was the same (1:1 v/v), the actual ACN:NC ratio was higher for the third purification cycle. As a result, using ACN for the third purification cycle was a harsher condition, and therefore expected to remove more excess ligand.

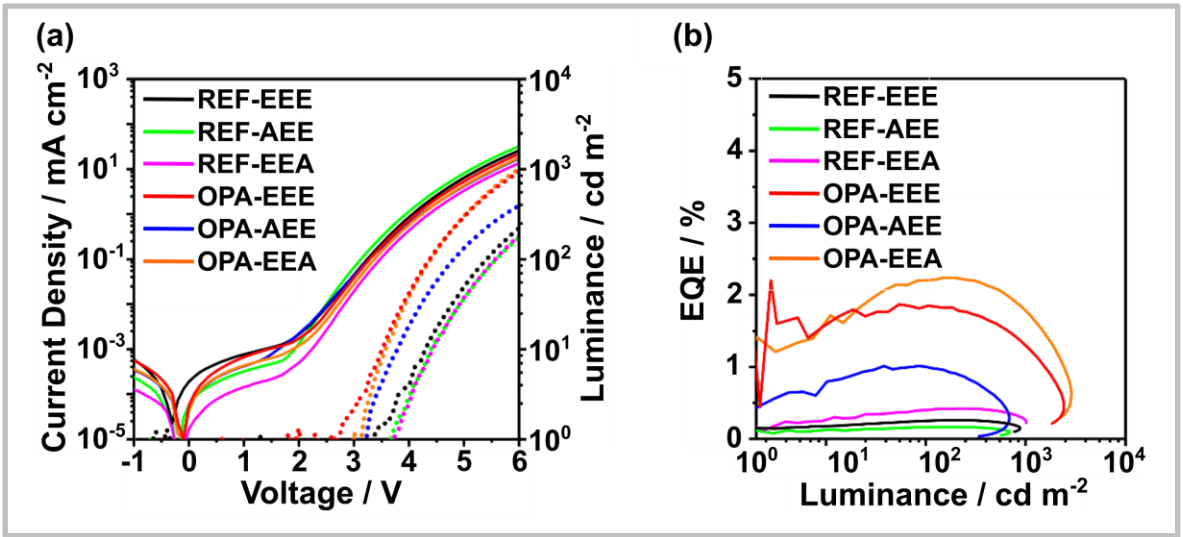

Figure 4.6 **Optoelectronic characterisation of LEDs fabricated from $CsPbBr_3$ nanocrystal inks purified by different protocols, with and without OPA treatment**

(a) Current density-voltage (solid lines) and luminance-voltage (dotted lines) plots, and (b) EQE against luminance plots.

In summary, there was a clear trend indicating that EtOAc was more suitable for the first purification cycle, but that ACN was an effective antisolvent for the final purification cycle. OPA–EEA provided reasonable EQE despite a relatively low PLQY of 30 %. Therefore, adjustments to the protocol were sought such that similarly effective excess ligand removal could be obtained without losing the PLQY enhancement afforded by OPA treatment. Based on the observations that one purification cycle was not sufficient, and three purification cycles was excessive, it was obvious that employing two purification cycles was the most promising option. It was also clearly logical to use EtOAc for the first cycle, followed by ACN for the second cycle.

4.3.2.3 Optimising Purification for PLQY Retention

Before testing the twice-purified $CsPbBr_3$ NCs in LEDs, further optimisation of the OPA concentration was conducted. Up to this point, an OPA concentration of 15.45 mM had been consistently employed. However, in Chapter 3.2, it was shown that the plot of photoluminescence intensity against OPA concentration plateaued between around 3 to 20 mM (Figure 3.2). This

indicated that $CsPbBr_3$ NCs treated with this range of OPA concentrations have comparable PLQY. It was useful to determine whether this was consistent through antisolvent purification, as ultimately the PLQY of the purified NC ink that is most important. When developing ligand systems targeted towards light-emitting diode applications, defect passivation must be retained in the ink used to deposit thin films.

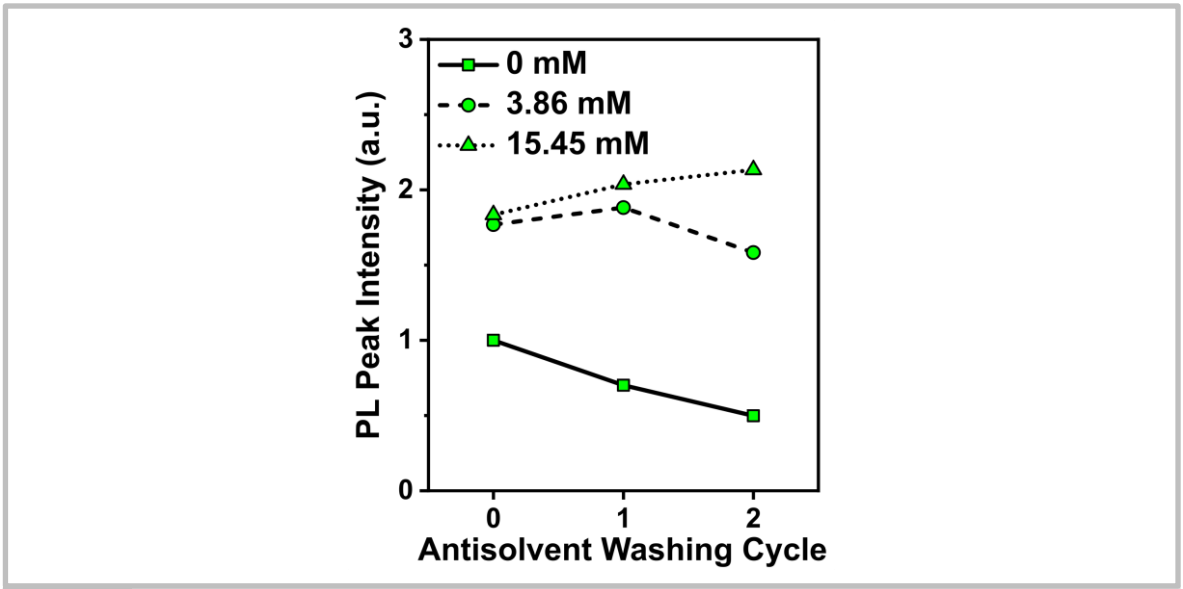

Figure 4.7 **The change in photoluminescence intensity of $CsPbBr_3$ NC solutions prepared with different OPA concentrations through antisolvent purification**

The sample treated with a higher OPA concentration displayed a marginally greater PL enhancement, which was logical as there should be a greater number of excess OPA ligands available to passivate vacated surface sites. This logic persisted, as after the ACN purification cycle, the PL intensity of the sample treated with 15.45 mM OPA increased further, while the PL of the 3.86 mM OPA sample dropped below its pre-purification intensity. It was explained in Chapter 3 that ACN promoted the preferential reconfiguration of OPA ligands bound by a few different modes into primarily the most strongly bound mode. More strongly bound OPA ligands should provide better passivation, which explained the increased PL intensity. As this effect was not observed for the lower OPA concentration, it can be concluded that the presence of excess OPA in the solution was crucial to this mechanism.

The final purified OPA-treated ink (15.45 mM) exhibited PL intensity around 4 times greater than the purified untreated sample. Photoluminescence quantum yield (PLQY) measurements of the OPA-treated and untreated samples were consistent with this result, obtaining PLQY values of 62 % and 20 %, respectively. It was important to note that excess OPA ligands in the NC ink would likely increase the resistivity of NC thin-films. However, as OPA ligands are much shorter than oleyl ligands, the effect should be less severe. Therefore, the 15.45 mM was confirmed as the optimised

OPA concentration. The absorbance and photoluminescence spectra of the optimised purified $CsPbBr_3$ NC ink was presented in Figure 4.8.

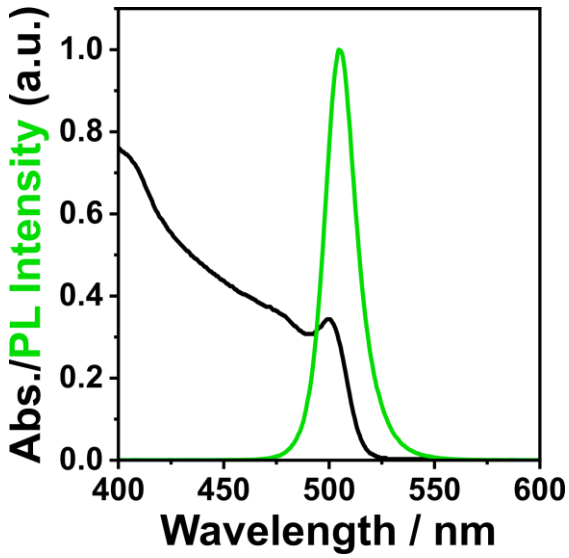

Figure 4.8 **Absorbance and photoluminescence spectra of $CsPbBr_3$ treated with 15.45 mM OPA and purified consecutively with EtOAc and ACN**

4.3.2.4 Time-Resolved Photoluminescence Spectroscopy

The enhancement of photoluminescence properties with OPA addition was investigated further using time-resolved photoluminescence spectroscopy (TRPL). This technique measured the decay of the photoluminescence intensity after pulsed excitation of the sample. The PL decay was fitted by a bi-exponential function to extract the non-radiative and radiative charge carrier lifetimes, and their relative amplitudes.

The TRPL spectra for thin films deposited from untreated reference (REF) and OPA-treated (OPA) NC inks extracted after EtOAc (1w) and ACN (2w) purification cycles are shown in Figure 4.9. The characteristic non-radiative (τ_1) and radiative (τ_2) decay lifetimes, their corresponding relative amplitudes (A), and the calculated average fluorescence lifetime (τ_{ave}) were displayed in Table 4.2.

The first important point to note about the TRPL data was that A_1 and A_2, the relative contributions of τ_1 and τ_2, were comparable for all samples. Under this circumstance, the τ_1 and τ_2 values for different samples could reliably be directly compared. The increase of τ_1 upon OPA addition is consistent with the PL intensity enhancement observed in Section 3.2. It indicated suppression of non-radiative recombination at the NC surface, which was attributed to improved surface passivation by OPA. OPA-2w had a higher τ_1 than OPA-1w, correlating well with the increased PL intensity after ACN purification, as shown in Figure 4.7.

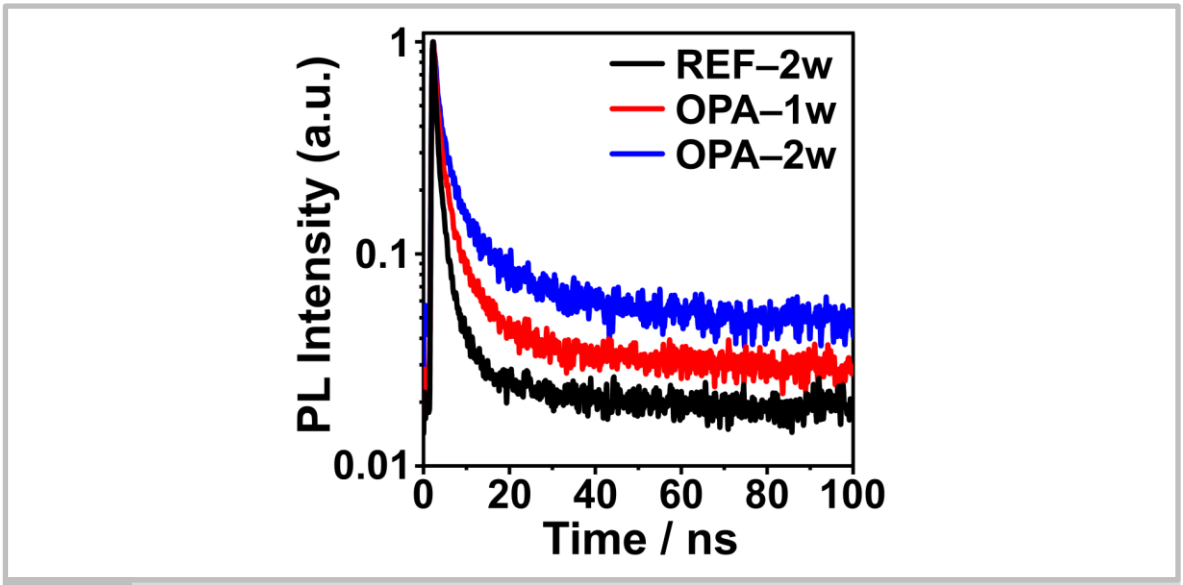

Figure 4.9 **Time-resolved photoluminescence spectra of $CsPbBr_3$ nanocrystal thin films, untreated (REF) and OPA-treated (OPA), after one (1w) or two (2w) purification cycles**

The τ_2 values follow the same trend as τ_1 - the addition of OPA increases τ_2, as did ACN purification. The increase of the radiative lifetime of the exciton suggested a reduction of ligand density in the film. Thus, the increase of τ_2 with OPA addition supported the substitution of longer oleyl ligands with shorter OPA ligands, which would reduce the total insulating organic content in the film. The increase of τ_2 from OPA-1w to OPA-2w demonstrated that the ACN purification step removed a significant quantity of excess ligand from the NC ink. Overall, TRPL provided evidence that OPA treatment replaced oleyl ligands, which passivated the surface of $CsPbBr_3$ NCs more effectively, and that this passivation was maintained while ACN removed a substantial quantity of excess ligand material.

Table 4.2 **Charge carrier lifetimes and their corresponding amplitudes obtained from time-resolved photoluminescence spectra of $CsPbBr_3$ nanocrystal thin films, untreated (REF) and OPA-treated (OPA) after one (1w) or two (2w) purification cycles**

Sample	A_1	τ_1 / ns	A_2	τ_2 / ns	τ_{ave} / ns
REF–2w	0.74	0.8	0.26	3.8	1.5
OPA–1w	0.72	1.1	0.28	6.1	2.5
OPA–2w	0.73	1.4	0.26	10.3	3.8

4.3.3 Optimised Light-Emitting Diodes

The photoluminescence retention and longer carrier lifetimes of OPA-treated $CsPbBr_3$ nanocrystals purified by the devised EtOAc/ACN two-cycle protocol were highly promising indicators. Ultimately though, the efficacy of the protocol must be supported by LED data. Therefore, LEDs were fabricated with four different inks: REF–1w, REF–2w, OPA–1w and OPA–2w. All four samples were tested to aid the decoupling of OPA-treatment and purification effects. The J-V-L and EQE-luminance plots for all four LEDs are shown in Figure 4.10a and b, respectively. The key characteristics are displayed in Table 4.3. The results obtained here needed to be understood in the context of the state-of-the-art perovskite NC LEDs. Table 4.4 compared the key LED characteristics of high-efficiency green-emitting perovskite NC LEDs from literature with the best-performing LED of this work.

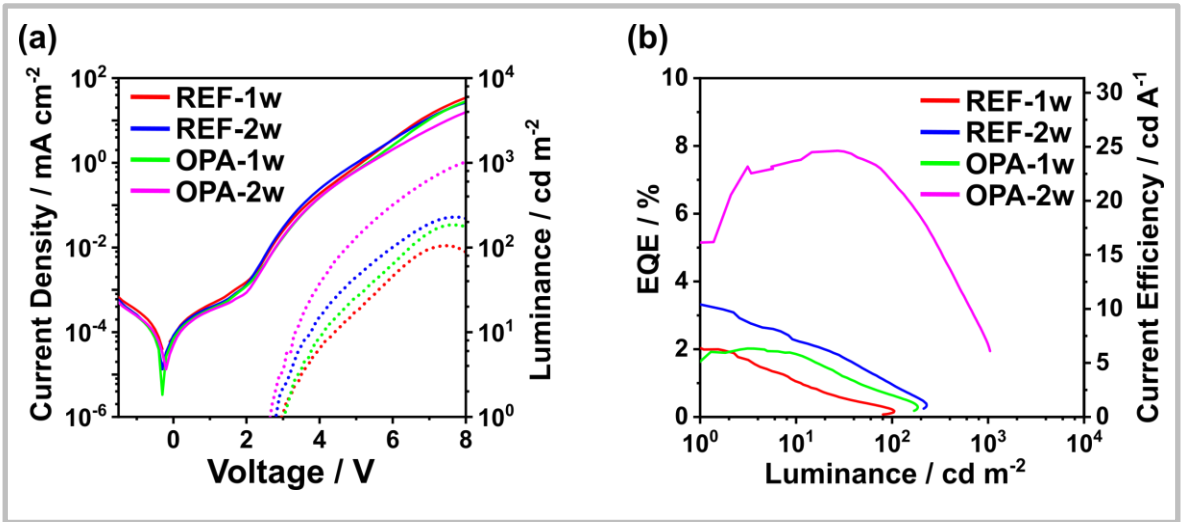

Figure 4.10 Optoelectronic characterisation of LEDs fabricated from $CsPbBr_3$ nanocrystal inks, untreated (REF) and OPA-treated (OPA) after one (1w) or two (2w) purification cycles

(a) Current density-voltage (solid lines) and luminance-voltage (dotted lines) plots, and (b) EQE against luminance plots.

It was apparent in Figure 4.10a that the J-V curve for all LEDs exhibited very similar diode behaviour. The OPA-2w device had the lowest turn-on voltage of 2.6 V (at 1 cd m^{-2}), while REF–2w and both 1w samples had turn-on voltages of 2.8 V and 3.0 V, respectively. $CsPbBr_3$ has a bandgap of around 2.4 eV, so ideal charge injection efficiency would lead to a turn-on voltage of around 2.4 V. Thus, the turn-on voltages for all devices can be considered reasonable, indicating that none of the devices exhibited significant interfacial energy barriers or had overly resistive NC films. However, the trend implies that a second purification cycle did improve the film conductivity, as anticipated.

The lower turn-on voltage of OPA–2w when compared to REF–2w can be attributed to the substitution of long C_{18} oleyl ligand chains for octyls during OPA ligand exchange.

Table 4.3 Characteristics of LEDs fabricated from $CsPbBr_3$ nanocrystal inks, untreated (REF) and OPA-treated (OPA) after one (1w) or two (2w) purification cycles

Sample	EL Peak / nm	Turn-on Voltage / V	Luminance / cd m^{-2}	EQE / %
REF–1w	514	3.0	105	1.8
REF–2w	514	2.8	229	3.6
OPA–1w	514	3.0	185	2.0
OPA–2w	514	2.6	1022	7.7

The plots of EQE against luminance in Figure 4.10b present a stark contrast between OPA–2w and the other three samples. The OPA–2w device achieved a maximum EQE of 7.7 %, which was remarkably higher than the 3.6 %, 2.0 %, and 1.8 % obtained from REF–2w, OPA–1w, and REF–1w devices, respectively. The EQE value of OPA–2w also compared decently with the state-of-the-art $CsPbBr_3$ NC LEDs reported in the literature at the time (Table 4.4). Interestingly, the OPA treatment only provided a minor enhancement of EQE for the 1w samples, despite exhibiting more than double the solution PL intensity (Figure 4.7). This suggested that excess OPA remaining from the ligand exchange inhibited charge injection, which offset the replacement of C_{18} ligands for C_8; this was supported by the higher turn-on voltage. The higher EQE achieved by REF–2w highlighted the importance of effective purification. The thermogravimetric analysis presented in Figure 3.11 in Section 3.3.3.4 demonstrated that the REF-2w sample had a substantially lower organic ligand content than the other three samples. Thus, reasonable EQE was obtained despite low PLQY (20 %). This result concurrently emphasised the fundamental limitation of the OA/OAm ligand system, that weak, dynamic binding renders effective purification and sufficient surface passivation mutually exclusive.

The maximum luminance values obtained were 1002 cd m^{-2} for OPA–2w, 229 cd m^{-2} for REF–2w, 185 cd m^{-2} for OPA–1w and 105 cd m^{-2} for REF–1w. These values are all relatively low, reflective of the low maximum current density values. This was an indication that despite the improvement of conductivity with the substitution of a fraction of oleic acid ligands for octylphosphonates, and the removal of excess organics through purification, the conductivity remained an order of magnitude or two below other high-efficiency LEDs reported in the literature. As only oleic acid was replaced by OPA, oleylammonium ligands were still present on the surface. Thus, there were still long C_{18} alkyl chains present to inhibit conductivity. To push the current density higher, and consequently increase the luminance, oleyl ligands must be removed entirely. This assertion was supported by

the fact that the highest luminance values from $CsPbBr_3$ shown in Table 4.4 were from nanocrystals which did not use either oleylamine or oleic acid.

Table 4.4 Characteristics of state-of-the-art green-emitting perovskite nanocrystal LEDs

Composition	Ligands	EL Peak / nm	Turn-on Voltage / V	Max. Luminance / cd m^{-2}	EQE / %	Ref.	Date (MM/YY)
$CsPbBr_3$	OA, OAm	512	3.4	15185	6.3	[116]	11/16
$CsPbBr_3$	OA, OAm, DDAB	512	2.6	≈1000	8.7	[117]	05/17
$CsPbBr_3$	OPA, TOPO	516	2.8	7085	6.5	[145]	01/18
$CsPbBr_3$	OA, OAm, OPA	514	2.6	1022	7.7	*[140]	06/19
$CsPbBr_3$	DDAB	512	2.7	34700	9.8	[151]	10/19
$CsPbBr_3$	OA, OAm	516	-	21000	18.7	[129]	08/20
$Cs_{0.85}FA_{0.15}PbBr_3$	OctA, DDAB, $ZnBr_2$	518	2.4	76940	16.5	[150]	10/18
$Cs_{0.85}FA_{0.15}PbBr_3$	OctA, DDAB, $ZnBr_2$	520	2.0	41900	21.6	[173]	08/20
$FAPbBr_3$	OA, OctAm	536	3.6	≈15000	17.1	[174]	01/20

OA = oleic acid, OAm = oleylamine, DDAB = didodecyldimethylammonium bromide, OPA = octylphosphonic acid, TOPO = trioctylphosphine oxide, OctAc = octanoic acid, OctAm = octylamine. * denotes the results from this work.

The EQE of the OPA-2w LED here exceeded the efficiency reported for the *in-situ* solely OPA-capped $CsPbBr_3$ NCs of Tan et al.[145] Although they achieved higher current density (10^2 mA cm^{-2}) and luminance (7085 cd m^{-2}), their EQE was 6.5 %. This demonstrated that, as suggested by the NMR results in Section 3.2.3.7, the surface passivation afforded by the ligand exchange and *in-situ* approaches were comparable. Closer inspection of Tan and co-workers' paper reveals that their OPA-$CsPbBr_3$ NC ink has a concentration of 3 mg mL^{-1}; this was significantly lower than typically reported concentrations, which are usually at least 10 mg mL^{-1}, often 20 mg mL^{-1}. A low concentration NC ink would lead to very thin NC films, which can reduce light outcoupling efficiency and increase the probability of charge carriers passing through the NC layer and injecting into the opposite charge transport layer before recombination can occur. In other words, the recombination zone moves away from the emitter layer. Presumably, the presence of only short OPA ligands on the NC surface limits colloidal stability. Herein, the retention of oleylammonium ligands allowed good colloidal stability to be maintained. This highlighted that a balance must be found between

reducing ligand length and maintaining colloidal stability to increase the efficiency of phosphonate-capped $CsPbBr_3$ NC LEDs further.

Despite a substantial improvement of LED performance characteristics with OPA ligand exchange, recent works have demonstrated much higher efficiency and luminance values. The retention of oleylammonium ligands on the surface of the nanocrystals here was likely to restrict the potential conductivity improvement possible. Many recent high-efficiency LEDs have utilised shorter quaternary ammonium ligands instead of oleylammonium.

There are various other aspects that were expected to contribute to the relatively low EQE recorded. To maximise EQE, the hole and electron injection should be balanced. This could be achieved by fabricating electron-only and hole-only devices, measuring the current densities of each with various charge transport layers of various thicknesses. A more nuanced and efficient approach would be to employ electronic device simulations for optimisation. Similarly, optical simulations could be used to optimise the thicknesses of each layer in the device stack for maximum light outcoupling. Waveguide losses could be further improved by employing a nanostructured PEDOT/perovskite interface and a hemispherical lens.[175]

The sharp reduction of the LED efficiency at high luminance values can be attributed to Auger recombination and Joule heating.[176] While mitigating Auger recombination is a complicated challenge, there are some reported approaches for reducing Joule heating. Doping of the charge transport layers to dramatically increase device conductivity was reported to allow better heat dissipation.[177] They improved thermal management further by utilising graphite sheets and copper bars as a heat spreaders and heat sinks, respectively, and by replacing glass substrates with more thermally conductive sapphire wafers.

4.4 Summary

In this chapter, an antisolvent protocol was devised and optimised for OPA-capped $CsPbBr_3$ nanocrystals prepared by ligand exchange, such that high-efficiency light-emitting diodes could be fabricated. Ethyl acetate and acetonitrile were first identified as the most promising antisolvents. The two antisolvents and the number of washing cycles were optimised. Two cycles, with ethyl acetate and acetonitrile consecutively, was determined to be the best option. It was also found that using a higher OPA concentration during ligand exchange enabled better retention of photoluminescence through antisolvent purification, despite low (3.86 mM) and high (15.45 mM) OPA concentrations providing similar initial PL intensities.

Light-emitting diodes were fabricated from $CsPbBr_3$ nanocrystals with or without OPA treatment, after each of the two antisolvent purification cycles. The nanocrystals treated with OPA and twice purified exhibited a maximum EQE of 7.7 % and maximum luminance of 1022 cd m^{-2}, which was significantly higher than the other three samples. Interestingly, the EQE of the twice-washed untreated nanocrystals (3.6 %) was almost twice the EQE of the once-washed OPA-treated nanocrystals (2.0 %). This indicated that the sufficient washing provided by the optimised purification protocol was crucial. These results demonstrated that the strong binding octylphosphonate ligands, together with an optimised antisolvent purification, could obtain a $CsPbBr_3$ nanocrystal ink with higher PLQY and a lower quantity of unbound ligand than the original OA/OAm ligand pair. This represented an enhancement of the suitability of these nanocrystals for electroluminescence applications.

Chapter 5 A Highly Tuneable Room Temperature $CsPbBr_3$ Nanocrystal Synthesis

5.1 Introduction

The previous two chapters demonstrated that octylphosphonic acid ligands could bind strongly to the surface of $CsPbBr_3$ nanocrystals, enhancing their photoluminescence and electroluminescence, and affording improved resistance to antisolvent purification. This represented an enhancement of commercial viability because these properties were more favourable for potential light-emitting applications. However, the methodology employed still relied on the high-temperature hot-injection synthesis.

As discussed extensively in the Literature Review, the hot-injection method inherently hinders the commercial viability of perovskite nanocrystals. Scaling up the Schlenk line setup is costly and complex, and the difficulty is further compounded by the necessity to instantaneously inject a large volume of a precursor followed by rapidly cooling by more than 100 °C within seconds. However, hot-injection has been a very successful and reliable approach. The size of nanocrystals synthesised by hot-injection can be controlled by the precise reaction temperature, and a wide range of perovskite nanocrystal compositions have been synthesised by this method, with emission peaks ranging from around 410 nm for $CsPbCl_3$ to 780 nm for $FAPbI_3$.[178–180]

There has been significant progress made with room temperature $CsPbBr_3$ NC syntheses over the last few years, yet there remains a lack of size control. In general, versatility is important for an industrial process because it offers the capability to tailor towards different applications; it is especially important for perovskite nanocrystals, where small changes in the diameter can greatly affect the optoelectronic properties. A room temperature process which could demonstrate the same size tuneability as hot-injection, particularly one conducted in an ambient environment, would be significantly more viable and commercially appealing than the high-temperature alternative.

In this chapter, a room temperature synthesis method was developed to directly incorporate OPA ligands onto the surface of $CsPbBr_3$ nanocrystals. A synthesis protocol was sought which followed similar chemistry to the hot-injection method; a polar solvent-free approach, exploiting ligand engineering to dissolve the precursors in non-polar solvents. The first section of this chapter discusses the reasoning underpinning the devised synthesis method. Later sections thoroughly examined the optoelectronic properties of the nanocrystals, demonstrating the extent of size

tuneability achieved. Fundamental insights were gained into the nucleation and growth mechanism at play, which allowed reasonable hypotheses to be proposed.

5.2 Materials and Methods

In this section, the methodology employed in this chapter will be described.

5.2.1 Chemicals

Lead bromide ($PbBr_2$, ≥ 99.999 % trace metals basis), cesium carbonate (Cs_2CO_3, 99.9% trace metals basis), octanoic acid (98 %), trioctylphosphine oxide (TOPO, 99 %), didodecyldimethylammonium bromide (DDAB, 98 %), ethyl acetate (EtOAc, anhydrous, >99.9 %), methyl acetate (MeOAc, anhydrous, >99.9 %), butyl acetate (BuOAc, anhydrous, >99.9 %), toluene (anhydrous, >99.8 %) and heptane (anhydrous, 99 %) were purchased from Sigma-Aldrich. Octylphosphonic acid (OPA, 98 %) was purchased from TCI. All chemicals were used without further purification.

5.2.2 Cesium Lead Bromide Nanocrystal Synthesis

5.2.2.1 Precursor Preparation

Cs_2CO_3 (32.6 mg, 0.1 mmol) was dissolved in octanoic acid (1 mL) with stirring at room temperature in a nitrogen-filled glovebox (0.2 M Cs^+). $PbBr_2$ (550 mg, 1.5 mmol) were dissolved in toluene (10 mL), by adding TOPO (5.8 g, 6.44 mL, 15 mmol) and heating at 80 °C for 10 minutes (0.091 M $PbBr_2$, 0.91 M TOPO). OPA or octanoic acid were added to the lead halide precursor solution at the desired concentration where appropriate and dissolved with stirring. DDAB (116 mg, 0.05 mmol) was dissolved in toluene (5 mL) with stirring. All precursor solutions were tightly sealed to prevent solvent evaporation and stored in air at room temperature.

5.2.2.2 Synthesis

The following describes a typical synthesis; any changes will be mentioned in the discussion. The scale described was the smallest used; the reaction was scaled up proportionally depending on the quantity of nanocrystals required.

For the synthesis of $CsPbBr_3$ nanocrystals, 55 µL Cs precursor was injected into 0.5 mL $PbBr_2$ solution at room temperature (approximately 25 °C) with vigorous stirring. After 30 to 2400 s, 156 µL DDAB solution was added. After a further 300 s, the precipitate was collected by centrifugation at 10000 rpm, with or without 1.5 mL ethyl acetate, and redispersed in 100 µL heptane.

5.2.2.3 Purification

The nanocrystal dispersion was centrifuged at 5000 rpm and the precipitate discarded. The supernatant was retained, and 300 µL methyl acetate was added to fully precipitate the

nanocrystals. The precipitate was collected by centrifugation at 10000 rpm and redispersed in 100 µL heptane. The dispersion was centrifuged at 5000 rpm and the precipitate discarded. The supernatant was placed in a weighed centrifuge tube, and another 300 µL methyl acetate was added to fully precipitate the nanocrystals again, followed by centrifugation at 10000 rpm. The supernatant was extracted, and the centrifuge tube containing the precipitate was weighed again to calculate the mass of $CsPbBr_3$ NCs obtained. The precipitate was redispersed at the desired concentration with heptane and was centrifuged at 5000 rpm. The supernatant was extracted as the fully purified $CsPbBr_3$ nanocrystal ink.

5.2.3 Characterisation Methodology

5.2.3.1 Optical Absorption Spectroscopy

Absorbance spectra were obtained using a Shimadzu UV-3600 spectrophotometer. The samples were prepared in Quartz cuvettes and diluted by a factor of between 60 and 600 (5 – 50 µL NC ink in 3 mL solvent). Typically, the spectra were excited at 365 nm and recorded over a wavelength range of 600 to 350 nm. The measurement settings were as follows: interval = 0.1 nm, integration time = 0.1 s.

5.2.3.2 Photoluminescence Spectroscopy

Photoluminescence spectra were collected using a Horiba Fluoromax-4 spectrophotometer. The samples were prepared in Quartz cuvettes and diluted by a factor of between 60 and 600 (5 to 50 µL NC ink in 3 mL solvent). A laser excitation wavelength of 365 nm was used. The other measurement settings were as follows: interval = 0.1 nm, integration time = 0.1 s, excitation slit width = 1 nm, emission slit width = 0.5 nm.

Where appropriate, the measured PL intensity was corrected for the absorbance intensity at the excitation wavelength according to:

Equation 5.1

$$I_{corr} = \frac{I_{meas}}{(1 - 10^{-A})}$$

where A was the absorbance at the excitation wavelength (i.e., at 365 nm).

5.2.3.3 Photoluminescence Quantum Yield Measurement

The PLQY measurement using a Labsphere integrating sphere. The sample was placed inside and excited with a Cobolt 445 nm continuous-wave diode laser. The output of the integrating sphere was coupled through an optical fibre to a charge-coupled device (Newton 920 CCD, Andor) in which the photon count was captured.

5.2.3.4 Transient Absorption Spectroscopy

Transient absorption data was collected by commercial a TA Ultrafast Systems HELIOS™ spectrometer. The spectrometer was powered by Coherent Libra™, which produced a ~50 fs pulsed laser with 800 nm fundamental wavelength at a 1 kHz repetition rate. The output beam was split into two. The first beam was frequency doubled using a β-barium borate (BBO) crystal (400 nm), which acted as the pump beam. The second beam was delayed by a mechanical stage and focused into a sapphire crystal to generate a white light continuum, which acted as the probe beam. The pump beam was mechanically modulated at 500 Hz by using an optical chopper to obtain a pump-induced change of probe transmission. The measurements were performed at transmission geometry.

5.2.3.5 Nuclear Magnetic Resonance (NMR) Spectroscopy

Solution ^{13}C and ^{31}P NMR experiments were completed at 9.40 T ($\nu_0(^1H)$ = 400.13 MHz; $\nu_0(^{13}C)$ = 150.92 MHz; $\nu_0(^{31}P)$ = 242.96 MHz) using a Bruker Avance I spectrometer with a Bruker 5 mm BBO probe. The ^{31}P experiments employed a proton-decoupled one- pulse sequence, with a $\pi/6$ pulse length of 2.7 μs. The ^1H experiments employed a one-pulse sequence, with a $\pi/2$ pulse length of 10 μs. A recycle delay of 1 s was used throughout. Samples were prepared with toluene-d8 solvent and were referenced internally.

Solid-state ^1H and ^{31}P NMR experiments were completed using a Bruker Avance III HD 600 MHz spectrometer with a Bruker 4 mm HXY magic-angle spinning (MAS) probe. The ^1H and ^{31}P MAS NMR were collected at a MAS frequency of 14 kHz, and resulting data was externally referenced with respect to ammonium dihydrogen phosphate ($(NH_4)_2HPO_4$ (s); δ_{iso} = 0.99 ppm) and adamantane ($C_{10}H_{16}$ (s); δ_{iso} = 1.82 ppm). The 1D ^{31}P experiments employed a proton-decoupled one-pulse sequence, with a $\pi/2$ pulse length of 4.6 μs and a recycle delay of 180 s. The 1D ^1H experiments employed a proton-decoupled one-pulse sequence, with a $\pi/2$ pulse length of 3.4 μs and a recycle delay of 3 s. The 2D ^{31}P-^1H heteronuclear correlation (HETCOR) NMR experiments employed a proton-decoupled CP correlation sequence, utilizing the same ^1H parameters as the one-pulse sequence and a contact pulse length of 5000 μs.

5.2.3.6 Transmission Electron Microscopy

Samples were prepared by placing a formvar TEM grid with Cu-200 mesh on the bottom of a vial, then submerging the grid in a concentrated nanocrystal dispersion. The solution was left to evaporate overnight, such that a nanocrystal superlattice was formed on the grid. HR-TEM images were taken with a JEOL 2100F, using an accelerating voltage of 200 kV and a beam current of 146 μA.

5.2.3.7 Small Angle X-ray Scattering

A Xenocs Nano-inXider equipped with a Dectris Pilatus 3 hybrid pixel detector was used to perform small-angle X-ray scattering. The effective scattering vector magnitude was measured in the range of $0.041 < q < 4.47$ nm^{-1} in SAXS. The samples were measured in sealed glass capillaries under vacuum at room temperature. Particle size distributions were obtained (form-free) from scattering curves using the Monte Carlo-based software package McSAS, using a convergence criterion of 5, with 20 calculating repetitions, and 500 contributions.[157]

5.2.3.8 X-ray Diffraction

All X-ray diffraction data was accumulated using a PANalytical X-ray diffractometer equipped with a Cu Kα X-ray tube operating at 40 kV and 30 mA. These diffraction patterns were acquired in air at room temperature using Bragg–Brentano geometry. All XRD samples were prepared by drop-casting a concentrated solution on a glass substrate.

5.3 Results and Discussion

5.3.1 Synthesis Design

The initial stage of synthesis design involved detailed familiarisation with the various methodologies employed previously, both by hot-injection and at room temperature. There were many components to the synthesis, which were adopted from others, and expanded upon. This section will systematically explain the reasoning for the inclusion of each component.

5.3.1.1 Solvent Selection

Room-temperature syntheses typically proceed by one of two methods: ligand assisted reprecipitation (LARP) or polar solvent-free. LARP utilises polar solvents to dissolve the precursors, while predictably, polar solvent-free methods use non-polar solvents. Although there have been a decent number of reports on both types, reaction scalability has only been demonstrated convincingly for the polar solvent-free approaches. A combination of the reliance of LARP on the large difference between the polarity of the two solvents used and the extremely fast kinetics of perovskite nanocrystal growth results in a highly sensitive reaction. It is therefore difficult to perform or scale reproducibly. Furthermore, the use of polar solvents in the synthesis of perovskite nanocrystals was concerning because they can be quickly degraded by the same solvents.

Polar solvent-free methods benefit from following similar chemistry to the hot-injection approach. It has already been shown that the reaction between the same precursors and ligands can be tuned by controlling the ligand concentration. A reasonable hypothesis can be made that the same control could be attainable at room temperature. However, alternative approaches must be devised to solubilise the precursor salts in a non-polar solvent, and to quench nanocrystal growth, both of which typically rely on temperature manipulation.

5.3.1.2 Precursor Formulation

5.3.1.2.1 The Cesium-containing Precursor

For hot-injection syntheses, as used in the earlier Chapters, the cesium precursors are usually cesium carboxylate salts dissolved in non-polar solvents with the aid of carboxylic acid ligands. Cesium carbonate is the most common salt used, often dissolved with a longer chain carboxylic acid, such as oleic acid, to form cesium oleate. Cesium oleate dissolves in the non-polar solvent above 100 °C. To circumvent the need for elevated temperatures, cesium carbonate was dissolved in a carboxylic acid directly.

Octanoic acid (OctAc) was selected instead of oleic acid (OA). The most important reason for this was that the shorter ligand should be more conducive to electronic device fabrication. The same reasoning was applied during the ligand exchange process in Chapter 3, where oleic acid was replaced with octylphosphonic acid. A secondary reason was that OctAc is less oily and viscous than OA, and consequently, it should be easier to swiftly inject a well-defined volume. The same resulting cesium octanoate precursor has previously been employed to synthesise $CsPbBr_3$ NCs at room temperature, leading to highly efficient $CsPbBr_3$ light-emitting diodes.[100] However, no nanocrystal size control was exhibited.

Ideally, a phosphonic acid would have been used instead, but short-chain phosphonic acids are not liquids at room temperatures. Diisooctylphosphinic acid is a liquid and was considered, but it was found to be very viscous and could not dissolve Cs_2CO_3 at the desired concentration (0.2 M).

5.3.1.2.2 The Lead Bromide Precursor

The standard hot-injection synthesis relies on primary alkylamine ligands to solubilise lead bromide in a non-polar solvent. However, the presence of amines has been widely established as problematic. Firstly, alkylamines are commonly used as an acid-base pair with carboxylic acids. As discussed at length earlier, their weak dynamic binding promotes ligand desorption during antisolvent purification.[149] Secondly, primary amines have been shown to facilitate Ostwald ripening, due to their capability to stabilise $PbBr_2$ extracted from the NC.[158] They have also been shown to aid the conversion of $CsPbBr_3$ to Cs_4PbBr_6 for the same reason.

An alternative to alkylamines for the dissolution of $PbBr_2$ was TOPO. TOPO has been used previously for high-temperature syntheses. Used in coordination with an acid, strongly acidic conditions can be employed without leading to anisotropic growth. The acidic conditions prevent Ostwald ripening because the hydrogen bonding of the acidic species to TOPO prevents $PbBr_2$ extraction.[131] The avoidance of Ostwald ripening was crucial to the goal of a size tuneability; therefore, TOPO was selected.

Rather than the ODE solvent typically employed during hot-injection syntheses, toluene was selected as the non-polar reaction solvent. For room temperature synthesis, it was unnecessary to use an oily, viscous reaction medium. Toluene was selected over alkane solvents because TOPO is known to be more soluble in toluene.

Initially, $PbBr_2$ was added to toluene, such that full dissolution would give a concentration of 0.1 M. TOPO was added gradually with stirring to observe any effect on solubility. However, even when

the concentration of TOPO reached 2 M, significant quantities of undissolved $PbBr_2$ remained. The same experiment was conducted at 80 °C; it was observed that a TOPO concentration of 1 M enabled full dissolution of $PbBr_2$.The dissolution was highly endothermic, with the vial becoming colder to the touch. Predictably, heating the solution of $PbBr_2$ and TOPO (molar ratio = 1:10) in toluene to 80 °C led to complete dissolution within 10 min.

It has previously been hypothesised that TOPO complexes $PbBr_2$ similarly to carbonyl groups, such that fluorescence was observed. Although no fluorescence was observed in the solution here, evaporation of the solvent yielded a white waxy solid with strong orange fluorescence under UV light. The material remained fluorescent after melting above 50 °C. Both the solid and molten fluorescent $PbBr_2$–TOPO are shown in Figure 5.1. This interesting observation was strong evidence of an interaction between the phosphonyl (P=O) group of TOPO and the Lewis acidic Pb^{2+}, whereby the three octyl groups of TOPO solubilised the complex in the non-polar medium. The solution formed by dissolving $PbBr_2$ and TOPO together in toluene was henceforth referred to as the $PbBr_2$ precursor solution.

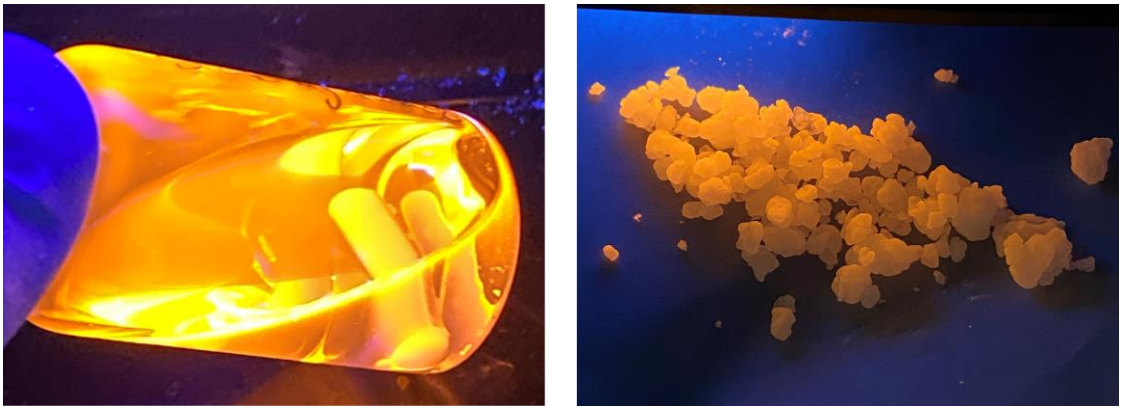

Figure 5.1 **Photographs of molten (left) and solid (right) samples of a $PbBr_2$–TOPO complex**

5.3.1.3 Ligand Selection

5.3.1.3.1 Octylphosphonic Acid

In Chapter 3, it was demonstrated that octylphosphonate ligands bound strongly to $CsPbBr_3$ nanocrystals. Also, they assembled into an inter-ligand hydrogen-bonded network on the nanocrystal surface. Based on these promising results, octylphosphonic acid was also employed in the room temperature synthesis.

It was found that OPA dissolved completely in the $PbBr_2$ precursor solution at concentrations > 1 M. This was much higher than the solubility limit of OPA in pure toluene, which was around 0.1 M. OPA can be expected to hydrogen bond with the phosphonyl group of TOPO, thus increasing its solubility dramatically. However, for OPA concentrations ([OPA]) greater than 0.6 M, white powder

began to appear a few minutes after dissolution. This was identified as $PbBr_2$, which precipitated out of solution as OPA competed for interaction with the phosphonyl group. Thus, the accessible range of [OPA] was identified as 0 to 0.6 M.

5.3.1.3.2 Didodecyldimethylammonium Bromide

It was hypothesised in Chapter 4 that the retention of oleylammonium ligands through ligand exchange and purification was essential to the colloidal stability of the nanocrystals. It was expected that the short OPA ligands alone could not have stabilised the 10 nm particles at sufficiently high concentrations for LED fabrication. Thus, for the room temperature synthesis, a second ligand was also sought.

Besides the original oleic acid and oleylamine ligand pair, a survey of the literature reveals didodecyldimethylammonium bromide (DDAB) to be the most ubiquitous ligand for $CsPbBr_3$ nanocrystals. As a quaternary ammonium salt, DDAB does not have any labile protons to exchange with acidic species in the reaction mixture. This suppresses the ligand binding equilibrium mechanism which destabilises primary amine ligands. The bulk of two dodecyl groups on DDAB have been shown to provide good colloidal stability, despite each chain being considerably shorter than oleyl ligands. Moreover, the bromide counterions of DDAB can passivate surface halide vacancies, enhancing the PLQY.

Considering these many favourable properties of DDAB, it was clear why it has proven so popular in the literature. It is common practice for DDAB to be employed post-synthetically, most often after initially synthesising the NCs with oleic acid and oleylamine,[128] analogous to the approach used in Chapter 3 and Chapter 4. Rather than first isolating the nanocrystals, the room temperature protocol pioneered by the group of Haibo Zeng, involving adding DDAB to the crude reaction mixture after a few minutes.[100] This was slightly more appealing because antisolvent addition, centrifugation or redispersion, could all cause the concentration of nanocrystals to vary from batch to batch; therefore, performing ligand treatment before any of these steps should result in a more reproducible process. Accordingly, DDAB was adopted in addition to OPA; it was added to the crude solution after first nucleating and growing the nanocrystals in the presence of OPA and TOPO.

5.3.1.4 Synthesis Details

There are many specifics of the synthesis protocol that can have a large influence on the resulting nanocrystals. The initial parameters were set by consulting similar approaches in the literature. Syntheses of $CsPbBr_3$ nanocrystals where the cesium source is a cesium carboxylate rather than

cesium halide are typically conducted under Cs-deficient/$PbBr_2$-rich conditions. Ensuring an excess of halide ions is important to suppress the formation of halide vacancies, which have been confirmed as the primary cause of PLQY degradation. Furthermore, the Cs-deficiency suppresses the competing formation of electronically zero-dimensional Cs_4PbBr_6, a common phase impurity in $CsPbBr_3$.

Specifically, regarding the use of DDAB, Cs-deficiency was useful because it promoted the formation of surface Cs vacancies. Thus, in addition to competing to substitute Cs^+ from surface sites, there will be numerous vacancies for DDA^+ to fill, thus improving the density of DDA^+ ligands on the surface and, consequently, the colloidal stability of the nanocrystals. The binding of more DDA^+ should concurrently introduce more bromide ions, ensuring higher PLQY.

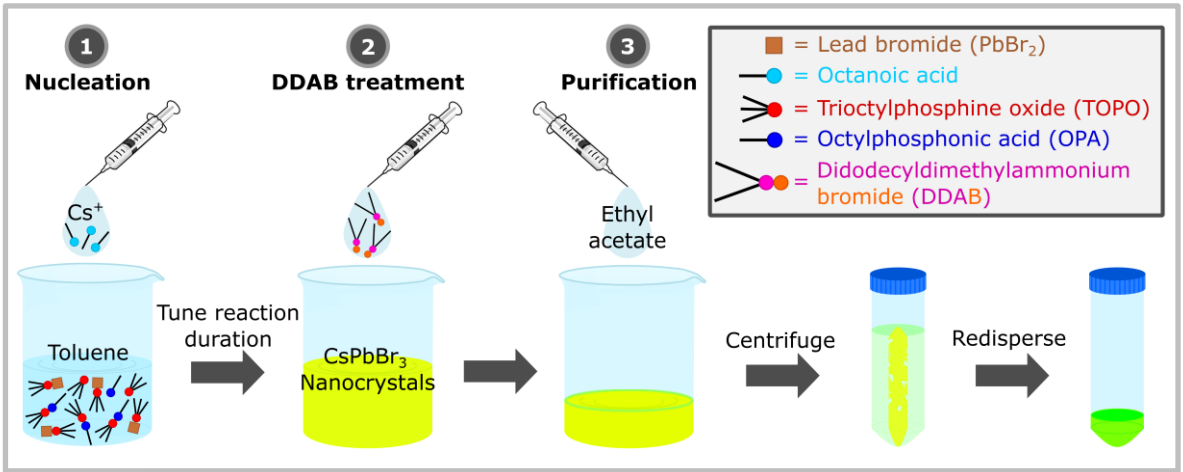

Figure 5.2 **An overview of the devised room temperature $CsPbBr_3$ nanocrystal synthesis method**

Based on the above reasoning, a Cs:$PbBr_2$ ratio of 1:4.14 was employed. The concentration of Cs and $PbBr_2$ in the precursors were 0.2 M and 0.09 M, respectively. These concentrations were at the upper end of the solubility limits to maintain a high nanocrystal concentration in the crude solution, thus promoting a high degree of supersaturation upon Cs precursor injection. Importantly, the $PbBr_2$ concentration was calculated by considering TOPO as a solvent. The volume of the solution increased by 64 % when the appropriate mass of TOPO was added to dissolve $PbBr_2$. A standard small scale synthesis was adopted for method development and optimisation experiments: 55 µL Cs precursor was injected into 500 µL $PbBr_2$ precursor (Cs:$PbBr_2$ = 1:9 v/v). An overview of the synthesis scheme adopted was presented in Figure 5.2.

5.3.2 Initial Synthesis Trial

5.3.2.1 Without Post-Synthetic DDAB Treatment

The room temperature synthesis was first tested using the following precursors: Cs_2CO_3 in octanoic acid (0.2 M) and $PbBr_2$ (0.091 M). A high concentration of OPA was used (0.4 M). The injection of the Cs precursor into an open vial of stirring $PbBr_2$–OPA solution caused the solution to immediately become a bright green-yellow colour (Figure 5.3). After 300 s, the absorbance and photoluminescence spectra of the crude nanocrystal solution was measured.

Figure 5.3 shows that the sample exhibited a PL peak centred around 509 nm with an FWHM of 20 nm, characteristic of $CsPbBr_3$ NCs. The gradual onset of absorption between 600 nm and 520 nm suggested that the crude solution contained a fraction of large, agglomerated nanocrystals. This was expected, typically this fraction can be easily removed by centrifugation.

The nanocrystals were precipitated from the crude solution by centrifugation with ethyl acetate and redispersed in fresh toluene. However, redispersion was difficult and produced a very turbid solution, from which the NCs swiftly precipitated. This confirmed that octylphosphonic acid alone could not stably disperse the $CsPbBr_3$ NCs.

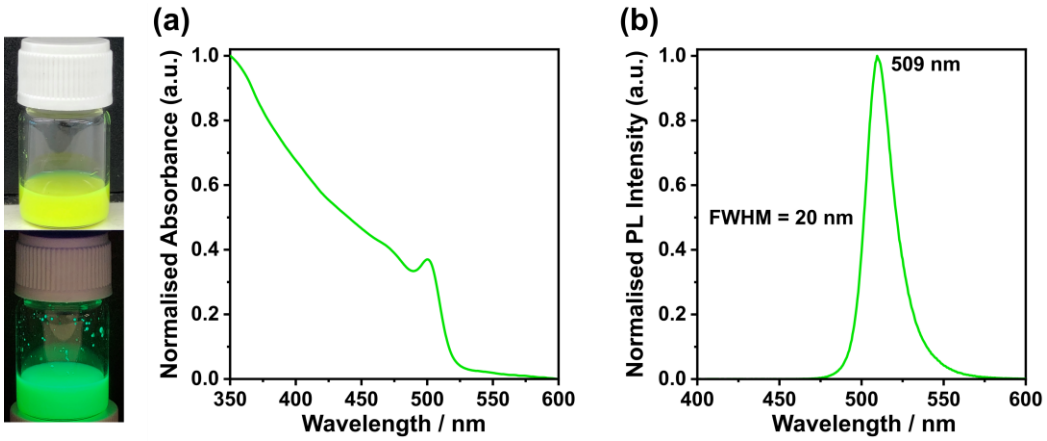

Figure 5.3 **Optical properties of the crude $CsPbBr_3$ nanocrystal solution obtained from the first trial synthesis at room temperature**

(a) Optical absorption and (b) photoluminescence spectra, with photographs of the nanocrystal solution under visible and UV light shown alongside

5.3.2.2 With Post-Synthetic DDAB Treatment

The room temperature synthesis was repeated, except with the inclusion of a DDAB treatment step. The same synthesis parameters were followed again, with [OPA] = 0.4 M. The DDAB solution was

added 300 s after the Cs^+ precursor then precipitated by centrifugation with ethyl acetate after another 300 s to precipitate the NCs. Notably, and in contrast to the nanocrystals synthesised without DDAB treatment, the supernatant retained bright luminescence, even though they were precipitated with antisolvent. Furthermore, after redispersing the precipitate, a significant fraction of the nanocrystals remained stably dispersed in the supernatant after a further slow speed centrifugation step. The absorbance and photoluminescence spectra of the resulting nanocrystal ink were presented in Figure 5.4.

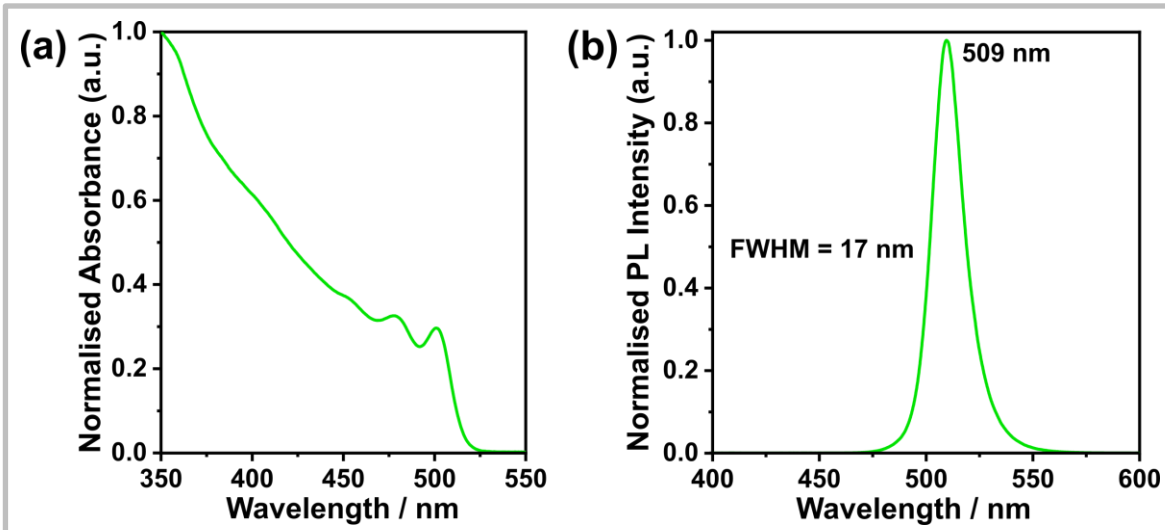

Figure 5.4 **Optical properties of the isolated $CsPbBr_3$ nanocrystal dispersion synthesised with [OPA] = 0.4 M and post-synthetic DDAB treatment**

(a) Optical absorption spectrum, and (b) photoluminescence spectrum.

The photoluminescence peak was distinctly narrower than that of the nanocrystals synthesised with only OPA (Figure 5.3). This may simply be attributable to the removal of larger nanocrystals by the purification cycle, as suggested by the sharper absorption onset. However, the peak position did not change. This suggested that a fraction of smaller nanocrystals must also have been removed in the first supernatant. The full-width half-maximum of 17 nm obtained compared well with the state-of-the-art $CsPbBr_3$ nanocrystal syntheses.

To assess the efficacy of ligand passivation, the photoluminescence quantum yield was measured. The DDAB-treated $CsPbBr_3$ nanocrystal exhibited PLQY = 89 %. This validated that the devised synthesis method could achieve excellent optoelectronic properties without elevated temperatures. The next step was to address the potential tuneability of the nanocrystal size.

5.3.2.3 Basic Nanocrystal Characterisation

5.3.2.3.1 X-ray Diffraction

Before developing the synthesis method further, it was pertinent to analyse the crystal structure of the $CsPbBr_3$ nanocrystals synthesised with OPA and DDAB ligands. The X-ray diffraction pattern for a drop-cast $CsPbBr_3$ nanocrystal thin-film was shown in Figure 5.5. The pattern matched well with the calculated reflections of bulk orthorhombic $CsPbBr_3$, with the broadened peaks indicative of the nanocrystalline domains. The orthorhombic structure is thermodynamically favoured for $CsPbBr_3$ nanocrystals synthesised at room temperature.[78] The lack of any peak around 12 ° suggested that the Cs_4PbBr_6 phase was not present. The zero-dimensional structure has often been observed alongside the three-dimensional perovskite phase.[181,182] However, it was likely that the Cs deficient reaction conditions here suppressed its formation.

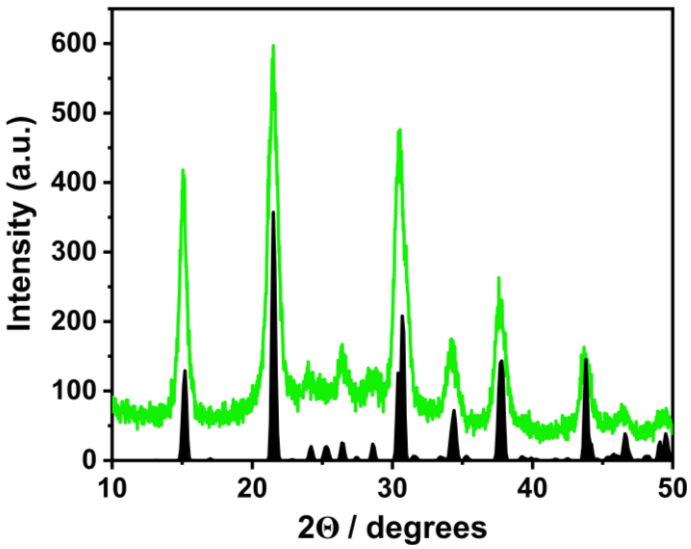

Figure 5.5 **X-ray diffraction pattern measured for a thin-film of $CsPbBr_3$ nanocrystals**

The calculated bulk X-ray reflections of orthorhombic $CsPbBr_3$ (space group: Pnma, ICSD number: 98751) were shown underneath for comparison (black peaks)

5.3.3 Investigation of Size Tuneability

5.3.3.1 Theoretical Hypothesis

In the introduction of this work (Chapter 1.3.3), the nucleation of colloidal nanocrystals was discussed. The following equation was provided to describe the influence of various parameters on the critical radius (r_c):

Equation 5.2

$$r_c = \frac{2\gamma V_m}{N_A k_B T \ln S}$$

Considering this equation in the context of room temperature $CsPbBr_3$ nanocrystal synthesis, Avogadro's number, N_A, the Boltzmann constant, k_B, molar volume, V_m, and temperature, T, should all be constant. Thus, it can be stated that $r_c \propto \frac{\gamma}{\ln S}$; in other words, the initial diameter of nuclei in the nanocrystal synthesis can be controlled by the surface energy and the supersaturation of the monomers in the reaction mixture.

Before any hypotheses were presented about how the synthesis parameters related to the surface energy or supersaturation, the proposed reaction mechanism must be described in more detail. Almeida et al. have previously investigated the synthesis of nanocrystals from $PbBr_2$ solubilised by TOPO.[131] They assert that nucleation was initiated by the competition between octanoic acid and $PbBr_2$ for the lone electron pair on TOPO when the cesium precursor was injected. This is a similar effect to the precipitation of $PbBr_2$ observed earlier when [OPA] was increased above 0.6 M. However, with the cesium source present, the release of $PbBr_2$ from TOPO coordination induced a rapid reaction with Cs(oleate), nucleating $CsPbBr_3$ nanocrystals. The quantity of $PbBr_2$ released by the injection of OctAc should depend on the concentration of OctAc and any other species in the solution which engage in competing interactions with TOPO, and the concentration of TOPO itself. Based on this, the concentration of OPA should modulate the release of $PbBr_2$ where [OctAc] and [TOPO] are constant.

Equation 5.3 shows that supersaturation can be expressed as the ratio between the concentration of monomers, *[M]*, and the equilibrium concentration of monomers, $[M]_0$, where S > 1 is the condition for supersaturation.

Equation 5.3

$$S = \frac{[M]}{[M]_0}$$

The release of $PbBr_2$ from TOPO can be considered a decrease of $[M]_0$; where $[M]_0$ essentially represents the solubility of $PbBr_2$, which reduced dramatically once it was no longer coordinated by TOPO. Therefore, [OPA] should essentially control supersaturation, with an increase of [OPA] resulting in smaller stable nuclei, according to Equation 5.2.

OPA should also have a significant impact on the other crucial variable, the surface energy of the nucleating nanocrystals. The increase of the total ligand concentration with increasing [OPA] should decrease the surface energy. The stronger binding of OPA to $CsPbBr_3$ in comparison with carboxylic acids could also be expected to decrease the surface energy even further. Referring to Equation 5.2 again, it was deduced that the decreasing surface energy with increasing [OPA] also correlated with a decreasing critical radius. Therefore, the theoretical analysis strongly suggested that the diameter of $CsPbBr_3$ nanocrystal nuclei may be tuned by adjusting [OPA].

5.3.3.2 Establishing a Growth Quenching Mechanism

It is important to emphasise that establishing control over the initial nuclei diameter does not guarantee good control over the diameter of the nanocrystals obtained. If nanocrystal growth occurs very quickly, the size of the nanocrystals will be influenced significantly by the growth rate. In any case, a mechanism to quench nanocrystal growth must be imposed.

Hot-injection syntheses exploit temperature to quench nanocrystal growth, cooling the reaction vessel in an ice bath to immediately reduce the temperature by more than 150 °C. This mechanism is not viable for a room temperature synthesis. One option commonly employed is quenching by precipitating the nanocrystals, either by adding a polar antisolvent or by centrifugation. These would both be less than ideal; the nanocrystal would be prone to agglomeration upon antisolvent addition and centrifugation does not impose a well-defined reaction duration, owing to the necessity to transfer the crude solution to a centrifuge tube first.

Conveniently, upon further investigation, it was apparent that DDAB essentially quenched nanocrystal growth. Multiple syntheses were conducted with different time intervals between the injection of the Cs precursor and the addition of DDAB. In all cases, the ethyl acetate antisolvent was added 600 s after the Cs precursor. No OPA was added (i.e. [OPA] = 0 M), to rule out any role of OPA in growth quenching. Figure 5.6 shows that the peak photoluminescence wavelength increased incrementally from 514.6 nm to 516 nm with increasing growth duration before DDAB addition. This suggested that NC growth ceased after DDA^+ ligands bound to the surface. Presumably, the steric bulk of the two dodecyl groups of DDA^+ hindered the reaction of further monomers on the NC surface. There was also a decrease of PLQY from 79 % to 66 %, but the full-

width half-maximum reduced from 18.2 nm to 17.1 nm. This suggested that, as anticipated, there was no significant size defocusing due to Ostwald ripening.

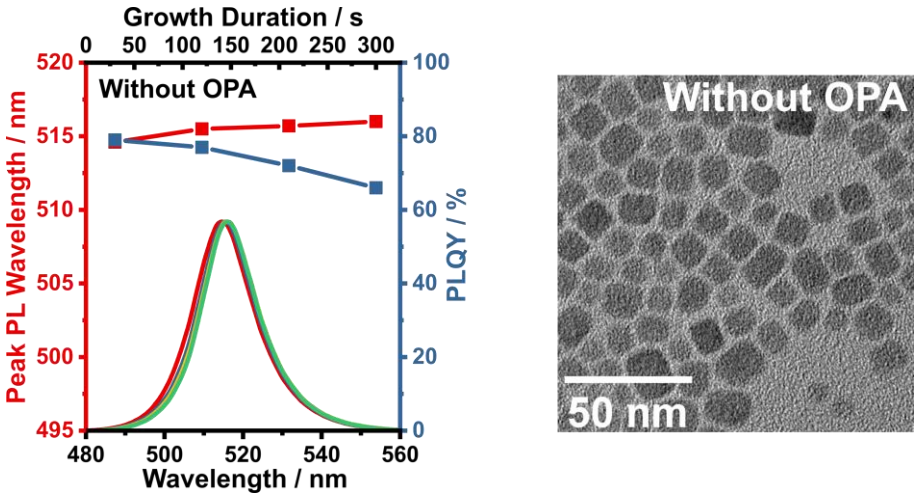

Figure 5.6 **Characterisation of room temperature synthesised $CsPbBr_3$ nanocrystals synthesised without OPA**

Peak photoluminescence wavelength and PLQY with different growth durations before DDAB addition (left), and TEM image of the nanocrystal sample after 300 s growth duration (right)

The increase in the PL peak wavelength was very slight, but for $CsPbBr_3$, emission centred around 515 nm was expected to correspond to relatively large nanocrystals, such that the diameter was substantially above the Bohr exciton diameter (around 7 nm). The TEM image in Figure 5.6 confirmed this, showing that the nanocrystals had a mean edge length of 12.2 ± 1.9 nm. The large standard deviation indicated a broad size distribution of the nanocrystals and they appeared to have irregular rounded cuboidal shapes. This may be an indication of poor ligand control over the nanocrystal growth with OPA.

Having established a mechanism for nanocrystal growth quenching, the growth mechanism could be systematically studied. To ascertain the relative influence of nucleation and growth phases on the nanocrystal size tuneability, multiple syntheses were conducted with various [OPA].

5.3.3.3 Influence of [OPA] on Nanocrystal Diameter

5.3.3.3.1 Effect of [OPA] with Constant Growth Duration

In Section 5.3.1.2, it was observed that a maximum [OPA] of 0.6 M could be added without inducing $PbBr_2$ precipitation. Accordingly, the impact of [OPA] on the size of $CsPbBr_3$ nanocrystals was assessed for 0 M ≤ [OPA] ≤ 0.6 M. For all syntheses, the growth duration was fixed at 300 s. Figure 5.7 showed the peak photoluminescence wavelength red-shifted gradually from 516 nm and 506

nm as [OPA] increased. This matched the expectation outlined in the previous section. The same figure demonstrated that PLQY was maintained above 80 % for all [OPA]. The sharp increase in PLQY from 0 M to 0.1 M OPA correlated with the results of the previous chapters that, as a softer and stronger acid than carboxylic acids, OPA can passivate under-coordinated Pb^{2+} more effectively.[113,114]

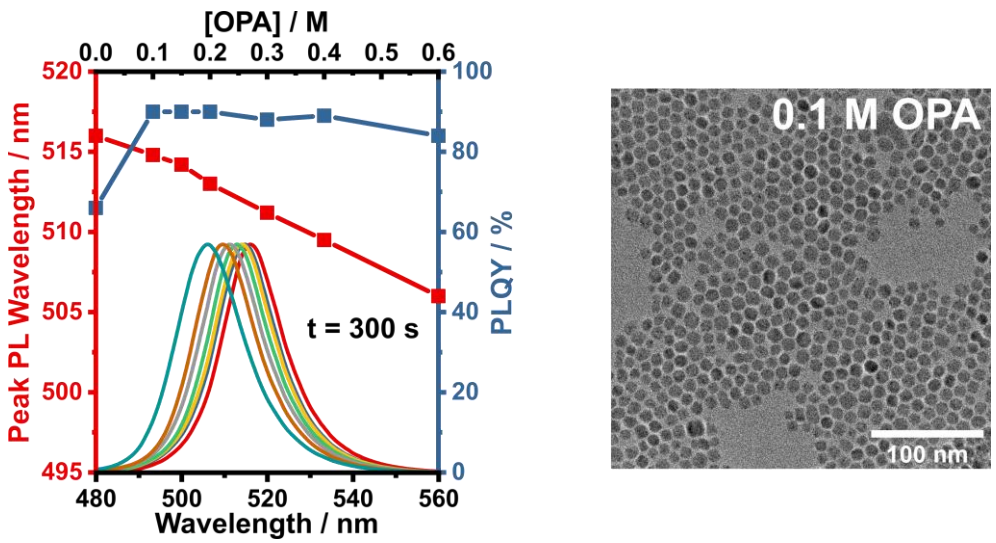

Figure 5.7 **Characterisation of room temperature synthesised $CsPbBr_3$ nanocrystals synthesised various concentrations of OPA**

Peak photoluminescence wavelength and PLQY with different [OPA] (left), and TEM image of the nanocrystal sample prepared with 0.1 M OPA (right)

The TEM image in Figure 5.7 shows that when 0.1 M OPA was used, the nanocrystals exhibited much better size regularity than without OPA. Improved shape regularity was also observed, as demonstrated by extensive hexagonal superlattice formed on the TEM grid, with 2D shapes varying between hexagonal and almost circular. The shape variation was understood by referring to a previous study on $CsPbBr_3$ NCs synthesised with phosphonic acid ligands at elevated temperature. They observed similarly shaped particles, which they identified as truncated octahedrons.[142] Truncated octahedrons have five distinct orthogonal projections, with apparent shapes ranging between hexagonal and pseudo-circular, as depicted in Figure 5.8.[183]

The TEM images for all different [OPA] concentrations employed are presented in Figure 5.9, while the corresponding histograms are found in Figure A4. The measured mean nanocrystal diameter decreased from 10.8 nm to 5.8 nm as [OPA] increased from 0.1 M to 0.6 M. This correlated well with the red-shifting of the PL peak in Figure 5.7. It should be noted that below an emission wavelength of around 510 nm, the diameter of the nanocrystals was expected to approach the Bohr

exciton diameter; in this strong quantum confinement regime, the bandgap is more sensitive to changes in nanocrystal diameter.

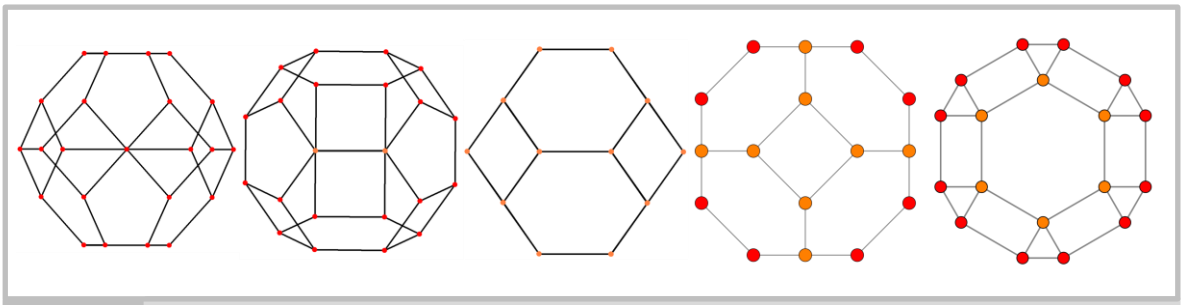

Figure 5.8 **The five orthogonal projections of a truncated octahedron**[183]

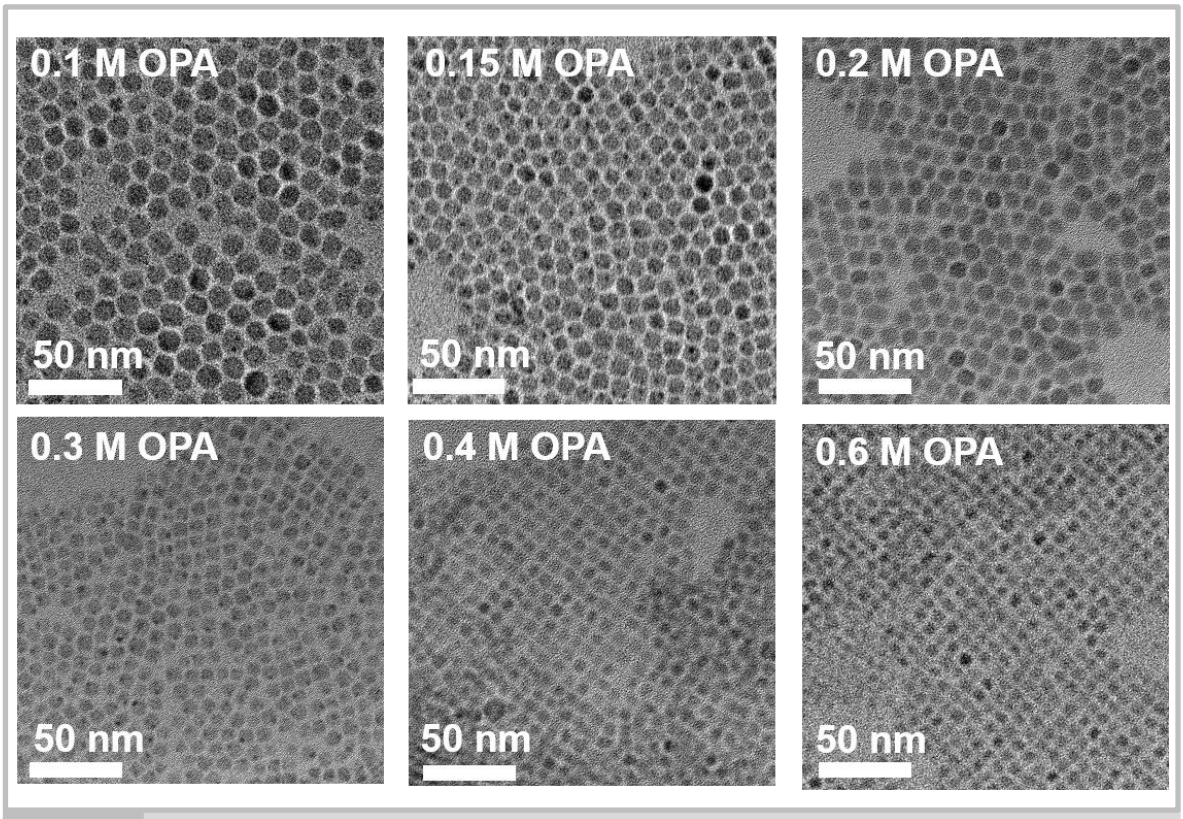

Figure 5.9 **Transmission Electron Microscope images of $CsPbBr_3$ nanocrystals synthesised at room temperature with various [OPA]**

Small-angle X-ray scattering (SAXS) provided an alternative method to measure the nanocrystal diameter, with much larger sample sizes, lower standard deviation, and no potential for observer bias.[184] SAXS data was fitted using a Monte Carlo approach developed by Bressler et al.,[157] which produced histograms of the nanocrystal size distributions for NCs synthesis by all [OPA], shown in Figure 5.10. The mean nanocrystal diameter decreased from 10.4 nm to 7.4 nm as [OPA] increased from 0.1 M to 0.6 M. It should be recognised that the fitting gave a volume-weighted size distribution, in contrast to the number-weighted distribution obtained from TEM. As a result, the mean diameters were slightly larger, particularly for the smaller NCs. This may also have reflected the difficulty of accurately identifying the edges of small NCs in the TEM images due to the poor

resolution. Regardless, the SAXS data exhibited the same trend as TEM, corroborating with the hypothesis that [OPA] can control the nanocrystal diameter. This was further supported by the narrowing of the nanocrystal size distribution with increasing [OPA].

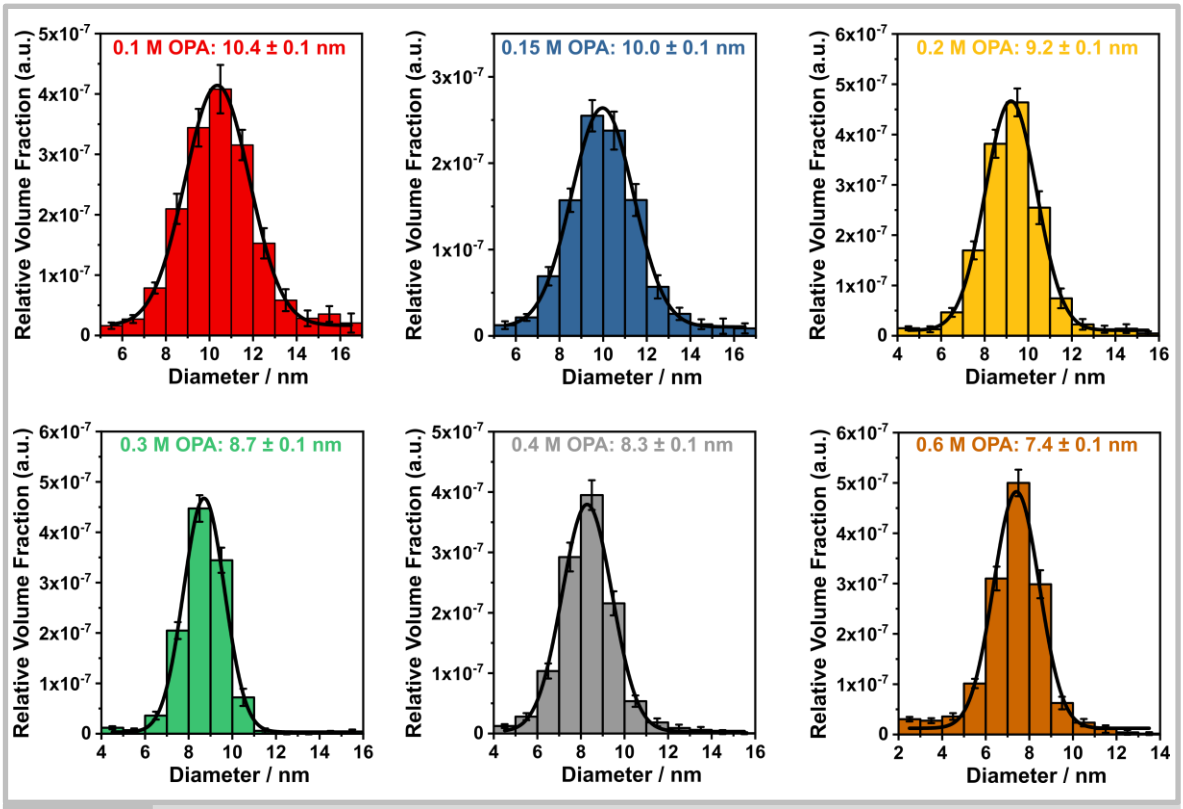

Figure 5.10 **Nanocrystal size distributions extracted from small-angle X-ray scattering measurements performed on $CsPbBr_3$ nanocrystal dispersions synthesised with different [OPA]**

The growth duration for all samples was 300 s. The mean nanocrystal diameter and the corresponding standard deviation are shown on each plot.

5.3.3.4 Comparison of [OPA] Effect for Different Growth Durations

The tuneability of the NC diameter with [OPA] for a fixed reaction duration suggested that OPA exerted control over the synthesis. However, it was not clear whether this control originated from modulation of the critical radius, as discussed in section 5.3.3.1, or of the growth rate. To investigate this, the extent of growth with different [OPA] was directly assessed by comparing the nanocrystal diameter at the earliest stages of growth was compared with the final nanocrystal diameter after 300 s.

5.3.3.4.1 Post-Nucleation Analysis

The DDAB quenching mechanism provided good control over the growth duration. However, for short growth durations, there was likely to be a large percentage error due to the necessity to add the DDAB solution manually, swiftly after injecting the Cs precursor. Therefore, it was first examined whether it was necessary to quench almost immediately after nucleation, or a relatively short, but more precise and reproducible, growth duration would suffice.

Figure 5.11 shows the absorbance and photoluminescence spectra, respectively, of $CsPbBr_3$ nanocrystals prepared with 0.3 M OPA, quenched after 5 s and 30 s. Importantly, there was no discernible change in the photoluminescence peak wavelength between 5 s and 30 s. [OPA] = 0.3 M was selected as it provided small nanocrystals, such that a small change in the diameter would be reflected by an obvious shifting of the PL peak. Therefore, it can be concluded that negligible growth occurred over the first 30 s.

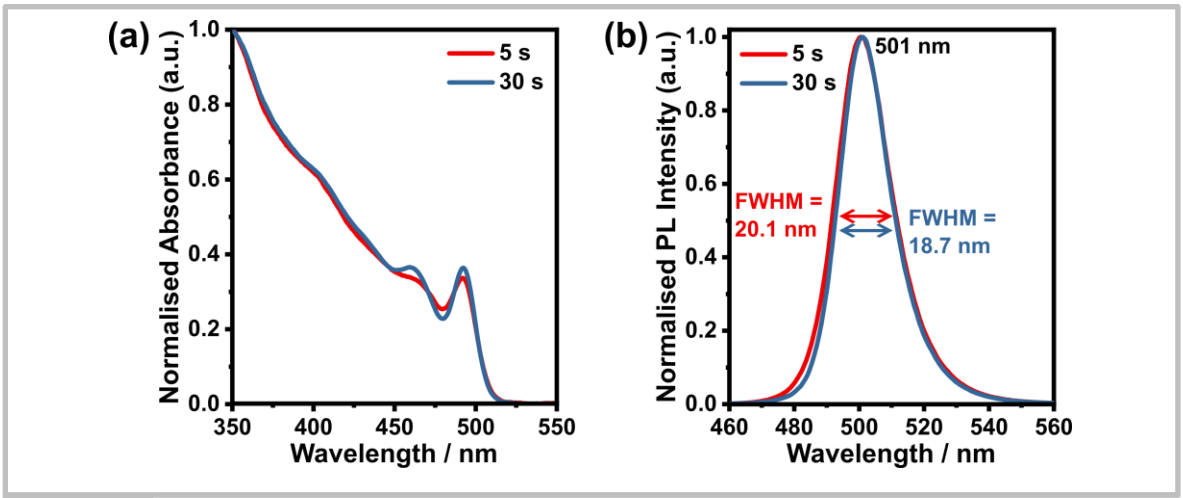

Figure 5.11 **Optical characterisation of $CsPbBr_3$ nanocrystals synthesised with 0.3 M OPA for growth duration of 5 s or 30 s**

(a) Absorbance spectrum, and (b) photoluminescence spectrum with peak wavelength and FWHM shown for each.

Intriguingly, there was a narrowing of the PL FWHM from 20.1 nm to 18.7 nm. This was accompanied by the enhancement of the peaks in the absorbance spectrum. A potential explanation for this observation was a change in the surface ligand composition. The peak at the onset of the absorbance spectrum has been shown to correspond to an excitonic transition - the excitation of electrons at the valence band maximum to a state formed by the interaction between a bound electron-hole pair (i.e. an exciton). Excitonic states are located just below the conduction band minimum, thus excitonic absorption occurs at an energy slightly less than the bandgap. Stronger binding ligands, such as OPA, can enhance quantum confinement effects, such that the strength of the excitonic absorption increases. Thus, the more prominent excitonic feature

observed may indicate that more OPA ligands attached to the NC surface over the first 30 s before nucleation. Enhanced quantum confinement may also explain the narrowing of PL peak, due to increased energy funnelling from smaller to larger nanocrystals (i.e. high to low bandgap).[85] These hypotheses will be revisited and explored in more detail later.

5.3.3.4.2 Growth Rate Comparison

To assess the extent of nanocrystal growth with different [OPA], the diameter of nanocrystals whose growth was quenched by DDAB 30 s after injection of Cs precursor was considered the initial nucleus diameter. Accordingly, $CsPbBr_3$ nanocrystals were synthesised with [OPA] ranging from 0 M to 0.6 M for 30 s growth durations. Figure 5.12 plots the mean nanocrystal diameter against [OPA], with the corresponding data points for 300 s growth duration shown on the same graph for convenient comparison.

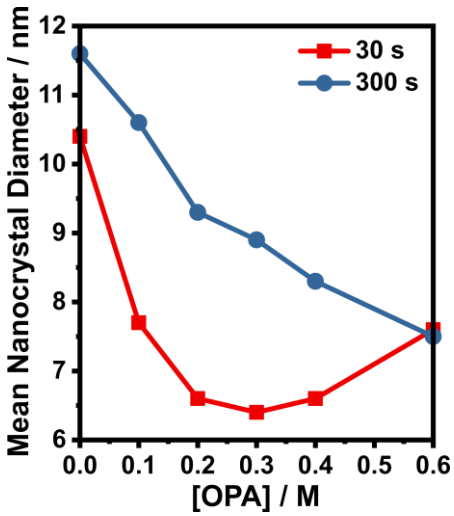

Figure 5.12 **The diameter of $CsPbBr_3$ nanocrystals synthesised with various [OPA] for 30 s or 300 s growth durations**

The difference between the mean NC diameter after 30 s and 300 s decreased with increasing [OPA], indicating that the growth rate reduced. This suggested that the rate-determining step for the growth of the nanocrystals was the surface reaction, rather than the diffusion rate of monomers to the surface. Given the efficacy of growth quenching with DDAB ligands, this was unsurprising. In fact, for [OPA] = 0.6 M, it appeared that growth was quenched even before DDAB addition, as the nanocrystal diameter was very similar after 30 s and 300 s. This provided strong evidence that [OPA] mediated the NC growth rate.

Unexpectedly, the trend across different [OPA] for NCs with 30 s growth duration did not entirely match that of the 300 s reactions. The diameter decreased from 10.4 nm to 6.4 nm as [OPA]

increased from 0 M to 0.3 M, however, the diameter increased again above 0.3 M, reaching to 7.6 nm at 0.6 M. This represented an inversion of the trend around [OPA] = 0.3 M. The contrasting trends of the 30 s and 300 s reactions suggested that [OPA] influenced the nucleation and growth phases differently.

The decrease of the initial nanocrystal diameter between 0 M and 0.3 M [OPA] correlated well with the theoretical hypothesis for the critical radius discussed earlier; OPA can reduce surface energy through binding and increase the supersaturation by competing with $PbBr_2$ for TOPO coordination. The inversion of the trend above 0.3 M must originate from further interactions that have not yet been considered.

5.3.3.4.3 Analysis of Reaction Equilibria

In search of interactions that may explain the increased initial nanocrystal diameter, the expected equilibria present in the reaction mixture were analysed. Firstly, the equilibria which existed before Cs precursor injection were deduced to be:

Equilibrium 5.1

$$\boldsymbol{R'PO(OH)_2 + R'_3PO \rightleftharpoons R'PO(OH)_2 \bullet OPR'_3}$$

Equilibrium 5.2

$$\boldsymbol{PbBr_2 + R'_3PO \rightleftharpoons R'_3PO \bullet PbBr_2}$$

Where R' are octyl groups ($-(CH_2)_7CH_3$). These equilibria illustrated the hypothesis proposed earlier that an increasing concentration of OPA ($R'PO(OH)_2$) would increase the hydrogen bonding to TOPO (OPR'_3) (Equilibrium 5.1 moves to the right), releasing more $PbBr_2$ (Equilibrium 5.2 moves to the left). Thus, supersaturation would increase, reducing the critical radius.

When the Cs precursor was added, the further competing equilibria were expected to be introduced:

Equilibrium 5.3

$$\boldsymbol{RCOOH + R'_3PO \rightleftharpoons R'_3PO \bullet CH_3(CH_2)_6COOH}$$

Equilibrium 5.4

$$\boldsymbol{RCOOH + R'_3PO \bullet PbBr_2 \rightleftharpoons R'_3PO \bullet RCOOH + PbBr_2}$$

Equilibrium 5.5

$$\boldsymbol{R'PO(OH)_2 + Cs(RCOO) \rightleftharpoons Cs(R'PO_2OH) + RCOOH}$$

where R = $–(CH_2)_6CH_3$ Equilibrium 5.3 and Equilibrium 5.4 merely indicated an extension of the mechanism illustrated by Equilibrium 5.1 and Equilibrium 5.2; OctAc (RCOOH) must compete with OPA and $PbBr_2$ for TOPO coordination. As OPA is the most acidic of the three species, increased [OPA] would lead to the same [OctAc] releasing a more $PbBr_2$.

It was, therefore, left to Equilibrium 5.5 to rationalise the increasing NC diameter from 0.3 M to 0.6 M OPA. As OPA is a stronger acid than OctAc, the equilibrium should lean towards the right when [OPA] ≈ [OctAc]. Octanoic acid was injected at a 1:9 v/v ratio to the $PbBr_2$ solution, so given the density (ρ) and molar mass (M) of OctAc were 910 g L^{-1} and 144 g mol^{-1}, respectively, [OctAc] could be calculated:

Equation 5.4

$$[\boldsymbol{OctAc}] = \frac{\boldsymbol{V_{OctAc}}}{\boldsymbol{V_{total}}} \times \frac{\boldsymbol{\rho_{OctAc}}}{\boldsymbol{M_{OctAc}}} = \frac{\mathbf{1}}{\mathbf{10}} \times \frac{\mathbf{910}}{\mathbf{144}} = \mathbf{0.63}\ \boldsymbol{M}$$

Therefore, as [OPA] approached 0.6 M, [OPA] ≈ [OctAc]. This should have resulted in the production of a significant concentration of Cs(OPA), at least comparable to [Cs(OctAc)]. Crucially, OPA is a diacid, so Cs(OPA) still has one remaining hydroxyl group with an acidic proton. Thus, it was reasonable to assume that Cs(OPA) would form hydrogen bonds with TOPO, as shown in Equilibrium 5.6, which Cs(OctAc) cannot.

Equilibrium 5.6

$$\mathbf{Cs}(\boldsymbol{R'PO_2OH}) + \boldsymbol{R'_3PO} \rightleftharpoons \mathbf{Cs}(\boldsymbol{R'PO_2OH}) \bullet \boldsymbol{OPR'_3}$$

The significance of the interaction between Cs(OPA) and TOPO was its influence on the supersaturation. It was hypothesised that the hydrogen bonding to TOPO would dramatically increase the solubility of Cs(OPA), a monomer, thus increasing the equilibrium monomer concentration, $[M]_0$, and decreasing supersaturation. This provided a rational explanation for the increased critical radius observed for high [OPA]. The inversion observed at 0.3 M OPA was considered the threshold [OPA], where this effect became dominant over the competing mechanism discussed earlier. The dominance may be attributable supersaturation of Cs monomers exerting a greater influence over the nucleation dynamics because $PbBr_2$ was present in large excess.

5.3.3.5 Comparison of Octanoic Acid and Octylphosphonic Acid

To test the hypothesis that hydrogen bonding between Cs(OPA) and TOPO increased the critical radius at high [OPA], $CsPbBr_3$ nanocrystal synthesis with 30 s growth duration were conducted using

OctAc in the $PbBr_2$ precursor instead of OPA. The concentration of OctAc in the $PbBr_2$ precursor solution was referred to as $[OctAc]_{tol}$. The same range of concentrations were employed, but with fewer data points.

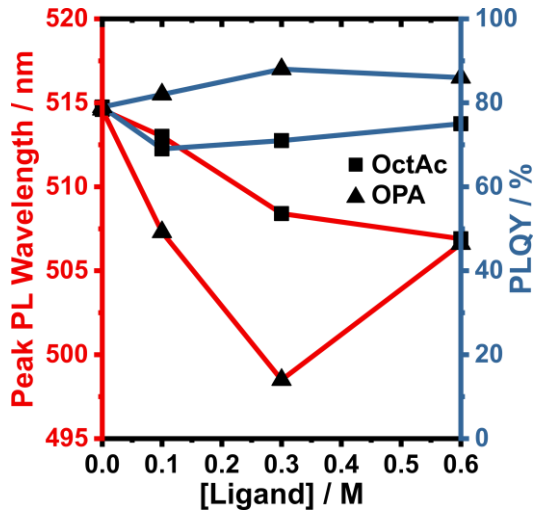

Figure 5.13 **A comparison of the effects of octanoic acid (OctAc) and octylphosphonic acid (OPA) ligand concentrations on the photoluminescence peak position and quantum yield**

For all samples, the growth duration was 30 s.

Figure 5.13 shows that for OctAc, the peak PL wavelength decreased steadily as $[OctAc]_{tol}$ was increased from 0 M and 0.6 M. There was no inversion of the trend, which supported the hypothesis that the inversion relied on the diacidity of OPA. The PL peak wavelength decreased less sharply with [OctAc]; this could be attributed to weaker interaction between OctAc and TOPO, such that increasing [OctAc] had less of an effect of solubility of $PbBr_2$ than increasing [OPA].

It was interesting to highlight similarities between the proposed implication here of the hydrogen bonding capability of Cs(OPA) monomers and a recent paper by Ashton et al.[185] They asserted that the hydrogen bonding between TOPO and the acidic proton on formamidinium in the FA(oleate) monomer disrupted their $FAPbBr_3$ nanocrystal synthesis. This emphasises the importance of understanding and manipulating the interactions between species in the reaction mixture, particularly where there are many species capable of hydrogen bonding.

The comparison of the optical properties of nanocrystals synthesised with either OctAc or OPA also had some interesting implications. In Figure 5.13, it was shown that the PLQY was consistently around 10 – 20 % lower with OctAc, varying from 65 – 75 %. Figure 5.14 shows that for nanocrystals of comparable size ([OctAc] = 0.4 M and [OPA] = 0.3 M), the first excitonic absorption peak was significantly more prominent. As explained earlier, this was likely indicative of enhanced quantum

confinement. This was further evidence that OPA was responsible for the prominent excitonic transitions.

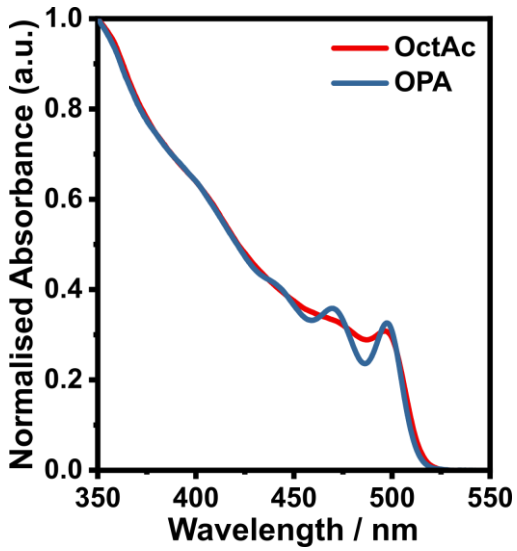

Figure 5.14 **The optical absorption spectra of $CsPbBr_3$ nanocrystals synthesised with OctAc (0.4 M) or OPA (0.3 M)**

For both samples, the growth duration was 300 s.

There were obvious similarities between the absorption spectra of the OctAc and OPA samples here, and the 0.3 M OPA 5 s and 30 s samples in Figure 5.11. Thus, it was hypothesised that when OPA was used, the initial post-nucleation phase (i.e. 0 – 30 s) was characterised by a surface ligand exchange of Cs(OctAc) for Cs(OPA). An implication of this was that the initial nuclei were mostly passivated by OctAc ligands. This helped to explain the shape differences observed in the TEM images of nanocrystals synthesised with different [OPA] (Figure 5.9). For high [OPA], there was minimal growth after nucleation, therefore the nanocrystals would retain the shape promoted by the OctAc ligands (i.e. cubic). For lower [OPA], significant growth would occur, governed by OPA ligands. Therefore, the shape of the final nanocrystals would be determined the crystal facets that OPA ligands promoted growth on (i.e. truncated octahedrons). The apparent mixture of cubic and hexagonal superlattice packing exhibited by the intermediate [OPA] = 0.3 M sample corroborated this.

5.3.3.6 Influence of Growth Duration on Nanocrystal Diameter

It was established that the nanocrystal diameter can be reliably controlled by the concentration of OPA in the $PbBr_2$ precursor. For a growth duration of 300 s, the viable range of [OPA] provided tuneability of the nanocrystal diameter between 11.6 nm and 7.5 nm (according to SAXS

measurement). This corresponded to photoluminescence peak wavelength range of 516 – 506 nm. While this represented good tuneability, the smaller nanocrystals obtained for a 30 s growth duration suggested that the accessible size range could be extended further by exploring temporal control.

For these experiments, [OPA] was fixed at 0.3 M, the concentration which yielded the smallest nanocrystal diameter for 30 s growth duration. This would be the minimum nanocrystal diameter attainable for the synthesis parameters defined in this work.

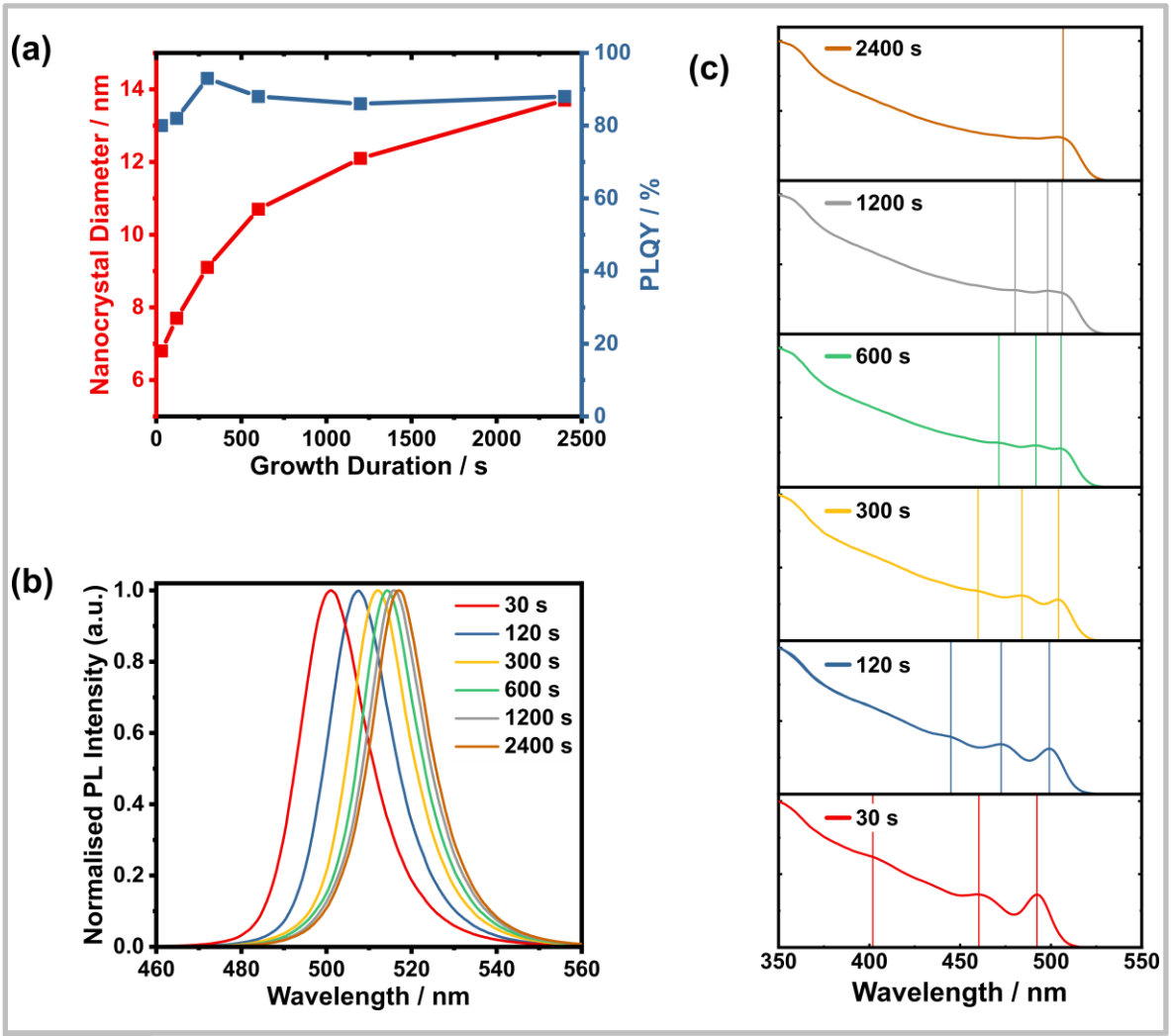

Figure 5.15 **Optical characterisation of $CsPbBr_3$ nanocrystals synthesised with [OPA] = 0.3 M and different growth durations**

(a) The nanocrystal diameter and PLQY plots, (b) photoluminescence spectra, and (c) absorbance spectra.

Multiple syntheses were conducted for [OPA] = 0.3 M with various growth durations ranging from 30 s to 2400 s. Figure 5.15a plotted the nanocrystal diameter and PLQY as a function of the growth duration; it was shown that the nanocrystal diameter increased from 6.8 nm to 13.7 nm as the growth duration was extended. The NC diameters were extracted from SAXS data, as plotted in

Figure A5. Once more, the PLQY remained above 80 % for all samples. These results were excellent evidence that the developed room temperature synthesis could tune the diameter of $CsPbBr_3$ nanocrystals across a wide range, without compromising their optical properties.

The data point for the nanocrystal diameter against growth duration could be well fitted by an exponential function, as shown in Figure A6. This was indicative of the growth rate decaying as the monomer concentration, and surface to volume ratio of the nanocrystals, decreased. Although the kinetics were not explored in this work, this demonstrated that the slow, controlled growth enabled by this method could facilitate a detailed understanding of perovskite nanocrystal growth. This may not have immediate relevance for the commercial viability of the technology, but ultimately, the capability to modulate the reaction kinetics would be valuable for the scalable and reproducible manufacture of perovskite nanocrystals.

Figure 5.15b demonstrated the expected red-shifting of the photoluminescence emission as the nanocrystal diameter increased. The peaks were very narrow for all growth durations, the FWHM remained below 19 nm, reaching as low as 16 nm for the larger nanocrystals. This strongly suggested that minimal Ostwald ripening occurred, which was crucial for maintaining size tuneability over extended growth durations.

The absorbance spectra in Figure 5.15 were most intriguing. The prominence of the first excitonic transition features was commented on earlier, but there were also another two well-resolved features in the absorbance spectra of most samples. The positions of these features were marked for clarity. A consultation of the literature revealed that there were multiple possible explanations for these peaks, therefore it was decided that the origin of these features warranted further investigation.

5.3.3.6.1 Analysis of Excitonic Absorption Features

The most common explanation for additional excitonic peaks in the absorbance spectrum of perovskite nanocrystals is a secondary population of nanocrystals, which are more strongly confined in one or more dimension. One example of this would be nanoplatelets; these are nanocrystals with layers of insulating organic spacer cations which create multiple separately confined domains. They absorb strongly at distinct wavelengths corresponding to the possible integer numbers of perovskite layers (i.e. n = 1, 2, 3, 4 etc.) between the organic spacers. Accordingly, nanoplatelets can be ruled out as a potential source of the excitonic absorption features here because the wavelength of the peaks vary between each sample.

Another possibility was the presence of a separate distribution of nanoplates. These are electronically three-dimensional nanocrystals which are significantly smaller in one geometric dimension. They exhibit strong excitonic absorption corresponding to the strong quantum confinement of the smaller dimension. To assess this possibility, size-selective purification was conducted. A lesser quantity of EtOAc antisolvent than normally used was added during the second purification cycle, such that after centrifugation there were significant quantities of NCs in both the precipitate and the supernatant. Thus, separating and fully purifying the supernatant and precipitate yielded two NC inks, containing fractions of smaller and larger NCs, respectively.

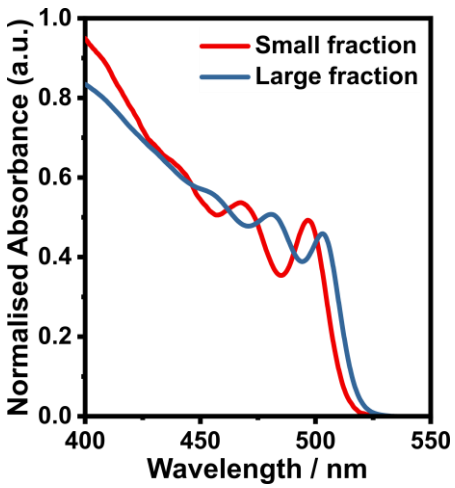

Figure 5.16 **Absorption spectra of two fractions of $CsPbBr_3$ nanocrystals separated by size-selective purification.**

[OPA] = 0.3 M and growth duration = 300 s

Figure 5.16 shows a comparison of the absorbance and photoluminescence spectra of the two separated fractions. It was clear that significant excitonic peaks remained in both fractions, and they were all blue-shifted in the smaller NC fraction. It was extremely unlikely that a distribution of nanoplates would be similarly evenly separated as a distribution of isotropic nanocrystals. The higher surface area of nanoplates should afford higher colloidal stability, such that they should mostly stay dispersed in the supernatant during centrifugation with antisolvent. This implied that the excitonic features all originate from the same nanocrystal population.

To probe these excitonic features further, transient absorption (TA) spectroscopy was performed on the two smallest NC samples: [OPA] = 0.3 M for 30 s and 120 s growth durations. TA measurements provide time-resolved absorption data, such that ultra-fast photophysical processes can be examined. A pump-probe technique was employed, whereby an initial ultra-short high energy laser pulse excited the sample (pump), followed by a second lower energy laser pulse which monitored the absorption changes resulting from the first pulse (probe). Analysis of the change in

absorption spectra for various time intervals between the pump and probe pulses on a femto- or picosecond timescale can reveal details such as the origin or lifetime of observed excitations.

The spectra in Figure 5.17 show the change in transmittance over the relevant wavelength range for different time intervals between 0.5 ps and 1000 ps, for growth durations of 30 s and 120 s, respectively. The main positive peak in both spectra corresponded to the absorption drop or "photobleaching" due to the first excitonic absorption of the pump pulse. The smaller photobleaching peak at lower wavelength corresponded the second excitonic transition, i.e. from a lower energy valence band level to a higher energy conduction band level. Both excitonic absorption peaks matched well with equivalent peaks in the steady-state absorption spectra (Figure 5.15). Therefore, it can be reliably concluded that these absorption features resulted from enhanced quantum confinement, rather than secondary populations of nanocrystals within the samples.

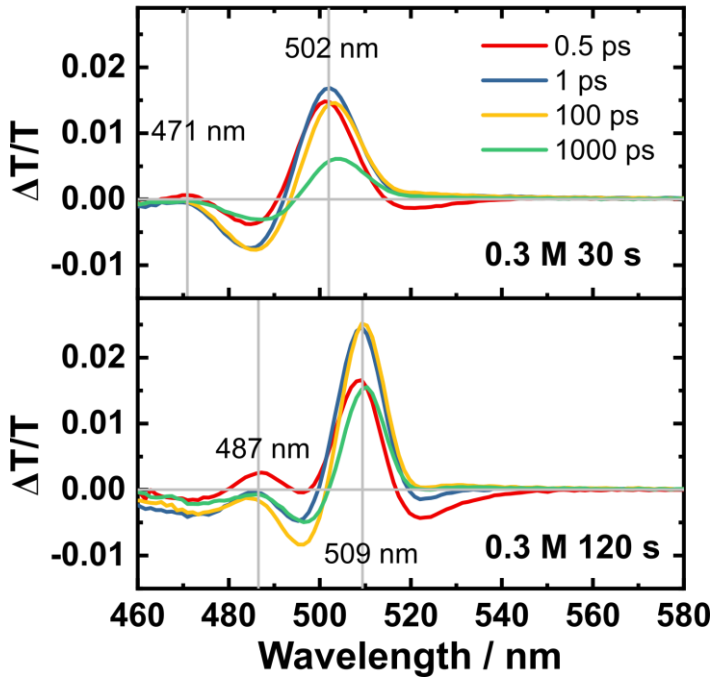

Figure 5.17 **Transient absorption spectra of $CsPbBr_3$ nanocrystals synthesised with [OPA] = 0.3 M for different growth durations**

The origin of the negative "induced absorption" peaks was more complicated. The induced absorption at higher wavelength has been attributed to the formation of a biexciton, a lower energy state induced by the attractive forces between two excitons.[186] While the induced absorption between the first two excitonic peaks has been attributed to the activation of a parity-forbidden transition due to sufficient lattice perturbation by polarons in strong-confined nanocrystals.[187]

Detailed discussion of the photophysics was beyond the scope of this work; these features were highlighted to demonstrate the remarkable extent of the quantum confinement imposed by OPA ligands.

Rossi et al. have previously suggested that the prominence of additional excitonic transition peaks for $CsPbBr_3$ were indicative of strong quantum confinement and a NC ensemble with a narrow size distribution.[146,187] The NC size distributions in Figure A5 confirmed the tight size distribution in the measured samples. This served as excellent validation that the room temperature protocol enabled robust control of the nanocrystal properties. It was also strong evidence that the quality of these nanocrystals synthesised at room temperature matched those prepared by hot-injection.

5.3.4 Ligand Study

In this chapter so far, the influence of ligands on the nanocrystal nucleation and growth, and on the resulting optoelectronic properties, have been thoroughly analysed. It was also pertinent to investigate which ligands ultimately remained in the nanocrystal ink through purification, and on the nanocrystal surface after purification. This was tightly linked to the spectroscopic analysis of ligand binding discussed in Section 3.3.3. Similarly, nuclear magnetic resonance spectroscopy was the key technique employed here.

5.3.4.1.1 Solution Nuclear Magnetic Resonance Spectroscopy

It was important to determine whether the purification protocol adopted for the room temperature synthesis effectively removed unbound ligand materials. In earlier chapters, it was demonstrated that it was crucial to remove as much unbound ligand as possible to improve the efficiency of electrically-driven LEDs. Solution NMR was useful for the analysis of unbound ligands, as resonances of free species in solution should appear sharp at well-defined chemical shifts.

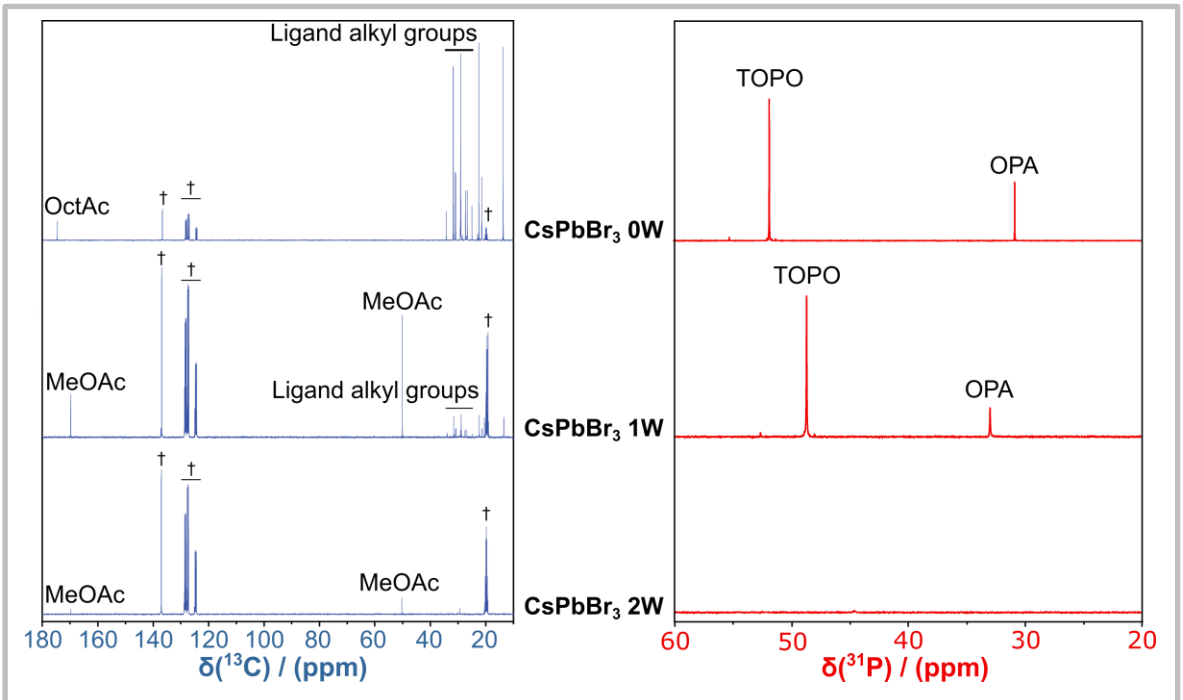

Figure 5.18 **Solution nuclear magnetic resonance spectra for $CsPbBr_3$ nanocrystal solutions before purification (0W), and after one (1W) or two (2W) purification cycles**

13C (left) and 31P (right) NMR spectra. Signals marked by † were attributed to toluene or toluene-d_8 solvent impurities.

Figure 5.18 displays the ^{13}C NMR spectra for $CsPbBr_3$ nanocrystal solutions prepared with [OPA] = 0.3 M and a 300 s growth duration. Three samples from different stages of the purification process

were examined. The 0W sample was prepared by centrifuging the crude nanocrystal solution without antisolvent, then redispersing the precipitate in toluene-d8. The 1W and 2W samples were purified once and twice with methyl acetate antisolvent, respectively. In the 0W spectrum, there was a cluster of high-intensity resonances around 30 ppm, which could only be attributed to the alkyl groups on any of the ligands. Importantly, the **C**-OOH resonance of octanoic acid was identified around 173 ppm. This peak was not observed in the 1W spectrum, indicating that octanoic acid was mostly removed by the first purification cycle. The alkyl group resonances were substantially reduced in intensity compared to the solvent impurity peaks, suggesting removal of a significant fraction of unbound ligand material. In the 2W spectra, the ligand alkyl group resonances were no longer visible.

Solution ^{31}P NMR was conducted to support the ^{13}C results. Without any antisolvent purification (0W), there were two sharp peaks in the ^{31}P spectrum, attributable to TOPO and OPA. After one antisolvent purification cycle (1W), these peaks are shifted towards one another, indicating less hydrogen bonding interaction between TOPO and OPA.[131] This can be correlated to a decrease in their relative concentrations, as implied by the corresponding ^{13}C spectra, reducing the frequency of those interactions. After the second antisolvent washing (2W), there were no sharp peaks observed, even after a significantly longer overnight measurement. Thus, it was concluded that two purification cycles with methyl acetate sufficiently removed unbound excess TOPO and OPA ligands from the NC ink.

Given that the PLQY remained above 80 %, this indicated that the binding of OPA was strong enough to resist desorption by methyl acetate, facilitating complete purification. As discussed earlier, for $CsPbBr_3$ nanocrystals with weak binding ligands, excess ligands and reaction impurities could not be removed from the nanocrystal solutions without also removing bound ligands, consequently degrading PLQY. The capability for complete purification is attractive for commercialisation, as paying customers would reasonably expect to receive both a highly pure and highly efficient nanocrystal ink.

5.3.4.1.2 Solid-State Nuclear Magnetic Resonance Spectroscopy

The binding of OPA ligands was analysed by solid-state ^{31}P NMR, to compare with the binding of OPA obtained by ligand exchange in Chapter 3. Nanocrystal powders were obtained similarly to Chapter 3, the final nanocrystal precipitate was allowed to dry naturally in air as the residual solvent evaporated. It was notable that the $CsPbBr_3$ NC solid produced by the room temperature method was not waxy, in contrast to those prepared by the hot-injection synthesis. It could easily be crushed into a fine powder. This was probably due to the lack of oily oleyl ligands used.

The solid-state ^{31}P proton-decoupled NMR spectrum for the $CsPbBr_3$ NCs, prepared with [OPA] = 0.3 M and growth duration of 300 s, was shown above the ^{31}P–^{1}H heteronuclear correlation (HETCOR) NMR plot in Figure 5.19a. The corresponding spectra for pure crystalline OPA were shown alongside in Figure 5.19b. There was a single resonance in the 1D ^{31}P spectrum of the NC samples, around 25 ppm, which matched well with the earlier assignment for octylphosphonate, $[CH_3(CH_2)_7PO_2OH]^-$. Notably, there was no sign of any other binding modes, reaffirming the hypothesis from Section 3.3.3 that there was a single thermodynamically favoured binding mode. This single resonance was shifted 12 ppm upfield from the ^{31}P resonance of pure OPA, as expected. These room temperature synthesised OPA-ligated NC also exhibited extensive inter-ligand hydrogen bonding. This was indicated by the correlation between the ^{31}P resonance and the hydrogen-bonded P-OH proton peak around 12 ppm (P-OH^h), at the same chemical shift as the proton resonance for inter-molecular hydrogen bonding in crystalline OPA.

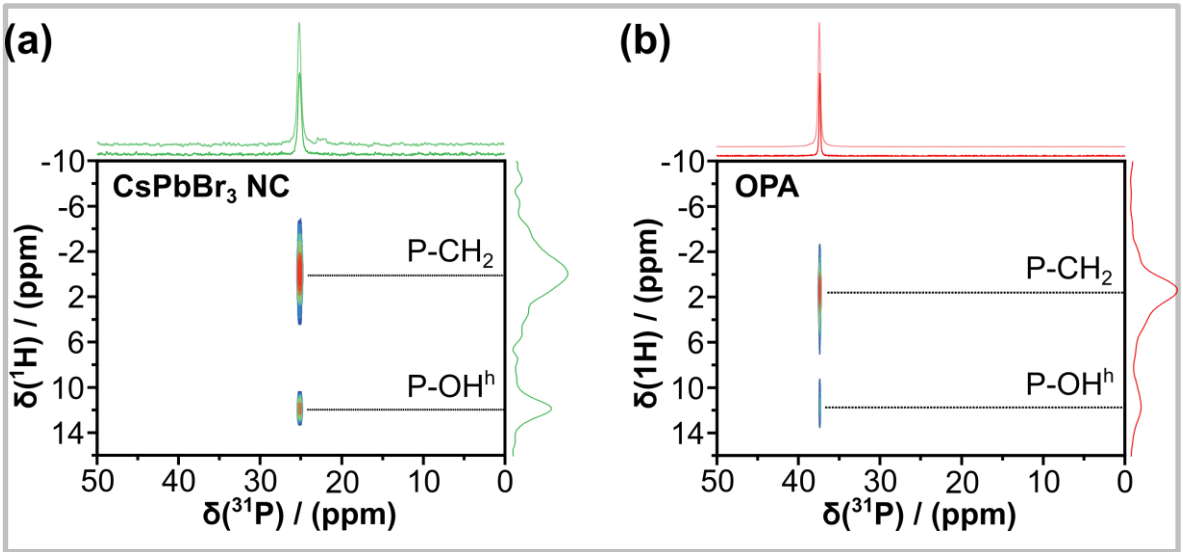

Figure 5.19 **^{31}P–^{1}H heteronuclear correlation (HETCOR) nuclear magnetic resonance (NMR) spectra**

(a) the twice-purified $CsPbBr_3$ NC powder, and (b) crystalline OPA. The ^{31}P proton-decoupled NMR spectra were presented above the projections.

The hydrogen-bonding network formed by OPA ligands on the nanocrystal surface may contribute towards the greater control exerted by OPA ligands on nanocrystal growth compared to OctAc. Similarly, it may be at least partly responsible for the enhanced quantum confinement observed. It would be challenging to decouple the relative influences of the increased binding strength and the inter-ligand hydrogen bonding on these two factors. Perhaps the effect of electron-donating or withdrawing groups on the alkyl group of the phosphonic acid could reveal whether the prominence of the excitonic features was dependant on the charge density on the binding P–O^-. Regardless of

the significance of their hydrogen bonding capability, it was clear the octylphosphonic acid ligands were crucial to the size tuneability demonstrated here for the first time from a room temperature $CsPbBr_3$ nanocrystal synthesis.

5.3.5 Assessment of the Synthesis Yield

It was important not to lose sight of the main aim of this work amongst the focused analytical discussion. Ultimately, for this method to be commercially viable, it must achieve reasonably high yield. Crucially, it must be a high yield of the purified nanocrystals. It would be futile if the economic advantages of a room temperature approach were forfeited because the nanocrystal yield was poor.

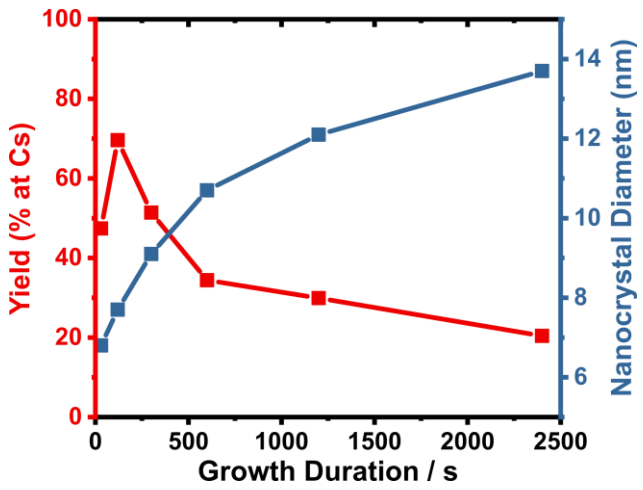

Figure 5.20 **The reaction yield of $CsPbBr_3$ nanocrystal syntheses for various growth durations**

The corresponding nanocrystal diameters are also shown. The yield was calculated from the concentration of the fully purified nanocrystal inks.

To calculate the yield, the final nanocrystal precipitate was weighed before redispersion. Any further precipitation during the last slow-speed centrifugation was also weighed and subtracted from the yield. The yield for six nanocrystal syntheses, which employed [OPA] = 0.3 M and various growth durations, were shown in Figure 5.20 alongside the corresponding nanocrystal diameters. The yield was given as the percentage of Cs^+ in the precursor solution converted into $CsPbBr_3$ nanocrystals, as $PbBr_2$ was in excess. It is important to note that the yield value includes the mass of the ligands attached to the nanocrystal surface. The yield was found to vary from 20 % to 70 %, generally decreasing as the NC size increased. The loss of nanocrystals with longer growth durations was probably due to the decreased colloidal stability of larger NCs. These were more prone to agglomerating and precipitating out of solution during the low-speed centrifugation steps. The drop off in the yield at the shortest growth duration was due to some nanocrystals remaining in the supernatant despite the addition of excess ethyl acetate to the crude solution.

The choice of antisolvent was a significant factor. Ethyl acetate was initially chosen as the antisolvent added to the crude solution mostly due to its ubiquitous use in literature. It was then compared with similar solvents to assess whether optimisations could be made. Butyl (BuOAc), ethyl (EtOAc), and methyl acetate (MeOAc) were compared with centrifugation without an antisolvent. For [OPA] = 0.1 M and growth duration of 300 s, there was little difference between washing with butyl acetate and without an antisolvent. Both approaches left a significant fraction of nanocrystals in the supernatant, which appeared bright green and highly luminescent. With EtOAc, the supernatant was only faintly green coloured, while with MeOAc the supernatant was colourless. The normalised photoluminescence spectra in Figure 5.21a demonstrated that EtOAc retained a fraction of small nanocrystal in solution, while MeOAc precipitated everything except some unidentified deep blue-emitting species. This emission had extremely low intensity, such that it was not discernible by eye under a UV lamp; it may be attributable to some metal-ligand complexes formed as by-products of the synthesis. The PL emission peaks of the redispersed nanocrystal precipitates after washing with EtOAc and MeOAc were shown in Figure 5.21b. As a result of retaining smaller NCs in the supernatant, the FWHM of the EtOAc-washed NCs was around 1 nm narrower than the MeOAc-washed NCs.

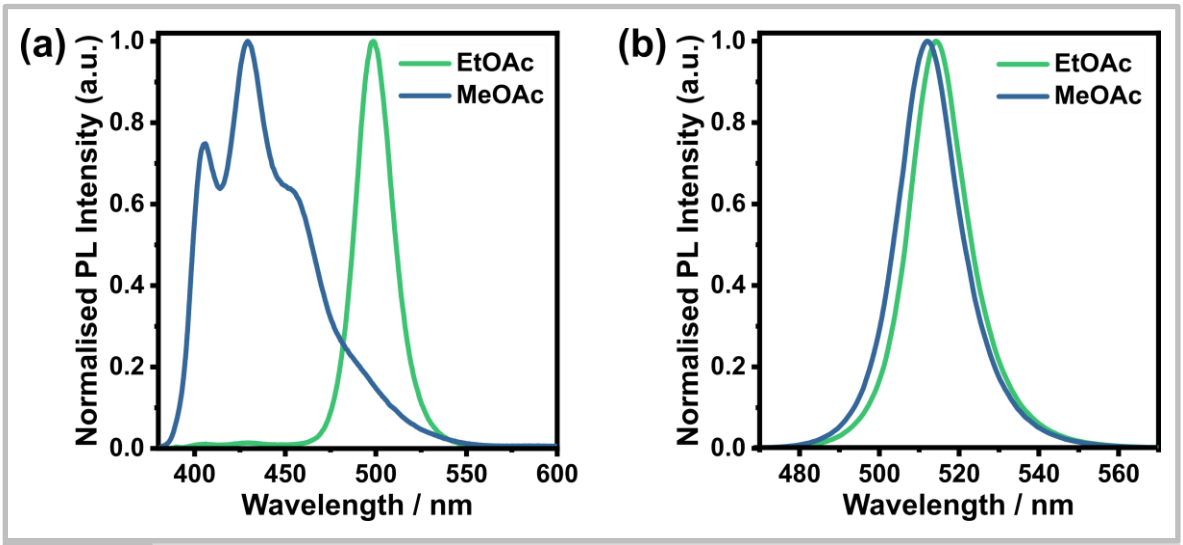

Figure 5.21 **Photoluminescence spectra comparison for $CsPbBr_3$ nanocrystals precipitated from the crude solution by ethyl or methyl acetate**

(a) the supernatants, and (b) the redispersed precipitates. For both, the synthesis parameters were [OPA] = 0.1 M and growth duration = 300 s.

The four NC samples precipitated from the crude solution with different solvents were all redispersed and purified once more with MeOAc. The comparison of the absorbance spectra of the same volume of each resulting NC ink, diluted identically for measurement, was shown in Figure 5.22. This demonstrated the impact of the solvent selection of the final NC ink concentration. Without using an antisolvent, the concentration, and therefore the yield, was around 4 times less

than using MeOAc. For BuOAc, the yield was even worse. Using EtOAc retained a higher yield, but it was still 25 % less than using MeOAc. After contemplating these results, it was decided that EtOAc should be adopted as the antisolvent for the crude solution to obtain a narrower NC size distribution. However, further purification cycles were conducted with MeOAc, to ensure minimal further NC yield was lost through purification.

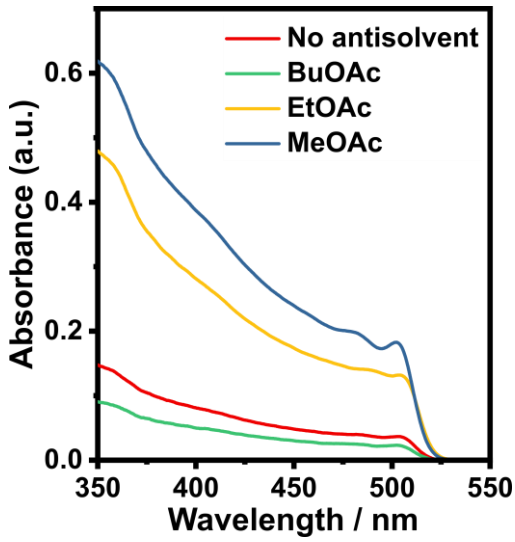

Figure 5.22 **The absorbance spectra of fully purified $CsPbBr_3$ nanocrystal solution precipitated initially from the crude solution by different antisolvents**

For all, the synthesis parameters were [OPA] = 0.1 M and growth duration = 300 s.

Typically, the yields of perovskite nanocrystal syntheses are not reported in the literature, so it was difficult to find the yield of hot-injection reactions to compare with. There was a suggestion that the yield of hot-injection syntheses were usually around 10 %,[131] but the values reported tend to be recorded before any isolation or purification processes. Another reported synthesis, which also utilises TOPO but at elevated synthesis temperatures in air, recorded an impressive yield in Pb of around 60 %. Their synthesis employed a $Cs:PbBr_2$ ratio of 1:1.5, which matched the stoichiometry of the reaction, therefore allowing them to get close to the theoretical maximum yield of 66.7 %.[131]

This leads conveniently to a discussion of one drawback of the synthesis devised in this chapter. The Cs-deficient conditions ($Cs:PbBr_2$ = 1:4.14) restricted the maximum attainable yield in Pb to 24.2 %. Ideally, the precursor ratio would match the stoichiometry of the reaction. For this synthesis method, it was found that less Cs-deficiency led to poorer colloidal stability, presumably due to less DDA^+ ligands binding to the surface with increased competition from Cs^+ ions. Accordingly, the actual yield obtained appeared to drop. However, this was not investigated sufficiently; it is possible

that in future, particularly with the deeper understanding of the synthesis mechanisms explained earlier, further adjustments could optimise the synthesis for high yield without Cs-deficient conditions.

It was important to point out also that another approach to improve the maximum possible yield would have been to use CsBr as the Cs source. However, the LARP synthesis methods that can utilise CsBr, commonly achieve very low yields due to the use of polar solvents and the low solubility of CsBr in dimethylformamide.[86] Thus, the realistically attainable yield would probably have been lower than the polar solvent-free approach.

Ultimately, this room temperature method attained yields in Pb (5 – 17 %) after complete purification with a narrow size distribution, which were comparable to those reported for hot-injection reactions before purification with broad size distributions. Therefore, while there was certainly room for improvement, the yields obtained were did not hinder the commercial viability relative to competing hot-injection syntheses.

5.4 Summary

In this chapter, a room temperature method was designed to prepare $CsPbBr_3$ nanocrystals capped by octylphosphonic acid ligands. It was found that OPA provided precise control over the nucleation and growth of the nanocrystals. Through the decoupling of these two phases, it was unveiled that the hydrogen bonding interaction between Cs(OPA) and TOPO had a strong influence on nucleation thermodynamics, while the concentration of OPA ligands modulated the growth kinetics and final NC morphology.

While OPA controlled the growth rate, another ligand, DDAB, modulated the reaction duration. Adding DDAB to the crude solution quenched nanocrystal growth, presumably due to the slowing of the rate-determining reaction of monomers at the nanocrystal surface. Accordingly, the nanocrystal diameter was tuneable from 6.6 – 13 nm, corresponding to PL peak wavelengths from 501 – 517 nm. The PLQY was maintained above 80 % for all sizes, while the PL FWHM remained between 16 and 19 nm. This represented the first example of flexible size tuneability for room temperature $CsPbBr_3$ nanocrystal syntheses. It signified a clear improvement in the commercial prospects of the material, by reducing the cost and complexity required to obtain high-quality optoelectronic properties.

The binding of OPA to the NC surface enhanced quantum confinement, which resulted in multiple well-resolved excitonic transitions, highlighting the excellent quality of the nanocrystal inks prepared. Solid-state NMR demonstrated that OPA presented the same binding mode as observed in Chapter 3, and the same inter-ligand hydrogen bonding. Also, we exhibited that the nanocrystal inks maintained high PLQY through antisolvent purification, thus they could potentially facilitate a wide range of optically and electrically-driven applications.

The commercial viability was assessed further by quantifying the yields for syntheses of different nanocrystal sizes, after complete nanocrystal purification. The yields ranged between 20 % and 70 % in Cs, generally decreasing for larger, less colloidally stable particles. However, it was important to note that the yield in Pb was much lower (5 – 17 %), hindered by the large excess in $PbBr_2$ employed.

Chapter 6 The Future of Perovskite Nanocrystals

This work has focused on a few different aspects that could enhance the commercial viability of perovskite nanocrystals. There were many other crucial avenues which were not pursued. Based on the experience acquired during the long process of preparing this work, and a critical analysis of the field, this penultimate chapter outlines some promising future research directions, which could accelerate the progress towards the adoption of perovskite nanocrystals by the consumer electronics industry. Most of this section was recently published as part of a Progress Report in Advanced Energy Materials.[112]

6.1 Novel Ligands

There has been a relative dearth of variety in the types of ligands utilised for perovskite nanocrystals. While good progress has been made identifying more strongly binding functional groups, only the length of the hydrophobic component (most often an alkyl group) has been commonly altered. Here, some potential improvements are proposed, which could enhance properties relevant for commercial applications.

6.1.1 Entropic Ligands

As mentioned earlier, the improved colloidal stability with DDAB ligands can be correlated to the presence of multiple long alkyl chains attached to a single binding group. This inhibits the interdigitation of alkyl chains, making NC aggregation less favourable. It is possible to further exploit this effect. It has been demonstrated that CdSe quantum dots were over 100 times more soluble with branched-chain ligands than straight-chain.[115] As well as reducing the enthalpic cost of dissolution, branched chains increased the entropy released due to a greater number of intramolecular bond rotation and bending freedoms. Thus, highly stable NC inks of high concentration should be attainable with short branched-chain ligands, which should minimize the contribution of ligands to resistivity in NC thin films. This agrees with the enormous increase in colloidal stability recently reported with the very long, highly branched, soy lecithin ligand.[188] However, this concept has not yet been explored for shorter chain ligands suitable for perovskite NC LEDs. There are many commercially available branched-chain carboxylic acids and amines, as well as recently reported syntheses of branched phosphonic acids.[189]

6.1.2 Polymerizable Ligands

The highly ionic nature of the perovskite lattice inevitably means that any nanocrystal surfaces remain prone to degradation by polar species even when capped by organic ligands. One approach to provide more robust protection of perovskite NCs is to mix with a polymer, which could lead to highly stable composite films.[190] Another option is synthesizing core-shell structures with a stable material such as SiO_2.[191] However, while useful for optically-driven applications, these routes are unsuitable for electrically-driven applications such as LEDs, where large domains of insulating material severely inhibit charge transport.

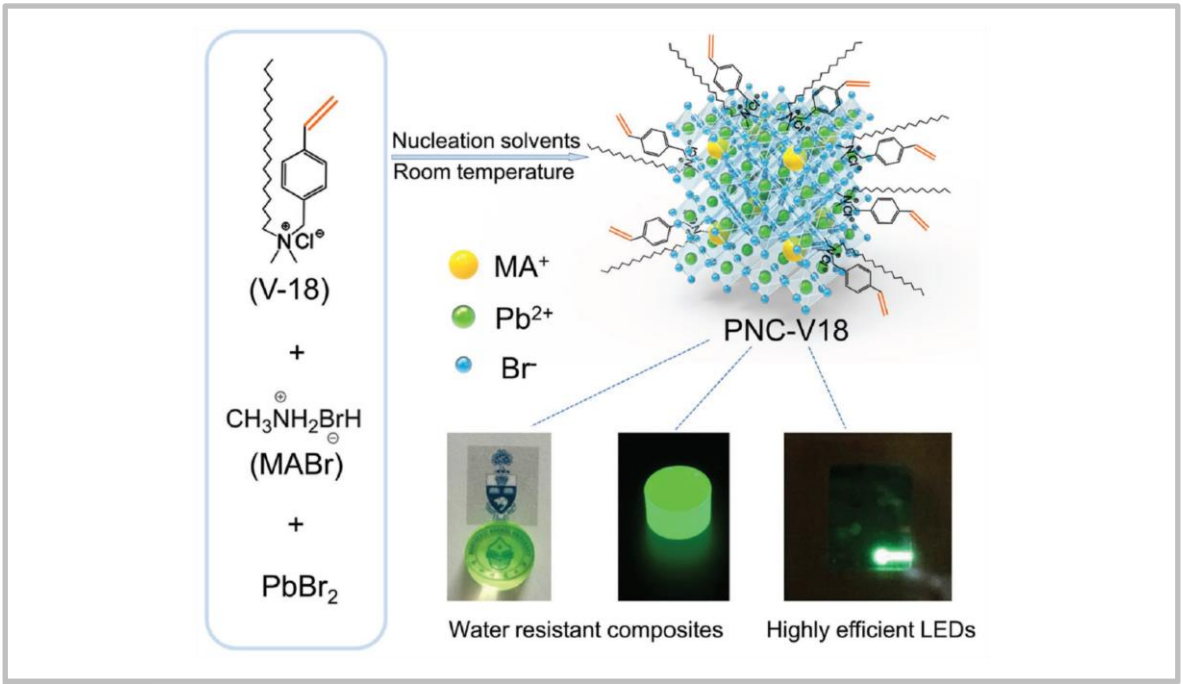

Figure 6.1 **A schematic of the synthesis of $MAPbBr_3$ nanocrystals with polymerizable ligands**

Reproduced with permission.[124] © John Wiley & Sons

Ideally, a thin, dense polymer shell would be employed, such that the shell contributes no more to the resistivity of the film than typical organic ligands. Polymerizable ligands may offer a route towards this, as cross-linking between chains would increase ligand shell coverage without increasing the distance between nanocrystals. Sun et al. investigated this approach, synthesizing a quaternary ammonium chloride salt containing a vinyl group, 4-vinylbenzyldimethyloctadecyl-ammonium chloride, and using it as a ligand for LARP-synthesised $MAPbBr_3$ NCs (Figure 6.1).[124] By adding the initiator azobisisobutyronitrile (AIBN) into the NC ink and heating the subsequently deposited NC film at 90 °C, ligand cross-linking was achieved. The stability of the film with respect

to moisture was improved slightly and LEDs were fabricated successfully with a maximum EQE of 0.58 %.

This work, from 2017, represented a substantial first step but there has been little advancement since. Given the wide range of monomer groups available, one could be sought which was cross-linked without heating the temperature-sensitive perovskite, or without adding an initiator. UV cross-linking is an attractive possibility, although there would be similar concerns about the light sensitivity of the perovskite material. It is also important to ensure the ligand chain is not too long, such that film conductivity is maintained, and to consider branching for good colloidal stability. Lastly, combining these properties with a strong binding head group, such as phosphonic or sulfonic acid, would ensure the ligand shell remained firmly attached to the NC surface. Clearly, designing the synthesis of such a molecule would be challenging, but it could prove crucial to upgrading the stability of perovskite NC films to a commercially acceptable level.

6.2 Compositional Engineering

The compositional versatility of the perovskite lattice is a very useful tool. In perovskite solar cell research, the cation and anion composition has been extensively optimised for the highest power conversion efficiency and long-term stability.[192] The effects of cation and anion mixing have not yet been as well explored for the compositions most relevant for light emission. Also, there is a wide range of potential minority dopants which could hold the key to stability improvement.

6.2.1 Metal Doping

The application of crown ethers to coordinate metal ions for perovskite NC synthesis is an interesting approach. Besides obvious extensions to the protocol designed by Veldhuis et al., which was mentioned in Section 2.3.1, such as solubilizing other alkali metal ions such as Rb^+ or K^+ for A-site doping or passivation,[48,50,126,143,144,193] the selectivity of crown ether coordination may allow the direct synthesis of transition metal-doped $CsPbX_3$ NCs at room temperature by coordinating Pb^{2+}.[194] Crown ethers coordinate more strongly to metal ions with an ionic radius close to their cavity size, thus selecting the appropriate crown ether for Pb^{2+} could impede the formation of the thermodynamically-favoured pure $CsPbX_3$ perovskite nanocrystals, allowing smaller dopant metal ions to occupy some lead sites. It has been previously proposed that NC doping is often a kinetically-controlled process, such that reduction of the growth rate promotes adsorption of dopants, thus increasing dopant incorporation.[195,196] Dutta et al. showed that this concept applies to perovskite NCs, by using solvent polarity to control the release of Pb^{2+} during $CsPbCl_3$ NC synthesis.[197] They

found that lower polarity solvents slowed the reaction rate, such that Mn^{2+} doping of up to 2 % was obtained with hexane, compared to less than 0.01 % when chloroform was used.

Doping of Pb^{2+} is considered a promising route to improve the inherent stability of the perovskite material. The influence of doping with a smaller cation on the lattice strain can enhance the thermal stability greatly. Such stability improvement is crucial for optically and electrically-driven device application, as the material must be able to withstand increased local operating temperatures without noticeable degradation of its performance.[198]

6.2.2 A-Site Doping

Various fundamental studies have shown that the organic cations in the perovskite lattice (MA or FA) enhance charge carrier lifetimes because the rotation of asymmetrical cations in the lead halide cages increases orbital overlap and promotes large polaron formation.[179,199–202] The implication of the aforementioned work by Song et al. is that this enhancement can be obtained when organic cations constitute only a small percentage of the lattice, as demonstrated by the time-resolved photoluminescence and LED plots for $CsPbBr_3$ and $Cs_{0.85}FA_{0.15}PbBr_3$ nanocrystals in Figure 6.2.[100]

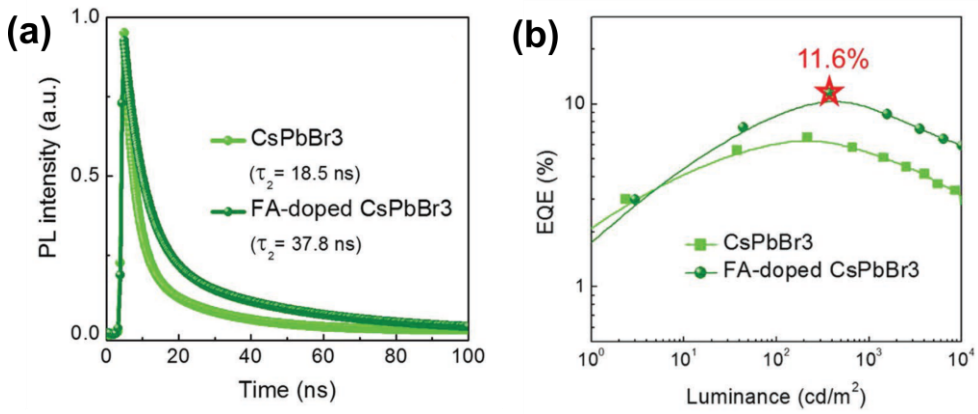

Figure 6.2 **A comparison of the properties of pure $CsPbBr_3$ and $Cs_{0.85}FA_{0.15}PbBr_3$ nanocrystals**

(a) time-resolved photoluminescence (TRPL) spectrum of NC thin films, and (b) performance of NC LEDs. Adapted with permission.[100] © John Wiley & Sons.

Given that the performance of pure $CsPbBr_3$ NC LEDs currently lags behind those containing organic cations, it may be the case that FA (or MA) doping is essential to obtain perovskite NC-based LEDs with EQE approaching the theoretical limit. It is therefore imperative that the impact of minor FA doping on $CsPbX_3$ NCs is analysed in more detail. It is particularly important to assess the impact on stability: colloidal, environmental and device. It would be highly attractive from a commercial

perspective if mixing of the Cs and FA cations could achieve the best of both worlds; retaining the higher stability of $CsPbBr_3$, and the better photophysical properties of $FAPbBr_3$, with emission closer to the desired green emission wavelength for wide-colour gamut displays (around 530 nm).

6.3 Scalable Deposition Techniques

The rapid rise of perovskite nanocrystal-based electronic devices has been almost exclusively facilitated by spin-coating. It is a simple, reproducible deposition method which can achieve good uniformity and precise thickness control for small area thin films. It was therefore ideal for early-stage research. However, spin-coating prevents full access to the benefits of solution-processing. Spin-coating is a batch process, with inherently limited scalability, which operates with significant material wastage; the vast majority of ink dropped onto the substrate is ejected from the surface during coating, which is highly undesirable both from economic and sustainability perspectives.

There are various more suitable, scalable deposition techniques, which have been pioneered in organic electronics and utilized frequently for perovskite solar cell fabrication. These include slot-die coating, blade (or bar) coating, inkjet printing, and spray coating.[203,204] Applying these techniques for bulk perovskite thin-film formation adds significant complexity. As crystallization occurs during deposition, it must be precisely controlled and expedited to obtain high-quality films. During spin-coating, crystallisation is hastened by the fast evaporation of solvent during spinning, while antisolvent can be dripped on the film to instantly induce crystallisation if necessary. For scalable deposition methods, neither of these approaches are feasible. The only perovskite LED fabricated by a scalable method was reported by Prakasam et al.; they utilized N_2 gas-assisted crystallization of $MAPbBr_3$ during slot-die coating.[205]

Perovskite nanocrystals offer a much simpler alternative; they are pre-synthesised, so crystallization and deposition processes are decoupled. There is no need for additional provisions such as N_2 gas flow or antisolvent dripping. Therefore, it seems entirely feasible that high-quality perovskite nanocrystals could be easily deposited by high-throughput, roll-to-roll compatible techniques, to form high-quality films for device applications. Some solvent engineering will likely be required so that the films dry efficiently, a process that is inherently achieved in-situ during spin-coating. Furthermore, the capability of different scalable deposition techniques to attain uniform films of a sufficient low thickness for minimal reabsorption must be explored. The existing extensive knowledge obtained from research on scalable deposition for organic electronics provides a strong starting point. Ultimately, successful optimization of uniform, scalable perovskite NC deposition is a realistic goal which would greatly enhance commercial viability.

6.4 Lead-Free Perovskite Nanocrystals

This thesis focused entirely on lead halide perovskites. However, it would be amiss to ignore the toxic elephant in the room; there are well-known toxicity concerns associated with the use of lead-containing materials in commercial optoelectronics, which weakens their industrial appeal. Regardless, as is the case for the perovskite solar cells being pushed towards the market, and the cadmium-containing quantum dots already used in QLED displays, the poor performance of non-toxic alternatives leaves the toxic material as the only currently viable option.[206–208]

Unsurprisingly, there is great interest in identifying and developing suitable lead-free alternatives.[209] Research remains in the early stages; there are many reports of moderate PLQY from lead-free perovskite or double perovskite nanomaterials.[210–212] Some of these were synthesised at room temperature; for example, Zhang et al. prepared $Cs_3Sb_2Br_9$ NCs that emit at 410 nm with PLQY = 46 % (Figure 6.3a),[213] while Leng et al. similarly synthesised $Cs_3Bi_2Br_9$ NCs with PLQY up to 19.4 % at the same wavelength.[214] Yang et al. reported that indium-doping of $Cs_2AgBiCl_6$ NCs changed the band-gap from indirect to direct, increasing the PLQY from 6.7 % to 36.6 % for emission around 570 nm (Figure 6.3b).[215] Similar to lead-based perovskite NCs, it is mainly solubility issues which have discouraged more room temperature syntheses for other lead-free materials. Therefore, adopting similar approaches to those covered earlier in this chapter should help tackle this.

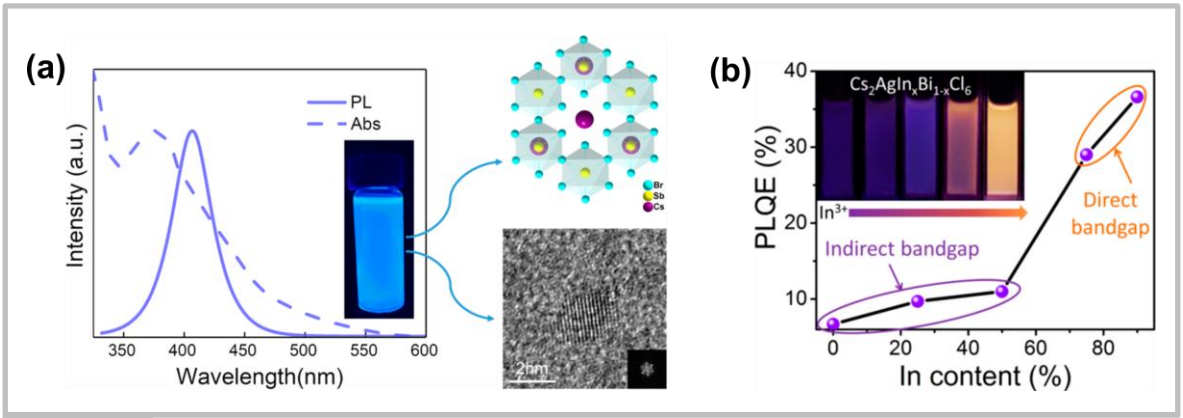

Figure 6.3 **The optical properties of some direct band-gap lead-free perovskite nanocrystals synthesised at room temperature**

(a) Absorbance, PL, structure and TEM images of $Cs_3Sb_2Br_9$ NCs, and (b) PLQY as a function of In^{3+} content for $Cs_2AgIn_xBi_{1-x}Cl_6$ NCs. Reproduced with permission[213,215]. © 2017 and 2018 American Chemical Society.

Despite improving PLQY, lead-free perovskite or double perovskite NCs have yet to demonstrate electroluminescence, so this remains an important challenge to prove their credentials as potential

materials for LED applications. Ultimately, while they are unlikely to be an imminently viable option, if the optoelectronic performance from lead-free perovskite nanocrystals can approach that of their lead-based counterparts in the future, there is no doubt that it would greatly enhance the commercial viability of the technology.

Chapter 7 Conclusions and Future Work

In this final chapter, a reflective view of the three research chapters was offered. First, some limitations of the methodologies employed were explained, with some suggestion as to how they may have been improved. Second, there was a discussion of promising future work which could expand on the results obtained here. Lastly, the key conclusions of this thesis were summarised, and their wider implications were highlighted.

7.1 Limitations

In Chapter 4, purification of the $CsPbBr_3$ nanocrystal solution was optimised to attain improved EQE in light-emitting diodes. However, the fabrication of the LEDs themselves was not optimised. Although a reasonable maximum EQE of 7.7 % was obtained, there are many improvements which could have increased this further. In the literature, a second hole transport layer is usually coated after PEDOT:PSS, to improve the energetic alignment between the HOMO of the hole transporting materials (HTMs) and the perovskite valence band.[116] A polymer HTM with a lower HOMO energy, such as poly(N,N'-bis-4-butylphenyl-N,N'-bisphenyl)benzidine (poly-TPD), would probably have improved the EQE and luminance attained. More recently, it has been shown that employing two electron transport materials (ETMs) can also improve charge injection efficiency into the emissive layer.[151,173] In general, judicious optimisation of the LED stack would likely have enabled better device performance.

Another factor that may have affected the electronic device characterisation was the thickness of the active layers. If nanocrystal solutions were not sufficiently concentrated, the resulting thin films could exhibit incomplete coverage of the substrate. This would provide pathways for short-circuit currents between the hole and electron transport materials. Furthermore, even when complete coverage is achieved, variations in the thicknesses of NC films obtained from different NC inks can alter the optical outcoupling efficiency of the device. Although the inks compared had similar concentrations according to optical absorption spectroscopy, there may have been differences in coated film thicknesses due to different quantities of unbound ligand in each solution. This may have hindered the analysis of the other device parameters, such as injection efficiency and EQE. Similarly, comparing the PL intensity (or PLQY), of different nanocrystal thin films would have improved experimental accuracy by quantifying the actual IQE in the LEDs, rather than relying on the solution PLQY values.

Ultimately, the most significant factor limiting the EQE of the LEDs was the PLQY. Despite improving the PLQY to 62 %, this remains significantly lower than the near-unity values achieved from the

room temperature synthesis, and other reports in the literature. This was likely due to an inability of OPA to fully passivate all the surface bromide vacancies, perhaps due to steric hindrance between the alkyl groups of OPA and OLA. The use of DDAB, in addition to OPA, is particularly useful because the bromide ions can passivate more sterically hindered vacancies, further enhancing the PLQY.

One limitation of the room temperature synthesis method outlined in Chapter 5 was already mentioned earlier. The Cs-deficient reaction conditions ($Cs:PbBr_2$ = 1:4.14) inherently limited the achievable yield. Although theoretically useful for the suppression of Cs_4PbBr_6 formation, and the promotion of Cs^+ vacancies which DDA^+ ligands could occupy, with optimisation it may have been possible to employ a stoichiometric $Cs:PbBr_2$ ratio of 1:1.5. This has the potential to dramatically increase the reaction yield, which is vitally important from a commercial perspective. Another economic drawback was the use of such a large excess of TOPO (molar ratio of Cs:TOPO = 1:41.4). Although TOPO is rather inexpensive, it would still make up a substantial portion of the synthesis cost and using fresh TOPO for each synthesis would be particularly wasteful. Ideally, a methodology would be devised to recycle TOPO for reuse in multiple syntheses. It should also be determined whether lower purity TOPO could obtain similar results.

7.2 Future Work

The most promising future direction for this work would be to expand the capabilities of the devised room temperature synthesis method. The synthesis framework could be adjusted in various ways to tailor the nanocrystals to specific applications.

The simplest expansions of the room temperature synthesis would involve demonstrating compositional tuneability. Synthesising mixed-halide perovskite nanocrystals would lead to blue and red emission. Preliminary work has indicated that the inclusion of zinc halide salts in the lead bromide precursor can shift the photoluminescence between approximately 450 nm and 640 nm, as the composition changes from $CsPbBr_{3-x}Cl_x$ to $CsPbBr_{3-x}I_x$. Photographs of mixed-halide perovskite nanocrystals with different emission wavelengths are shown in Figure 7.1, indicating that precise control over the emission wavelength could be achieved by manipulating the $PbBr_2:ZnX_2$ ratio. However, there are some foreseeable difficulties. It may be challenging to maintain control over both the halide content and the nanocrystal size simultaneously, and mixed-halide nanocrystals are notoriously susceptible to halide segregation under an electric field or UV irradiation. This could hinder their colour stability under those common device conditions.

The narrow bandwidths of perovskite nanocrystals mean that blue and red-emitting nanocrystals could help further increase the coverage of the CIE colour space, in combination with the green nanocrystals reported earlier. However, the emission wavelength range obtained for the $CsPbBr_3$ nanocrystals does not cover the ideal green wavelength for display applications. This could be addressed by exploring the synthesis of pure $FAPbBr_3$ nanocrystals or mixed Cs/FA compositions, using the same room temperature method. Preliminary work indicated that this is a viable strategy, such that the emission wavelength could be extended as high as 531 nm. However, there were serious issues regarding size control and colloidal stability. It is likely that the capability of FA(octanoate) to hydrogen bond to TOPO through the acidic FA^+ cation disrupts the synthesis mechanism. Furthermore, it may be more difficult for DDA^+ ligands to displace FA^+ than Cs^+ due to hydrogen bonding between FA^+ and Br^- on the nanocrystal surface. In general, careful optimisation would be required to understand how FA^+ influences the nucleation and growth phases, in competition with OPA.

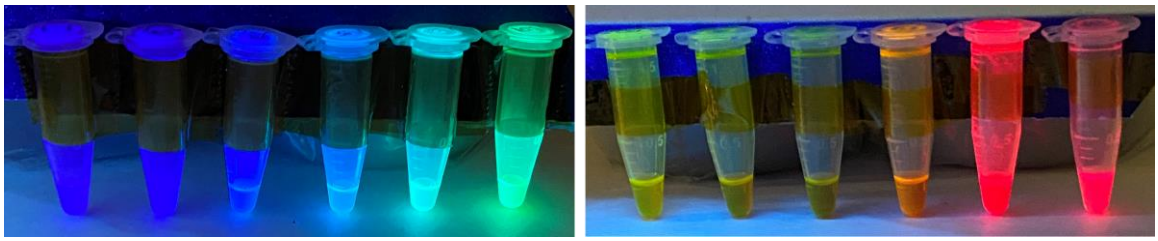

Figure 7.1 **Photographs of $CsPbBr_{3-x}Cl_x$ (left) and $CsPbBr_{3-x}I_x$ (right) nanocrystals prepared by room temperature syntheses with $PbBr_2$, and $ZnCl_2$ or ZnI_2**

Lastly, it is reasonable to expect that octylphosphonic acid could be successfully replaced with a different phosphonic acid ligand. This would open a wide range of possibilities. For example, using a slightly longer phosphonic acid may allow even smaller nanocrystals to be obtained, such that the emission of $CsPbBr_3$ may be shifted into the blue region. The replacement of the alkylphosphonic acids with an aromatic phosphonic acid may facilitate improved charge transport, potential enhancing the efficiency of light-emitting diodes. Some preliminary syntheses with cinnamylphosphonic acid (CPA) achieved similar results to OPA; The synthesis yield improved slightly, although PLQY was around 10 % lower, which may be attributable to a lower surface ligand density with the bulkier aromatic ligand. Regardless, an initial assessment of the influence of CPA on $CsPbBr_3$ NC LEDs showed that the EQE was almost doubled when CPA replaced OPA, increasing from around 2.5 % to almost 5 %. Combining this with significant FA doping, an EQE of 11.8 % was achieved at a peak emission wavelength of 532 nm – some exciting preliminary results.

More creative approaches could be devised by exploring phosphonic acids with additional functionalities. An additional binding group on the other end of the molecule may facilitate inter-

particle bridging by ligands, potential stitching together NCs in thin film to achieve a more compact layer. Some preliminary investigations were conducted using an acrylate-terminated phosphonic acid to synthesise $CsPbBr_3$ nanocrystals; it was found that the ligand provided exceptional solvent resistance, so much so that they could not be redispersed in any common laboratory solvents. This led to the intriguing discovery that the powder obtained from the crude nanocrystal precipitate could retain bright photoluminescence for a few days submerged in deionised water (Figure 7.2). It was speculated that these NC may have been dissolvable in an acrylate polymer resin.

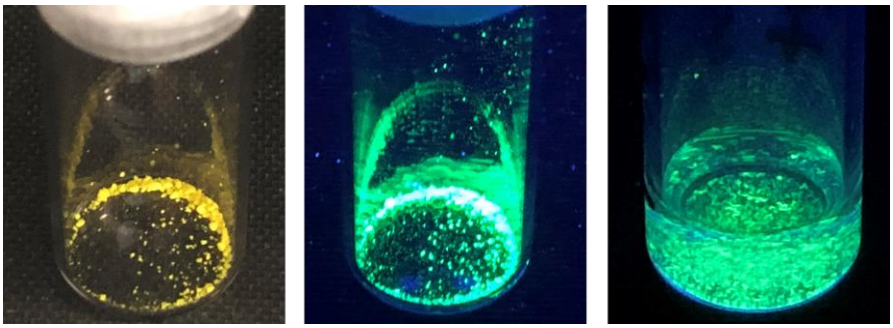

Figure 7.2 **Photographs of $CsPbBr_3$ nanocrystals synthesised using an acrylate-terminated phosphonic acid ligand**

The images shown are dry nanocrystal powder under visible light (left), UV light (middle) and the powder submerged in deionised water under UV light (right).

In general, the synthetic framework investigated in detail in Chapter 5 offered a platform from which the properties of perovskite nanocrystals could be enhanced, adjusted or diversified, without any specialised equipment or advanced experimental techniques. This versatility and accessibility make a substantial contribution to the commercial viability of the method.

7.3 Conclusions

The central aim of this thesis was to enhance the commercial viability of perovskite nanocrystals for light-emitting applications. To achieve this goal, the typical long-chain, weak binding ligands used to passivate $CsPbBr_3$ nanocrystals were replaced with shorter, stronger binding octylphosphonic acid (OPA) ligands. First, a ligand exchange strategy was designed to substitute oleate ligands for OPA, while the native oleylammonium ligands remained on the surface to provide colloidal stability. With an optimised OPA concentration of 15.45 mM, the post-purification PLQY was increased from 20 % to 62 %. The strong binding mechanism of OPA was investigated, unveiling that it was initially bound by four different modes. During antisolvent washing, these four modes reconfigured preferentially into a monodentate octylphosphonate mode. In this mode, the

otherwise uncoordinated P−OH and P=O groups of OPA drove the self-assembly of a hydrogen-bonded inter-ligand network.

An optimised two-cycle antisolvent purification protocol facilitated the fabrication of $CsPbBr_3$ NC light-emitting diodes. The robust passivation of OPA yielded a maximum EQE of 7.7 %, significantly higher than unmodified NCs, which obtained an EQE of 3.6 %. Thus, it was demonstrated that OPA ligands could enhance the commercial prospects of perovskite light-emitting diodes.

The application of OPA ligands was extended further by designing a room temperature synthesis of $CsPbBr_3$ nanocrystals capped by OPA. It was discovered that OPA imposed precise control over the nucleation and growth of the nanocrystals. Through the decoupling of these two phases, it was revealed that hydrogen bonding interactions between Cs(OPA) and TOPO had a strong influence on nucleation thermodynamics, while the concentration of OPA ligands modulated the growth kinetics and final NC morphology. Combining the control over the growth rate offered by OPA with the control over the growth duration obtained by quenching with DDAB ligands, the nanocrystal diameter was tuneable from 6.6 to 13 nm. This corresponded to PL peak wavelengths between 501 and 517 nm. The PLQY was maintained above 80 % for all sizes, while the PL FWHM remained between 16 and 19 nm.

Many features of this synthesis were considered commercially appealing. It does not require the strict environmental controls or high temperatures that the hot-injection method does, which should reduce cost. No time-consuming precursor preparation or drying was required, nor were any advanced laboratory techniques necessary; the protocol was efficient, simple and versatile. Also, the established synthesis framework has vast scope for customisation. The combination of these factors with the excellent optoelectronic properties and size tuneability achieved undoubtedly enhanced the prospects of $CsPbBr_3$ nanocrystals for a wide range of optically and electrically-driven applications.

Contributions

The author of this thesis independently designed the experiments, conducted most of the practical work, analysed all experimental data, and ultimately devised the resulting hypotheses. However, there were significant contributions from other researchers, particularly for characterisation data collection.

- Dr Thomas J.N. Hooper conducted all nuclear magnetic resonance spectroscopy, produced the resulting spectra, and assisted with the spectral analysis.
- Small-angle X-ray scattering measurements were performed by Dr Pio J.S. Buenconsejo.
- Dr Xin Yu Chin and the author cooperated for the fabrication of light-emitting diodes.
- Transmission electron microscopy images from Chapter 3 were collected at Wintech Nanotechnology Services in Singapore, and those in Chapter 5 were taken by Dr Parth Vashishtha. The author was always present during the measurements to guide image acquisition.
- Dr Annalisa Bruno performed the time-resolved photoluminescence spectroscopy and provided her expertise during the analysis of the results.
- Dr David Giovanni performed all transient absorption spectroscopy, analysing the data and producing the spectra.

The author is grateful for the important contributions of his colleagues, and thanks them for their assistance and helpful discussion.

Appendix A

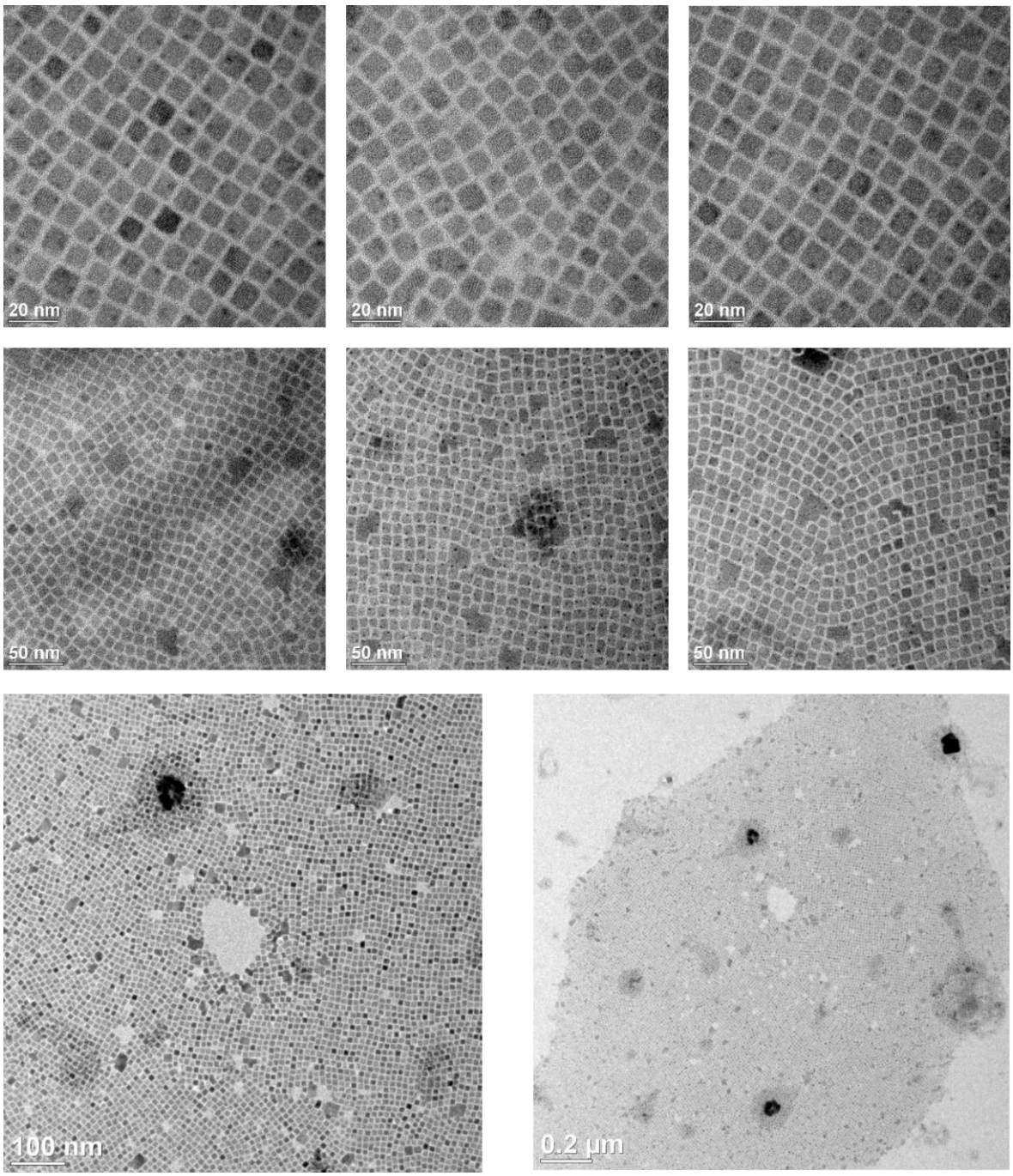

Figure A1: Additional transmission electron microscopes images at various magnifications for the OPA-treated $CsPbBr_3$ nanocrystals studied in Chapter 3.3.2.

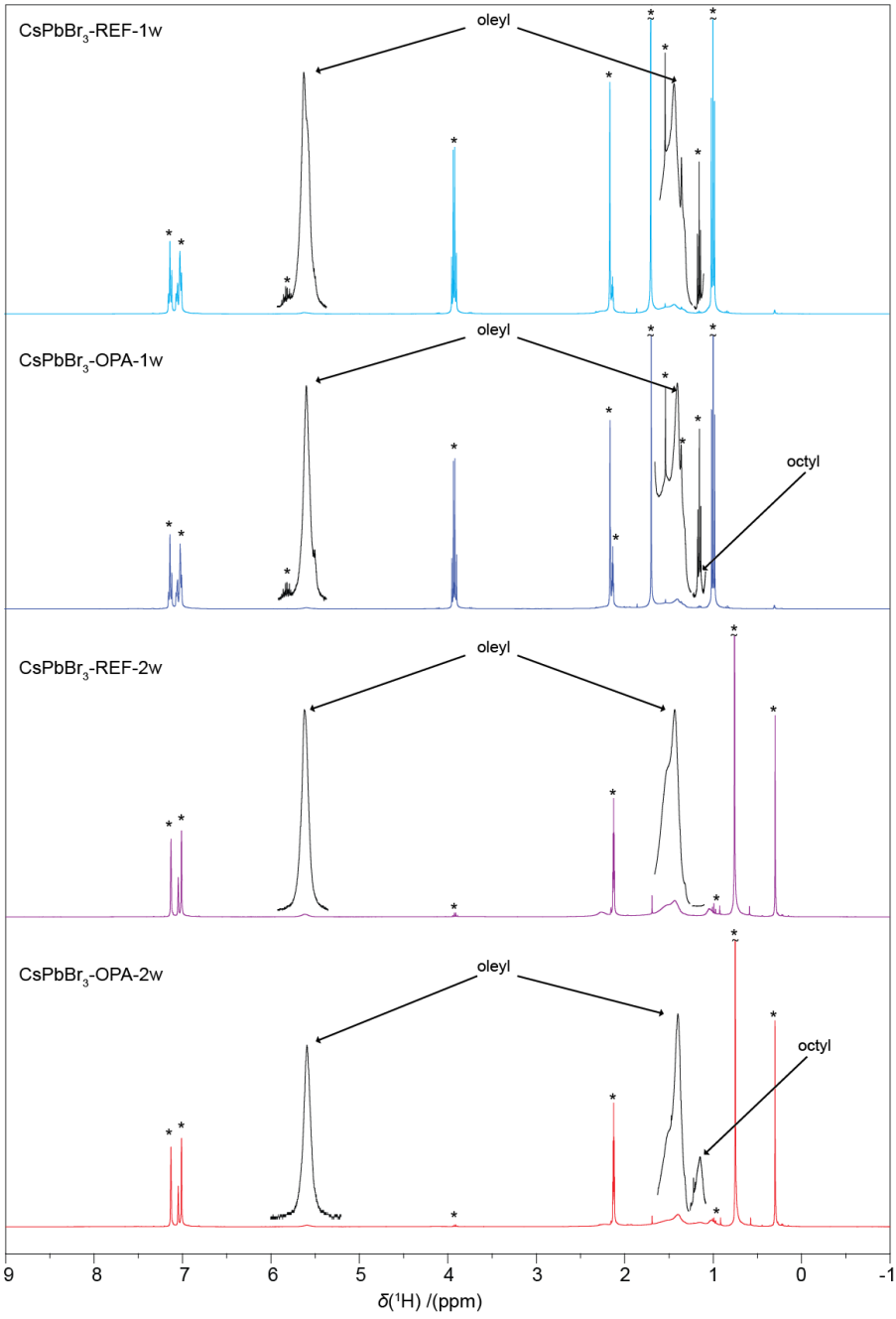

Figure A2: Solution ^{1}H NMR spectra untreated reference (REF) and OPA-treated (OPA) $CsPbBr_3$ NC solutions, after the first (1w) and second (2w) antisolvent washing steps.

Asterisks (*) denote residual proton signals from the solvent (toluene-d8, toluene) and the antisolvents (ethyl acetate and acetonitrile). Observable broad resonances corresponding to protons in oleyl and octyl chains of the respective bound ligands (OLA/OA and OPA) are labelled.

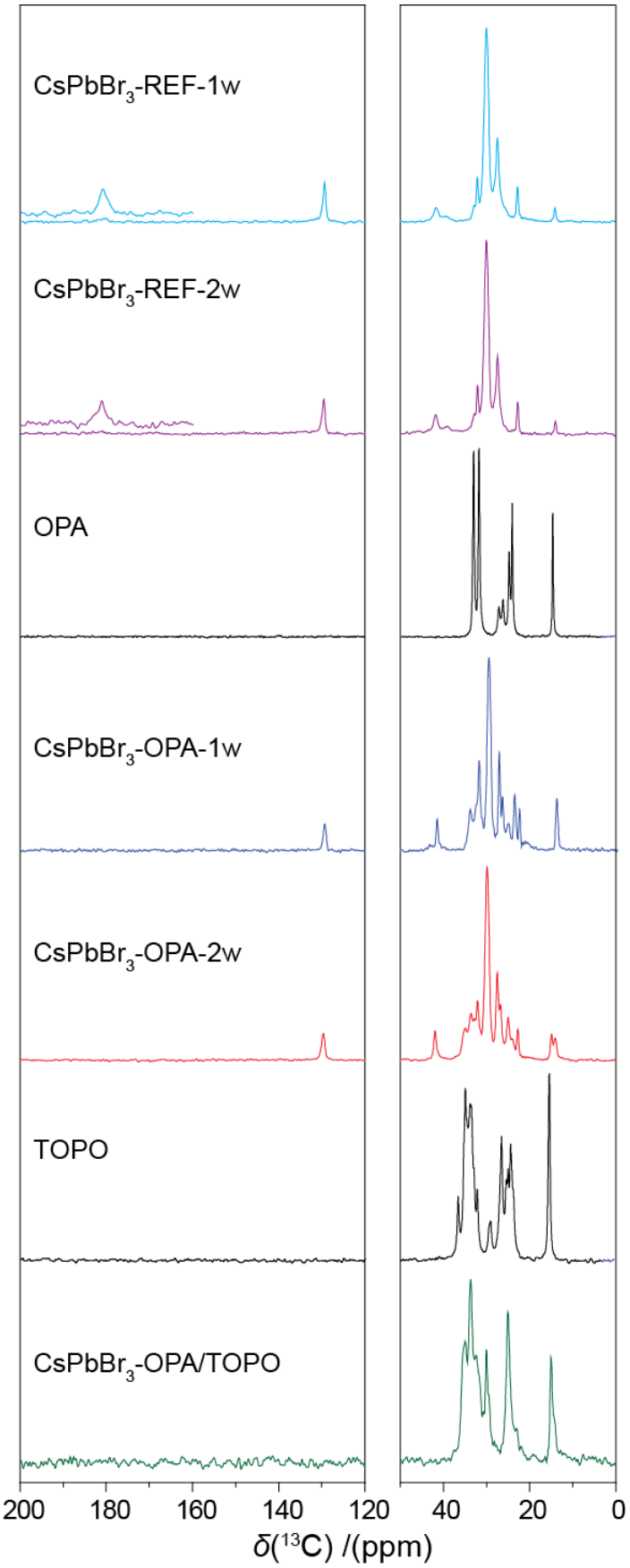

Figure A3: **^{13}C cross-polarization magic-angle spinning (CPMAS) NMR spectra**

Crystalline OPA and TOPO, and the untreated and OPA-treated $CsPbBr_3$ NC samples are shown.

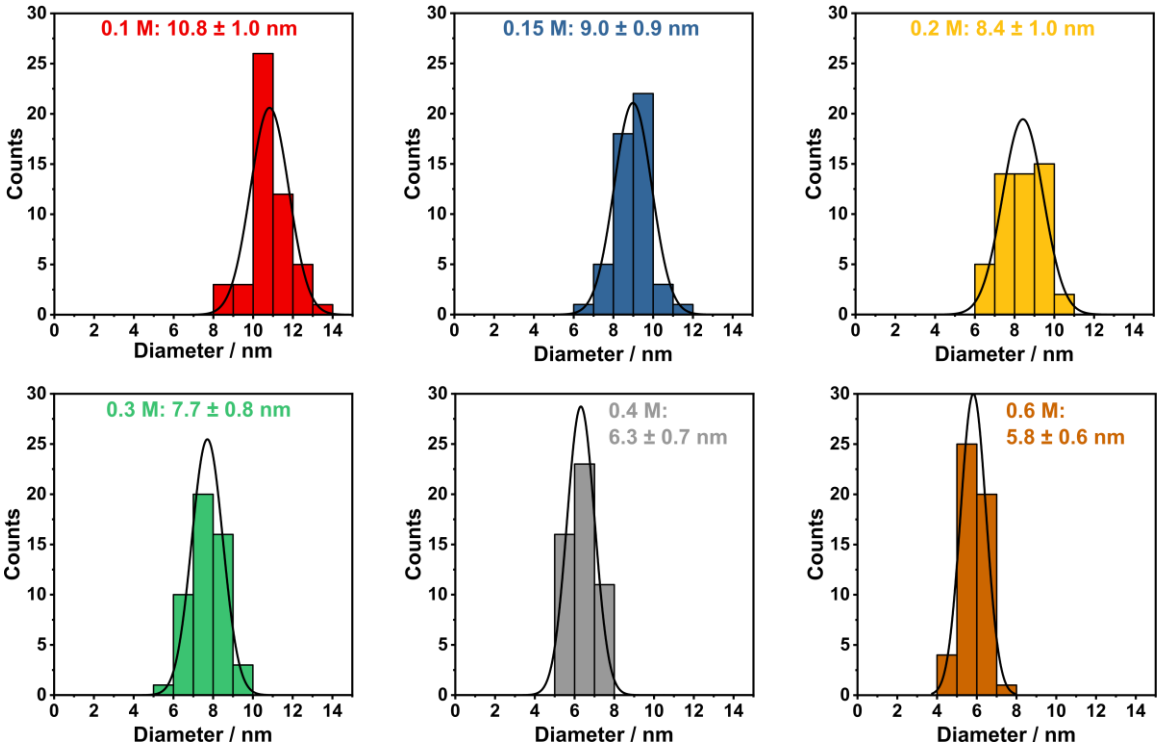

Figure A4: The corresponding histograms for the TEM images of $CsPbBr_3$ nanocrystals synthesised at room temperature with various [OPA], presented in Figure 5.9

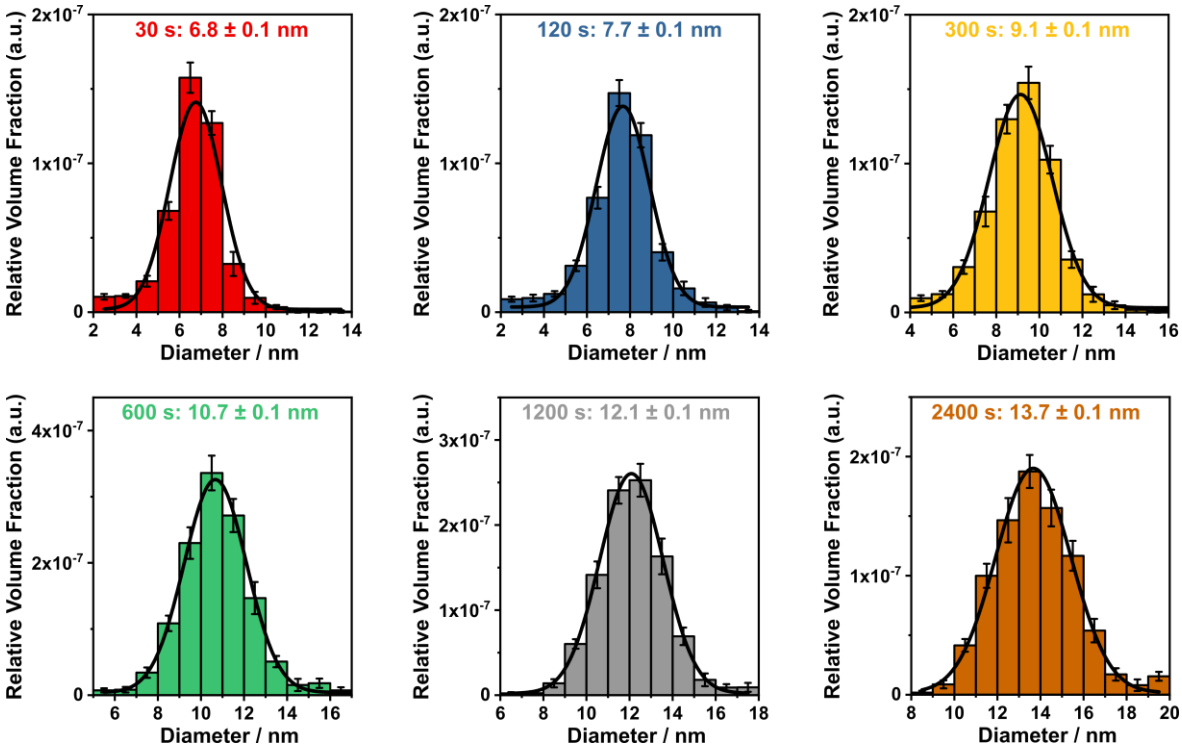

Figure A5: Nanocrystal size distributions extracted from small-angle X-ray scattering measurements performed on $CsPbBr_3$ nanocrystal dispersions synthesised with different growth durations

For all samples, [OPA] = 0.3 M. The mean nanocrystal diameter and the corresponding standard deviation are shown on each plot.

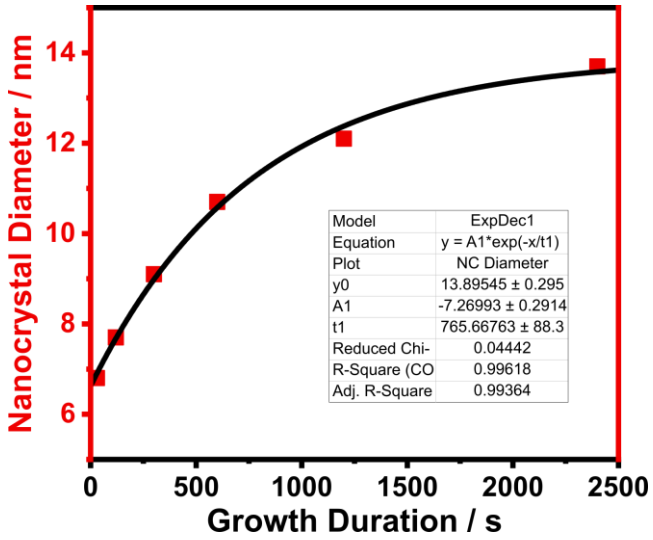

Figure A6: The fitting of an exponential function to the plot of $CsPbBr_3$ nanocrystal diameter against the growth duration

Bibliography

1 Q. A. Akkerman, G. Rainò, M. V. Kovalenko and L. Manna, *Nat. Mater.*, 2018, **17**, 394–405.

2 S. A. Veldhuis, P. P. Boix, N. Yantara, M. Li, T. C. Sum, N. Mathews and S. G. Mhaisalkar, *Adv. Mater.*, 2016, **28**, 6804–6834.

3 C. H. A. Li, Z. Zhou, P. Vashishtha and J. E. Halpert, *Chem. Mater.*, 2019, **31**, 6003–6032.

4 M. V Kovalenko, L. Protesescu and M. I. Bodnarchuk, *Science (80-.).*, 2017, **358**, 745–750.

5 G. Almeida, I. Infante and L. Manna, *Science (80-.).*, 2019, **364**, 833–834.

6 M. Liu, H. Zhang, D. Gedamu, P. Fourmont, H. Rekola, A. Hiltunen, S. G. Cloutier, R. Nechache, A. Priimagi and P. Vivo, *Small*, 2019, **15**, 1–29.

7 X. Li, Y. Wu, S. Zhang, B. Cai, Y. Gu, J. Song and H. Zeng, *Adv. Funct. Mater.*, 2016, **26**, 2435–2445.

8 M. Lu, Y. Zhang, S. Wang, J. Guo, W. W. Yu and A. L. Rogach, *Adv. Funct. Mater.*, 2019, **29**, 1–35.

9 H. Lee, J. Park, S. Kim, S. C. Lee, Y. H. Kim and T. W. Lee, *Adv. Mater. Technol.*, 2020, **2000091**, 1–19.

10 X. Wang, Z. Bao, Y.-C. Chang and R.-S. Liu, *ACS Energy Lett.*, 2020, 3374–3396.

11 T. Leijtens, K. Bush, R. Cheacharoen, R. Beal, A. Bowring and M. D. McGehee, *J. Mater. Chem. A*, 2017, **5**, 11483–11500.

12 S. H. Turren-Cruz, A. Hagfeldt and M. Saliba, *Science (80-.).*, 2018, **362**, 449–453.

13 M. Saliba, T. Matsui, J. Y. Seo, K. Domanski, J. P. Correa-Baena, M. K. Nazeeruddin, S. M. Zakeeruddin, W. Tress, A. Abate, A. Hagfeldt and M. Grätzel, *Energy Environ. Sci.*, 2016, **9**, 1989–1997.

14 L. Protesescu, S. Yakunin, M. I. Bodnarchuk, F. Krieg, R. Caputo, C. H. Hendon, R. X. Yang, A. Walsh and M. V. Kovalenko, *Nano Lett.*, 2015, **15**, 3692–3696.

15 M. Imran, V. Caligiuri, M. Wang, L. Goldoni, M. Prato, R. Krahne, L. De Trizio and L. Manna, *J. Am. Chem. Soc.*, 2018, **140**, 2656–2664.

16 K. Brooks, *Geol. Today*, 2020, **36**, 33–38.

17 H.-R. Wenk and A. Bulakh, *Minerals: their constitution and origin*, Cambridge University Press, 2004, vol. 42.

18 B. Jiang, J. Iocozzia, L. Zhao, H. Zhang, Y. W. Harn, Y. Chen and Z. Lin, *Chem. Soc. Rev.*, 2019, **48**, 1194–1228.

19 M. K. Wu, J. R. Ashburn, C. J. Torng, P. H. Hor, R. L. Meng, L. Gao, Z. J. Huang, Y. Q. Wang and C. W. Chu, *Phys. Rev. Lett.*, 1987, **58**, 908–910.

20 M. R. Ibarra and J. M. De Teresa, *J. Magn. Magn. Mater.*, 1998, **177**–**181**, 846–849.

21 A. Kojima, K. Teshima, Y. Shirai and T. Miyasaka, *J. Am. Chem. Soc.*, 2009, **131**, 6050–6051.

22 E. M. Anastassakis and J. D. Joannopoulos, *The Physics of Semiconductors*, Springer International Publishing, 3rd edn., 1990.

23 P. W. Atkins, T. L. Overton, J. P. Rourke, M. T. Weller and F. A. Armstrong, *Inorganic chemistry*, Oxford University Press, Fifth., 2010.

24 C. Kittel, *Introduction to Solid State Physics, 8th edition*, John Wiley & Son, 8th edn., 2004.

25 A. P. Alivisatos, *J. Phys. Chem.*, 1996, **100**, 13226–13239.

26 F. T. Rabouw and C. de Mello Donega, *Top. Curr. Chem.*, 2016, **374**, 1–30.

27 D. V. Talapin, J. S. Lee, M. V. Kovalenko and E. V. Shevchenko, *Chem. Rev.*, 2010, **110**, 389–458.

28 T. D. Krauss and J. J. Peterson, in *Colloidal Quantum Dot Optoelectronics and Photovoltaics*, eds. G. Konstantatos and E. H. Sargent, Cambridge University Press, 2013, pp. 59–86.

29 J. Butkus, P. Vashishtha, K. Chen, J. K. Gallaher, S. K. K. Prasad, D. Z. Metin, G. Laufersky, N. Gaston, J. E. Halpert and J. M. Hodgkiss, *Chem. Mater.*, 2017, **29**, 3644–3652.

30 J. W. Mullin, *Crystallization*, Elsevier, 2001.

31 S. G. Kwon and T. Hyeon, *Small*, 2011, **7**, 2685–2702.

32 R. Becker and W. Döring, *Ann. Phys.*, 1935, **416**, 719–752.

33 N. T. K. Thanh, N. Maclean and S. Mahiddine, *Chem. Rev.*, 2014, **114**, 7610–7630.

34 V. K. Lamer and R. H. Dinegar, *J. Am. Chem. Soc.*, 1950, **72**, 4847–4854.

35 V. K. La Mer, *Ind. Eng. Chem.*, 1952, **44**, 1270–1277.

36 M. Sessolo, M.-G. La-Placa, L. Martínez-Sarti and H. J. Bolink, in *Halide Perovskites*, 2018, 199–221.

37 S. D. Stranks, R. L. Z. Hoye, D. Di, R. H. Friend and F. Deschler, *Adv. Mater.*, 2019, **31**, 1803336.

38 G. Xing, B. Wu, X. Wu, M. Li, B. Du, Q. Wei, J. Guo, E. K. L. Yeow, T. C. Sum and W. Huang, *Nat. Commun.*, 2017, **8**, 14558.

39 P. Vashishtha, M. Ng, S. B. Shivarudraiah and J. E. Halpert, *Chem. Mater.*, 2019, **31**, 83–89.

40 S. Körbel, M. A. L. Marques and S. Botti, *J. Mater. Chem. C*, 2016, **4**, 3157–3167.

41 M. R. Filip and F. Giustino, *J. Phys. Chem. C*, 2016, **120**, 166–173.

42 H. Lin, C. Zhou, Y. Tian, T. Siegrist and B. Ma, *ACS Energy Lett.*, 2018, **3**, 54–62.

43 K. Hong, Q. Van Le, S. Y. Kim and H. W. Jang, *J. Mater. Chem. C*, 2018, **6**, 2189–2209.

44 V. M. Goldschmidt, *Nat. Sci.*, 1926, **14**, 477–485.

45 D. B. Mitzi, *Synthesis, structure, and properties of organic-inorganic perovskites and related materials*, 2007, vol. 48.

46 J. Feng and B. Xiao, *J. Phys. Chem. Lett.*, 2014, **5**, 1278–1282.

47 W. Travis, E. N. K. Glover, H. Bronstein, D. O. Scanlon and R. G. Palgrave, *Chem. Sci.*, 2016, **7**, 4548–4556.

48 Y. Shi, J. Xi, T. Lei, F. Yuan, J. Dai, C. Ran, H. Dong, B. Jiao, X. Hou and Z. Wu, *ACS Appl. Mater. Interfaces*, 2018, **10**, 9849–9857.

49 Y. Hu, E. M. Hutter, P. Rieder, I. Grill, J. Hanisch, M. F. Aygüler, A. G. Hufnagel, M. Handloser, T. Bein, A. Hartschuh, K. Tvingstedt, V. Dyakonov, A. Baumann, T. J. Savenije, M. L. Petrus and P. Docampo, *Adv. Energy Mater.*, 2018, **8**, 1703057.

50 A. Kanwat, E. Moyen, S. Cho and J. Jang, *ACS Appl. Mater. Interfaces*, 2018, **10**, 16852–16860.

51 R. E. Brandt, V. Stevanović, D. S. Ginley and T. Buonassisi, *MRS Commun.*, 2015, **5**, 265–275.

52 Q. Chen, N. De Marco, Y. Yang, T. Bin Song, C. C. Chen, H. Zhao, Z. Hong, H. Zhou and Y. Yang, *Nano Today*, 2015, **10**, 355–396.

53 P. Gao, M. Grätzel and M. K. Nazeeruddin, *Energy Environ. Sci.*, 2014, **7**, 2448–2463.

54 J. P. Correa-Baena, A. Abate, M. Saliba, W. Tress, T. Jesper Jacobsson, M. Grätzel and A. Hagfeldt, *Energy Environ. Sci.*, 2017, **10**, 710–727.

55 M. T. Weller, O. J. Weber, J. M. Frost and A. Walsh, *J. Phys. Chem. Lett.*, 2015, **6**, 3209–3212.

56 J. K. Chen, J. P. Ma, S. Q. Guo, Y. M. Chen, Q. Zhao, B. Bin Zhang, Z. Y. Li, Y. Zhou, J. Hou, Y. Kuroiwa, C. Moriyoshi, O. M. Bakr, J. Zhang and H. T. Sun, *Chem. Mater.*, 2019, **31**, 3974–3983.

57 J. Kang and L. W. Wang, *J. Phys. Chem. Lett.*, 2017, **8**, 489–493.

58 H. S. Kim, C. R. Lee, J. H. Im, K. B. Lee, T. Moehl, A. Marchioro, S. J. Moon, R. Humphry-Baker, J. H. Yum, J. E. Moser, M. Grätzel and N. G. Park, *Sci. Rep.*, 2012, **2**, 591.

59 M. M. Lee, J. Teuscher, T. Miyasaka, T. N. Murakami and H. J. Snaith, *Science (80-.).*, 2012, **338**, 643–647.

60 NREL National Renewable Energy Laboratory, NREL Efficiency chart, http://www.nrel.gov/ncpv/images/efficiency_chart.jpg.

61 J. Cook, N. Oreskes, P. T. Doran, W. R. L. Anderegg, B. Verheggen, E. W. Maibach, J. S. Carlton, S. Lewandowsky, A. G. Skuce, S. A. Green, D. Nuccitelli, P. Jacobs, M. Richardson, B. Winkler, R. Painting and K. Rice, *Environ. Res. Lett.*, 2016, **11**, 048002.

62 H. Kim, J. S. Han, J. Choi, S. Y. Kim and H. W. Jang, *Small Methods*, 2018, **2**, 1700310.

63 H. Wang and D. H. Kim, *Chem. Soc. Rev.*, 2017, **46**, 5204–5236.

64 Y. Li, Z. F. Shi, X. J. Li and C. X. Shan, *Chinese Phys. B*, 2019, **28**, 017803.

65 X. Wang, M. Li, B. Zhang, H. Wang, Y. Zhao and B. Wang, *Org. Electron.*, 2018, **52**, 172–183.

66 G. Li, M. Price and F. Deschler, *APL Mater.*, 2016, **4**, 091507.

67 Z. Zhu, Q. Sun, Z. Zhang, J. Dai, G. Xing, S. Li, X. Huang and W. Huang, *J. Mater. Chem. C*, 2018, **6**, 10121–10137.

68 M. A. Stoeckel, M. Gobbi, S. Bonacchi, F. Liscio, L. Ferlauto, E. Orgiu and P. Samorì, *Adv. Mater.*, 2017, **29**, 1702469.

69 V. B. Mykhaylyk, H. Kraus and M. Saliba, *Mater. Horizons*, 2019, **6**, 1740–1747.

70 X. Liu, D. Yu, X. Song and H. Zeng, *Small*, 2018, **14**, 1801460.

71 Z. K. Tan, R. S. Moghaddam, M. L. Lai, P. Docampo, R. Higler, F. Deschler, M. Price, A. Sadhanala, L. M. Pazos, D. Credgington, F. Hanusch, T. Bein, H. J. Snaith and R. H. Friend, *Nat. Nanotechnol.*, 2014, **9**, 687–692.

72 E. J. Juarez-Perez, Z. Hawash, S. R. Raga, L. K. Ono and Y. Qi, *Energy Environ. Sci.*, 2016, **9**, 3406–3410.

73 A. Latini, G. Gigli and A. Ciccioli, *Sustain. Energy Fuels*, 2017, **1**, 1351–1357.

74 J. W. Lee, D. H. Kim, H. S. Kim, S. W. Seo, S. M. Cho and N. G. Park, *Adv. Energy Mater.*, 2015, **5**, 1501310.

75 R. J. Sutton, G. E. Eperon, L. Miranda, E. S. Parrott, B. A. Kamino, J. B. Patel, M. T. Hörantner, M. B. Johnston, A. A. Haghighirad, D. T. Moore and H. J. Snaith, *Adv. Energy Mater.*, 2016, **6**, 1502458.

76 M. Kulbak, S. Gupta, N. Kedem, I. Levine, T. Bendikov, G. Hodes and D. Cahen, *J. Phys. Chem. Lett.*, 2016, **7**, 167–172.

77 T. Matsui, J. Y. Seo, M. Saliba, S. M. Zakeeruddin and M. Grätzel, *Adv. Mater.*, 2017, **29**, 2–6.

78 P. Cottingham and R. L. Brutchey, *Chem. Mater.*, 2018, **30**, 6711–6716.

79 Y. Zhou and Y. Zhao, *Energy Environ. Sci.*, 2019, **12**, 1495–1511.

80 W. Huang, S. Sadhu and S. Ptasinska, *Chem. Mater.*, 2017, **29**, 8478–8485.

81 J. A. Christians, P. A. Miranda Herrera and P. V. Kamat, *J. Am. Chem. Soc.*, 2015, **137**, 1530–1538.

82 T. A. Berhe, W. N. Su, C. H. Chen, C. J. Pan, J. H. Cheng, H. M. Chen, M. C. Tsai, L. Y. Chen, A. A. Dubale and B. J. Hwang, *Energy Environ. Sci.*, 2016, **9**, 323–356.

83 N. Aristidou, I. Sanchez-Molina, T. Chotchuangchutchaval, M. Brown, L. Martinez, T. Rath and S. A. Haque, *Angew. Chemie - Int. Ed.*, 2015, **54**, 8208–8212.

84 X. X. Gao, W. Luo, Y. Zhang, R. Hu, B. Zhang, A. Züttel, Y. Feng and M. K. Nazeeruddin, *Adv. Mater.*, 2020, **32**, 1–9.

85 X. Y. Chin, A. Perumal, A. Bruno, N. Yantara, S. A. Veldhuis, L. Martínez-Sarti, B. Chandran, V. Chirvony, A. S. Z. Lo, J. So, C. Soci, M. Grätzel, H. J. Bolink, N. Mathews and S. G. Mhaisalkar,

Energy Environ. Sci., 2018, **11**, 1770–1778.

86 S. A. Veldhuis, Y. F. Ng, R. Ahmad, A. Bruno, N. F. Jamaludin, B. Damodaran, N. Mathews and S. G. Mhaisalkar, *ACS Energy Lett.*, 2018, **3**, 526–531.

87 P. Vashishtha and J. E. Halpert, *Chem. Mater.*, 2017, **29**, 5965–5973.

88 L. Zhao, K. M. Lee, K. Roh, S. U. Z. Khan and B. P. Rand, *Adv. Mater.*, 2019, **31**, 1–6.

89 G. Divitini, S. Cacovich, F. Matteocci, L. Cinà, A. Di Carlo and C. Ducati, *Nat. Energy*, 2016, **1**, 15012.

90 C. C. Stoumpos, C. D. Malliakas and M. G. Kanatzidis, *Inorg. Chem.*, 2013, **52**, 9019–9038.

91 G. Xing, N. Mathews, S. Sun, S. S. Lim, Y. M. Lam, M. Graẗzel, S. Mhaisalkar and T. C. Sum, *Science (80-.).*, 2013, **342**, 344–347.

92 G. Hodes and P. V. Kamat, *J. Phys. Chem. Lett.*, 2015, **6**, 4090–4092.

93 C. Wehrenfennig, G. E. Eperon, M. B. Johnston, H. J. Snaith and L. M. Herz, *Adv. Mater.*, 2014, **26**, 1584–1589.

94 B. Zorman, M. V. Ramakrishna and R. A. Friesner, *J. Phys. Chem.*, 1995, **99**, 7649–7653.

95 J. Rivnay, S. Inal, B. A. Collins, M. Sessolo, E. Stavrinidou, X. Strakosas, C. Tassone, D. M. Delongchamp and G. G. Malliaras, *Nat. Commun.*, 2016, **7**, 1–9.

96 X. Peng, M. C. Schlamp, A. V. Kadavanich and A. P. Alivisatos, *J. Am. Chem. Soc.*, 1997, **119**, 7019–7029.

97 M. I. Bodnarchuk, S. C. Boehme, S. Ten Brinck, C. Bernasconi, Y. Shynkarenko, F. Krieg, R. Widmer, B. Aeschlimann, D. Günther, M. V. Kovalenko and I. Infante, *ACS Energy Lett.*, 2019, **4**, 63–74.

98 Y. Dong, Y. Wang, F. Yuan, A. Johnston, Y. Liu, D. Ma, M. Choi, B. Chen, M. Chekini, S. Baek, L. K. Sagar, J. Fan, Y. Hou, M. Wu, S. Lee, B. Sun, S. Hoogland, R. Quintero-bermudez, H. Ebe, P. Todorovic, F. Dinic, P. Li, H. T. Kung, M. I. Saidaminov, E. Kumacheva, E. Spiecker, L. Liao, O. Voznyy, Z. Lu and E. H. Sargent, *Nat. Nanotechnol.*, 2020, 1–7.

99 J. H. Park, A. Y. Lee, J. C. Yu, Y. S. Nam, Y. Choi, J. Park and M. H. Song, *ACS Appl. Mater. Interfaces*, 2019, **11**, 8428–8435.

100 J. Song, J. Li, L. Xu, J. Li, F. Zhang, B. Han, Q. Shan and H. Zeng, *Adv. Mater.*, 2018, **30**, 1800764.

101 T. Udayabhaskararao, M. Kazes, L. Houben, H. Lin and D. Oron, *Chem. Mater.*, 2017, **29**, 1302–1308.

102 J. Cho and S. Banerjee, *Chem. Mater.*, 2018, **30**, 6144–6155.

103 T. Chiba, Y. Hayashi, H. Ebe, K. Hoshi, J. Sato, S. Sato, Y. J. Pu, S. Ohisa and J. Kido, *Nat. Photonics*, 2018, **12**, 681–687.

104 Y.-H. Kim, S. Kim, A. Kakekhani, J. Park, J. Park, Y.-H. Lee, H. Xu, S. Nagane, R. B. Wexler, D.-H. Kim, S. H. Jo, L. Martínez-Sarti, P. Tan, A. Sadhanala, G. Park, Y. Kim, B. Hu, H. J. Bolink, S. Yoo, R. H. Friend, A. M. Rappe and T. Lee, *Nat. Photonics*, , DOI:10.1038/s41566-020-00732-4.

105 Z. He, C. Wang, J. Zhao, X. Du, H. Yang, P. Zhong, C. Zheng, H. Lin, S. Tao and X. Zhang, *J. Mater. Chem. C*, 2019, **7**, 11806–11812.

106 H. Shen, Q. Gao, Y. Zhang, Y. Lin, Q. Lin, Z. Li, L. Chen, Z. Zeng, X. Li, Y. Jia, S. Wang, Z. Du, L. S. Li and Z. Zhang, *Nat. Photonics*, 2019, **13**, 192–197.

107 S. Sudheendran Swayamprabha, D. K. Dubey, Shahnawaz, R. A. K. Yadav, M. R. Nagar, A. Sharma, F. C. Tung and J. H. Jou, *Adv. Sci.*, 2021, **8**, 1–29.

108 Y.-K. Kuo, T.-H. Wang and J.-Y. Chang, *Appl. Phys. Lett.*, 2012, **100**, 031112.

109 Z. Wu, P. Liu, W. Zhang, K. Wang and X. W. Sun, *ACS Energy Lett.*, 2020, **5**, 1095–1106.

110 Y. H. Won, O. Cho, T. Kim, D. Y. Chung, T. Kim, H. Chung, H. Jang, J. Lee, D. Kim and E. Jang, *Nature*, 2019, **575**, 634–638.

111 E. Jang, Y. Kim, Y. H. Won, H. Jang and S. M. Choi, *ACS Energy Lett.*, 2020, **5**, 1316–1327.

112 A. A. M. Brown, B. Damodaran, L. Jiang, J. N. Tey, S. H. Pu, N. Mathews and S. G. Mhaisalkar, *Adv. Energy Mater.*, 2020, **10**, 1–19.

113 D. P. Nenon, K. Pressler, J. Kang, B. A. Koscher, J. H. Olshansky, W. T. Osowiecki, M. A. Koc, L. W. Wang and A. P. Alivisatos, *J. Am. Chem. Soc.*, 2018, **140**, 17760–17772.

114 S. R. Smock, T. J. Williams and R. L. Brutchey, *Angew. Chemie - Int. Ed.*, 2018, **57**, 11711–11715.

115 Y. Yang, H. Qin, M. Jiang, L. Lin, T. Fu, X. Dai, Z. Zhang, Y. Niu, H. Cao, Y. Jin, F. Zhao and X. Peng, *Nano Lett.*, 2016, **16**, 2133–2138.

116 J. Li, L. Xu, T. Wang, J. Song, J. Chen, J. Xue, Y. Dong, B. Cai, Q. Shan, B. Han and H. Zeng, *Adv. Mater.*, 2017, **29**, 1603885.

117 T. Chiba, K. Hoshi, Y. J. Pu, Y. Takeda, Y. Hayashi, S. Ohisa, S. Kawata and J. Kido, *ACS Appl. Mater. Interfaces*, 2017, **9**, 18054–18060.

118 K. Hoshi, T. Chiba, J. Sato, Y. Hayashi, Y. Takahashi, H. Ebe, S. Ohisa and J. Kido, *ACS Appl. Mater. Interfaces*, 2018, **10**, 24607–24612.

119 S. Wei, Y. Yang, X. Kang, L. Wang, L. Huang and D. Pan, *Inorg. Chem.*, 2017, **56**, 2596–2601.

120 L. C. Schmidt, A. Pertegás, S. González-Carrero, O. Malinkiewicz, S. Agouram, G. Mínguez Espallargas, H. J. Bolink, R. E. Galian and J. Pérez-Prieto, *J. Am. Chem. Soc.*, 2014, **136**, 850–853.

121 F. Zhang, H. Zhong, C. Chen, X. G. Wu, X. Hu, H. Huang, J. Han, B. Zou and Y. Dong, *ACS Nano*, 2015, **9**, 4533–4542.

122 Y. Hassan, O. J. Ashton, J. H. Park, G. Li, N. Sakai, B. Wenger, A. A. Haghighirad, N. K. Noel, M. H. Song, B. R. Lee, R. H. Friend and H. J. Snaith, *J. Am. Chem. Soc.*, 2019, **141**, 1269–1279.

123 H. Huang, J. Raith, S. V. Kershaw, S. Kalytchuk, O. Tomanec, L. Jing, A. S. Susha, R. Zboril and A. L. Rogach, *Nat. Commun.*, 2017, **8**, 996.

124 H. Sun, Z. Yang, M. Wei, W. Sun, X. Li, S. Ye, Y. Zhao, H. Tan, E. L. Kynaston, T. B. Schon, H. Yan, Z. H. Lu, G. A. Ozin, E. H. Sargent and D. S. Seferos, *Adv. Mater.*, 2017, **29**, 1701153.

125 L. Protesescu, S. Yakunin, M. I. Bodnarchuk, F. Bertolotti, N. Masciocchi, A. Guagliardi and M. V. Kovalenko, *J. Am. Chem. Soc.*, 2016, **138**, 14202–14205.

126 F. Yang, H. Chen, R. Zhang, X. Liu, W. Zhang, J. Bin Zhang, F. Gao and L. Wang, *Adv. Funct. Mater.*, 2020, **30**, 1908760.

127 J. Park, H. M. Jang, S. Kim, S. H. Jo and T. W. Lee, *Trends Chem.*, 2020, 1–13.

128 J. Pan, L. N. Quan, Y. Zhao, W. Peng, B. Murali, S. P. Sarmah, M. Yuan, L. Sinatra, N. M. Alyami, J. Liu, E. Yassitepe, Z. Yang, O. Voznyy, R. Comin, M. N. Hedhili, O. F. Mohammed, Z. H. Lu, D. H. Kim, E. H. Sargent and O. M. Bakr, *Adv. Mater.*, 2016, **28**, 8718–8725.

129 L. Xu, J. Li, B. Cai, J. Song, F. Zhang, T. Fang and H. Zeng, *Nat. Commun.*, 2020, **11**, 1–12.

130 Q. Zhao, A. Hazarika, X. Chen, S. P. Harvey, B. W. Larson, G. R. Teeter, J. Liu, T. Song, C. Xiao, L. Shaw, M. Zhang, G. Li, M. C. Beard and J. M. Luther, *Nat. Commun.*, 2019, **10**, 2842.

131 G. Almeida, O. J. Ashton, L. Goldoni, D. Maggioni, U. Petralanda, N. Mishra, Q. A. Akkerman, I. Infante, H. J. Snaith and L. Manna, *J. Am. Chem. Soc.*, 2018, **140**, 14878–14886.

132 J. Li, D. Yim, W. D. Jang and J. Yoon, *Chem. Soc. Rev.*, 2017, **46**, 2437–2458.

133 E. Moyen, A. Kanwat, S. Cho, H. Jun, R. Aad and J. Jang, *Nanoscale*, 2018, **10**, 8591–8599.

134 E. Moyen, H. Jun, H. M. Kim and J. Jang, *ACS Appl. Mater. Interfaces*, 2018, **10**, 42647–42656.

135 Y. Zou, M. Ban, W. Cui, Q. Huang, C. Wu, J. Liu, H. Wu, T. Song and B. Sun, *Adv. Funct. Mater.*, 2017, **27**, 1603325.

136 Q. A. Akkerman, M. Gandini, F. Di Stasio, P. Rastogi, F. Palazon, G. Bertoni, J. M. Ball, M. Prato, A. Petrozza and L. Manna, *Nat. Energy*, 2017, **2**, 16194.

137 F. Ye, H. Zhang, W. Li, Y. Yan, J. Cai, R. S. Gurney, A. J. Pearson, D. Liu and T. Wang, *Small Methods*, 2019, **3**, 1800489.

138 J. Pan, Y. Shang, J. Yin, M. De Bastiani, W. Peng, I. Dursun, L. Sinatra, A. M. El-Zohry, M. N. Hedhili, A. H. Emwas, O. F. Mohammed, Z. Ning and O. M. Bakr, *J. Am. Chem. Soc.*, 2018, **140**, 562–565.

139 H. Wu, Y. Zhang, M. Lu, X. Zhang, C. Sun, T. Zhang, V. L. Colvin and W. W. Yu, *Nanoscale*, 2018, **10**, 4173–4178.

140 A. A. M. Brown, T. J. N. Hooper, S. A. Veldhuis, X. Y. Chin, A. Bruno, P. Vashishtha, J. N. Tey, L. Jiang, B. Damodaran, S. H. Pu, S. G. Mhaisalkar and N. Mathews, *Nanoscale*, 2019, **11**, 12370–12380.

141 D. Yang, X. Li, W. Zhou, S. Zhang, C. Meng, Y. Wu, Y. Wang and H. Zeng, *Adv. Mater.*, 2019, **31**, 1900767.

142 B. Zhang, L. Goldoni, J. Zito, Z. Dang, G. Almeida, F. Zaccaria, J. De Wit, I. Infante, L. De Trizio and L. Manna, *Chem. Mater.*, 2019, **31**, 9140–9147.

143 J. N. Yang, Y. Song, J. S. Yao, K. H. Wang, J. J. Wang, B. S. Zhu, M. M. Yao, S. U. Rahman, Y. F. Lan, F. J. Fan and H. Bin Yao, *J. Am. Chem. Soc.*, 2020, **142**, 2956–2967.

144 P. Todorović, D. Ma, B. Chen, R. Quintero-Bermudez, M. I. Saidaminov, Y. Dong, Z. H. Lu and E. H. Sargent, *Adv. Opt. Mater.*, 2019, **7**, 1901440.

145 Y. Tan, Y. Zou, L. Wu, Q. Huang, D. Yang, M. Chen, M. Ban, C. Wu, T. Wu, S. Bai, T. Song, Q. Zhang and B. Sun, *ACS Appl. Mater. Interfaces*, 2018, **10**, 3784–3792.

146 Y. Dong, T. Qiao, D. Kim, D. Parobek, D. Rossi and D. H. Son, *Nano Lett.*, 2018, **18**, 3716–3722.

147 F. Ambroz, W. Xu, S. Gadipelli, D. J. L. Brett, C. T. Lin, C. Contini, M. A. McLachlan, J. R. Durrant, I. P. Parkin and T. J. Macdonald, *Part. Part. Syst. Charact.*, 2020, **37**, 1–10.

148 W. J. Mir, A. Swarnkar and A. Nag, *Nanoscale*, 2019, **11**, 4278–4286.

149 J. De Roo, M. Ibáñez, P. Geiregat, G. Nedelcu, W. Walravens, J. Maes, J. C. Martins, I. Van Driessche, M. V. Kovalenko and Z. Hens, *ACS Nano*, 2016, **10**, 2071–2081.

150 J. Song, T. Fang, J. Li, L. Xu, F. Zhang, B. Han, Q. Shan and H. Zeng, *Adv. Mater.*, 2018, **30**, 1–9.

151 Y. Shynkarenko, M. I. Bodnarchuk, C. Bernasconi, Y. Berezovska, V. Verteletskyi, S. T. Ochsenbein and M. V. Kovalenko, *ACS Energy Lett.*, 2019, **4**, 2703–2711.

152 Y. Yang, H. Qin and X. Peng, *Nano Lett.*, 2016, **16**, 2127–2132.

153 F. Krieg, S. T. Ochsenbein, S. Yakunin, S. Ten Brinck, P. Aellen, A. Süess, B. Clerc, D. Guggisberg, O. Nazarenko, Y. Shynkarenko, S. Kumar, C. J. Shih, I. Infante and M. V. Kovalenko, *ACS Energy Lett.*, 2018, **3**, 641–646.

154 N. N. Greenwood and A. Earnshaw, *Chemistry of the Elements*, Elsevier, 1997.

155 S. T. Ochsenbein, F. Krieg, Y. Shynkarenko, G. Rainò and M. V. Kovalenko, *ACS Appl. Mater. Interfaces*, 2019, **11**, 21655–21660.

156 Y. Zu, J. Xi, L. Li, J. Dai, S. Wang, F. Yun, B. Jiao, H. Dong, X. Hou and Z. Wu, *ACS Appl. Mater. Interfaces*, 2020, **12**, 2835–2841.

157 I. Bressler, B. R. Pauw and A. F. Thünemann, *J. Appl. Crystallogr.*, 2015, **48**, 962–969.

158 G. Almeida, L. Goldoni, Q. Akkerman, Z. Dang, A. H. Khan, S. Marras, I. Moreels and L. Manna, *ACS Nano*, 2018, **12**, 1704–1711.

159 F. Li, Y. Liu, H. Wang, Q. Zhan, Q. Liu and Z. Xia, *Chem. Mater.*, 2018, **30**, 8546–8554.

160 V. K. Ravi, P. K. Santra, N. Joshi, J. Chugh, S. K. Singh, H. Rensmo, P. Ghosh and A. Nag, *J. Phys. Chem. Lett.*, 2017, **8**, 4988–4994.

161 S. K. Davidowski and G. P. Holland, *Langmuir*, 2016, **32**, 3253–3261.

162 D. Geldof, M. Tassi, R. Carleer, P. Adriaensens, A. Roevens, V. Meynen and F. Blockhuys, *Surf. Sci.*, 2017, 655, 31–38.

163 G. P. Holland, R. Sharma, J. O. Agola, S. Amin, V. C. Solomon, P. Singh, D. A. Buttry and J. L. Yarger, *Chem. Mater.*, 2007, **19**, 2519–2526.

164 R. Gomes, A. Hassinen, A. Szczygiel, Q. Zhao, A. Vantomme, J. C. Martins and Z. Hens, *J. Phys. Chem. Lett.*, 2011, **2**, 145–152.

165 J. S. Owen, J. Park, P. E. Trudeau and A. P. Alivisatos, *J. Am. Chem. Soc.*, 2008, **130**, 12279–12281.

166 K. De Keukeleere, S. Coucke, E. De Canck, P. Van Der Voort, F. Delpech, Y. Coppel, Z. Hens, I. Van Driessche, J. S. Owen and J. De Roo, *Chem. Mater.*, 2017, **29**, 10233–10242.

167 J. W. Blanchard, T. L. Groy, J. L. Yarger and G. P. Holland, *J. Phys. Chem. C*, 2012, **116**, 18824–18830.

168 P. Cottingham and R. L. Brutchey, *Chem. Commun.*, 2016, **52**, 5246–5249.

169 F. Brodard-Severac, G. Guerrero, J. Maquet, P. Florian, C. Gervais and P. H. Mutin, *Chem. Mater.*, 2008, **20**, 5191–5196.

170 I. O. Perez De Berti, M. V. Cagnoli, G. Pecchi, J. L. Alessandrini, S. J. Stewart, J. F. Bengoa and S. G. Marchetti, *Nanotechnology*, 2013, **24**, 1–11.

171 L. C. Thomas and R. A. Chittenden, *Spectrochim. Acta*, 1964, **20**, 489–502.

172 L. C. Thomas and R. A. Chittenden, *Spectrochim. Acta*, 1964, **20**, 467–487.

173 T. Fang, T. Wang, X. Li, Y. Dong, S. Bai and J. Song, *Sci. Bull.*, 2020, **3**, 1–8.

174 H. Chen, L. Fan, R. Zhang, C. Bao, H. Zhao, W. Xiang, W. Liu, G. Niu, R. Guo, L. Zhang and L. Wang, *Adv. Opt. Mater.*, 2020, **8**, 1901390.

175 Y. Shen, L. P. Cheng, Y. Q. Li, W. Li, J. De Chen, S. T. Lee and J. X. Tang, *Adv. Mater.*, 2019, **31**, 1901517.

176 F. Yan, S. T. Tan, X. Li and H. V. Demir, *Small*, 2019, **15**, 1902079.

177 L. Zhao, K. Roh, S. Kacmoli, K. Al Kurdi, S. Jhulki, S. Barlow, S. R. Marder, C. Gmachl and B. P. Rand, *Adv. Mater.*, 2020, **32**, 2000752.

178 A. Dutta, R. K. Behera, P. Pal, S. Baitalik and N. Pradhan, *Angew. Chemie - Int. Ed.*, 2019, **58**, 5552–5556.

179 M. Hao, Y. Bai, S. Zeiske, L. Ren, J. Liu, Y. Yuan, N. Zarrabi, N. Cheng, M. Ghasemi, P. Chen, M. Lyu, D. He, J. H. Yun, Y. Du, Y. Wang, S. Ding, A. Armin, P. Meredith, G. Liu, H. M. Cheng and L. Wang, *Nat. Energy*, 2020, **5**, 79–88.

180 L. Protesescu, S. Yakunin, S. Kumar, J. Bär, F. Bertolotti, N. Masciocchi, A. Guagliardi, M. Grotevent, I. Shorubalko, M. I. Bodnarchuk, C. J. Shih and M. V. Kovalenko, *ACS Nano*, 2017, **11**, 3119–3134.

181 P. Vashishtha, S. A. Veldhuis, S. S. H. Dintakurti, N. L. Kelly, B. E. Griffith, A. A. M. Brown, M. S. Ansari, A. Bruno, N. Mathews, Y. Fang, T. White, S. G. Mhaisalkar and J. V Hanna, *J. Mater. Chem. C*, 2020, **8**, 11805–11821.

182 A. Kanwat, N. Yantara, Y. F. Ng, Y. F. Ng, T. J. N. Hooper, P. J. S. Rana, B. Febriansyah, P. C. Harikesh, T. Salim, P. Vashishtha, S. G. Mhaisalkar, S. G. Mhaisalkar, N. Mathews and N. Mathews, *ACS Energy Lett.*, 2020, **5**, 1804–1813.

183 P. Cromwell, in *Polyhedra*, Cambridge University Press, 1999, pp. 79–86.

184 J. Maes, N. Castro, K. De Nolf, W. Walravens, B. Abécassis and Z. Hens, *Chem. Mater.*, 2018, **30**, 3952–3962.

185 O. J. Ashton, A. R. Marshall, J. H. Warby, B. Wenger and H. J. Snaith, *Chem. Mater.*, 2020, **32**, 7172–7180.

186 J. Aneesh, A. Swarnkar, V. Kumar Ravi, R. Sharma, A. Nag and K. V. Adarsh, *J. Phys. Chem. C*, 2017, **121**, 4734–4739.

187 D. Rossi, H. Wang, Y. Dong, T. Qiao, X. Qian and D. H. Son, *ACS Nano*, 2018, **12**, 12436–12443.

188 F. Krieg, Q. K. Ong, M. Burian, G. Rainò, D. Naumenko, H. Amenitsch, A. Süess, M. J. Grotevent, F. Krumeich, M. I. Bodnarchuk, I. Shorubalko, F. Stellacci and M. V. Kovalenko, *J. Am. Chem. Soc.*, 2020, **141**, 19839–19849.

189 J. De Roo, Z. Zhou, J. Wang, L. Deblock, A. J. Crosby, J. S. Owen and S. S. Nonnenmann, *Chem. Mater.*, 2018, **30**, 8034–8039.

190 J. Tong, J. Wu, W. Shen, Y. Zhang, Y. Liu, T. Zhang, S. Nie and Z. Deng, *ACS Appl. Mater. Interfaces*, 2019, **11**, 9317–9325.

191 Q. Zhong, M. Cao, H. Hu, D. Yang, M. Chen, P. Li, L. Wu and Q. Zhang, *ACS Nano*, 2018, **12**, 8579–8587.

192 L. K. Ono, E. J. Juarez-Perez and Y. Qi, *ACS Appl. Mater. Interfaces*, 2017, **9**, 30197–30246.

193 Y. Liu, G. Pan, R. Wang, H. Shao, H. Wang, W. Xu, H. Cui and H. Song, *Nanoscale*, 2018, **10**, 14067–14072.

194 S. Kafashi, M. R. Yaftian and A. A. Zamani, *J. Solution Chem.*, 2015, **44**, 1798–1811.

195 S. C. Erwin, L. Zu, M. I. Haftel, A. L. Efros, T. A. Kennedy and D. J. Norris, *Nature*, 2005, **436**, 91–94.

196 D. J. Norris, A. L. Efros and S. C. Erwin, *Science (80-.).*, 2008, **319**, 1776–1779.

197 A. Dutta, R. K. Behera and N. Pradhan, *ACS Energy Lett.*, 2019, **4**, 926–932.

198 C. Bi, S. Wang, Q. Li, S. V. Kershaw, J. Tian and A. L. Rogach, *J. Phys. Chem. Lett.*, 2019, **10**, 943–952.

199 A. Mahata, D. Meggiolaro and F. De Angelis, *J. Phys. Chem. Lett.*, 2019, **10**, 1790–1798.

200 H. Zhu, K. Miyata, Y. Fu, J. Wang, P. P. Joshi, D. Niesner, K. W. Williams, S. Jin and X. Y. Zhu, *Science (80-.).*, 2016, **353**, 1409–1413.

201 D. J. Kubicki, D. Prochowicz, A. Hofstetter, P. Péchy, S. M. Zakeeruddin, M. Grätzel and L. Emsley, *J. Am. Chem. Soc.*, 2017, **139**, 10055–10061.

202 D. H. Fabini, T. A. Siaw, C. C. Stoumpos, G. Laurita, D. Olds, K. Page, J. G. Hu, M. G. Kanatzidis, S. Han and R. Seshadri, *J. Am. Chem. Soc.*, 2017, **139**, 16875–16884.

203 Y. Galagan, *J. Phys. Chem. Lett.*, 2018, **9**, 4326–4335.

204 N.-G. Park and K. Zhu, *Nat. Rev. Mater.*, 2020, **5**, 333–350.

205 V. Prakasam, D. Tordera, F. Di Giacomo, R. Abbel, A. Langen, G. Gelinck and H. J. Bolink, *J. Mater. Chem. C*, 2019, **7**, 3795–3801.

206 W. Ke and M. G. Kanatzidis, *Nat. Commun.*, 2019, **10**, 1–4.

207 S. Ghosh and B. Pradhan, *ChemNanoMat*, 2019, **5**, 300–312.

208 J. Sun, J. Yang, J. I. Lee, J. H. Cho and M. S. Kang, *J. Phys. Chem. Lett.*, 2018, **9**, 1573–1583.

209 S. Khalfin and Y. Bekenstein, *Nanoscale*, 2019, **11**, 8665–8679.

210 M. M. Yao, L. Wang, J. S. Yao, K. H. Wang, C. Chen, B. S. Zhu, J. N. Yang, J. J. Wang, W. P. Xu, Q. Zhang and H. Bin Yao, *Adv. Opt. Mater.*, 2020, **1901919**, 2–9.

211 Y. Liu, Y. Jing, J. Zhao, Q. Liu and Z. Xia, *Chem. Mater.*, 2019, **31**, 3333–3339.

212 F. Locardi, M. Cirignano, D. Baranov, Z. Dang, M. Prato, F. Drago, M. Ferretti, V. Pinchetti, M. Fanciulli, S. Brovelli, L. De Trizio and L. Manna, *J. Am. Chem. Soc.*, 2018, **140**, 12989–12995.

213 J. Zhang, Y. Yang, H. Deng, U. Farooq, X. Yang, J. Khan, J. Tang and H. Song, *ACS Nano*, 2017, **11**, 9294–9302.

214 M. Leng, Y. Yang, K. Zeng, Z. Chen, Z. Tan, S. Li, J. Li, B. Xu, D. Li, M. P. Hautzinger, Y. Fu, T. Zhai, L. Xu, G. Niu, S. Jin and J. Tang, *Adv. Funct. Mater.*, 2018, **28**, 1–11.

215 B. Yang, X. Mao, F. Hong, W. Meng, Y. Tang, X. Xia, S. Yang, W. Deng and K. Han, *J. Am. Chem. Soc.*, 2018, **140**, 17001–17006.